THE UNIVERSITY *of* EDINBURGH

Nanodeposition and plasmonically enhanced Raman spectroscopy on individual carbon nanotubes

Kirsten M. Strain

A thesis presented for the degree of
Doctor of Philosophy
The University of Edinburgh
2013

Declaration

This thesis has not been previously submitted, in whole or in part, for any degree at this or any other university. The work is original and my own, carried out under the supervision of Prof. Eleanor Campbell; where this is not so, credit has been duly given.

(*Kirsten M. Strain*)

Acknowledgements

If any of you lacks wisdom, let him ask God, who gives generously to all without reproach, and it will be given him. James 1:5

My first thanks go to Eleanor who has been an amazing supervisor for the duration of my Ph.D. She has always made time whenever asked, despite having so many other responsibilities, and had the perfect balance of scientific understanding, critical thinking and motivational words. I consider myself very fortunate to have been her student.

Thanks to the others in Eleanor's research group. In particular, thanks to Oleg for always being ready to give a physics lesson and to Andrei for reminding me it's ok to be a chemist. Thanks to Olof for sharing his enthusiasm for science and sometimes running, to Johan for being my academic big brother, to Gordon for football coaching and to Chaweewan for quiet encouragement and understanding. More recently, thanks to Sasha for sharing in song together, to Arran for maintaining optimism and to Elvira for patience and company in the hard final months. Thanks also to those who were part of the group for a shorter period: Ada, who brought fun, and David, Ben and Alasdair who worked hard under my floundering supervision.

I also want to thank those that made the office a fun place to be, collected postcards, tolerated my Christmas decorations and regularly shared in fika: Craig, David, Matt, Stuart, Paul, Paul, Hayleigh, Xiaojiao, Alasdair, Evert and Alberto. Thanks to the Portobello Mushrooms, the Chemistry Tercentenary Choir, the Phys-Chem meetings participants and to everyone else in the department that

made it a pleasure to work in.

Thanks to NanoSci-Europe for funding the NANOSPEC project, of which my work was part. Thanks also to the other participants of the project with whom interesting discussion was enjoyed, technical and scientific expertise was shared and foreign adventures were had: Aaron, Stephanie, Stefan, Sebastian, Christian, Roberto and Talia.

The support of the Nanonics staff is also worthy of acknowledgement, in particular to Hesham, Yulia and Rimma, who gave their time to help me during my time in Jerusalem and remotely afterwards. In Edinburgh, the help of Steve at the SEM and Andy in the SMC was also appreciated. Johannes and Niklas in Sweden provided important samples, even if they didn't know it at the time.

It would be impossible to name everyone that has made my time in Edinburgh as amazing as it has been. These people are included in, but not limited to, the orienteers of EUOC and SEDS, members of Girlguiding Scotland, especially the 72nd City of Edinburgh Guides, the Thursday hill reps group and those at Charlotte Chapel and Carrubbers Christian Centre.

Among all my friends, particular thanks are due to my flatmates Rachael, Alyssa and Chelsey for their constant support; to Anthony for understanding and proofreading and to Andrew for being there with loving encouragement and hugs, always believing in me more than I did.

Finally, thanks to my family, especially Mum, Dad and Murray, for all forms of support: taking an interest in my research, encouraging and understanding during tough times, taking me out of the city to regular orienteering events and always answering the phone, even past bedtime. Thank you from my heart.

Abstract

Single-walled carbon nanotubes (SWNTs) exhibit extraordinary properties: mechanical, thermal, optical and, possibly the most interesting, electrical. These all-carbon cylindrical structures can be metallic or semi-conducting depending on their precise structure. They have the potential to allow faster transistor switching speeds and smaller, more closely-packed interconnects in microelectronics. However, such applications are hindered by the difficulties of positioning the correct type of SWNT in a spatially precise location and orientation. In addition, greater understanding of the fundamental limits of SWNTs, such as the limit of current density, is needed for optimum operation in applications.

The primary aim of this project was to increase the understanding of current density limitation by using *in situ* plasmonically enhanced Raman spectroscopy during electrical transport. The use of plasmonic metal nanostructures to enhance the Raman scattering should allow the acquisition of informative spectra from SWNTs away from their intrinsic resonance conditions. To achieve this aim, SWNTs must be integrated with plasmonic metal structures as well as electrical connections. This thesis presents two approaches for the integration of SWNTs with other nanometre-scaled features, in particular plasmonic nanoparticles.

Fountain pen nanolithography uses a hollow nanopipette in place of the probe tip in an atomic force microscope (AFM), through which material can be delivered to a spatially precise position on a surface. Aqueous SWNT dispersion was delivered to chemically-functionalised silicon in this way, through pulled quartz pipettes with aperture diameters of 50 nm, 100 nm and 150 nm. The heights, widths and continuity of lines drawn on the surface by the nanopipette depended on the size, setpoint and lateral speed of the tip. A small bias voltage applied

between the SWNT dispersion inside the pipette and the substrate allowed the deposition to be switched on or off depending on the polarity of the voltage, through the action of electroosmotic effects within the quartz capillary. The quality and density of the SWNT dispersion was found to be important for successful deposition to occur, since too low a concentration results in the lines deposited from the pipette being only surfactant but too high a concentration of bundles would quickly block the small tip of the pipette. Polarised Raman spectroscopy on SWNT deposited by fountain pen nanolithography showed that they had a high level of alignment parallel to the direction in which the pipette moved.

Spherical gold nanoparticles with plasmonic properties suitable for enhancing Raman scattering were dropped onto samples containing individual SWNTs supported on a Si/SiO_2 surface. Nanomanipulation with an atomic force microscope was used to push the gold nanoparticles onto the SWNTs. Raman spectra measured with and without the gold particles showed that the gold nanoparticles gave local enhancement factors of 24 for a single 150 nm nanoshell and 130 for a small cluster of 150 nm nanoshells. Polarised Raman studies on the cluster showed that the angle dependence deviated significantly from that expected of a bare SWNT.

Electrical transport experiments with *in situ* plasmonically enhanced Raman spectroscopy may be performed on samples prepared from the methods described here. Such experiments would increase understanding of the electrical properties of SWNTs and how they relate to the vibrational and optical properties.

Lay Summary

Single walled carbon nanotubes (SWNTs) are a novel form of carbon, with hollow cylindrical structures with a diameter of approximately one nanometre (10^{-9} m). An exciting potential application for the future is in micro- or nano-electronics, where they could enable faster and smaller microprocessors. For this to become a reality, advances must be made both in how to position precisely the SWNT with respect to other very small components and in the fundamental understanding of their electronic properties. This thesis describes a new method for placing SWNTs in spatially precise positions – fountain pen nanolithography – and presents progress towards experiments exploring the electrical properties of SWNTs with the use of enhanced Raman spectroscopy.

Fountain pen nanolithography is a method that allows an SWNT-containing 'ink' to be 'written' onto a surface, using an atomic force microscope to hold a nanopipette as the 'pen', with a tip diameter of around 100 nanometres. When the pen was pressed onto the surface of a silicon wafer, the ink flowed out and lines of well-aligned SWNTs could be drawn in precise locations.

Raman spectroscopy is useful for investigating SWNTs, however it generally gives very weak signals. An enhanced signal can be obtained if the SWNT has one or more gold nanoparticles very close to it within the laser spot. Here, an atomic force microscope was used to push gold nanoparticles several micrometres over a surface until they were positioned on a SWNT. The Raman spectroscopy signal obtained with the gold nanoparticles correctly positioned was up to 20 times stronger than it was without the enhancement from the gold.

Passing electricity along a SWNT while simultaneously doing enhanced Raman spectroscopy would improve understanding of SWNT fundamental properties.

Abbreviations and Acronyms

ACCEP	atomic-force-controlled capillary electrophoretic nanoprinting
AFM	atomic force microscope or microscopy
APTES	(3-aminopropyl) triethoxysilane
AuNP	gold nanoparticle
BSA	bovine serum albumin
CCD	charged couple device
CMC	critical micelle concentration
CNT	carbon nanotube
CVD	chemical vapour deposition
DMF	dimethyl formamide
DMSO	dimethyl sulfoxide
DOS	density of states
DPN	dip pen nanolithography
DWNT	double-walled carbon nanotube
EBL	electron-beam lithography
FET	field-effect transistor
FIB	fast ion beam etching
FPN	fountain pen nanolithography
FWHM	full width at half maximum
IPA	iso-propyl alcohol
IR	infrared
LSP	localised surface plasmon-polariton
MWNT	multi-walled carbon nanotube
MHA	16-mercaptohexadecanoic acid

ND	nanodiamond
NDC	negative differential conductance
NADIS	nanoscale dispensing
NFP	nanofountain probe
ODF	orientation distribution function
ODT	1-octadecanethiol
PDMS	polydimethylsiloxane
PEG	polyethylene glycol
PSD	position-sensitive detector
PSPP	propagating surface plasmon-polariton
PZT	lead zirconium titanate
RIE	reactive ion etching
RRS	resonance Raman scattering or spectroscopy
SDBS	sodium dodecylbenzenesulfonate
SDS	sodium dodecyl sulfate
SERRS	surface-enhanced resonance Raman scattering or spectroscopy
SERS	surface-enhanced Raman scattering or spectroscopy
SEM	scanning electron microscope or microscopy
SM-SERS	single-molecule surface-enhanced Raman scattering
SICM	scanning ion conductance microscope or microscopy
SPM	scanning probe microscope or microscopy
SPP	surface plasmon-polariton
STM	scanning tunnelling microscope or microscopy
SWNT	single-walled carbon nanotube
TEM	transmission electron microscope or microscopy
TERS	tip-enhanced Raman spectroscopy
UV	ultraviolet

Contents

List of Figures

List of Tables

Chapter 1

Introduction

Carbon nanotubes, hollow cylinders comprising only carbon atoms, have fascinating properties and a beautiful structure. This is particularly true for single-walled carbon nanotubes (SWNTs), with their walls of a single layer of carbon atoms, arranged in a honeycomb structure. With a diameter on the order of a nanometre and a length on the order of a micrometre, the SWNT has one-dimensional characteristics [1]. As such, it has interesting and potentially useful properties such as ballistic transport and quantised conductance [2], while being large enough for an individual nanotube to be easily imaged with microscopies such as atomic force microscopy and scanning electron microscopy. In addition, resonance Raman spectroscopy can be performed on individual carbon nanotubes, making single-molecule studies a reality. These aspects of SWNTs make them well-suited to be used as model structures for probing the properties and behaviours of nano-scaled systems.

The field of plasmonics, that is, the study of nano-scaled metallic structures that support plasmons, is a rapidly emerging field, where theoretical studies led the earlier development [3] and experimental work was required to confirm or refute the theoretical predictions. The NANOSPEC project, funded by Nano-Science Europe, aimed to explore experimentally the interface between such plasmonic structures and molecules in their vicinity, using SWNTs as the test molecule. SWNTs were appropriate for this investigation because they are large enough to be visualised by atomic force microscopy and can be characterised with

resonance Raman spectroscopy independently of plasmonic enhancement. By obtaining an additional Raman spectrum from plasmonically enhanced Raman spectroscopy (also known as surface-enhanced Raman spectroscopy (SERS)), one may obtain information about the polarisation of the light the SWNT experienced from the plasmonic structure, as well as about the structure and temperature of the SWNT.

An additional advantage of using SWNTs as the model system for investigating the plasmonic structures is that useful information may also be obtained about the SWNTs themselves. The presence of the plasmonic structure should enhance the strength of the Raman scattering signal obtained from the SWNT [4]. While a single SWNT may be measured with resonance Raman spectroscopy, if conditions caused the SWNT to move out of resonance then the signal strength would rapidly drop and the information-rich Raman spectrum would be lost. This could occur when a high bias voltage is applied to the SWNT, inducing an electrical current. In this case, electron–phonon coupling causes the temperature of the SWNT to rise significantly [5, 6] and the additional vibrational energy contained in the SWNT could push the transition energy of the SWNT away from that of the excitation laser [7]. As such, studies of SWNTs experiencing a large range of bias voltages, from those giving low currents up to the point of current limitation or electrical breakdown, cannot be performed with resonance Raman spectroscopy. If a plasmonic structure was effectively interfaced with the SWNT then, even if increasing vibrational energy caused resonance to be lost, the remaining weak Raman signal would be sufficiently plasmonically enhanced to render it measurable and useful information may be gleaned. So, through interfacing electrically-contacted SWNTs with plasmonic structures, the NANOSPEC project aimed to enable *in situ* Raman spectroscopy on current-carrying SWNTs and increase the fundamental understanding of current limitation and electrical breakdown in SWNTs, as well as increasing the fundamental understanding of the interface between a plasmonic structure and a SWNT.

The work presented in this thesis formed part of the NANOSPEC project. This part of the project was mostly completed in Edinburgh where the

emphasis was on device creation and preparation for electrical measurements, supported by Prof. Eleanor Campbell, Dr Oleg Nerushev and Dr Andrei Gromov. Other project participants were Prof. Aaron Lewis and Talia Yeshua from the Hebrew University, Jerusalem, Israel, who specialised in atomic force microscopy techniques such as nanodeposition and multi-probe systems; Prof. Stephanie Reich, Sebastian Heeg and Christian Lehmann of the Free University, Berlin, who brought expertise in the Raman spectroscopy of carbon nanotubes; and Prof. Stefan Maier and Roberto Fernández-García of Imperial College, London, UK, specialising in plasmonics. Where work presented in this thesis was performed with or by one or more of these people it will be stated clearly.

This thesis contains five chapters, in addition to this short introduction and a short overall conclusion at the end. It will start with some background on carbon nanotubes, the main methods used in their study and other relevant areas such as the use of plasmonics to enhance Raman spectroscopy (Chapter 2). This will be followed by a chapter detailing the instrumentation and experimental methods used in all areas of this work (Chapter 3). Attention then will be turned to various approaches involved in creating devices of interfaced nanoscale objects: firstly fountain pen nanolithography for deposition of carbon nanotubes (Chapter 4) and secondly the deposition of plasmonic gold nanoparticles and subsequent atomic force microscope nanomanipulation (Chapter 5). This will be followed by a chapter discussing Raman–transport experiments on SWNTs and the potential of the devices created in the earlier chapters (Chapter 6).

Chapter 2

Background and Theory

2.1 Carbon nanotubes

2.1.1 Discovery

Carbon nanotubes (CNTs) were first distinguished from other fibrous carbon structures by observation of their nanometre-scale hollow core in a transmission electron microscope. The first experimental images showing this were produced in 1952 [8] and others were reported over the following years [9]. The breakthrough in their popularity came in 1991 with the high-profile publication by Iijima [10] and the wave of studies that it prompted has continued since. Of particular note to fundamental physical studies was the discovery of single-walled carbon nanotubes in 1993 [11, 12], which opened up the possibility of comparing theoretical predictions of their properties with experimental measurements.

2.1.2 Structure

As suggested by the name, carbon nanotubes are tubes, or hollow cylinders, made entirely of carbon atoms and having a diameter on the order of nanometres, that is, 10^{-9} m. In the case of single-walled carbon nanotubes (SWNTs), the cylinder is made of a single-atom-thick layer of carbon atoms, bonded in a hexagonal arrangement (Figure 2.1a). In multi-walled carbon nanotubes (MWNTs) there are two or more layers of atoms such that the cross-section has two or more

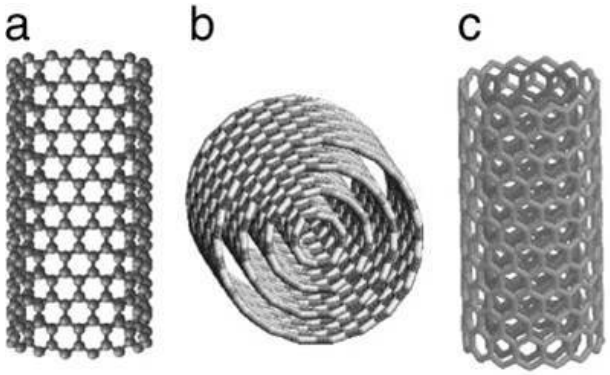

Figure 2.1: Schematic diagram of different types of carbon nanotubes: (a) single-walled carbon nanotube (SWNT), (b) multi-walled carbon nanotube (MWNT) and (c) double-walled carbon nanotube (DWNT). From reference [15].

concentric circles and the overall structure resembles that of a Russian doll (Figure 2.1 b and c). While the diameter of SWNTs typically ranges from 0.7 nm to 1.5 nm, and MWNTs may have a diameter of tens of nanometres, the length is often on the order of microns (10^{-6} m) and can be up to tens of centimetres [13, 14]. Their large aspect ratio gives carbon nanotubes unique and interesting properties.

Carbon nanotubes are one of several allotropes of carbon. The most common forms of pure carbon are diamond and graphite, both of which are three-dimensional crystals. In diamond the valence electrons of each carbon atom are all hybridised to form four equivalent sp^3 orbitals, each of which is used to bond to a nearest-neighbour carbon atom in an extended covalent network. In graphite the s, p_x and p_y orbitals hybridise to form three sp^2 orbitals, which make bonds to other carbon atoms in a planar arrangement. The p_z orbital remains unhybridised normal to the plane and holds a single electron, giving electron density in a delocalised π system above and below the plane. Graphite is formed of stacks of such planar sheets of carbon atoms, held together by non-covalent bonding. Of the family of low-dimensional carbon nanomaterials, graphene is the two-dimensional (2-D) version, a single sheet from the graphite structure. Carbon nanotubes are effectively 1-D due to their large aspect ratio. On the other extreme, the spherical cage-structures of fullerenes such as C_{60} are the 0-D type of carbon nanomaterial.

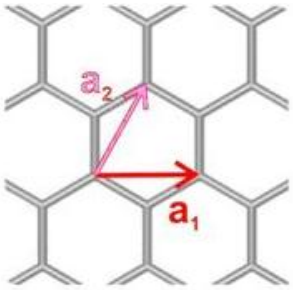

Figure 2.2: Graphene lattice vectors, $\mathbf{a}_1$ (red) and $\mathbf{a}_2$ (pink), each of which has a length of 2.46 Å. Adapted from reference [16].

The exact atomic arrangement within the cylinder structure governs some of the properties of the carbon nanotube. The most convenient way to describe this is to imagine that the nanotube has been cut open along its length and unrolled to form a graphene ribbon. A line drawn between the edges of the nanotube perpendicular to the nanotube axis is called the chiral vector, $\mathbf{c}$, and can be described as a sum of the lattice vectors of graphene, $\mathbf{a}_1$ and $\mathbf{a}_2$ (Figure 2.2). The coefficients n and m are called the chiral indices and the structure of the SWNT is often described in the form (n, m). As an example of this see Figure 2.3, which shows the structure of a $(7, 0)$ SWNT and a $(4, 4)$ SWNT. These are described as zigzag and armchair, respectively, which describes the shape of atom positions around the circumference. These classes have higher symmetry than other SWNTs, which are described as chiral, such as the $(5, 3)$ SWNT also shown in Figure 2.3.

The lattice vectors have length $|\mathbf{a}_1| = |\mathbf{a}_2| = 2.46$ Å. The length of the chiral vector may be calculated by adding the appropriate numbers of $\mathbf{a}_1$ and $\mathbf{a}_2$:

$$\mathbf{c} = n\mathbf{a}_1 + m\mathbf{a}_2. \tag{2.1}$$

Since the chiral vector is equivalent to the circumference of the SWNT, the diameter, d, can then be simply calculated:

$$d = \frac{|\mathbf{c}|}{\pi} = \frac{|\mathbf{a}_1|}{\pi}\sqrt{n^2 + nm + m^2}. \tag{2.2}$$

In addition, the chiral angle, θ, defined as the angle between $\mathbf{a}_1$ and the chiral

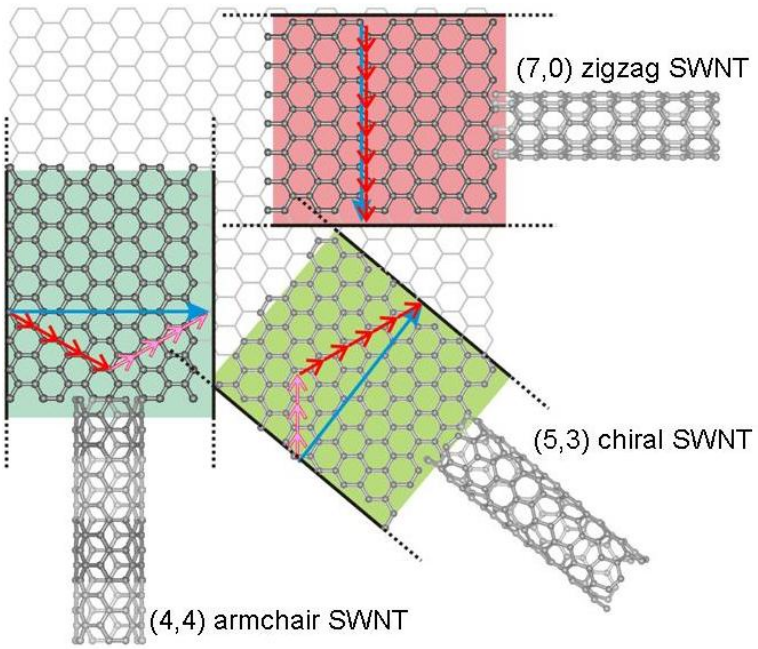

Figure 2.3: Three examples of SWNT structures shown as cylinders and as unrolled onto a graphene lattice. The chiral vectors $\mathbf{c}$ are shown by blue arrows and the graphene lattice vectors $\mathbf{a}_1$ and $\mathbf{a}_2$ are indicated by red and pink arrows, respectively. Counting the number of red and pink arrows required to map the path between the start and end of the blue arrow gives the values of n and m respectively. Adapted from reference [16].

vector, can be obtained from the following expression:

$$\cos\theta = \frac{\mathbf{a}_1 \cdot \mathbf{c}}{|\mathbf{a}_1||\mathbf{c}|} = \frac{n + m/2}{\sqrt{n^2 + nm + m^2}}. \tag{2.3}$$

2.1.3 Electronic properties

One of the most interesting features of SWNTs is that they can be either semiconducting or metallic depending on their structure. On average one-third are metallic and two-thirds are semiconducting [2].

To understand the electronic properties of SWNTs, it is best to start by looking at the band structure of graphene. As described above, the sp^2 orbitals are involved in covalent bonds with neighbouring carbon atoms, but the p_z orbitals form delocalised π bonding systems across the sheet. The conductivity is therefore governed by the π and π^* bands. In reciprocal space, the hexagonal graphene lattice gives a hexagonal pattern with high-symmetry points Γ, K, K$'$ and M

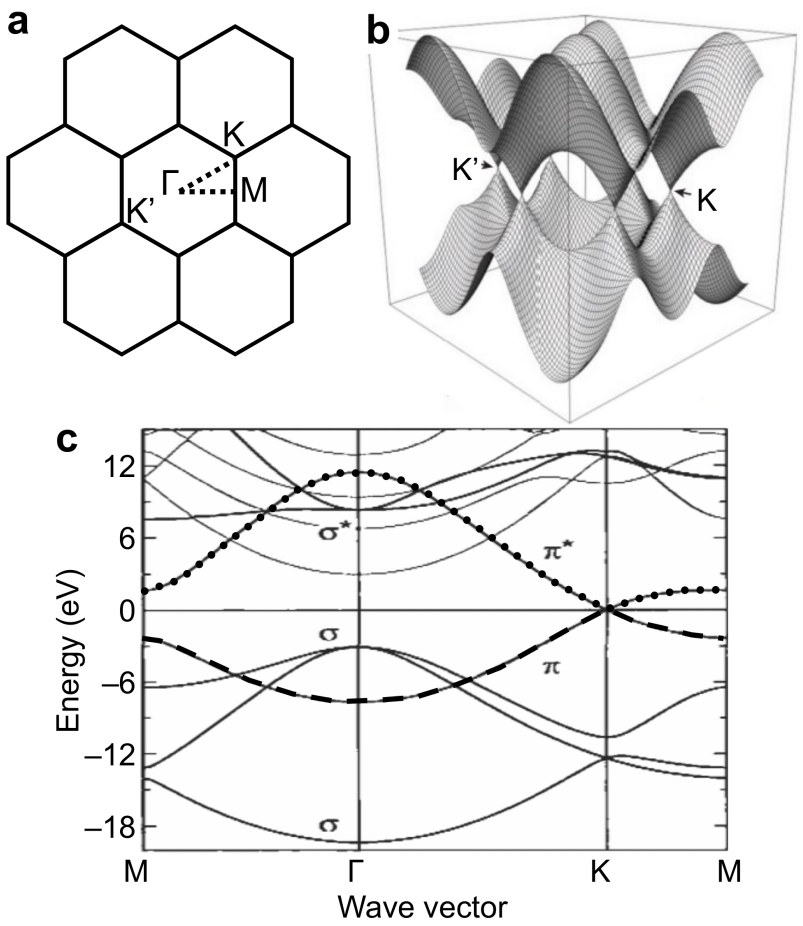

Figure 2.4: (a) Graphene represented in reciprocal space with the high symmetry points (Γ, K, K′ and M) in a Brillouin zone shown. (b) The π and π^* bands, illustrated as surfaces that meet at K and K′ points. (c) A 2-D representation of the dispersion relation, with the π and π^* bands highlighted with dashed and dotted lines, respectively. Part a is based on reference [17], part b is adapted from reference [2] and part c is adapted from reference [1].

(Figure 2.4a). The π and π^* bands are shown in Figure 2.4b and it can be seen that they meet with cone shapes only at certain points at the corners of the first Brillouin zone. Of these points, two are irreducible, K and K′. The energy dispersion can also be represented in the form given in Figure 2.4c, where it can be seen that graphene has a linear dispersion near the Fermi energy and is a zero bandgap semiconductor or semimetal [17, 18].

When graphene is rolled into a cylinder to form a nanotube, confinement in the circumferential direction gives additional restrictions on the allowed wave-functions. This can be represented as slices through the graphene Brillouin zone, with the direction of the slices being dependent on the chiral indices of the SWNT

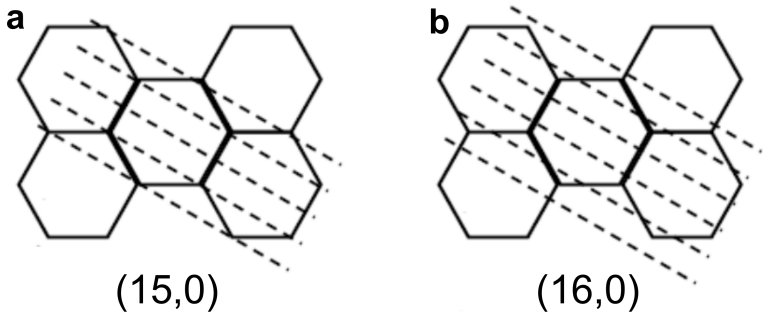

Figure 2.5: SWNT quantised wave vectors for (a) a metallic $(15, 0)$ and (b) a semiconducting $(16, 0)$ SWNT. If the dashed lines cross exactly at the corner of the hexagons (the K points) then the SWNT is metallic, if not then there is a bandgap. Adapted from reference [19].

(Figure 2.5). If a slice passes through the K point then the dispersion relation is linear and the SWNT is metallic but if the slices all miss the K point then there is a bandgap and the SWNT is semiconducting. It can be shown that the ratio obtained from all possible ways of slicing is $1 : 2$ [1, 2, 17]. The reason for this can be illustrated in a visual way, shown in Figure 2.6 based on the K-point wavefunction of graphene. The coloured carbon atoms represent the three different phases that wavefunctions corresponding to those atoms may have (0°, 120° and 240°) and the effect of rolling into a cylinder is then considered in terms of which atoms overlap. If like colours overlap then the wavefunction satisfies the boundary condition implying that that particular K-point wavefunction is valid and the SWNT is metallic. If the colours are mismatched then that wavefunction is not valid and the lowest quantised wavefunction lies away from the K point and the SWNT is semiconducting. The bandgap, E_{g}, is dependent on the diameter and is given by:

$$E_{\mathrm{g}} = \frac{4\hbar\nu_{\mathrm{F}}}{3d} \approx \frac{0.7 \text{ eV}}{d[\text{nm}]}, \tag{2.4}$$

where $\hbar$ is the reduced Planck's constant, ν_{F} is the Fermi velocity ($\approx 8\times10^5$ ms^{-1}) and d is the diameter of the SWNT [2].

On the simplest level, a SWNT is metallic if the difference in its chiral indices is divisible by three, that is, $n - m = 3p$, where p is an integer. Possible SWNTs are shown in Figure 2.7. It can be seen that armchair SWNTs, where $n = m$, are all metallic and zigzag SWNTs, where $m = 0$, are metallic if $n = 3p$ or

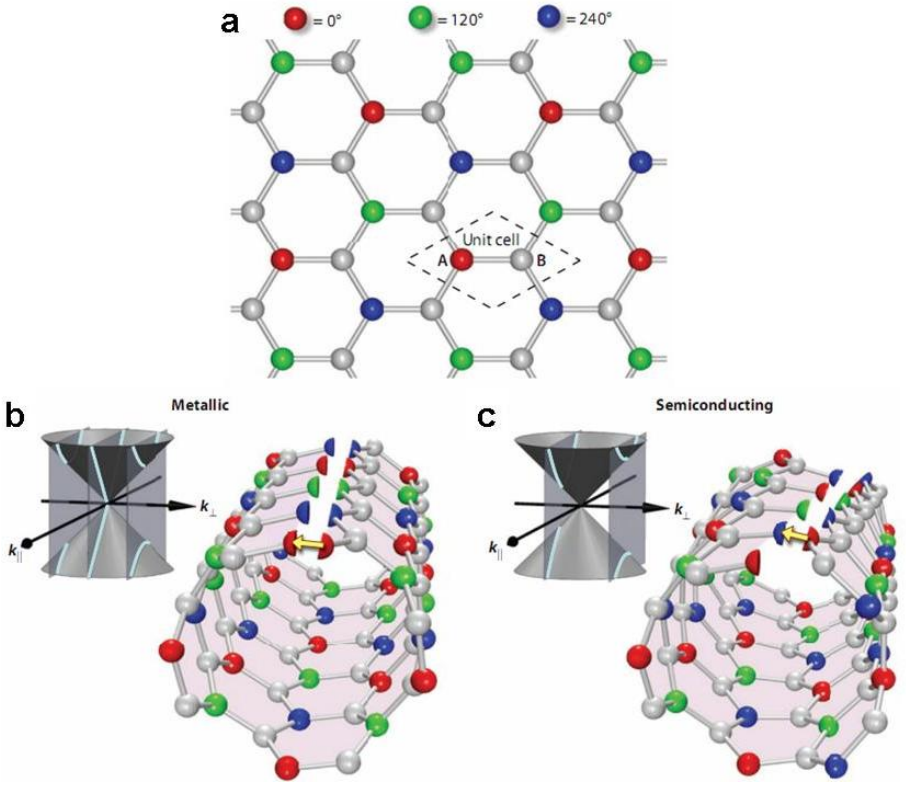

Figure 2.6: Schematic representation of (a) graphene, (b) a metallic SWNT and (c) a semiconducting SWNT, showing how the phase of the wavefunction on the carbon atoms dictates the type of SWNT. The three colours represent the three phases of the wavefunction. In the metallic case (b) a red atom is rolled onto another red atom so their phases match and the wavefunction is allowed. In the semiconducting case (c) a red atom is rolled onto a blue atom so there is a phase difference in their wavefunctions, which means the nearest valid wavefunction is not at the K point so the SWNT is semiconducting. Adapted from reference [2].

semiconducting if $n \neq 3p$. In fact the curvature of the SWNT adds a small bandgap to most SWNTs that would generally be classed as metallic, except in the case of armchair SWNTs, which are truly metallic [19].

The density of states (DOS) of a metallic (m-) and a semiconducting (sc-) SWNT is shown in Figure 2.8. The sharp peaks are van Hove singularities. It can be seen that the DOS of the sc-SWNT goes to zero at the Fermi level, while the DOS of the m-SWNT has a finite value at the Fermi level. Note that this is in contrast to graphene, which does not have a finite DOS at the Fermi level and thus is not truly metallic [17]. The DOS and van Hove singularities will be discussed again in terms of their importance in Raman spectroscopy in Section 2.2.1.2.

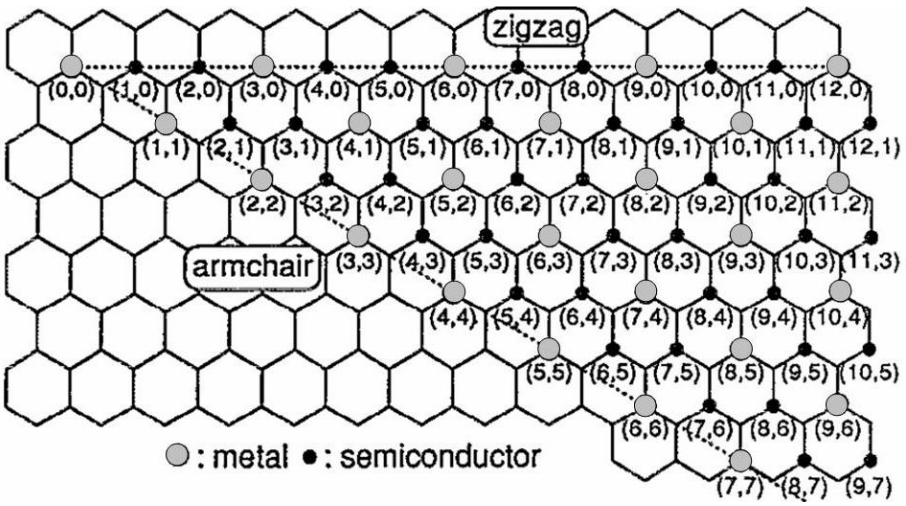

Figure 2.7: Possible (n, m) SWNTs and their classification as metallic or semiconducting. Adapted from reference [20].

Since SWNTs can be considered as 1-D systems, their conductance, G, is described by the Landauer formula:

$$G = (4e^2/h)T, \tag{2.5}$$

where e is the electron charge, h is Planck's constant and T is the transmission coefficient for electrons through the sample [19]. If the transport is ballistic, no scattering occurs and the resistance of a metallic SWNT is $R_{\mathrm{CNT}} \sim 6.5$ kΩ. In practice, although SWNTs have been observed to have near-ballistic transport, the resistance usually measured is significantly higher due to the resistance at the electrode contacts, R_{C}, and resistance caused by scattering, R_{S}. The total measured resistance, R_{tot}, is given by:

$$R_{\mathrm{tot}} = R_{\mathrm{CNT}} + R_{\mathrm{C}} + R_{\mathrm{S}}. \tag{2.6}$$

The resistance due to scattering in solid materials can arise from two types of scattering interaction: with static defects or with phonons (collective vibrational modes). The high symmetry of SWNTs means that the scattering due to defects is suppressed and the dominant scattering effect is with phonons [17]. Research into the interaction between conducting electrons and phonons is discussed in

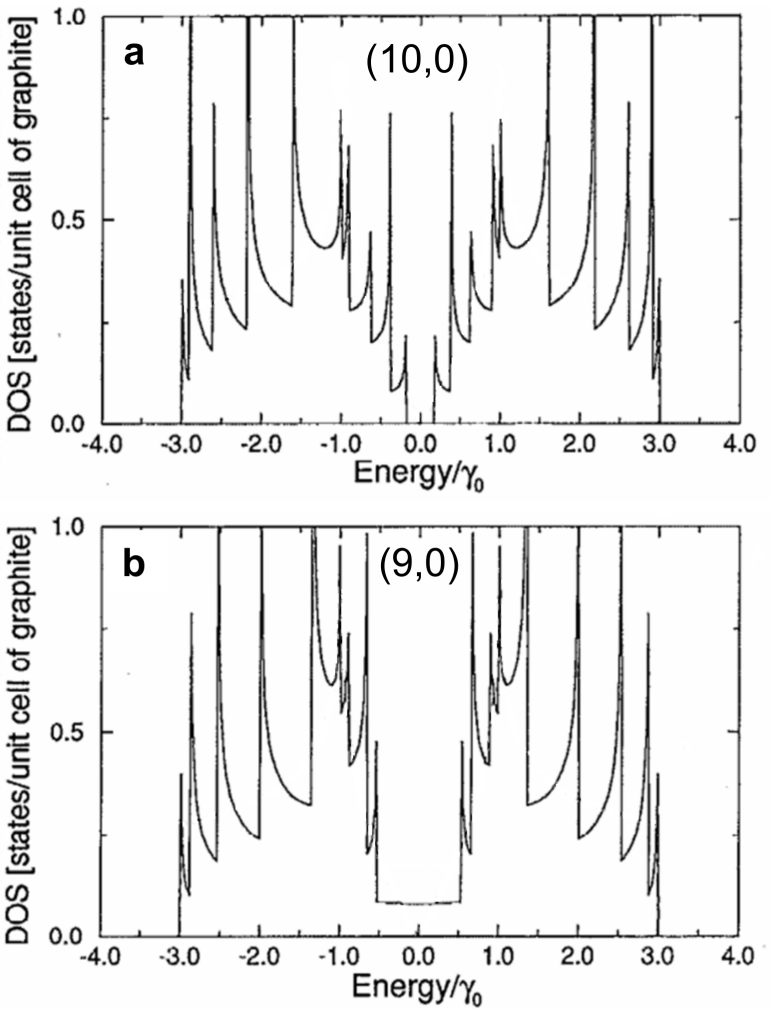

Figure 2.8: Calculated density of states (DOS) of (a) a semiconducting $(10, 0)$ SWNT and (b) a metallic $(9, 0)$ SWNT. The energy units γ_0 represent the nearest-neighbour overlap integral. Adapted from reference [20].

greater detail in Chapter 6.

2.1.4 Synthesis

Carbon nanotubes can be made by a number of different methods. Each method requires a source of carbon and a source of energy, while the forms that each takes can vary. Arc discharge has historical significance and chemical vapour deposition (CVD) has the most relevance to this thesis so these methods will be described here in greater depth than other techniques such as laser ablation or organic chemistry. More details about CNT synthesis are reviewed by Szabo *et al.* [21].

Arc discharge was the first method used in carbon nanotube science, for example in Iijima's 1991 report of MWNTs [10] and in both of the first SWNT reports [11, 12], leading on from methods of synthesising fullerenes. In this method, two graphite electrodes are placed within a vacuum chamber and a high voltage is applied between them (Figure 2.9), creating an arc. CNTs are found in the soot produced both on the chamber walls and on the cathode. If the anode is pure graphite then only MWNTs are formed but if a metal, typically Fe, Ni, Co or Mo, is mixed in with the anode graphite then SWNTs are also produced. The temperature between the electrodes is very high (> 1700 °C) so carbon is vapourised from the anode, forming a plasma. In general, the atmosphere used is a low pressure of inert gas but experiments have shown improvements with the addition of other reactant gases (such as ethanol, hexane, acetone), sulfur-containing promoters and hydrogen. The important factors governing the type, size and quantity of CNTs produced include the carbon vapour concentration, the temperature inside the reactor and the catalyst composition. A significant disadvantage of this method is that any CNTs produced are mixed in with a large quantity of other carbonaceous material so purification processes must be employed to isolate the CNTs. However the quality of arc discharge-produced CNTs is good, with a high degree of crystallinity and relatively few defects [21, 22].

Laser ablation is similar to arc discharge in that it uses graphite as the carbon source. As the name suggests, a laser is used to provide the energy to sublime the carbon and allow the creation of new structures, which then condense on a cold finger after being carried by inert gases. Generally, laser ablation produces SWNTs, not MWNTs. As with arc discharge, metal catalysts are often mixed with the graphite to obtain better results for CNT growth and variations in the gas environment affect the nature of the CNTs produced. The temperature of the chamber is another factor that can be controlled; usually a high temperature (> 1000 °C) is used but room temperature has been used, in which case the laser creates a local high temperature. The laser properties are, of course, very important for this technique and CNT production has been studied with a range of energy fluence, laser power and wavelength and with both continuous wave and pulsed lasers. In general, laser ablation produces high quality CNTs with a lower

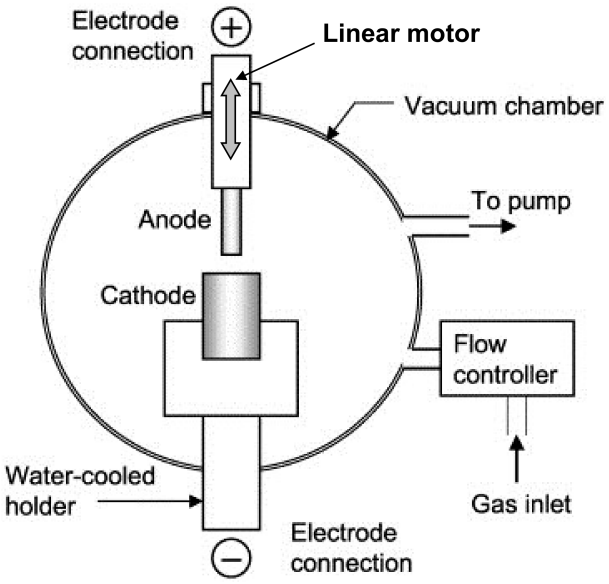

Figure 2.9: Schematic of the arc discharge method of CNT synthesis. A high voltage is applied between the anode and cathode, while a low-pressure gas atmosphere is controlled. The anode is consumed during the reaction so a linear motor allows a constant anode–cathode distance to be maintained. Adapted from reference [23].

quantity of carbonaceous impurities than the arc discharge method [21, 22].

Chemical vapour deposition (CVD) was first used to produce CNTs in 1993 [24] and since then has become the most common method of production. It can work at a lower temperature than the methods described above, typically in the range 700 °C to 950 °C. Instead of solid graphite, the source of carbon is a gas, commonly a hydrocarbon such as ethylene, acetylene or methane or a small alcohol or carbon monoxide. The carbon-containing gas decomposes on a metal catalyst particle, the carbon dissolves into the catalyst and from there CNTs grow. The catalyst is generally a transition metal, in particular Fe, Co or Ni. The choice of catalyst, carbon gas, flow rate, pressure, temperature and other gases present all affect the CNT growth. SWNT and MWNT can be selectively grown depending on the conditions used: generally SWNTs are preferentially grown at higher temperatures than MWNT and with ethylene or methane, while MWNTs can be grown with acetylene [21, 22].

CVD growth methods can be classified as either surface-supported or floating catalyst processes [21]. In the former, the catalyst is on a substrate such as silicon,

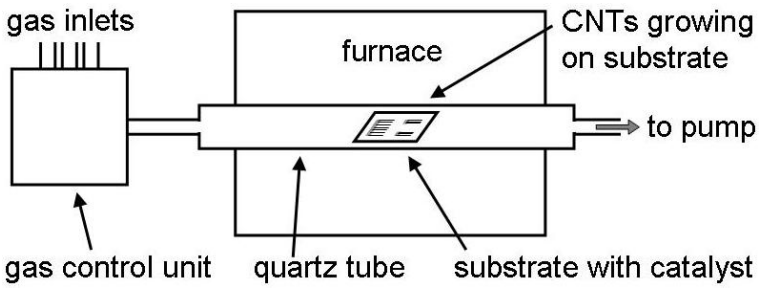

Figure 2.10: Schematic of a typical setup for the surface-supported CVD method of CNT growth.

silicon oxide or quartz and the CNTs grow on the substrate, remaining attached to it (Figure 2.10). In the latter process, the catalyst is in aerosol form and CNTs form within a growth volume and are separated from the exhaust gases on a cold finger or filter. There are pros and cons of each approach. Floating catalyst growth can be performed continuously so it is suitable for creating large quantities of material at relatively low cost. However this comes with the disadvantage that the catalyst particles are not separated from the CNTs so there remains a non-negligible quantity of metal in the produced CNT material. In addition, amorphous carbon is also produced and, if relatively low temperatures are used, the CNTs can be of lower quality, with more defects. In contrast, surface-supported growth can produce very high-quality CNTs with negligible amorphous carbon [25]. Because the CNTs only grow where the catalyst is present, they can be grown directly in the desired locations, and careful control of the conditions can enable vertically or horizontally aligned growth. The batch-processing nature and high temperatures of this growth mean that it is suitable for specialist applications and research but CNTs grown in this way are not commercially available [21, 22].

The HiPco process is one form of floating catalyst CVD growth that enables large quantities of SWNTs to be produced and sold commercially. The process, which was developed by Smalley and co-workers [26, 27], uses iron pentacarbonyl ($Fe(CO)_5$) as the iron-containing catalyst precursor and carbon monoxide (CO) as the carbon feedstock. The $Fe(CO)_5$ decomposes in the high-temperature furnace to create iron clusters, on the surface of which the CO disproportionation reaction

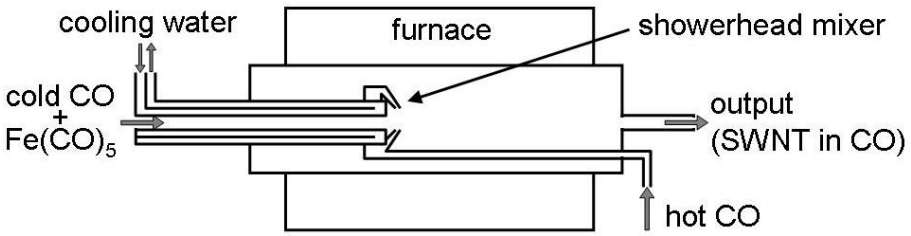

Figure 2.11: Schematic of experimental setup for the HiPco method of SWNT growth. Adapted from [26].

occurs and SWNTs can grow. Typical operating conditions are a temperature of 1050 °C and a pressure of 30 atm. Rapid heating of the $Fe(CO)_5$, to enable optimised cluster sizes, is achieved by mixing cooled $Fe(CO)_5$ with pre-heated CO ejected into the furnace through a series of channels in a showerhead arrangement (Figure 2.11). The SWNTs produced are separated from the CO exiting the furnace by filters and cold surfaces. With optimised temperature, pressure and catalyst precursor concentration, the process can produce SWNTs with negligible amorphous carbon, though a non-zero quantity of iron will be present [27].

A range of advanced CVD methods have also been developed. These include plasma-enhanced CVD, microwave plasma-enhanced CVD, alcohol CVD, hot-filament CVD, water-assisted CVD and oxygen-assisted CVD [21, 22].

Another variation of growing CNTs by CVD is the local heating technique [28], where the high temperature required for growth is provided from resistive heating of a small metal bar lithographically patterned on a substrate with catalyst material on top. This method has the advantage of not heating the rest of the substrate so heat-sensitive components may be present and not damaged.

To date, none of the synthesis methods are able to selectively produce only metallic or semiconducting SWNTs or those of a particular chirality. The mechanism for growth is still not well understood and is the subject of much continued study. Some schemes have been proposed but computational modelling has not yet effectively replicated experimental results.

A completely contrasting method to synthesise SWNTs with control over chirality would be to use organic chemistry (Figure 2.12). This challenge can be broken down into two steps: firstly to form aromatic macrocycles with the

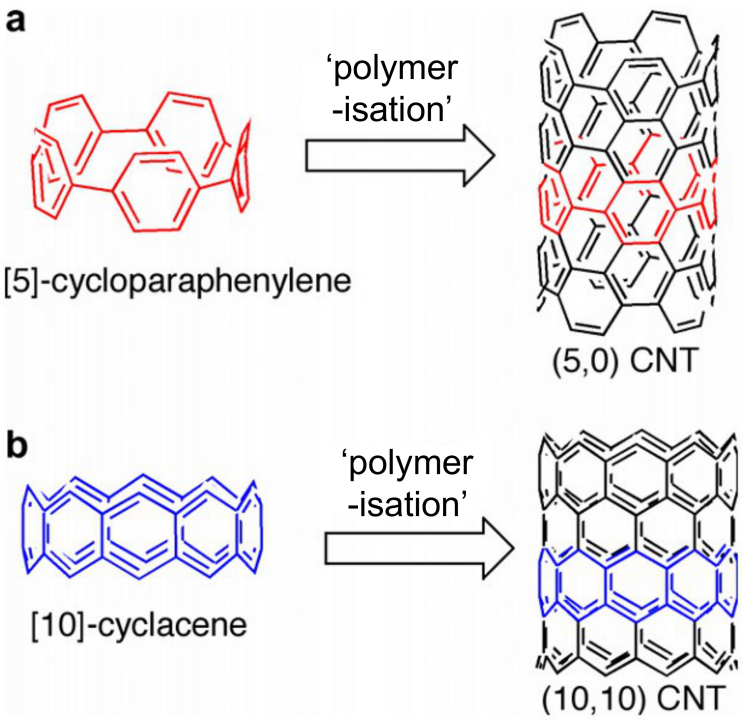

Figure 2.12: Organic chemistry approach to SWNT synthesis for (a) armchair SWNTs and (b) zigzag SWNTs. Adapted from reference [29].

correct size and chirality to use as building blocks and secondly to join these building blocks together in a form of polymerisation. Some progress has been made towards this goal, such that the most basic monomer of the armchair and zigzag SWNTs can be synthesised, but complete nanotubes have yet to be formed [22, 29].

2.1.5 Processing

Carbon nanotubes are generally produced in the solid phase and are collected as a black powder on a filter or cold finger or found on the substrate on which they were grown. For many applications, however, it is desirous to handle them in a liquid, which enables processes to be up-scaled and the CNTs to be separated if necessary. For example, in the field of advanced materials, the CNTs must be uniformly dispersed in order to confer their beneficial properties to composite materials. For fundamental research, good dispersions are also required when desiring uniform coverage of well-separated, individual SWNTs for electrical or

spectroscopic studies. In addition, solution processes provide a route towards sorting SWNTs by their conductivity or chirality, opening a huge range of possibilities of working with a selected type of SWNT and comparing experimental results directly with theory.

Making good dispersions with separate individual CNTs is not easy because in almost all production methods they form close-packed bundles. These bundles are strongly bound by van der Waals interactions with a strength of 500 eV/μm of CNT length [30].

In general, dispersions are produced by adding a stabilising agent to CNTs submersed in a solvent and then providing mechanical energy in the form of ultrasonication. Effectively, the ultrasonication breaks up the bundles into separate individual CNTs and the stabilising agent non-covalently binds to the CNTs and prevents them agglomerating again. The mechanism for this is likely to be like that proposed by Strano *et al.* [31], whereby ultrasonication causes the ends of the bundle to separate slightly, like a rope fraying, and then the stabilising agent starts to bind to and stabilise the loose ends, gradually allowing more of the CNT to become detached from the bundle.

The earliest and still the most commonly used stabilising agents for aqueous CNT dispersions are surfactants. Surfactants can come in several types such as anionic, cationic, non-ionic or zwitterionic. Particularly common are sodium dodecyl sulfate (SDS) and sodium dodecyl benzene sulfonate (SDBS), shown in Figure 2.13 a and b. These molecules do not form chemical bonds to CNTs, which means they do not cause damage or affect the fundamental properties of the CNTs, but the mechanism by which they bind to the CNTs is still under debate. Proposed arrangements include the complete enclosure of the CNT in a cylindrical micelle, hemimicellular structures adsorbed on the CNT or a random arrangement of individual surfactant molecules adsorbed onto the CNT surface (Figure 2.14). Experimentally these are hard to distinguish and are inferred indirectly from measurements or are justified from simulations. The chemical structure of the surfactant and the concentrations of surfactant and CNTs will determine which arrangement occurs [30, 32, 33].

It was shown by Angelikopoulos *et al.* [32] that with SDS and SDBS, surfactant

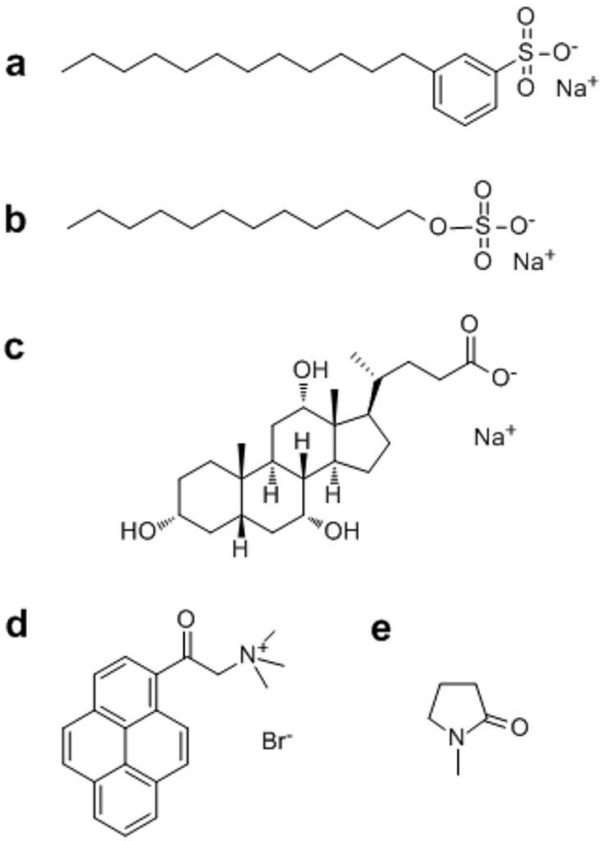

Figure 2.13: Chemical structures of surfactants and other dispersion stabilising agents: (a) SDBS, (b) SDS, (c) sodium cholate, (d) pyrene derivative: trimethyl-(2-oxo-2-pyrene-1-yl-ethyl)-ammonium bromide, and (e) NMP.

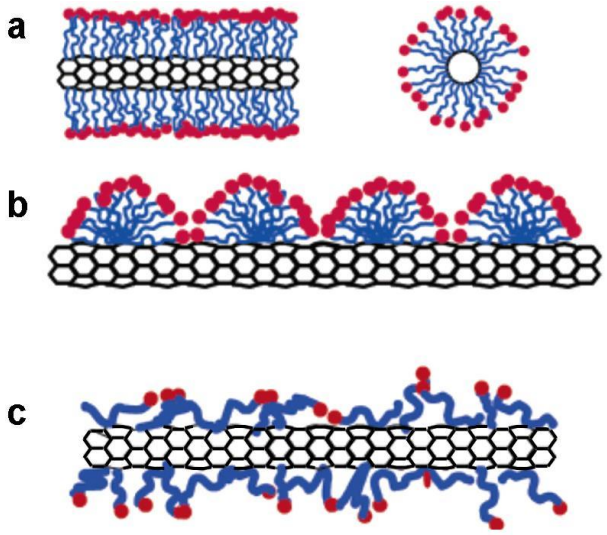

Figure 2.14: Schematic impression of different arrangements surfactant molecules may adopt on the surface of the CNT: (a) cylindrical micelle, (b) hemimicellular adsorption or (c) random adsorption of surfactant molecules. Adapted from reference [33].

concentrations below the critical micelle concentration (CMC) were effective at dispersing SWNTs. Computational simulations predicted that adsorption should be complete at a concentration of 0.5 CMC, and higher concentrations of surfactant would have little effect. In fact, they observed that surfactant concentrations above the CMC produced dispersions with a larger average diameter, meaning a smaller proportion of individual SWNTs [32].

Other stabilising agents may be used instead of SDS or SDBS. These may be designed to have stronger interaction with the CNT surface, for example making use of π-stacking interactions, such as pyrene derivatives (example shown in Figure 2.13d). Sodium cholate is another surfactant that has shown the ability to disperse CNTs, with the polycyclic aliphatic system adsorbing on the CNT surface (Figure 2.13c). Instead of surfactants, polymers can also be used as stabilising agents. Both synthetic polymers and biopolymers can be used in this way [30].

Organic solvents have also been explored in a quest to form dispersions in the absence of surfactants. Only a small number of solvents will have any potential and one particular solvent is currently standing ahead of the rest: *N*-methyl-2-pyrrolidone (NMP) (Figure 2.13e). Theoretical explanations are available for the strength of this solvent and it has shown good experimental results. Further theoretical work showed that other organic solvents derived from NMP can produce even better dispersions [34] but these solvents are more expensive and specialised, so NMP remains the most widely used. There is still some debate about the stability of NMP dispersions, with reported lifetimes ranging from days to weeks [30, 35].

All of the methods described so far require ultrasonication to begin the debundling process and achieve a state of dispersion. Recent developments have shown that this can be avoided, for example in the work by Shaffer and co-workers [36, 37]. Negatively charging the CNTs in liquid ammonia with the addition of alkali metals causes them to separate spontaneously with no ultrasonication or even stirring and removal of the liquid ammonia solvent leaves the CNTs in their anionic form. When a dry organic solvent such as dimethyl formamide (DMF) is added the CNTs again spontaneously dissolve and give individual CNTs. By

avoiding ultrasonication, there is no shortening of the length of the CNTs or risk of increasing defects [36].

An important use of individually dispersed SWNTs is their separation according to conductivity (whether metallic or semiconducting) or their diameter. Sorting by length or specific chiral indices may also be desirable. In preparation for separation, SWNTs are often functionalised, either by non-covalent interactions as just described or with covalent sidewall functionalisation, in such a way that amplifies differences in properties to enable easier separation. This uses all the dispersion techniques described above and others [38].

A number of different methods may then be used to separate the different types of SWNT: selective destruction, electrophoresis, dielectrophoresis, chromatography and, most importantly, centrifugation, in particular density-gradient ultracentrifugation. Selective destruction, such as burning in air, is used particularly for removing metallic SWNTs from devices such as field-effect transistors (FETs). Electrophoresis may be used to separate different materials on the basis of charge and mobility, through gel, capillaries or solution. In gels and capillaries molecular weight is important so shorter SWNTs travel fastest and in solution electronic type can be most important. Similarly, dielectrophoresis, using an ac electric field, can selectively place m-SWNTs between electrodes in preference over sc-SWNTs. Chromatography in its various forms is an important technique in the separation of SWNTs. Size-exclusion chromatography allows length separation and ion-exchange chromatography on DNA-wrapped SWNTs enables diameter separation [38]. Gel filtration is a related method, which can effectively separate metallic from semiconducting SWNTs [39]. Together these techniques can produce pure samples of specific chiral indices, though not effectively at large diameters. Finally, ultracentrifugation is invaluable in achieving good separation. Conventional ultracentrifugation separates bigger bundles from individual SWNTs. Of most importance is density-gradient ultracentrifugation. This allows diameter separation to be achieved with the surfactant on all the SWNTs: those of different diameters will form distinct layers in the centrifuge tube. Beyond that, selective functionalisation opens other possibilities. For example, if a heavier and lighter surfactant are preferentially

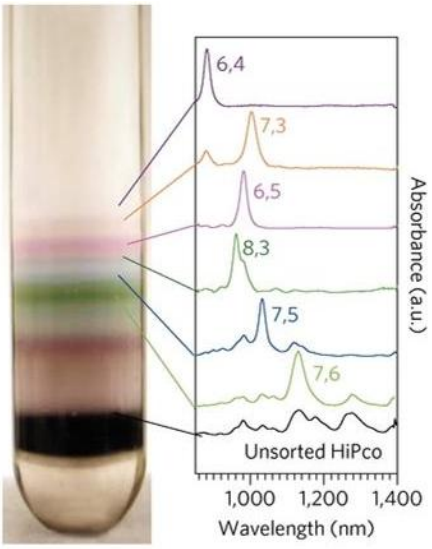

Figure 2.15: Results of density-gradient ultracentrifugation used to separate SWNTs according to their (n, m) indices. From reference [41].

bound to m- and sc-SWNTs, respectively, then separation by electronic character is possible [38, 40]. Careful choice of the density medium and dispersant can even allow separation according to (n, m) indices (Figure 2.15) [41].

2.2 Characterisation techniques

Raman spectroscopy is one of the most important techniques for the characterisation of SWNTs. Information available from the spectrum includes the diameter, the type of electrical conductor, the quality and the orientation/alignment of the SWNTs. A description of how Raman spectroscopy applies to SWNTs and what useful information can be obtained is given here after a general introduction to the technique.

Atomic force microscopy (AFM) and scanning electron microscopy (SEM) both also have important roles in the study of carbon nanotubes, primarily to identify the length and location of the CNT and, in the case of AFM, to measure its diameter. A description of these techniques and their application to CNT study is given after that of Raman spectroscopy.

2.2.1 Raman spectroscopy

2.2.1.1 Theory of Raman spectroscopy

The Raman effect was first observed in 1928 by Raman and Krishnan [42], having been earlier predicted by theory in 1923 [43] as a way of probing the vibrations of molecules.

To explain Raman spectroscopy, it can be helpful to begin with infrared (IR) absorption spectroscopy, a conceptually easier method of probing vibrations. In IR spectroscopy, molecules are irradiated with IR light. Some of the light, where the photon energy corresponds to the energy difference between vibrational states, is absorbed by the molecules, putting them into excited vibrational states. The light that passes through the sample to the detector therefore has a lower intensity at certain energies and these intensities are presented in an IR absorption spectrum, giving information about the vibrational energy levels. In order for molecular vibrations to absorb the light they must be 'IR-active', which means they must have a change in dipole moment between the ground and excited states [44].

Raman spectroscopy is an alternative method for probing molecular vibrations, with different fundamental principles and selection rules from those relevant to IR absorption. In Raman spectroscopy, the sample is irradiated with monochromatic visible light, some of which is inelastically scattered with a change in energy corresponding to the difference between vibrational states. Detection of the inelastically scattered light provides information about the vibrational energy levels. The intensity of Raman scattered light is

$$I \propto \nu^4 I_0 N f(\alpha^2), \tag{2.7}$$

where I_0 is the intensity of the exciting light, N is the number of scattering molecules in a given state, ν is the frequency of the exciting light and α is the polarisability of the sample [45].

Raman scattering is a two-photon process, as illustrated in Figure 2.16, in contrast to IR absorption, which is a one-photon process. The first photon is

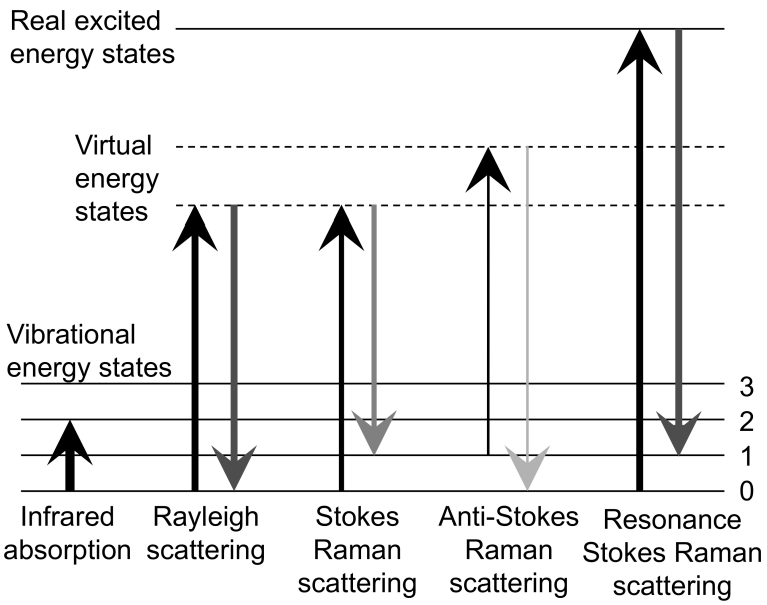

Figure 2.16: Energy level diagram for spectroscopic methods of probing vibrations. IR absorption is shown in comparison with Raman scattering, in Stokes and anti-Stokes modes. Resonance Raman spectroscopy, where the absorption of a photon causes excitation to a real, rather than virtual, state is also shown.

momentarily absorbed by the analyte molecule, which goes into a virtual excited energy state. The molecule then relaxes back to the ground electronic state with the emission of a second photon. The second photon may have the same energy, lower energy or higher energy than the first, in the cases of Rayleigh, Stokes and anti-Stokes scattering, respectively. Of these, Rayleigh scattering is the most abundant and anti-Stokes is the least likely, because it requires the molecule to be initially in an excited vibrational state. The comparison of intensities of anti-Stokes and Stokes scattering provides a measure of the temperature of the analyte, since the population of molecules in a vibrationally excited state is temperature dependent, according to the Boltzmann distribution:

$$\frac{N_k}{N_0} = e^{-(E_k - E_0)/kT}, \tag{2.8}$$

where N_k and N_0 are the populations of the excited and ground vibrational states, respectively, E_k and E_0 are the energies of the excited and ground vibrational states, respectively, k is Boltzmann's constant and T is the temperature [45].

In comparison to IR absorption spectroscopy, which relies on a change in dipole moment within the molecule being probed, for Raman spectroscopy a molecule must undergo a change in polarisability. The theoretical basis of Raman spectroscopy will now be introduced briefly. Polarisability may be thought of as how much the electrons in a molecule or system can respond to an external electric field. If an electric field, $\boldsymbol{E}$, is applied it causes an induced dipole, $\boldsymbol{\mu}$:

$$\boldsymbol{\mu} = \boldsymbol{\alpha}\boldsymbol{E} \tag{2.9}$$

where $\boldsymbol{\alpha}$ is the polarisability tensor. This may equivalently be written as:

$$\begin{bmatrix} \mu_X \\ \mu_Y \\ \mu_Z \end{bmatrix} = \begin{bmatrix} \alpha_{XX} & \alpha_{XY} & \alpha_{XZ} \\ \alpha_{YX} & \alpha_{YY} & \alpha_{YZ} \\ \alpha_{ZX} & \alpha_{ZY} & \alpha_{ZZ} \end{bmatrix} \begin{bmatrix} E_X \\ E_Y \\ E_Z \end{bmatrix}. \tag{2.10}$$

The electric field, $\boldsymbol{E}$, oscillates at a frequency, ω, which will cause the induced dipole moment to oscillate with respect to time, t:

$$\mu(\omega) = \alpha E_0 \cos(\omega t). \tag{2.11}$$

In addition, the molecular vibrations Q_m (where $1 \leqslant m \leqslant 3N-6$) with frequencies of ω_m modulate the polarisability:

$$\alpha = \alpha_0 + \frac{\delta\alpha}{\delta Q_m} Q_0^m \cos(\omega_m t). \tag{2.12}$$

This means that the induced dipole moment is:

$$\mu = \alpha_0 E_0 \cos(\omega t) + \frac{\delta\alpha}{\delta Q_m} Q_0^m E_0 \cos(\omega_m t)\cos(\omega t), \tag{2.13}$$

or equivalently:

$$\mu = \alpha_0 E_0 \cos(\omega t) + \frac{1}{2}\frac{\delta\alpha}{\delta Q_m} Q_0^m E_0[\cos(\omega - \omega_m)t + \cos(\omega + \omega_m)t]. \tag{2.14}$$

The first, second and third terms of this expression show that the induced dipole

moment oscillates with frequencies of ω, $(\omega - \omega_m)$ and $(\omega + \omega_m)$, respectively. When a photon is emitted in the scattering process it will have the same frequency as the oscillating dipole, so these three cases correspond to Rayleigh, Stokes and anti-Stokes scattering, respectively [45].

Further examination of the polarisability tensor gives the expression for Raman scattering:

$$\alpha_{\alpha\beta} = \frac{2}{\hbar} \sum_m \frac{\omega'}{\omega'^2 - \omega^2} \langle \psi_{e\nu} | \mu_\alpha | \psi_{e'\nu'} \rangle \langle \psi_{e'\nu'} | \mu_\beta | \psi_{e\nu'} \rangle, \tag{2.15}$$

where e and ν represent the electronic and vibrational ground states, e' and ν' represent the electronic and vibrational excited states, ω' is the frequency of the transition, α and β subscripts indicate the appropriate Cartesian components of the polarisability tensor and ψ is a stationary state wavefunction. This expression clearly shows that two photons are involved in the process because of the two electronic transition dipole moment expressions. It also shows that the selection rules for Raman spectroscopy are for vibrations with binary components $x \cdot x$, $x \cdot y$ and so on in the Cartesian displacements. This is different to the selection rules for IR absorption, so IR absorption and Raman scattering can probe different vibrational modes and the information they provide is complementary [45].

A particular strength of Raman spectroscopy is that additional information is contained in the polarisation of the scattered light. Unlike IR absorption spectroscopy, Raman spectroscopy can produce light with a different polarisation direction to that of the incident light. This arises from the vectors $\mathbf{E}$ and μ not necessarily being collinear. If linearly polarised light is used then the general case given in Equation 2.10 can be simplified. For example, light travelling in the Z direction and polarised in the X direction has $E_Y = E_Z = 0$ so Equation 2.10 becomes:

$$\begin{aligned} \mu_X &= \alpha_{XX} E_X \\ \mu_Y &= \alpha_{XY} E_X \\ \mu_Z &= \alpha_{XZ} E_X \end{aligned} \tag{2.16}$$

The depolarisation ratio, ρ, is defined as the ratio of intensities of light scattered with polarisation perpendicular to the initial polarisation direction and parallel

to it. In the case of linear polarisation in the X direction, the expression is:

$$\rho = \frac{I_Y^Z}{I_Y^X}, \tag{2.17}$$

where I_Y^Z and I_Y^X are the intensities measured after filtering out all but light with polarisation perpendicular and parallel to the incident light polarisation direction, respectively. The theoretical range of values ρ may take is from 0 to 0.75, with most observed examples falling between 0.01 and 0.6 [45].

The signal from Raman scattering is inherently very weak, due to the low probability of inelastic scattering, but it can be significantly enhanced in the case of resonance Raman spectroscopy (RRS). In this case, when the sample absorbs the photon, it is excited to a real electronically excited state instead of to a virtual state (shown in Figure 2.16). This is described quantitatively by Equation 2.14 in the case where ω' becomes close to ω then the denominator $(\omega'^2 - \omega^2)$ becomes small and the polarisability tensor $\alpha_{\alpha\beta}$ becomes very large. There are two advantages that this brings: one is that the signal is enhanced by up to five orders of magnitude so measurements can be made for shorter periods or on smaller samples; the other is that information can then be obtained about the electronic structure because this enhancement effect will only occur when the excitation laser is of the same energy as a difference in the sample's electronic energy levels [45].

Another way of obtaining stronger signals than conventional Raman spectroscopy would give is with surface enhanced Raman spectroscopy (SERS). This is also called plasmonic enhancement, as it uses collective motions of electrons called plasmons in a metal such as gold or silver to create a region with a stronger electromagnetic field, from which an enhanced Raman scattering intensity may be obtained. This will be described in more detail in Section 2.3.

The essential components of a Raman spectrometer will now be described. Firstly, a monochromatic light source, usually a laser, is needed to provide the excitation energy, which is usually in the visible range. This can be continuous wave or pulsed. The most common lasers to use are: He-Ne lasers, giving a line at 632.8 nm, Ar-ion lasers, giving lines at 488.0 nm and 514.5 nm, Kr-ion

lasers, giving a line at 647 nm or diode lasers with wavelengths around 780 nm [45]. A number of factors must be considered regarding the best laser line to use. Firstly, as seen in Equation 2.7, the signal intensity depends on ν^4 meaning that stronger signals are obtained with shorter wavelengths of laser light. The type of sample being studied might also influence the choice, for example biological tissue is transparent to near-IR light but not visible light, so to probe inside biological samples a suitable wavelength such as 780 nm should be used. Having a range of wavelengths available is particularly useful for resonant Raman spectroscopy. Different wavelengths allow different optical transitions to be probed. Similarly, if plasmonic enhancement is used then it is important to match the resonance frequency of the plasmonic structure with the laser light.

The laser light then enters the spectrometer and passes through a number of optical elements to reach the sample. In the case of micro-Raman spectroscopy (also called Raman microscopy) an objective lens is used to focus the light on the sample with a spot size usually on the order of microns. The scattered light from the sample, which contains the useful information about vibrations, is emitted in all directions. Conventional Raman spectrometers usually collect the scattered light at 90° to the incoming light [45], but in the case of Raman microscopy the backscattered light is collected through the same objective lens used to focus the laser light. Due to the probabilities of the different processes, the vast majority of the light that is collected is of the same frequency as the incoming light, that is, Rayleigh scattered light. To detect the Raman scattered light without saturating the detector, the Rayleigh light must be filtered out. This is done by means of a notch filter or edge filter. Notch filters cut out a small range of wavelengths but let through shorter and longer wavelengths so Stokes and anti-Stokes signals can both be measured. Edge filters cut out all wavelengths above or below a given point, so they are specific to either Stokes or anti-Stokes scattering. Edge filters can allow through wavelengths closer to the laser wavelength, so information about more low-energy vibrations is available. While notch filters allow more flexibility in measurements, they degrade more rapidly over time and are more expensive in comparison with edge filters [46].

The final task of the spectrometer is to determine the different frequencies

and relative intensities of the Raman scattered light. Older spectrometers did so by means of a monochromator (or a double monochromator), photomultiplier and detector such as a digital photon counter [45]. Alternatively, more recent spectrometers have charged couple device (CCD) detectors, which measure the intensity of light hitting spatially distinct positions on an array. Thus a single diffraction grating is sufficient to split the scattered light according to its frequency and the CCD measures the different intensities.

2.2.1.2 Raman spectroscopy of carbon nanotubes

Raman spectroscopy is one of the most common techniques used in the characterisation of carbon nanotubes due to the wealth of information available as well as its easy application without laborious sample preparation steps. This section describes the essential points for interpreting spectra. The effects of electron–phonon coupling on Raman spectra of CNTs are discussed in Chapter 6.

Resonance conditions

As described in the previous section, resonance Raman spectroscopy can increase signal intensities by several orders of magnitude. This is important for carbon nanotubes, where their density of states has van Hove singularities arising from their one-dimensional structure (as described in Section 2.1.3). Optically allowed transitions are shown on Figure 2.17, labelled as E_{11} or E_{22} and so on. If the excitation laser energy matches the energy of one of these transitions then resonance enhancement will occur and a spectrum may be measured, even from a single SWNT [47].

The energies of the van Hove singularities, and therefore the energies of the optically allowed transitions, depend on the chirality and the diameter of the SWNT. Figure 2.18 shows a Kataura plot, which shows the relationship between electronic transitions and diameter, for metallic and semiconducting SWNTs. If a given laser wavelength is used then only a selection of SWNTs will be resonant and therefore give a strong enough Raman signal to be observed [47].

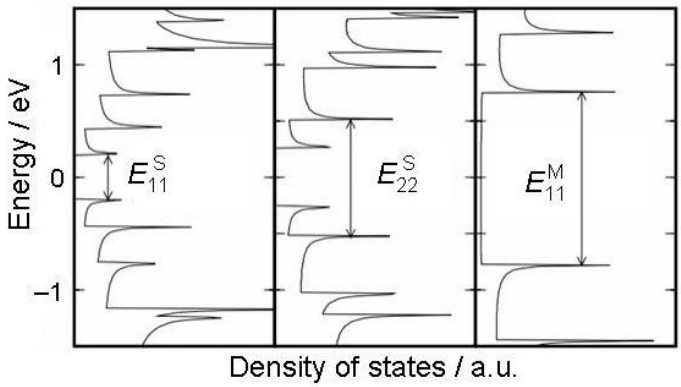

Figure 2.17: DOS and optically allowed transitions E_{11}^{S} and E_{22}^{S} of semiconducting SWNTs $(22, 0)$ and $(11, 9)$, respectively, and E_{11}^{M} of a metallic (armchair) SWNT $(10, 10)$. Adapted from reference [47].

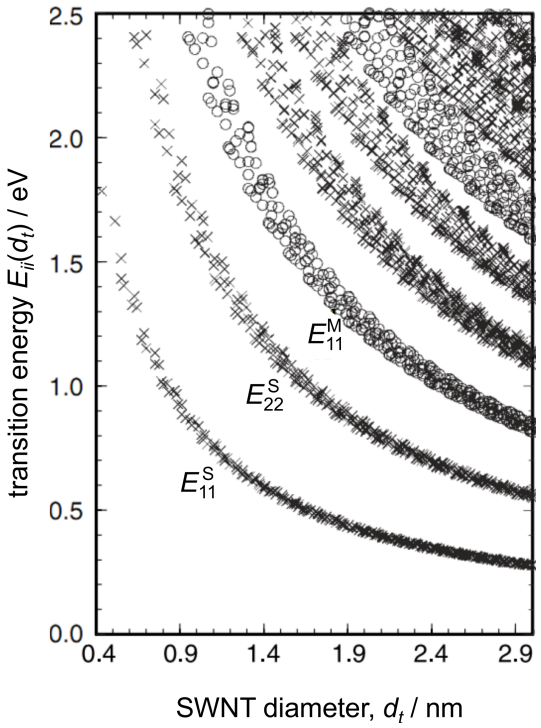

Figure 2.18: Kataura plot of optically active transition energy against SWNT diameter. Crosses represent semiconducting SWNTs and circles represent metallic SWNTs. The vertical axis is proportional to the excitation laser energy, so with a given laser line, SWNTs appearing in the horizontal line for that laser energy can be excited. Adapted from reference [47].

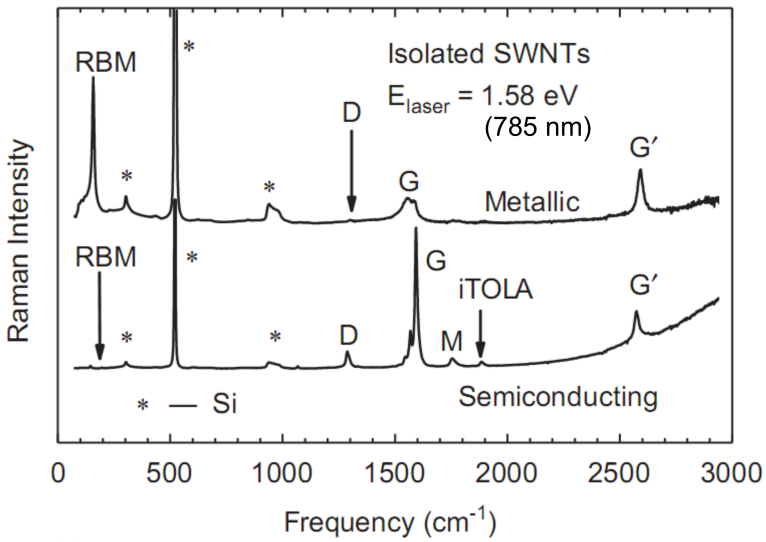

Figure 2.19: Typical Raman spectra for individual metallic and semiconducting SWNTs on an oxidised silicon surface. The important bands are labelled, as described in the text. Adapted from reference [48].

Important Raman modes

An example spectrum of a SWNT is shown in Figure 2.19 with the important peaks labelled. The first region of importance is between 120 cm^{-1} and 250 cm^{-1}, where the radial breathing mode (RBM) appears. This peak arises from a coherent motion of carbon atoms towards and away from the centre of the nanotube in the plane of the circumference (Figure 2.20a). The position of the peak is related to the diameter of the nanotube:

$$\omega_{\text{RBM}} = A/d + B, \tag{2.18}$$

where ω_{RBM} is the measured Raman shift, d is the nanotube diameter in nanometres and A and B are empirical parameters dependent on the substrate used, the degree of bundling, whether the nanotube is suspended or supported and the structure of the nanotube, amongst other factors. For individual SWNT on an oxidised silicon surface typical values are $A = 248$ cm^{-1}nm and $B = 0$ [47].

Knowledge of the excitation laser energy and the diameter as obtained from Equation 2.18 may be combined when looking at the Kataura plot (Figure 2.18). Since every spot represents a specific (n, m) SWNT, this gives a significantly

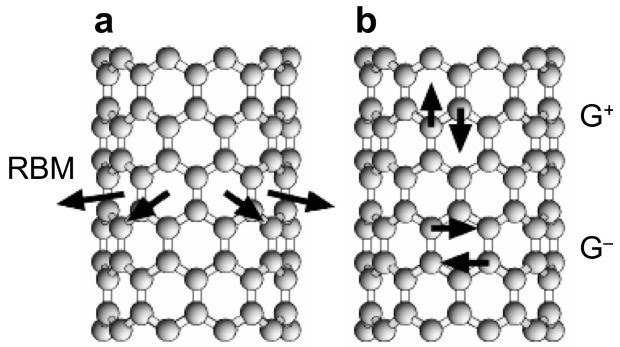

Figure 2.20: Pictorial illustration of (a) the radial breathing mode (RBM) of a SWNT and (b) the vibrations accounting for the G^+ and G^- peaks of a SWNT Raman spectrum. Adapted from reference [47].

reduced pool of possible chiral indices of the SWNT under study.

In addition, as the RBM has the smallest resonance window of the Raman peaks of a SWNT, it gives the best measure of the E_{ii} transition energy. This may be obtained with a tunable laser, or by comparison of the Stokes and anti-Stokes RBM positions obtained from a single laser line [47].

Another very important region of the Raman spectrum is the G band, appearing as multiple peaks around 1580 cm^{-1}. The resonance window for the G band is wider than that for the RBM so, while it cannot easily give such precise data about the nanotube diameter, it often gives a stronger signal that is rich in information about the metallic or semiconducting nature of the nanotubes. The name refers to the tangential mode in a graphite Raman spectrum, but the curvature of the nanotube breaks the graphite symmetry and splits the peak into a band comprising up to six peaks in a first-order Raman process. Of those six modes, two are particularly strong, labelled as the G^+ mode for atomic displacements along the tube axis and the G^- mode for atomic displacements along the circumferential direction (Figure 2.20b). The G^- mode is particularly sensitive to the size and type of nanotube. The curvature causes the G^- mode to be downshifted with respect to the graphite G peak, with the size of the change depending on the diameter of the nanotube. In semiconducting carbon nanotubes the G^- peak adopts a Lorentzian lineshape, in common with all other Raman spectrum features, whereas the G^- peak of a metallic carbon nanotube is broadened due to coupling between the phonon and electrons and is fitted with a

Breit-Wigner-Fano (BWF) line. The splitting between G^+ and G^- peaks can be used to gain a measure of nanotube diameter, as long as individual SWNT are being examined [47].

Another interesting feature of a CNT Raman spectrum is the D band, meaning the 'disorder induced' band or simply the 'defect' band. This arises from a double resonance process and appears at approximately 1300 cm^{-1}, depending on the excitation laser wavelength as well as the diameter and chirality of the SWNT. The ratio of intensities of the D and G bands is taken to give a measure of defects present in the sample. The D band of a SWNT has a small linewidth (40 cm^{-1} to 7 cm^{-1}), which is in contrast to amorphous carbon which has a much broader D peak [47].

The G′ band also arises from a double resonance process and occurs in the region of 2700 cm^{-1}. It is also known as the 2D band since it is an overtone of the D band. As such, its position is also laser wavelength, diameter and chirality dependent. However, its appearance in the Raman spectrum does not depend on the presence of defects [48].

There are more peaks that can be observed in the Raman spectra of carbon nanotubes but usually with much lower intensities than the peaks already described. Some of these peaks can provide insight for understanding electron transport, thermal and mechanical properties of CNT and for determination of the chirality of individual SWNTs [47].

Polarisation analysis

Due their highly anisotropic nature, individual SWNT respond very differently to light polarised in different directions. This antenna-like behaviour is conceptually understandable since the delocalised π electrons are more easily polarisable in the direction of the SWNT axis and more confined in the direction perpendicular to the axis. For simply obtaining a good spectrum from a SWNT, the signal can be optimised by rotating the laser polarisation direction with addition of a $\lambda/2$ waveplate until the light polarisation direction is parallel to the SWNT axis [47].

More sophisticated polarisation studies require knowledge of the Raman

intensity as a function of polarisation direction. Figure 2.21 shows this dependence measured experimentally for the RBM and G^+ and G^- modes. The different Raman peaks all show the same angular dependence, in contrast to the behaviour expected according to the symmetries of the vibrational modes (A_{1g} for RBM and A_{1g}, E_{1g} and E_{2g} for G band modes) in non-resonant Raman scattering [49]. It is, however, consistent with the angular dependence expected for resonant Raman scattering of a one-dimensional object. In this case the polarisability tensor, $\boldsymbol{\alpha}$, for a carbon nanotube orientated with the axis in the z direction and incident light polarised in the z direction becomes:

$$\boldsymbol{\alpha} = \begin{bmatrix} \alpha_{XX} & 0 & 0 \\ 0 & \alpha_{YY} & 0 \\ 0 & 0 & \alpha_{ZZ} \end{bmatrix} \cong \begin{bmatrix} 0 & 0 & 0 \\ 0 & 0 & 0 \\ 0 & 0 & 1 \end{bmatrix}. \tag{2.19}$$

As the CNT is rotated with respect to the incident laser polarisation, such that ϕ measures the angle between CNT axis and laser polarisation, the intensity of the light scattered with polarisation parallel to the incident light is given by:

$$VV(\phi) \propto \cos^4 \phi, \tag{2.20}$$

and the intensity of the light scattered with polarisation perpendicular to the incident light is given by:

$$VH(\phi) \propto (\cos^2 \phi)(\sin^2 \phi), \tag{2.21}$$

which is consistent with the experimental dependence as shown in Figure 2.21 [50, 51]. With this information, the alignment of an ensemble of SWNTs may be quantified [51, 52].

2.2.2 Atomic force microscopy (AFM)

Atomic force microscopy (AFM) is a method of imaging the topography of a surface using a sharp tip that scans over a small area, 'feeling' how the height changes as it traverses the sample.

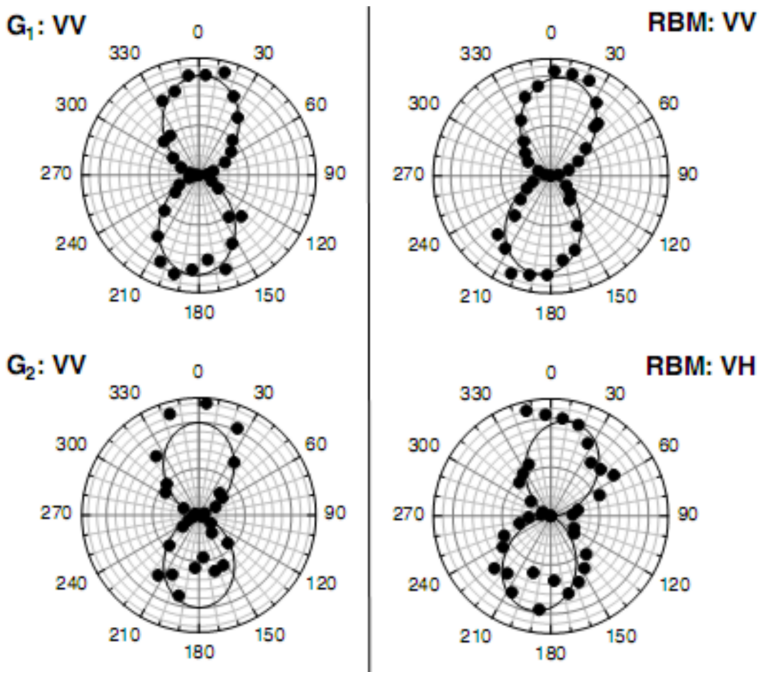

Figure 2.21: Polarisation dependence of CNT Raman G (left) and RBM (right) bands. G_1 and G_2 represent the G^+ and G^- peaks, respectively. VV means that the scattered light was detected only if it was polarised parallel to the polarisation of the incident light. VH means the detected scattered light was perpendicular to the incident polarisation. The angle (in degrees) is measured from the CNT axis to the incident light polarisation direction. The solid lines are a fit to the experimental data. Adapted from reference [49].

Before AFM was developed, less sophisticated methods were available for detecting topographies or height profiles of a sample surface. In the 1920s a stylus profiler enabled magnification of the height by more than 1000× [53]. In this technique a sharp tip was dragged over a surface and a beam of light, after reflecting off a mirror on the back of the tip, was detected on photographic paper. The sample could be damaged by the tip, however, since the contact between tip and surface was not controlled. A notable development was by Binnig and Rohrer who made the first scanning tunnelling microscope (STM) in 1981 [54]. This used the tunnelling current between a sharp conducting tip and a conducting surface to detect very small distances between the tip and the surface. Feedback electronics connected to piezoelectric actuators controlled the separation distance so as to maintain a constant current while the tip scanned over the surface, even when it encountered depressions or protrusions. This development led to the Nobel Prize

for physics in 1986 being awarded to Binnig and Rohrer [55]. The first AFM followed shortly after the STM, developed in 1986 by Binnig, Quate and Gerber [56], addressing the problem that STM works only for conducting samples. From this launchpad AFM has grown into a widely used versatile microscopic technique, particularly due to easier distance-detection methods, mass production of probe tips and the development of various modes of operation. As a result of their similarities, STM and AFM are often referred to together as scanning probe microscopies (SPM) [57, 58].

To create topography images in SPM systems there must be a sharp tip, a method of moving the tip with respect to the sample surface and a method of detecting the tip–sample contact or distance. In addition, for the practical implementation of the technique, it is important to have mechanical control for larger changes in tip–sample relative positions and isolation from acoustic and mechanical vibrations. Finally, an optical microscope is helpful for positioning. Although there are several methods available for detecting tip–sample contact, the laser-deflection method is the most common and is the only one discussed here. A schematic illustration of a typical instrument, using laser-deflection feedback, is shown in Figure 2.22 [57, 58]. These components will now be discussed in greater detail.

The sharp tip used in an AFM to probe the surface is found at the end of a cantilever held in a mount within the instrument head (Figure 2.23). Typically the cantilever has a length, l, of around 100 µm, a width, w, of around 30 µm and a thickness, t, of around 2 µm and the tip at the end protrudes by 10–15 µm with a final tip curvature radius of 10 nm. They are manufactured in bulk by microfabrication processes, most commonly from silicon or silicon nitride (Si_3N_4). The material properties of the cantilever affect how the tip interacts with the sample, for example a softer material such as Si_3N_4 produces probes with lower force constants, which will press more gently on the surface. The spring constant for normal bending, k_N, for a rectangular cantilever is quantified by:

$$k_N = \frac{Ewt^3}{4l^3}, \tag{2.22}$$

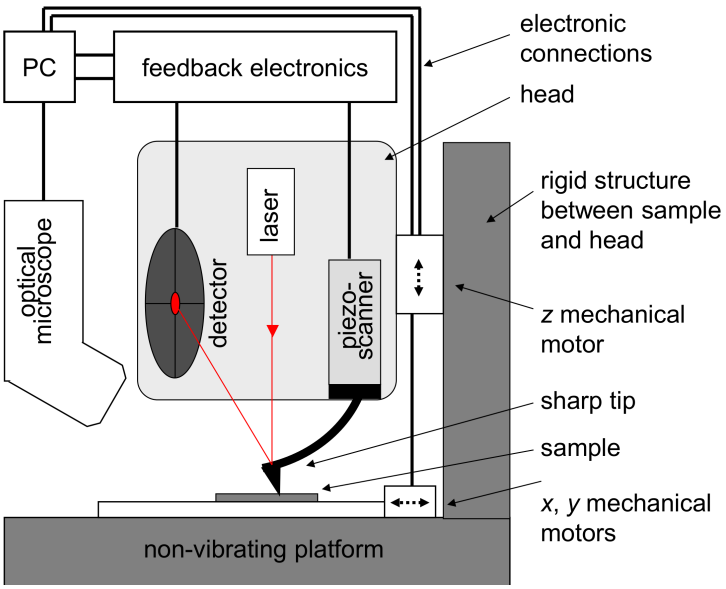

Figure 2.22: Schematic diagram showing the important parts of a typical atomic force microscope, where the feedback is provided by laser-deflection and the tip is scanned over a stationary sample.

where E is the Young's modulus of the material. Different modes of AFM operation, which will be described later, require probes with different force constants: less than 1 N/m for contact mode and usually greater than 10 N/m for tapping mode where the tip oscillates vertically over the surface (described in more detail below). The material properties also govern the resonance frequency of the tip vibration. For the probe to operate effectively in tapping mode, the resonance frequency must be independent of external vibration sources such as building vibrations and sounds waves. This means frequencies above 10 kHz, up to 100s of kHz, are used. A metal coating is sometimes added to the backside of the cantilever to enhance the reflectivity for the laser spot and generate a stronger signal [57, 58].

Another essential component of an AFM is the scanner, which moves the tip with respect to the sample, with control on the nanometre range or smaller. This small movement is achieved with piezoelectric actuators, which change their size and shape slightly when a voltage is applied. As a simple model, a bar of a piezoelectric material such as lead zirconium titanate (PZT) will expand by approximately 0.2 nm for each volt applied to it. Thus to achieve

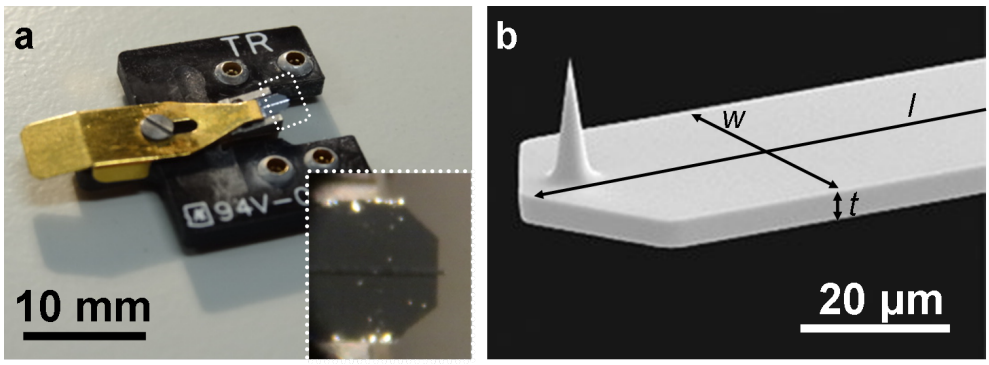

Figure 2.23: (a) Photograph of an AFM probe in its holder. The dotted box indicates the location of the tip, and (inset) a zoomed-in photograph of this region reveals the cantilevered tip extending out from the larger silicon substrate, held by the holder. (b) A SEM image illustrates the definition of the length, l, width, w, and thickness, t, as well as showing the tip protrusion from the cantilever. SEM image from www.nanoscience.com.

movements on the micron scale, high voltages must be applied. In AFM instruments, piezoelectric actuators are arranged in a way that allows control in the x, y and z directions. In practice, creep, hysteresis and non-linearity can add complexity to the system, so calibration must be carried out and repeated at regular intervals over time. Closed-loop systems, which have in-built sensors for measuring changes in the x, y and z positions of the piezo scanner, are more robust against these problems. Commonly, the piezo scanner scans the tip while the sample is fixed stationary under it but in an alternative configuration the sample may be controlled by the piezo scanner and move under a fixed tip [57, 58].

AFM differs from other SPM technologies in that it detects the force exerted between the probe tip and the sample surface. As already mentioned, the most common method of detecting this is by measuring the position of a laser spot after it has reflected off the back of the cantilever. Other methods that can be used include the use of interferometry, capacitance, piezoresistance, piezoelectricity, electron tunnelling or vibrations of a crystal oscillator. As seen in Figure 2.22, the laser is detected by a photodetector after it has been reflected off the back of the probe cantilever. If the force increases or decreases then the cantilever will exhibit a greater or smaller bend and the laser spot will hit the detector in a higher or lower position. The photodetector is sometimes called the position-sensitive

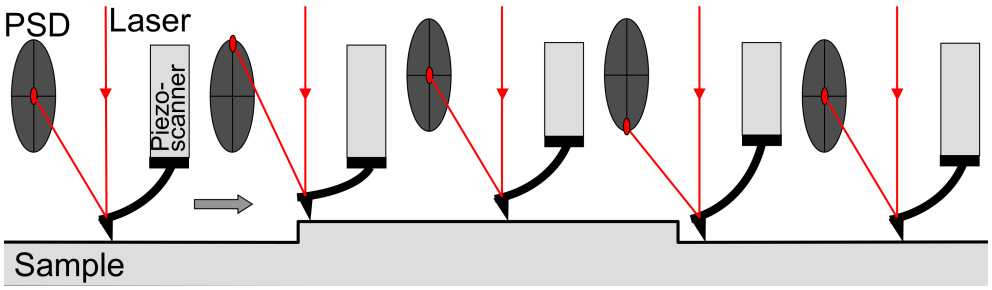

Figure 2.24: Schematic illustration of laser-deflection AFM feedback system. As the tip traverses the surface from left to right it encounters a step up, which causes the cantilever to bend more and shift the laser spot to higher position on the PSD. The piezo scanner corrects for this so that the cantilever bend is equal to its initial state. Similarly, as the tip encounters a downward step the cantilever bend decreases and the spot moves down until the piezo scanner again corrects for the change in height.

detector (PSD) and it usually has four quadrants. The normal force is measured by taking the difference in signal between the top two and bottom two quadrants. This value is compared with a 'setpoint' value set by the operator and the 'error' is the difference between the measured signal and the setpoint. Feedback electronics, through a proportional–integral–derivative (PID) controller, control the voltage applied to the z-piezo to reduce the error signal to zero, operating continuously as the tip scans over the surface. The relation between the measured error signal, Z_{err}, and the voltage to be applied to the z-piezo, Z_V, is:

$$Z_V = P \times V_{\text{err}} + I \times \int Z_{\text{err}} \mathrm{d}t + D \times \frac{\mathrm{d}Z_{\text{err}}}{\mathrm{d}t}, \tag{2.23}$$

where P, I and D are the values selected in the PID controller and t is time [58]. Figure 2.24 illustrates the changing cantilever bend and corresponding change in laser-spot PSD position caused by the tip encountering steps on the surface. As the tip scans in a raster fashion over the chosen area, a computer records Z_{err} as well as Z_V or, in the case of a closed-loop system, the z-sensor signal, and images may be built up line-by-line representing the sample surface [57, 58].

Thus far, most of the description of AFM has described operation in contact mode, where the only z-motion of the tip is in response to changes in the surface height. Contact mode can give good resolution and relatively fast operation but

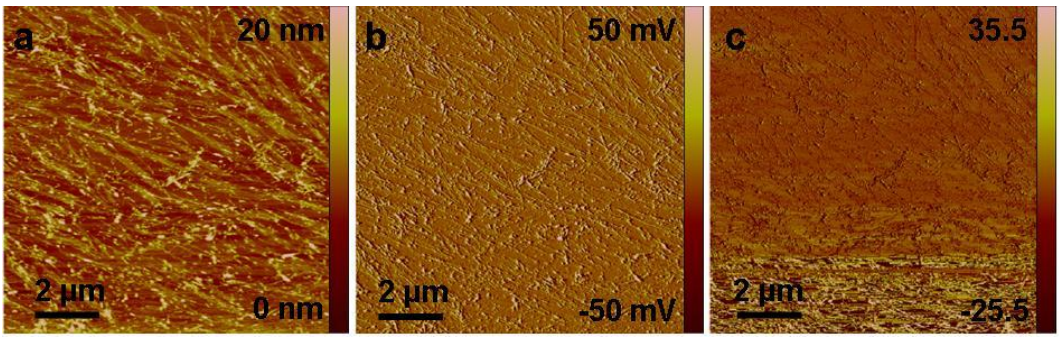

Figure 2.25: Example AFM images showing (a) height, (b) amplitude error and (c) phase of carbon nanotubes lying on a flat surface.

as the tip moves over the surface high lateral forces can cause damage on the surface such as movement or removal of adsorbed species. Tapping mode is an alternative to contact mode, where the tip constantly oscillates in the space above the sample surface. This oscillation, at or close to the cantilever's resonance frequency, is created by an additional small piezoelectric actuator close to the cantilever. As the tip is brought down from free space into proximity to the sample surface, the amplitude of vibration becomes curtailed. Just as in contact mode, the operator chooses a setpoint at which point the tip stops approaching the surface. In tapping mode the setpoint refers to a proportion of the free-space amplitude and is usually in the region of 80%. During scanning, the z-sensor or z-correction data are recorded to form the height image and additional channels can record the error signal, which is the difference in detected amplitude from the setpoint, and the phase of the vibration, which is also affected by changes in the height of the tip above the surface. Since, in tapping mode, most of the time the tip is not touching the surface, it is sometimes named a non-contact mode but a more accurate description is to call it intermittent-contact mode. The main advantage of tapping mode is that there is almost no lateral force exerted on the sample due to the slow lateral speed in comparison with the speed of the vibrational motion, so imaging is less likely to damage the sample [57, 58].

AFM height images are commonly presented in a colour-scale in which brighter shades represent higher or raised features and dark shades correspond to depressions on the surface (Figure 2.25). The images must be interpreted with educated

judgement in order to differentiate between artefacts and the true topography. Firstly, the lateral resolution obtainable from AFM measurements is largely determined by the sharpness of the tip used (Figure 2.26a). Standard silicon AFM tips have a tip diameter of the order of ten of nanometres, so features on the surface will be 'blurred' by this amount. For example, two small features of less than 10 nm each positioned adjacent to one another will appear as a single feature. Ultra-sharp tips can be made, by special sharpening techniques or by addition of a rigid carbon nanotube, which can improve the resolution, but their lifetime is significantly shorter than standard tips and their manufacture cost is greater. In general, height measurements have greater precision and accuracy then lateral distances, although the latter can be interpreted if care is taken to deconvolute the tip and sample contributions. Secondly, if the PID gains and setpoint are not chosen appropriately during the measurement then artefacts can occur. For example, if the gains are too low (Figure 2.26b) then sharp steps in the topography will appear smeared out but if the gains are too high oscillations will appear and the tip will appear to overshoot in the case of sharp steps (Figure 2.26c). Thirdly, thermal drift can cause the sample to move with respect to the tip, apart from the raster scanning movement. On large and/or fast scans this is usually negligible but when performing slow high-resolution scans on small areas it can appear quite pronounced (Figure 2.26 d and e). Finally, the probe can become contaminated, with something adsorbing onto the tip. The effect of this is that every feature on the sample appears to have the shape of the contaminated tip (Figure 2.26f). Usually this requires the tip to be replaced [57, 58].

2.2.2.1 AFM of carbon nanotubes

The use of AFM in the study of carbon nanotubes is usually to measure their position and/or size after they have been grown or deposited on a flat surface. CNTs can be recognised as a linear feature, with a height corresponding to the diameter of the nanotube, so approximately 1 nm for an individual SWNT or up to tens of nanometres for a MWNT or a bundle of SWNTs. The width of a nanotube normally looks significantly larger than the diameter because of

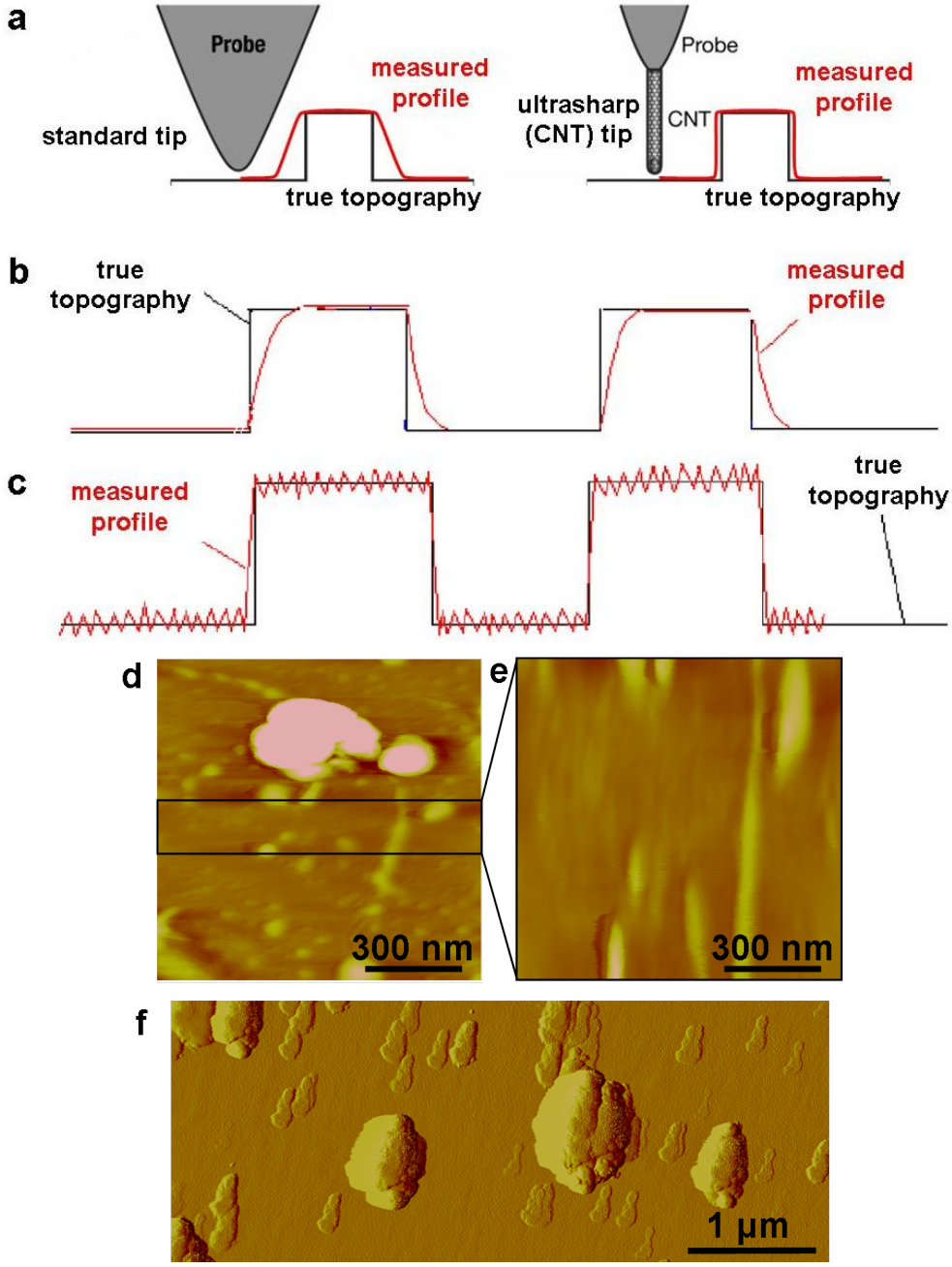

Figure 2.26: Illustrations of artefacts that can occur during AFM scanning. (a) A blunt tip causes a loss of resolution so features appear more rounded, but can be improved with special ultrasharp tips. (b) Setting the feedback gains too low causes smearing as the tip does not respond quickly enough to changes in height. (c) Setting the feedback gains too high introduces oscillating noise. Thermal drift can (d) contract or (e) stretch an image depending whether the drift direction is against or with the direction of the slow scan axis, respectively. The images (d and e) were of the same area (black rectangle) measured in different directions. A contaminated tip appears to give its shape to everything that it encounters (f, amplitude error image). Part a is adapted from reference [59] and parts b and c are adapted from reference [60].

convolution with the tip diameter, so this measurement is not commonly used. In the work presented in this thesis, AFM has been used primarily to locate SWNTs, with reference to other features on the surface that are visible in an optical microscope. This allows other techniques such as Raman spectroscopy to be performed at the correct location despite the carbon nanotube itself not being visible. In addition, advanced AFM-based techniques will be presented, for example replacing the tip with a nanopipette in fountain pen nanolithography in Chapter 4 and using a standard tip to control the relative positions of objects on a surface with nanomanipulation in Chapter 5.

2.2.3 Scanning electron microscopy (SEM)

Scanning electron microscopy (SEM) is a useful technique for creating images of a surface that look like greyscale photographs but which have a resolution far exceeding that of a camera or optical microscope at very high magnifications. In light microscopy, the maximum theoretical resolution is related to the light's wavelength. As an approximation, two features will not be identified as distinct if their separation is less than half the wavelength of the light. So with light in the visible region, with wavelengths ranging from 400 nm to 700 nm, the smallest features that may be resolved are around 200 nm [61]. Electrons, however, have a wavelength defined by the de Broglie equation and at the electron energies typical to SEM this gives a wavelength of less than 0.01 nm [62]. The theoretical resolution is thus much improved in a microscope that uses electrons instead of photons. In practice the resolution is limited by other experimental factors, such as the electron-beam width, so most SEMs have a resolution of under ten nanometres, down to one or two nanometres. The range of magnifications offered is large: from 10× to 100,000×. As well as increased resolution and magnification range, SEM images have a bigger depth of field than optical microscopes, so more of the sample can appear in focus simultaneously, even on rough samples.

The scanning electron microscope was initially developed just after the transmission electron microscope (TEM) in the 1930s, building on Ernst Ruska's Nobel Prize-winning work on electron optics [55, 61]. The first commercial

instrument was available in 1965, with an expected market demand of just ten instruments, which was exceeded one hundredfold within the first decade alone [61]. Since then developments have improved the resolution and sensitivity available, lowered the accelerating voltage required and have added extra analytical functions to the instrument [61, 63].

The basic elements of a scanning electron microscope are shown schematically in Figure 2.27. The first requirement is a beam of electrons, which comes initially from an electron gun such as a tungsten filament hot-cathode gun or, for better resolution, a field-emission gun. The electron beam is controlled by electromagnetic lenses before it hits the surface of the sample being analysed. The condenser and objective lenses dictate the size of spot that the electrons make on the sample and the range of angles the electrons may approach from, which in turn affects the resolution of the image and the depth of field. Within the objective lens there are coils that allow the beam to be raster-scanned over the chosen area of the sample. At each point of the scan, the electron beam causes some electrons to be inelastically scattered at low energies and released from the sample. These so-called secondary electrons are extracted and detected and the number of them governs the brightness of that spot on the image. Thus the image obtained after a full scan is not a direct picture of the surface but is actually a map of the extent of secondary electron emission over the scanned area. The whole apparatus must be under high vacuum or, for field-emission guns, ultrahigh vacuum to allow the electron gun to operate at high voltages without arcing occurring and to give the electrons in the beam a long enough mean-free path. The exception to this is an environmental SEM, which has the sample chamber at near atmospheric pressure, while having the rest of the instrument in vacuum [61].

The reason why the images produced show the topography and, to some extent composition, of a surface will now be explained. When the electrons in the beam hit the atoms of surface, scattering events occur as they interact. In some cases the scattering is elastic and the electron loses no energy but in other cases inelastic scattering occurs and the electron energy is reduced from kilovolts to a few volts. The scattering occurs in a teardrop-shaped region within the sample Figure 2.28. The low-energy, secondary electrons are only able to leave the surface and reach

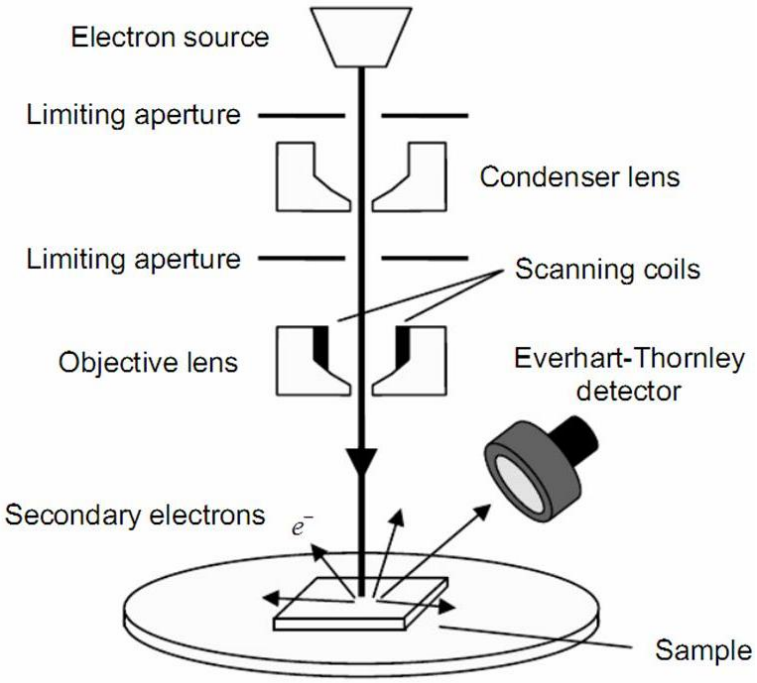

Figure 2.27: A schematic diagram of the essential components of a scanning electron microscope. From reference [64].

the detector if they are scattered from part of the volume very close to the surface. The surface morphology therefore affects how much of the scattering volume is close to the surface and therefore how many secondary electrons are detected from that spot (Figure 2.28 b and c). Overall this results in a picture that is intuitive to the human eye because it shows raised bumps brighter and hollows as darker, or shadowed, just as if looking at a subject illuminated by a light point source. In addition, the material of the sample affects the scattering volume and the depth from which secondary electrons may escape, so on a sample with a mixture of light and heavy elements there will be contrast even if the features are planar and smooth [61].

One of the main limitations of SEM is that the sample must be conducting, or the beam of electrons will cause the sample to charge and the image will become distorted. Environmental SEM goes some way to minimise this limitation because the gas molecules in the sample chamber can remove charge from the sample as it is imaged. Another disadvantage of using SEM to image samples is that it causes a build-up of amorphous carbon wherever the electron beam hits, due to

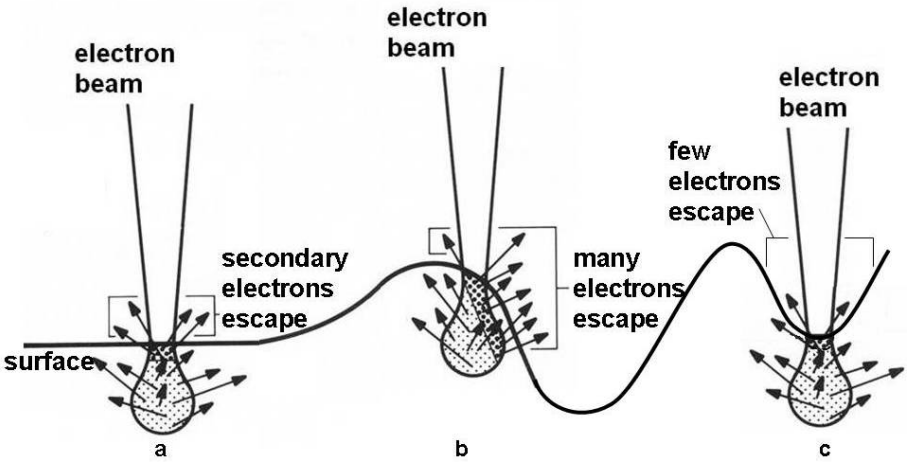

Figure 2.28: The volume in which secondary electrons are scattered when an electron beam hits a sample. Only the electrons scattered near the surface (dark shading) are able to escape and be detected so (b) more electrons are detected from raised areas and (c) fewer are detected from hollows in comparison with (a) flat areas of the surface. Adapted from reference [61].

unavoidable traces of carbon-containing gases, even at ultrahigh vacuum. This causes the pictures to become darker if they are imaged for a period of time, and it contaminates samples, which might cause loss of function, altered properties, or the appearance of deterioration. The carbon contamination can be minimised by lowering the accelerating voltage but if it is to be avoided entirely then alternative imaging methods such as AFM must be used instead [61].

SEM is a valuable tool for providing high resolution and easy-to-interpret images of a sample surface, at very high magnifications and resolutions, despite having some disadvantages.

2.2.3.1 SEM of carbon nanotubes

Carbon nanotubes normally appear in SEM images as bright lines (Figure 2.29). Even SWNTs may be visualised in this way despite their diameter being smaller than the instrument resolution. There are a number of proposed explanations for this, for example the insulating substrate immediately around the SWNT becoming charged and therefore giving a higher probability of electron emission. SWNTs suspended over a surface appear sharper and brighter than those in contact with the surface [65].

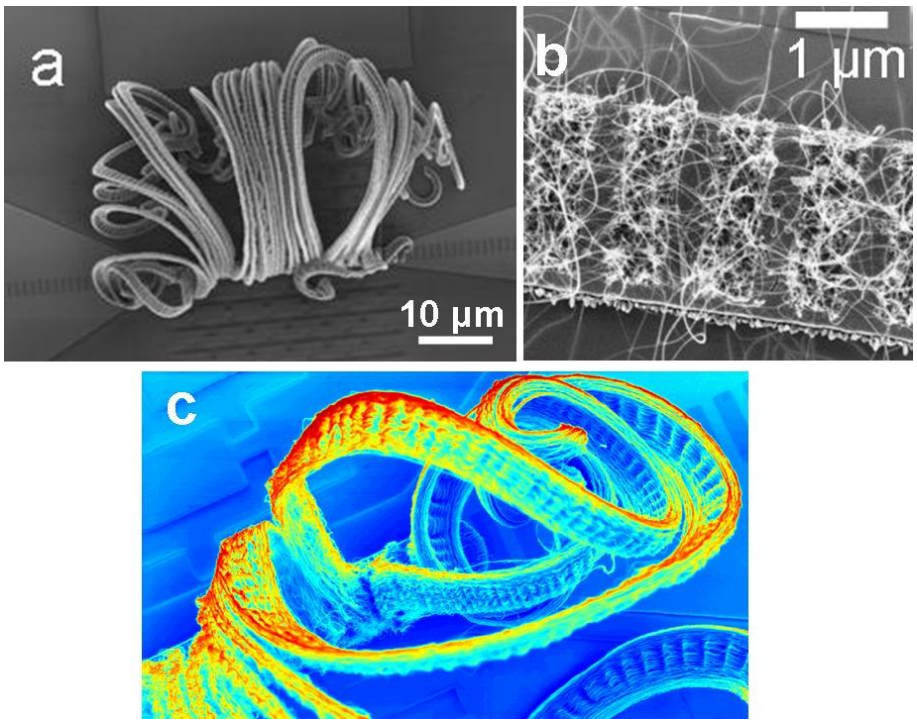

Figure 2.29: SEM images of carbon nanotubes, showing how the nanotubes are brighter than the surrounding surfaces. (a) Large numbers of MWNT projecting from a surface in thick ropes. (b) SWNTs as grown from a metal bar (centre) and lying on and over a silicon oxide surface (top and bottom). SWNTs in contact with the SiO_2 surface appear broader and blurrier than SWNTs suspended above the surface. (c) Artisan version of a section of part a showing the possibilities of alternative colour scaling. Adapted from reference [66].

SEM is a useful technique for identifying the location of CNTs with respect to other features on the sample, for quickly revealing how many CNTs are present in a given location and for making a clear and easy-to-interpret image of the sample for purposes of communicating device designs. However, it has risks that must not be forgotten or ignored. At high electron energy (80 keV or higher) carbon atoms can be ejected from the nanotube's structure by the electron, resulting in irreversible damage. Keeping the electron beam at lower energies prevents this dramatic form of damage but the CNTs are still adversely affected. Low-energy irradiation damage has been observed for electron energies of <10 eV. Raman scattering, photoluminescence, chemical and electrical properties can all be affected by this damage, which is a direct result of the electron beam causing small localised defects. These are not well defined but might include broken C–C bonds, Stone-Wales defects or adatom-vacancy defects resulting from

migratory C atoms. In addition, contaminant effects are almost always seen where hydrocarbons in the chamber decompose onto the sample as a carbon deposit, visible as a darkened area where the electron beam has scanned. Because of these types of damage, SEM should not be performed on CNT-containing samples until all other measurements have been completed, and if a large-area image is to be made as well as a high-resolution image of a smaller area, the large-area image must be made first to avoid the appearance of a dark square of carbon contamination on the smaller scan area [67].

2.3 Enhancement of Raman scattering by plasmonic nanostructures

2.3.1 Introduction to SERS and plasmonics

Surface-enhanced Raman spectroscopy (SERS) can give Raman scattering signals many orders of magnitude higher than in conventional Raman spectroscopy. This is due to the so-called plasmon resonances that occur at a metal surface when it is irradiated with light of a certain wavelength. The electromagnetic field close to the metal surface is enhanced, which in turn enhances the Raman scattering intensity of a Raman scatterer located in the vicinity of the metal surface, as will be described in this section.

Plasmons can be described as 'collective charge oscillations of the free electrons of a metal,' and 'the study, fabrication and application of plasmon-supporting structures' is known as plasmonics [68]. Plasmonics and SERS are inseparable. SERS, which is used to increase the sensitivity of Raman spectroscopy, is completely reliant on plasmons and can be optimised with a good understanding of them. It is used in a very wide range of multi-disciplinary applications, including chemistry, biology and medical research. Plasmonics itself as a research field concerns the physics and fundamental understanding of plasmonic systems. For this, SERS is a useful probe, allowing the measurement of enhancement factors from different plasmonic structures, which can then be related to theory and computational models. The enhancement observed in SERS has been

attributed to two different causes: electromagnetic and chemical. The chemical effect is still less well understood and is generally recognised to be of secondary importance, so here only the electromagnetic enhancement will be discussed [68].

Plasmons are more accurately defined as 'quantum quasi-particles representing the elementary excitations or modes of the charge density oscillations in a plasma,' [68] comparable to the photon being the quantum particle for free electromagnetic field oscillations. When considering SERS, an important point is how plasmons interact with light. Some plasmons, such as bulk plasmons, are not able to couple to light at all. Other plasmon modes can couple to an incoming photon and in doing so they create plasmon-polaritons, which can been thought of as electromagnetic waves in an optically responsive medium. Of most note is a family of modes called surface plasmon-polaritons (SPPs), which exist at the interface between a metal and a dielectric. If one is most interested in the optical response of the system then these SPPs can be considered as electromagnetic modes, while the actual dynamics of the charge density oscillations need not be emphasised. SPPs can be either propagating (PSPP) or localised (LSP) depending on the geometry of the metal/dielectric interface: whether the interface is larger or smaller than the wavelength of the incident light, respectively. Due to the law of conservation of momentum, PSPPs on a flat metal surface cannot couple to light so some grating or surface roughness needs to be created, breaking the translational invariance and locally relaxing momentum conservation. In contrast, the plasmons of metal particles with nanometre dimensions are able to couple to light because of the finite geometry providing momentum exchange between LSP and the metal lattice [68, 69].

The dielectric function of the metal as a function of the frequency of light, $\epsilon(\omega)$, can be described by the Drude model using the Lorentz model:

$$\epsilon(\omega) = \epsilon_\infty(1 - \frac{\omega_p^2}{\omega^2 + i\gamma_0\omega}), \tag{2.24}$$

where $\epsilon_\infty \geq 1$ represents the background from the positive ions of the crystal, γ_0

describes damping and the plasmon frequency, ω_p, is defined as:

$$\omega_p = \sqrt{\frac{ne^2}{m\epsilon_0\epsilon_\infty}}, \tag{2.25}$$

where n is the number of free electrons per unit volume and m is their mass [68]. In these terms, the frequency of the plasmon will be in the visible range and helpful for SERS applications when the real part of Equation 2.24 is negative and the imaginary part is small [68].

The choice of metal is very important and affects both the real and imaginary parts of Equation 2.24. For example, platinum and palladium have too high a value of the imaginary part of $\epsilon(\omega)$, which means there is too much absorption. Aluminium would be appropriate only at ultraviolet (UV) wavelengths. It has been found that gold and silver are the most effective metals to use. In theory, silver should be better, being appropriate for the visible range, while gold is best at wavelengths above 600 nm, but in practice the improved stability and ease of processing for gold means it is often preferred [68].

As well as the choice of metal, important factors affecting the LSP resonance of the nanostructure are the size and shape of the structure and the dielectric constant of the surrounding medium. The simplest nanostructure is a sphere, which has the advantage of being easy to model computationally and is a good starting point for understanding plasmonic systems. More sophisticated geometries include rectangles, triangles, shells, stars and structures of two or more particles together with a nanometric gap between them. SERS from spherical nanoparticles is described further in Section 2.3.2 and more sophisticated structures are treated in Section 2.3.3.

Metal nanostructures are used for SERS because they act as optical antennas. This means that they take incident light from the far-field and 'concentrate' it in smaller volume, through the action of LSPs. The electromagnetic field close to the metal surface can be enhanced by several orders of magnitude when irradiated with the right frequency of light. Enhancement is often said to occur from surface plasmon resonances (SPRs), which occur when the plasmon frequency matches that of the photon and therefore effective coupling occurs. In the case of

Raman spectroscopy, a two-photon process, the Raman signal can be enhanced in two ways. Firstly, the local electromagnetic field is enhanced, so a probe molecule experiences a stronger incident field. Secondly, in a process called modified spontaneous emission, the scattered signal is enhanced. Enhancements are multiplicative, so the total enhancement is the product of these two enhancements and, if present, the chemical enhancement. Because effective enhancement only occurs when there is resonance between the plasmon and the photon energies, the SERS effect is highly wavelength dependent. The size and structure of a nanoantenna governs the resonance wavelength at which it will operate best. It should be remembered that Raman scattering is a process involving two photons of different energies, one as the incident photon and one of lower or higher energy for Stokes or anti-Stokes scattering, respectively. Since the enhancement given by the nanoantenna is wavelength-dependent, either the incoming or outgoing photon may be in resonance with the antenna and obtain maximum enhancement. In the case of a small Raman shift, both signals may be within the resonance window and be enhanced [68, 69].

Quantification of SERS enhancement factors is a subject of debate. The comparison of 'with' and 'without' SERS is generally complicated by uncertainties in the number of molecules being detected and other parameters such as their orientation, which would affect the strength of their Raman signal. Two main types of enhancement factor may be given: average or maximum. In the case of a SERS substrate, which may contain many metal nanostructures, often randomly distributed and orientated, it is common for some regions to have very large local electromagnetic field enhancements. These 'hotspots' can exhibit field enhancements orders of magnitude larger than other regions close by. If a molecular analyte covers the sample, then the average enhancement may be given for the whole incident laser-spot area, which will encompass hotspots and dark regions. The maximum enhancement can be several orders of magnitude higher than the average and is located in a hotspot. The maximum enhancement is relevant for single-molecule studies, where one analyte molecule positioned at the optimum position may itself have a strong enough Raman signal to be detected. The maximum enhancement factor is hard to measure experimentally but can be

easier to quantify using computational modelling than the average enhancement [68]. The situation is simplified when performing SERS on individual carbon nanotubes. In this case, since carbon nanotubes are large enough to be imaged with microscopic methods, their orientation and position with respect to the metal nanostructure are known. In addition, their length can allow the same carbon nanotube to be measured in a micro-Raman spectrometer at the position of the nanoantenna and far from it, giving a 'with' and 'without' SERS comparison on the same molecule with no changes in experimental setup.

2.3.2 Plasmonic spherical nanoparticles

Spherical metal nanoparticles are often used as a starting point for explanations of plasmonic particles. These particles may be modelled by Mie theory [68, 70], which gives an exact analytical solution to the electromagnetic problem. For more complicated geometries numerical simulations must be used. The electrostatic approximation gives a simpler model that can be used for small spheres (below 10 nm radius). Although it is not as robust as Mie theory, it can be used to explain many of the phenomena exhibited by metal spheres [68].

LSPs in a sphere can be modelled most simply as dipoles located in the center of the sphere. In this case, when light is incident on the sphere, it induces a polarisation that in turn creates an electric field acting in addition to the incident electric field. The particle's response to incident light can be characterised by the non-dimensional polarisability, β_S:

$$\beta_S = \frac{\epsilon(\omega) - \epsilon_M}{\epsilon(\omega) + 2\epsilon_M}, \tag{2.26}$$

where $\epsilon(\omega)$ is the wavelength-dependent dielectric constant of the metal (see Equation 2.24) and ϵ_M is the dielectric constant of the surrounding environment [68]. Resonance will occur when β_S diverges to infinity, that is, when $\epsilon(\omega) = -2\epsilon_M$. Since $\epsilon(\omega)$ is complex, this condition is most closely met when the imaginary part is small and the resonance then depends on the real part, $\epsilon'(\omega_{res}) = -2\epsilon_M$ [68].

This simple formula, based on the electrostatic approximation, explains the

dependence on the surrounding medium. The resonance frequency is red-shifted in water with respect to air due to the higher ϵ_{M} of water. According to this formula, the resonance frequency for a given metal in a given environment is fixed, with no dependency on the size of the particle, given by its radius, a. This is a weakness of the electrostatic approximation, which the Mie theory improves on, so as to predict that the resonance frequency is red-shifted with increasing a [68].

One of the reasons why the Mie theory predicts a difference from the electrostatic approximation for larger particle sizes is that the electrostatic approximation does not take into account radiative damping, which increases in significance as the particle size increases. This damping causes both the red-shift and a broadening of the resonance. Another difference is the increasing contribution of higher-order resonances, such as quadrupoles rather than just dipoles. In comparison with the dipolar resonance these modes have smaller, blue-shifted resonances, however, as the particle size increases, the broadening and red-shift is less pronounced for these modes so they remain sharp for longer and may begin to dominate at larger a [68].

The choice of metal is important for plasmonic particles. Small silver spheres have a dipole resonance of 346 nm in air and this red-shifts as the particles increase in size, so the resonance can be tuned throughout the visible range by varying particle size. Small gold spheres have a dipole resonance at 480 nm, which also red-shifts with increasing particle size. Due to absorption and other effects the resonance of spherical gold particles is more damped and broadened than that of silver spheres. Non-spherical geometries can strengthen and sharpen the plasmon resonance of gold particles, as will be discussed later [68].

When interested in the application of plasmonic metal spheres for SERS, it is the local-field enhancement that is of most importance. The local-field intensity enhancement factor, M_{loc}, is related to the local SERS enhancement factor (for zero-Stokes shift), $F^0_{E4}(\omega)$, by the $|E|^4$-approximation [68]:

$$F^0_{E4}(\omega) = (M_{\mathrm{loc}}(\omega))^2. \tag{2.27}$$

The total local-field intensity enhancement factor is the sum of its components normal:

$$M_{\mathrm{loc}}^{\perp}(\theta,\omega) = A_{\mathrm{S}}^{\perp}(\omega)\cos^2\theta, \quad \text{where} \quad A_{\mathrm{S}}^{\perp}(\omega) = |1+2\beta_{\mathrm{S}}(\omega)|^2, \tag{2.28}$$

and parallel:

$$M_{\mathrm{loc}}^{\parallel}(\theta,\omega) = A_{\mathrm{S}}^{\parallel}(\omega)\sin^2\theta, \quad \text{where} \quad A_{\mathrm{S}}^{\parallel}(\omega) = |1-\beta_{\mathrm{S}}(\omega)|^2, \tag{2.29}$$

to the surface of the sphere:

$$M_{\mathrm{loc}}(\omega)) = M_{\mathrm{loc}}^{\perp} + M_{\mathrm{loc}}^{\parallel} = A_{\mathrm{S}}^{\parallel}(\omega) + (A_{\mathrm{S}}^{\perp}(\omega) - A_{\mathrm{S}}^{\parallel}(\omega))\cos^2\theta. \tag{2.30}$$

When light is incident on a small metal sphere, the local field arising from its plasmonic response is not uniform over its surface but depends on the polarisation of the incident light. In the dipolar approximation, the local-field intensity will be greatest at the points on the surface of the sphere that are on the axis of the incident polarisation. There, the local field is orientated normal to the sphere surface. Conversely, at the points on the sphere surface tangential to the incident polarisation direction, the local field is tangential and the local-field enhancement is minimal. At the resonance frequency, the SERS enhancement factors at the maxima are approximately 16 times larger than at the minima [68].

Using the electrostatic approximation, an estimate may be made of the maximum SERS enhancement possible at the optimum position on the sphere surface. For small silver spheres, SERS enhancement factor of 10^5 to 10^7 may be expected, at wavelengths of 350–400 nm. For small gold spheres, SERS enhancement factors of 10 to 10^3 may be expected, in the wavelength range of 460–530 nm, where there is the damping effect of absorption. Of course if the analyte is a molecular species present at all points on the sphere surface then an average SERS enhancement will be achieved. This is approximately one third of the maximum SERS enhancement [68].

Using Mie theory, the results obtained for small spheres are largely in agreement with the electrostatic approximation results already described. For larger spheres, when multipolar resonances have a greater contribution, the points of

maximal enhancement move away from the points described, which are maxima for dipolar resonances but are not maxima for quadrupolar resonances. Mie theory also gives a larger distribution of enhancement factors over the sphere surface for larger spheres. Instead of a factor of 16 between maximum and minimum SERS enhancement factors predicted for small spheres, a factor of around 400 is predicted for a sphere with $a = 50$ nm [68].

These enhancement factors quoted so far represent the value at the surface of the sphere. It can also be important to consider how the enhancement changes further away from the surface. Using the electrostatic approximation, the local field intensity enhancement factor at a distance, d, from the surface decays as $1/(a+d)^6$ and the SERS enhancement factor decays as $1/(a+d)^{12}$. Close to the surface, where $a \gg d$, this results in a modest decay, for example a particle where $a = 30$ nm would have a decay of only a factor of two at $d = 2$ nm, more than the typical thickness of a molecular monolayer. At larger distances however, when d is comparable to or larger than a the decay is rapid. Mie theory also gives this result for the dipolar resonance and adds that quadrupolar and higher resonances decay faster with distance, so at wavelengths closer to the quadrupolar resonance and at certain positions above the surface the rate of decay is higher [68].

2.3.3 Other plasmonic structures

Going beyond the simple metal sphere there are two principal ways of achieving higher SERS enhancement factors: changing the shape of the nanoparticle and creating a small gap between two metal structures.

Changing the shape

Starting with the electrostatic approximation for the simple metal sphere, small changes may be made to explore the effects of changing shape. If, instead of a sphere of radius a, one has a metal ellipsoid with semi-axis lengths $a \geq b \geq c$ then instead of one non-dimensional polarisability, $\beta(\omega)$, there will be three:

$$\beta_i(\omega) = \frac{\epsilon(\omega) + \epsilon_{\mathrm{M}}}{3L_i\epsilon(\omega) + (3 - 3L_i)\epsilon_{\mathrm{M}}} \tag{2.31}$$

where

$$0 < L_1 \leqslant L_2 \leqslant L_3 < 1, \quad \text{and} \quad L_1 + L_2 + L_3 = 1. \tag{2.32}$$

As previously, resonance will occur when $\beta(\omega)$ is large, that is, when its denominator tends to zero (see Equation 2.26). In the case of the ellipsoid, the resonance conditions are:

$$\epsilon'(\omega_i) = -\left(\frac{1}{L_i} - 1\right)\epsilon_{\mathrm{M}}, \tag{2.33}$$

which means that there are three resonances, one for each axis of the particle [68].

The value of L_i contains information about the resonances of the particle. In particular it is useful to consider if $L_i < 1/3$ or $L_i > 1/3$ when comparing to the results for a sphere, which has $L_i = 1/3$. An example of this is a prolate ellipsoid, where $a > b = c$, as in a rugby ball. Its shape with respect to one axis is more pointy than a sphere would be, and for that axis, $L_1 < 1/3$. With respect to the other two axes, the prolate ellipsoid is less pointy or more flat than a sphere would be, and $L_2 = L_3 > 1/3$. It can be shown that if $L_i < 1/3$ then the resonance will be red-shifted and stronger than that of a sphere and if $L_i > 1/3$ then the resonance is blue-shifted and weaker than that of a sphere [68].

In terms of the local field enhancement and the resulting SERS enhancement, the model of a sphere may also serve as a starting point, modified according to the value of L_i. Expressions equivalent to Equations 2.28, 2.29 and 2.30 exist for defining how the local field intensity enhancement factor depends on $\beta_i(\omega)$ and L_i. Just as in the case of the sphere, the maximum local-field intensity enhancement and SERS enhancement is located at the tips of the particle in the axis of incident polarisation. Since, as already stated, the resonance is stronger if this axis of the particle corresponds to $L_i < 1/3$, the enhancement is also stronger, compared to that of a sphere. The converse is also true, if $L_i > 1/3$ then the enhancement located at the (flatter) tips of the particle is smaller than that of a sphere. This difference in enhancements is more significant for the component of the field normal to the surface than the component tangential to the surface [68].

Although all ellipsoidal particles by definition must have at least one axis with $L_i < 1/3$ and at least one with $L_i > 1/3$, the former has the strongest resonance

and gives the largest enhancements so it is most worthy of consideration. The stronger resonance means that every point on the particle surface experiences a greater enhancement in comparison to a sphere, but this is especially so at the points where the maximum enhancement occurs. In fact, the enhancement at the points is increased in comparison with the other parts of the surface by a factor of approximately $((1/L_i - 1)/2)^2$. This is an example of what is called the 'lightning-rod' effect, common to all plasmonic structures, where the enhancement is strongest at corners or positions with a small radius of curvature [68].

The lightning-rod effect can be illustrated with a prolate ellipsoid (rugby-ball shape) that is twice as long as it is wide. The stronger resonance achieved when $L_i = 1/6$ means that even the minimum enhancement is increased by a factor of 16 in comparison to a sphere, while the lightning-rod effect means that the maximum enhancement, located at the point, is 625 times that of a sphere. However, this applies only to small particles, and the values may be lower in practice for larger ellipsoids [68].

As the ellipsoid becomes increasingly elongated, the enhancements at the points become increasingly large and simultaneously more localised. The result is that for a needle-like particle the enhancement at the tips can be very large but apply to an area on the surface only large enough for a single molecule. This is an example of a hotspot [68].

The example of an ellipsoid serves to illustrate principles that apply to structures of other geometries too. In general the resonance position can be tuned by changing the size and shape, the enhancement is largest at points or corners, pointy shapes give larger distributions of enhancement factors and the coupling of a plasmonic mode to incident light depends on the polarisation of the light. The electrostatic approximation is useful for small simple systems, Mie theory gives more exact solutions for larger spherical metal nanoparticles and numerical simulations are required for more complicated geometries [68].

Another change that can be made to the shape of a spherical particle, instead of elongating to form an ellipsoid, is to remove the core to form a plasmonic nanoshell. The core is replaced with a dielectric, either air or, more commonly, silica. The plasmon resonances that can occur in these particles can be seen as a

hybrid of the plasmon resonances of a metal sphere and the plasmon resonances of a spherical cavity in a metal. As in molecular-orbital theory, the hybridisation of these two resonances results in an in-phase and an out-of-phase combination at lower and higher energy, respectively. It is found that the resonance position of nanoshells is more tunable by varying their dimensions than in the case of solid metal spheres. Spherical nanoshells are described by the outer and inner radii of the shell. As the shell thickness is reduced the hybridisation increases and with it the shift in resonance position. Just as with solid metal spheres, the resonances are red-shifted with increasing particle size and at larger sizes higher-order modes can be excited while the main mode is dipolar in nature. Another difference is that nanoshells are more sensitive to their environment with the resonance position moving depending on the dielectric constant of the environment, to a much greater extent than in the case of solid particles. Finally a practical advantage of nanoshells over solid particles for large scale applications is the reduced quantity of expensive metal required [71].

Creating a small gap

In addition to changing the shape of a plasmonic particle, the resonances can be shifted and enhancements increased by coupling two plasmonic particles together with a small gap in between. The coupling of two spheres can be modelled semi-analytically with generalised Mie theory and other structures can be evaluated with numerical methods. As before, spherical metal particles can serve as an example that is representative of more general coupled nanostructures [68].

The main plasmon resonance occurring when two spherical particles form a dimer is the dipolar coupling of their dipolar resonances. It occurs at a longer wavelength than the separate dipolar resonances and is excited by light polarised in the direction of the dimer axis. Other resonances may also occur either from dipolar coupling of higher-order resonances of the separate particles or from higher-order interactions of the dipole resonances of the particles. As before, these higher-order resonances occur at shorter wavelengths and do not give such high enhancements. The new resonances obtained when two particles come together

can be called coupled-LSP resonances or gap-plasmon resonances. The latter term accurately implies that the most important region in the dimer is the small space between the two particles. This location acts as a hotspot, giving very high but localised enhancements [68].

The size of the gap between the two particles is critical for the coupling and therefore governs the enhancement and resonance wavelength of the coupled LSP. Largest enhancements are obtained for smaller gaps, down to 1 nm. With a gap of this size, SERS enhancement factors can be higher than 10^{11} in the gap, for both silver and gold dimers. An increase in gap size of only 1 nm can reduce the SERS enhancement by an order of magnitude. The localisation is always related to the magnitude of the enhancement, so a larger gap gives a larger volume in which a large enhancement is achievable [68].

Optimised real structures

The principles already described can be combined together to achieve high local enhancements: both changing the shape of plasmonic particles and coupling particles together to get a hotspot in the gap. With numerical simulations, they can be modelled iteratively to optimise the enhancing capability for a specific application, for example coupling to a given frequency of laser light for an effective antenna.

The situation in practice is not exactly as in the simple model systems described so far. One important factor is the substrate on which these plasmonic systems are located. Whether this is silicon or silicon oxide is important, since their dielectric constants are different.

How the plasmonic features are manufactured introduces other factors needing consideration. If electron beam lithography (EBL) is used then as well as the plasmonic metal such as gold, there is often a thin 'sticking' layer of another metal, which is likely to affect the LSP resonances. The corners of any features made in practice by methods such as EBL have a finite radius of curvature. Simulations performed with perfectly sharp corners are therefore not good models of the real system. Spherical nanoparticles and nanoshells can be purchased

from commercial sources but may not be perfectly spherical and smooth. Any roughness could then give regions of higher local enhancement through the lightning-rod effect.

An example of simulations performed to optimise a plasmonic antenna for coupling to 785 nm light is given in Figure 2.30. The basic structure is a pair of cuboids lying on a substrate. The effect of different substrates and a sticking layer is shown, albeit still with unrealistically sharp corners. The local field intensity enhancement is visualised with a colour plot at wavelengths resonant with the dipolar and quadrupolar resonances. With the constraints of a real sample of a silicon surface and a chromium sticking layer, different sizes of cuboid were tested to find a good resonance with the chosen frequency of light. It was shown that a length of 85 nm was optimal.

2.4 NANOSPEC sample requirements

The work presented in this thesis was completed as part of the NANOSPEC project. The original aim of this project was to interface plasmonic nanostructures with carbon nanotubes and perform electrical transport with *in situ* plasmonically enhanced Raman spectroscopic measurements, thereby monitoring changes in the CNTs resulting from the application of current. This would give a better understanding of the plasmonic antenna–carbon nanotube interface as well as fundamental properties of the carbon nanotube such as the limits of current density [73].

The optimised plasmonic antenna structures for an ideal device have been described in Section 2.3. These structures have been designed to enable a very high enhancement only in a small region of space, so the carbon nanotube must be positioned in a spatially precise location. In addition, to perform electrical measurements on the nanotube it must be connected to electrodes leading to an electrical source, leaving a clear optical path to the antenna so that *in situ* measurements may be made.

It was understood from the outset that creating suitable devices – with a carbon nanotube interfaced with a plasmonic antenna and electrodes – would pose

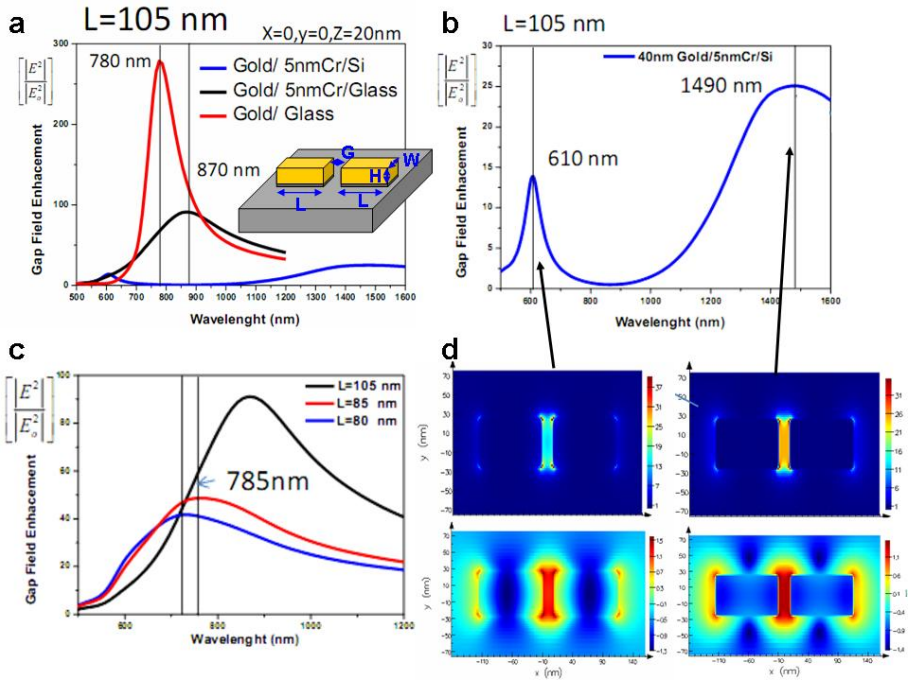

Figure 2.30: Results of numerical simulations of a plasmonic dimer antenna formed by two cuboids (a, inset) of length (L) 105 nm, width (W) 50 nm, height (H) 40 nm and gap (G) 20 nm. (a) The effect of adding a chromium sticking layer and switching between glass and silicon substrates. (b) The case with sticking layer and silicon is plotted again where the two resonances of the dipolar (1490 nm) and quadrupolar (610 nm) coupling LSPs are shown. (d) The local field intensity enhancements at each of these resonance wavelengths is illustrated in (top) linear and (bottom) logarithmic colour scales. (c) The effect of changing the length of the antenna, showing that with the best length for coupling with 785 nm light is found at L = 85 nm. From reference [72].

challenges and the best approach to take was not known. As such, a number of different pathways towards the ultimate aim were taken, generally compromising on one or more aspect of the ideal device in order to develop and test the other components and their functionality. In some cases this involved several steps of iteration and cooperation between different project participants from different research institutions.

For example, the manufacture of nanoantennas according to the simulations performed by Roberto Fernández-García (Imperial College, London) was found to push conventional nanofabrication techniques to their limit, particularly to achieve the small (<40 nm) gaps between the two halves of the structure. Fast ion beam etching (FIB), performed in Jerusalem, was found to have this capability

but optical measurements, in Berlin, showed that the etching of the surrounding area was not smooth enough or over a large enough area for the samples to be compatible with Raman studies. A second set of antennas were then developed using a combination of FIB and EBL, which allowed a clearer and larger area around the antennas while still achieving the small gaps sizes. However, differences between these fabricated antennas and the simulated antennas remained, so more simulations were performed, in London, with more accurate materials and geometry based on the requirements and limitations of the fabrication process. This shows that the development of suitable nanoantennas alone, without any of the other device components, was a significant part of the project's research.

Approaches to devices with at least two of the components interfaced included a Fischer surface with a low density of SWNTs randomly distributed over it, where the surface acted as an antenna and the SWNT Raman spectrum could be measured, exhibiting wavelength-dependent enhancement, as shown by Christian Lehmann (Free University, Berlin). Another approach was to form simplified antenna structures such as disks by EBL within a sample designed for dielectrophoretic deposition of SWNTs from dispersion. Again, this gave SWNTs interfaced with non-optimised antennas and the enhanced Raman spectrum could be measured, as was shown by Sebastian Heeg (Free University, Berlin). In addition, it is hoped the conducting AFM with special non-blocking probes would enable electrical transport on these samples, as being tried by Christian Lehmann and Talia Yeshua (Hebrew University, Jerusalem), thereby getting very close to the idealised device.

One approach developed in this thesis follows on from the optimisation of design and fabrication of antennas, as described above. This is the deposition of carbon nanotubes in spatially precise locations by fountain pen nanolithography. If carbon nanotubes could be deposited controllably from a nanopipette onto the optimum position on a nanoantenna then a strong enhancement should be seen and this would experimentally test the antenna's enhancing affect. If that was achieved then future development would consider how to interface electrodes. Chapter 4 contains details of the experimental methods and results of fountain pen nanolithography of carbon nanotubes.

Another approach to device creation that was explored and is presented in this thesis is the deposition and nanomanipulation of gold nanoparticles onto SWNTs. This approach is fully described in Chapter 5. Long SWNTs were previously grown on a silicon oxide surface then when one or more gold nanoparticles were put onto the SWNT by nanomanipulation enhancement could be measured. Once again this uses a simplified sub-optimal antenna design so a lower enhancement factor would be expected but it has the advantage of being more readily applied, including to samples where the SWNT has been contacted with electrodes by EBL. In that case Raman–transport experiments may be performed.

This is not a complete list of approaches taken towards the NANOSPEC aim but serves as an example of the range and focuses on those routes leading closest to the goal. More details are found in the project summary report [74].

Chapter 3

Experimental Methods

This chapter discusses only techniques that are found throughout the rest of this thesis. For techniques that are specific to particular areas of work, experimental details will be given within the relevant chapter.

3.1 Raman spectroscopy

3.1.1 Our instrument

The Raman microscope used for the work presented in this thesis is a Renishaw InVia micro-Raman spectrometer (Figure 3.1), with excitation laser wavelengths of 785 nm and 514 nm, from a Renishaw near-IR diode laser and Melles-Griot argon/krypton mixed-gas laser, respectively. In this instrument, laser light is incident normal to the sample and the scattered light is collected in a backscattering arrangement (Figure 3.2).

A Prior ProScan II mechanical ball-bearing stage gave spatial control of approximately 1 μm. WiRE 2.0 software was used to control the spectrometer and the Prior stage. If required, finer spatial control was obtained by use of the Nanonics piezo scanner taken from a MV1000 atomic force microscope and operated by Quartz II software. A range of objective lenses from 5× to 100× was available for use for optical microscopy and Raman spectroscopy. In general, a long working-distance 50× objective lens was used, with a numerical aperture of 0.45 and a working distance of 15 mm. In the work presented here this objective

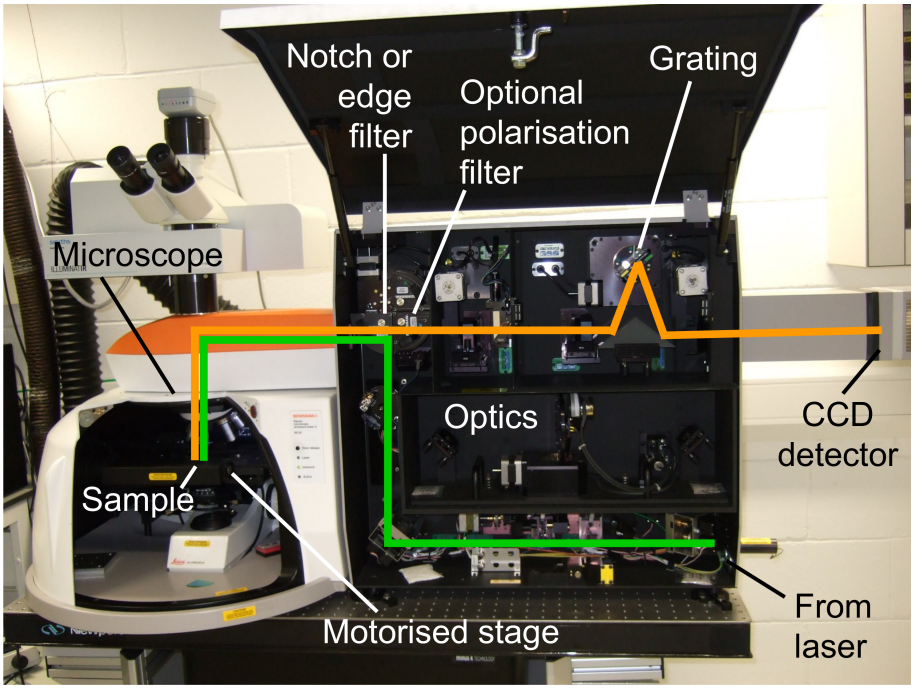

Figure 3.1: Photograph of Raman microscope, showing laser beam path (green line) and scattered light path (orange line).

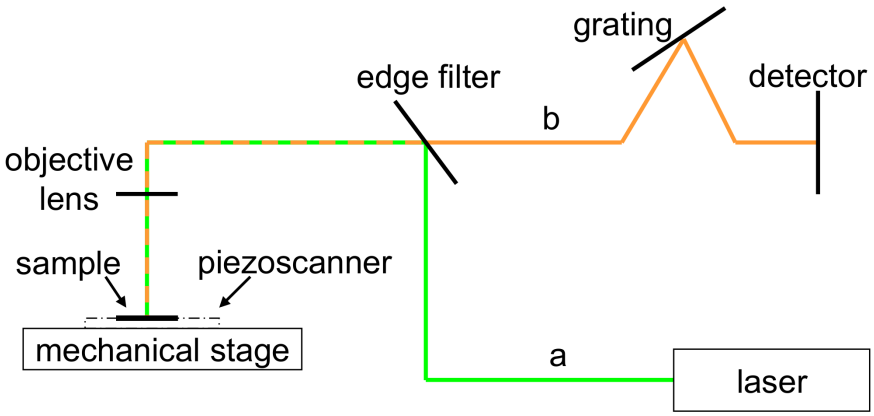

Figure 3.2: Schematic diagram of Raman spectrometer showing laser light in green and Raman scattered light in orange. The labels a and b refer to positions relevent for polarised Raman measurements, acting on the laser light and scattered light, respectively.

lens was used for Raman spectroscopy unless otherwise stated. Alternatively, where it is stated that a 100× objective lens was used, it had a numerical aperture of 0.90 and a short working distance.

3.1.2 Polarisation measurements

In the standard configuration of the Raman microscope, as used unless otherwise stated, the laser light is linearly polarised and reaches the sample polarised in the x direction. No polarisation filters are present in the path of the scattered light so the detector measures all of the scattered light, albeit with a polarisation-dependent detection efficiency.

A polarisation filter, or analyser, may be placed within the spectrometer in the path of the scattered light before the detector (position b on Figure 3.2) to allow through only light that is polarised in the x direction when at the sample. In addition, if a $\lambda/2$ waveplate is inserted immediately before the analyser then the detector receives only scattered light that was polarised in the y direction at the sample.

Placing a $\lambda/2$ waveplate where the beam exits the laser (position a on Figure 3.2) rotates the incident laser polarisation by 90° so the sample experiences light polarised in the y direction. Similarly, a $\lambda/4$ waveplate inserted at this point gives circularly polarised laser light.

Simple polarised Raman measurements are commonly made in the 'parallel' configuration, where only the scattered light polarised parallel to the polarisation of the incident laser light is measured. In the Renishaw InVia spectrometer this is achieved by simply including the analyser in the scattered light, for polarisation in the the x direction, and by including the $\lambda/2$ waveplate in the laser path and both $\lambda/2$ waveplate and analyser in the scattered light path, for polarisation in the y direction. 'Perpendicular' or 'crossed' polarisation measurement may also be made with these components in the opposite combination.

More advanced polarised Raman measurements require a range of polarisation directions in between those of the orthogonal configuration described above. To achieve this, the $\lambda/2$ waveplate in the laser light beam path must be held by

a rotation mount instead of in its standard slot, which holds it in one fixed orientation. When linearly polarised light encounters a $\lambda/2$ waveplate, its polarisation is rotated by twice the difference between the incident polarisation direction and the waveplate's axis [75]. Thus if the waveplate's axis and the incident polarisation are parallel then there is no change of polarisation direction, whereas if they have a difference of 45° then the light leaving the waveplate has been rotated by 90° with respect to the incident light. Crucially, rotating the waveplate to any intermediate angle can give light linearly polarised in any direction. Although this method allows the polarisation of the laser light incident on the sample to be set to any arbitrary direction, the Raman InVia microscope does not allow for the same rotation of the scattered light, due to space constraints between the sample and the detector. As described above, with the options of adding the $\lambda/2$ waveplate and analyser, the scattered light can be detected polarised in the x and y directions.

The parallel component of the scattered light, $I_{\parallel}$, that is, the light that is scattered with a polarisation direction parallel to the incident laser polarisation direction, may be extracted from knowledge of the x- and y-scattered light,

$$I_{\parallel} = I_x \cos^2\theta + I_y \sin^2\theta, \tag{3.1}$$

where I_x is the intensity of the x-polarised light, I_y is the intensity of the y-polarised light and θ is the angle between the incident laser light and the x direction. Similarly, the perpendicular component of the scattered light, $I_{\perp}$, can be obtained:

$$I_{\perp} = I_x \sin^2\theta + I_y \cos^2\theta. \tag{3.2}$$

To take account of the inherent polarisation dependence of the instrumentation, measurements were performed on the (111) surface of calcium fluoride. Its Raman peak at 322 cm^{-1} has a depolarisation ratio of 2/3 and a scattering efficiency that is independent of the laser polarisation's relation to the crystal axis [76]. Thus, in theory when the measurements are taken at a range of polarisation angles as described above, the $I_{\parallel}$ and $I_{\perp}$ values should be independent of θ, and the $I_{\perp}$

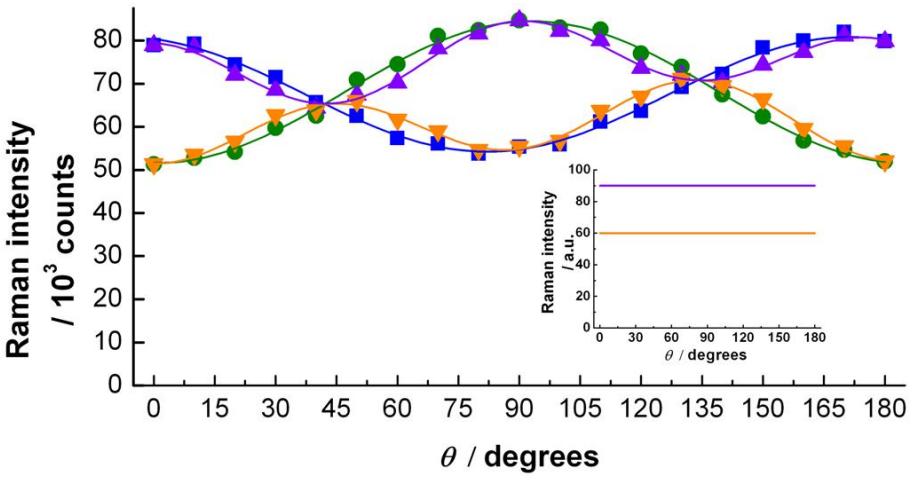

Figure 3.3: Raman intensities from CaF_2, which are used to calibrate the spectrometer for polarisation measurements. Blue squares and green circles, I_x and I_y, respectively. Purple upward triangles and orange downward triangles, $I_\parallel$ and $I_\perp$, respectively. The solid lines through the points are given as an aid to the eye. The inset represents the theoretical values for $I_\parallel$ and $I_\perp$ (purple and orange lines, respectively) for Raman scattering by CaF_2.

values should be 2/3 of the $I_\parallel$ values (Figure 3.3, inset). The actual intensities measured by the instrument are given in Figure 3.3, clearly showing a discrepancy from the theoretical values, particularly around 45° and 135°. Therefore, when polarisation measurements were made on samples, the values measured for I_x and I_y were first converted to $I_\parallel$ and $I_\perp$ *via* Equation 3.1 and then these values were multiplied by a correction factor based on the calcium fluoride measurements, which took into account the polarisation dependence of the instrument. For example, if a sample was measured to have a parallel polarisation intensity $I_{\parallel,\text{sample}}$ at a polarisation angle of $\theta = 60°$ then the corrected intensity would be $I_{\parallel,\text{sample}} \times \frac{1}{I_{\parallel,CaF_2,60°}}$, which is approximately $\frac{I_{\parallel,\text{sample}}}{70\times10^3}$, according to the value taken from Figure 3.3. It should be noted that there are always instrumental variations in Raman intensities measured from day to day, so the values obtained after these corrections are counted in arbitrary units and comparisons between different measurements, for example between different polarisations, are valid only between measurements made within one experimental session.

3.1.3 Raman fine mapping with Nanonics scanner

Raman maps can be made within the WiRE software with step sizes down to one micron. Since the laser spot size using the 50× objective lens is approximately one micron, that step size is sufficient for most measurements. However for some applications a smaller step size is desired, for example in order to ensure the maximum signal is obtained from a given position on the sample. In this case a coarse, micron-step map might only measure the given position at the edge of the laser spot and therefore give a weaker signal than if the position was in the centre of the laser spot. If a map was performed with sub-micron steps, such as 200 nm, then one of the measurements will represent the true maximum signal from that point. This is particularly important if the intensity is important, for example when comparing an enhanced and non-enhanced signal.

For such fine step size maps the Prior stage does not have precise enough control. Instead, a piezo scanner must be used, such as the Nanonics piezo scanner. The scanner is controlled by Quartz II software, which interfaces with WiRE through a program called QuartzSpec. Parameters such as step size and scan area are set within Quartz, while the settings of the spectral acquisition are set in QuartzSpec and executed by WiRE. A set of instructions for performing this type of measurement is given in Appendix C.

3.2 Atomic force microscopy

3.2.1 Veeco Nanoman VS

The instrument used for most AFM work presented in this thesis was a Veeco Nanoman VS with Dimension 3100 controller (Figure 3.4). It was controlled with Veeco's 7.20 or 7.30 software.

The particular strengths of this instrument are a good user interface and ease-of-use and the many functions it offers beyond simple topography imaging. For example it can perform magnetic force measurements or tunnelling AFM as well as nanomanipulation. In addition it has a very good vibration-isolation system making sensitive measurements possible. Its limitation is that it is not well suited

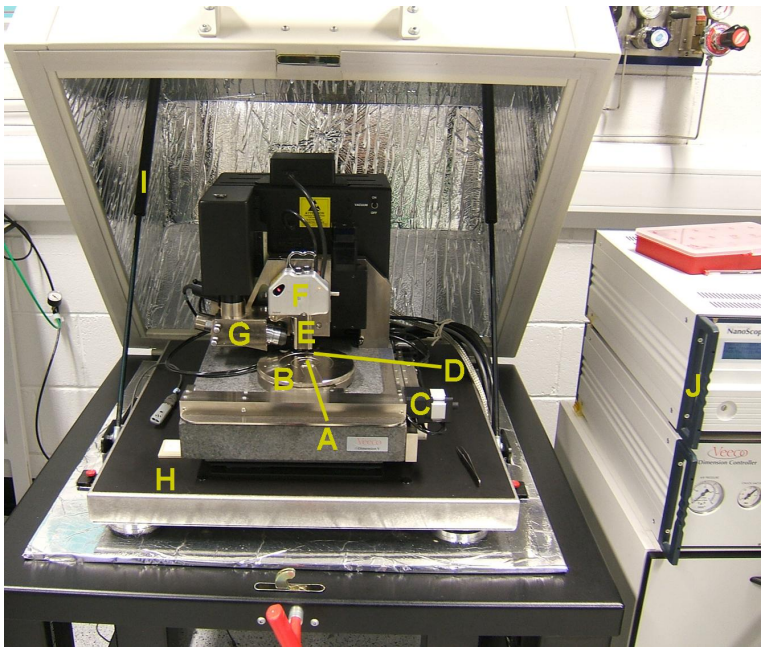

Figure 3.4: Photograph of Veeco Nanoman VS atomic force microscope. A: sample, B: sample holder plate, C: x and y translational motors, D: tip, E: piezo scanner, F: laser source and detector, G: optical microscope and camera, H: vibration-damping table, I: acoustic-insulating hood, J: controller boxes.

for integrating with other instruments for combined measurements.

Processing of files from this instrument for analysis and image creating was usually performed on Veeco's 7.20 software or Veeco's NanoScope Analysis software. WSxM [77] was another AFM analysis package that could also be used on the files.

3.2.2 Nanonics MV1000

An alternative AFM that was used for selected work in this thesis was the Nanonics MV1000 AFM (Figure 3.5). Its configuration differs from the description given above but it works by the same overall principles. The principal difference is that the piezo scanner is used to move the sample while the tip and laser are stationary during operation. The feedback system works in the same way as described above and the topography is similarly obtained. The software used to operate this instrument was either Nanonics' NWS1760A or Cavendish Instruments' Quartz II.

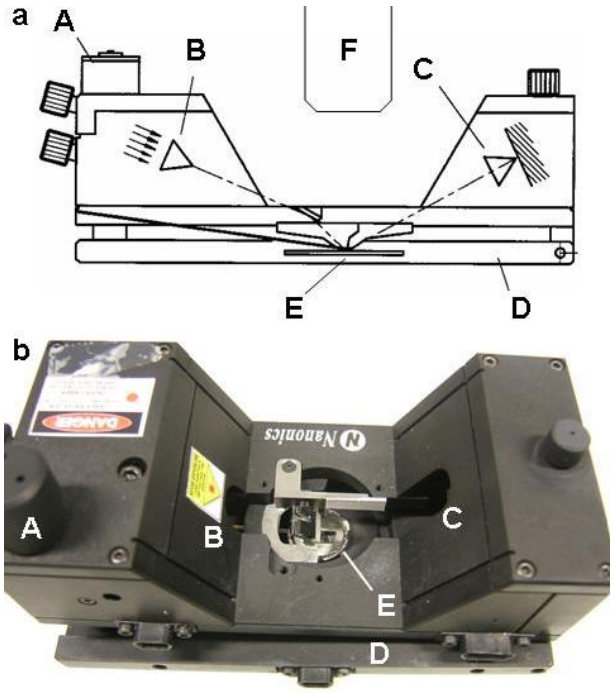

Figure 3.5: (a) Schematic diagram and (b) photograph of the Nanonics MV1000 instrument. A: stepper motor, B: diode laser, C: position-sensitive detector, D: Nanonics 3D Flat Scanner^{TM}, E: sharp tip on surface, F: far-field microscope objective. Part a is adapted from reference [78].

This instrument has some advantages over the Veeco. Firstly and most importantly, the Nanonics MV1000 allows a clear optical path to the very point of the tip. This, combined with the small and relatively portable nature of the AFM head, means simultaneous AFM–Raman measurements can be made within the Raman spectrometer. Another advantage is the flexibility of probe type that may be used, for example the replacement of a standard sharp tip with a nanopipette for the delivery of material to the surface, as is described in Chapter 4. Finally, this instrument allows the piezo scanner to be used in the absence of a probe of any sort, as described in Section 3.1.3. The downside of this instrument is the lack of effective vibration isolation. It is not possible for it to be surrounded by an acoustic hood, as the Veeco AFM is, while it is operated within the confines of the Raman spectrometer. A Minus K vibration-isolation platform is positioned under the whole Raman spectrometer, insulating it from building vibrations, but the spectrometer itself has sources of vibration that cannot be isolated from the AFM. This problem renders tapping-mode measurements almost impossible and

lowers the reliability and sensitivity of contact-mode measurements.

The files of AFM images produced by the Nanonics MV1000 could be saved as .nan files and analysed in NWS1760A or saved in a general format and processed in WSxM [77].

3.3 Scanning electron microscopy

The SEM instrument used for work presented in this thesis was a Hitachi 4700II cold field-emission scanning electron microscope. Samples were held by carbon tabs on aluminium stubs, both sourced from Agar Scientific (UK). The pressure of the sample chamber was 1×10^{-3} Pa. Typically a sample distance of 5–10 mm was used for measurements, decreasing to 3.6 mm for the highest resolution images. It was operated at 5.0 kV for almost all measurements, increasing to 30 kV for high-resolution images of samples where the potential for damage was not a concern. The current was approximately 20 μA.

3.4 Sample preparation

3.4.1 Cleaning procedure for silicon wafer

For several areas of research, the starting point was a standard silicon wafer. This silicon has no artificial oxide layer deposited or grown on it, so only the top few nanometres of the silicon are oxidised to silica as the so-called native oxide layer. The wafer was scored with a diamond pen to create lines along which the wafer was broken into small chips. The diamond pen was sometimes also used at this stage to create shallow scratch lines in a grid pattern that could be used as a location marker during experiments.

The silicon wafer chips were cleaned by chemical procedures. The first step was submersion in a solution of decon-90 in an ultrasonic bath for 5 minutes. This was followed by rinsing three times in deionised water. A two-step piranha procedure was then followed: 98% H_2SO_4, 6 ml + 30% H_2O_2, 5 ml for 20 minutes at 90 °C followed by conc. NH_4OH, 1 ml + 30% H_2O_2, 1 ml + distilled H_2O, 5 ml

for 15 minutes at 70 °C. Finally the chips were submersed in iso-propyl alcohol (IPA) in an ultrasonic bath for 5 minutes, rinsed in fresh IPA and dried with nitrogen gas.

An alternative cleaning method was to use plasma cleaning instead of the piranha step. This technique uses a dedicated plasma etcher (SPI Plasma Prep III) with oxygen gas. A plasma of high-energy atoms and radicals is created, which reacts with and removes any contaminants on the silicon surface. The end result of cleaning with this method is comparable to the solution method described above.

For some applications, where it was desired for carbon nanotubes to have a higher affinity for the surface and 'stick down' when applied, a surface monolayer of (3-aminopropyl) triethoxysilane (APTES) was made [79]. This was done by immersing the chips in an aqueous solution of APTES for three minutes, allowing it to form a self-assembled monolayer with amino groups pointing upwards ready to bind carbon nanotubes.

3.4.2 Microfabrication

Some samples used for parts of this work have sophisticated patterns of carbon nanotubes, electrodes and other features. These have been created using electron beam lithography (EBL). This was performed by collaborators and colleagues in different universities. The majority of samples were prepared in Gothenburg in Sweden by Niklas Lindahl, many of which were designed by Johannes Svensson. In addition, some EBL was performed by Roberto Fernández-García in London, Mila Palchan in Israel and Hak Seong Kim and Miri Seo in South Korea.

EBL is a standard technique for creating micron-scaled features on silicon wafers. The wafer is first covered in a thin layer or sometimes two thin layers of a polymer 'resist'. An electron beam is then directed over the surface in a computer-controlled pattern corresponding to the areas where features are desired, which causes those areas of resist to become more soluble (in the case of positive resist). A solvent is then used to wash away just the exposed areas of resist, leaving the bare substrate below. Metal is then deposited through an evaporation process

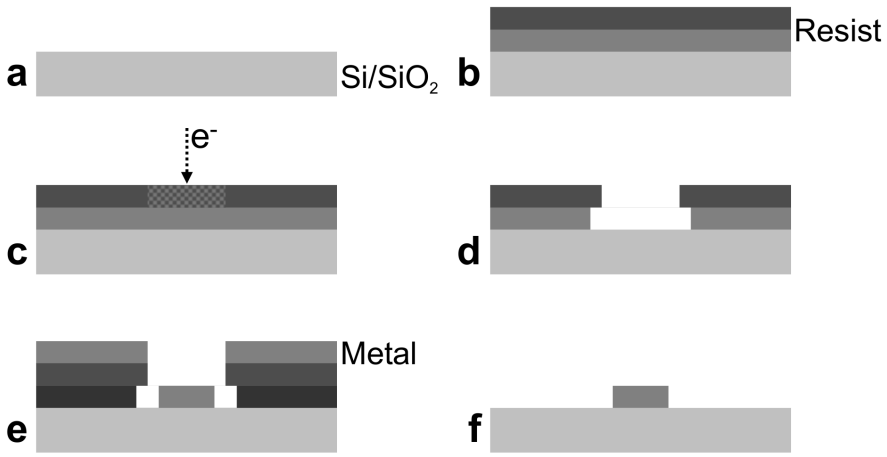

Figure 3.6: Schematic diagram of the process of electron beam lithography for patterning small metal features on a silicon wafer: (a) a clean wafer of silicon is used, (b) one or two thin layers of resist are formed by spincoating and baking, (c) the resist is exposed to an electron beam in chosen areas, causing an increase in solubility, (d) the exposed areas or resist are washed away with solvent, (e) metal is deposited over the whole area by evaporation, (f) all remaining resist is removed along with any metal not bound directly to the substrate.

onto the wafer. Finally another solvent washes away the remainder of the resist including any metal that landed on top of it, leaving only metal on the areas that were patterned with the electron beam (Figure 3.6) [80].

The samples with interfaced carbon nanotubes and electrodes have undergone several steps of lithography in addition to the other steps in the process. A typical example is shown in Figure 3.7 and is as follows: EBL or photolithography is used to make relatively large electrode contact pads surrounding a central area with grid markers and, in a separate step, CNT-growth catalyst particles. Then carbon nanotube growth is performed by conventional CVD: heating the sample in a chamber and applying a mixture of gases containing argon, hydrogen and ethylene. SEM is used to identify exactly where the nanotubes have grown, then further steps of EBL are performed to connect the large electrode pads with smaller wires to parts of the carbon nanotube. A more detailed description of this process is given in Appendix D [18, 81].

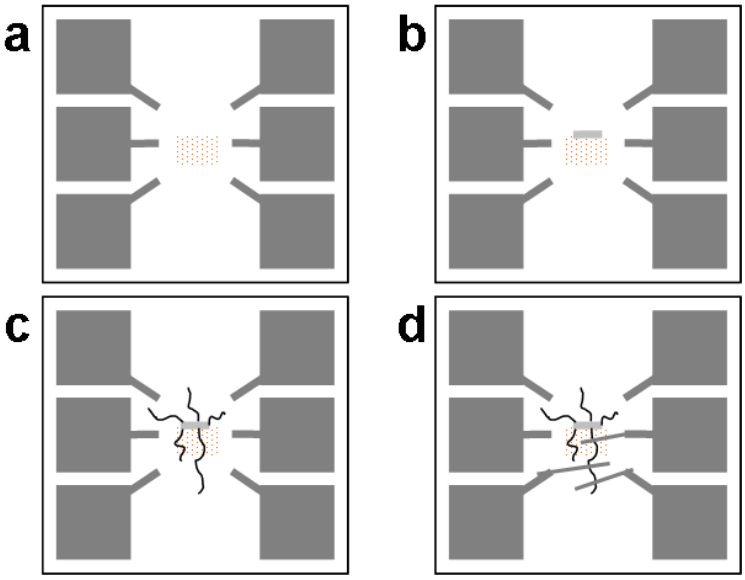

Figure 3.7: Schematic diagram of the stages involved in sample preparation: (a) large electrode pads and marker grid and (b) CNT-growth catalyst patterned by lithography then (c) CVD growth of CNTs, followed by SEM (not shown) and (d) further lithography to make electrical connections between contact pads and CNT.

Chapter 4

Fountain Pen Nanolithography (FPN) for CNT Deposition

4.1 Literature survey

4.1.1 Motivation and context

As described in Section 2.4, the ultimate aims of the NANOSPEC project require samples with an individual SWNT interfaced with a plasmonic nanoantenna, connected by electrodes with a configuration suitable for *in situ* Raman–transport measurements. This Chapter describes an approach taken towards this ultimate aim, with the target of being able to controllably deposit SWNTs in precisely the correct location to be interfaced with nanoantenna(s) and/or electrodes.

Given a sample prepatterned with a nanoantenna and/or electrodes by methods such as electron-beam lithography (EBL) or fast ion beam etching (FIB), a number of methods could be used to add SWNTs. The first two methods would start by placing a drop of SWNT dispersion over the whole area of the sample. One could then either let the drop sit stationary until it dried or was rinsed off, as in the case of drop-coating, or spin the sample to force the drop to spread out over the surface, as in the case of spin-coating. Both methods would give a random orientation of SWNTs all over the surface. Ideally a SWNT would fall exactly on the antenna with the optimum orientation and no other SWNTs would be within the laser spot area. The enhanced region within the antenna has

a size on the order of 10 nm and a typical laser spot has an area of approximately 1 μm, so even with an optimised density of one SWNT per laser spot area, there is only 0.1% chance of the SWNT lying in the antenna's area, and less chance of the orientation being good.

A more directed method of depositing SWNTs is dielectrophoresis [82]. By applying an ac current between two electrodes, onto which a drop of SWNT dispersion is placed, this can give well-positioned SWNTs between the electrodes [83] although it is not without its disadvantages. While a single individual SWNT is desired, often multiple SWNTs or bundles of SWNTs are found in the gap between electrodes. Additionally, the electrode gap is typically smaller than the laser spot used for Raman spectroscopy so spectra may be affected by electrode luminescence and the electrode configuration for dielectrophoresis might not be optimal for further NANOSPEC studies. Finally, this method works most efficiently for metallic SWNTs [84] so obtaining devices with semiconducting SWNTs would be additionally challenging.

Fountain pen nanolithography (FPN) was investigated as an alternative method of depositing SWNTs, with spatial precision and with no special electrode arrangement requirements or preference for metallic SWNTs. The technique uses a cantilevered nanopipette or 'nanofountain pen' held within an AFM to deliver a solution or 'ink' through the nanopipette onto a surface. The AFM gives control of the contact between pipette and surface as well as sub-micron lateral precision.

CNT deposition was not the only possible application that FPN had within the NANOSPEC project. Depositing spherical gold nanoparticles through nanopipettes was used as a means of delivering antenna-like particles onto or near SWNTs. Similarly, gold salt was investigated as an ink, for post-deposition reduction to gold metal for both antenna and electrical connection. Finally, nanopen techniques could be used to write patterns of CNT-growth catalyst in highly precise positions [85], but this was not explored within the scope of the project.

4.1.2 Development of fountain pen nanolithography

Just as in the macroscopic world, dip-pens were used for creating drawings or writings thousands of years before fountain-pens, 'dip-pen nanolithography' [86] is the predecessor to the technique of deposition from a reservoir though a nanopipette, also called 'fountain pen nanolithography' [78].

Dip-pen nanolithography (DPN) [86] uses a standard AFM tip to transfer material from a reservoir to the surface by first dipping the tip in the reservoir and then touching the tip onto the surface using the control afforded by the AFM instrument (Figure 4.1). This direct writing technique can deliver small amounts of solution in a simple and direct way that uses readily available instrumentation and has no messy processing stages unlike most lithography processes [86]. In the first example of this method by Piner *et al.* in 1999, 'writing' was performed on a gold surface [86]. There are a number of parameters that affect the size of the lines or spots created on the surface: the time for which the tip was in contact with the surface, the speed at which the tip moved over the surface, the roughness of the surface, the affinity for the surface of the molecules being transferred and the relative humidity during the process; implying that the mechanism relies on transfer through the water meniscus that forms between tip and substrate [86]. DPN has been developed over subsequent years and 15 nm features can now be routinely produced. While DPN has many strengths in the resolution it can achieve and the simplicity of the required instrumentation it cannot overcome the necessity to leave the writing area to replenish its supply of ink, which reduces its throughput and loses alignment information.

Fountain pen nanolithography (FPN) has a continual supply of solution to the tip, which gives it an advantage over DPN. Lewis *et al.* developed a method of holding a micropipette within an AFM instrument in order to perform fountain pen chemistry [78]. Their first experiments involved passing an etchant through the micropipette to create trenches in a chrome surface. They used a Nanonics (AFM)/NSOM-100 (Nanonics Ltd., Jerusalem, Israel) to hold the cantilevered micropipette and control its approach to the surface using conventional laser-reflection AFM feedback. A pressure regulator was attached to the larger end

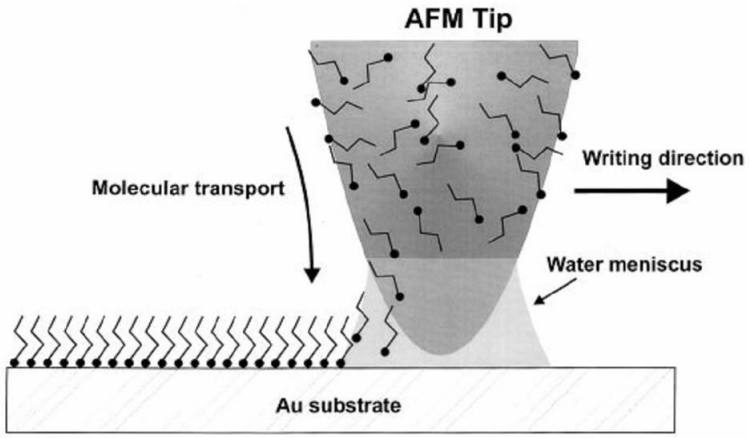

Figure 4.1: Schematic diagram of DPN depositing molecules from an AFM tip onto a surface though a water meniscus. From reference [86].

of the micropipette to control the delivery of the etchant and high humidity conditions were used to prevent globule formation, which prohibits smooth writing. They discovered that there are a significant number of parameters that could affect the results of the writing. The pressure of the solution in the pipette and the force of the tip on the surface were two that could be easily controlled. They discovered that the temperature of the surroundings and the concentration of the solution were also important. Other factors they thought might prove important were using intermittent (*i.e.* tapping) contact-mode instead of continuous contact between tip and surface, changing the chemical properties of the surface or the tip and optimising the geometry of the tip [78].

The Nanonics FPN system was then developed to enable protein printing with high precision [87]. Cantilevered nanopipettes with diameters of 100 nm were used and they were able to achieve protein lines of width 500 nm or spots of diameter 200 nm deposited onto the surface (Figure 4.2). In this case the protein solution was syringed into the nanopipette before writing commenced, then simple capillary action brought the solution through to the tip instead of pressure from an external pressure regulator. The writing was shown to work on substrates that would form a chemical bond with the protein and substrates with no chemical affinity for proteins. No special temperature or humidity controls were found to be necessary, though it was noted that slight improvements may

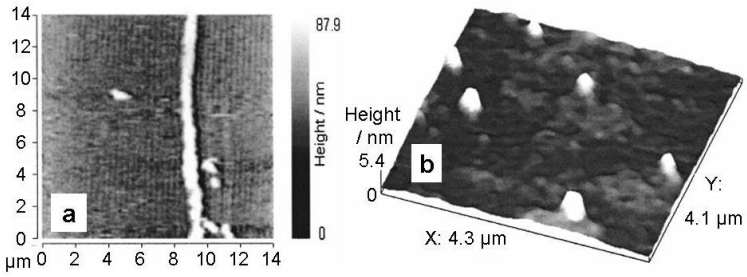

Figure 4.2: AFM images of proteins in (a) lines or (b) spots on functionalised glass substrates. The line shown in part a has a width of approximately 500 nm and height of approximately 20 nm. The dots in part b have diameters less than 300 nm and heights of approximately 2 nm. Adapted from reference [87].

be achieved with their optimisation [87].

The application of electric fields yielded extra control of protein printing using nanopipettes with the Nanonics AFM [88]. Capillary-electrophoresis technology was combined with the nanofountain-pen configuration to give a new technique called atomic-force-controlled capillary electrophoretic nanoprinting (ACCEP). The addition of one electrode attached to the outside of the tip and another electrode in the solution within the large end of the nanopipette (Figure 4.3) allowed for electrical control including electrophoresis and electro-osmosis. Electrophoretic control was demonstrated with bovine serum albumin (BSA) conjugated with a fluorescent dye in a 500 nm pipette, the aperture of which was studied with fluorescence spectroscopy. Different conditions could be used so that electroosmotic effects dominated the control. In this case a 150 nm pipette was used, with fluorescence spectroscopy testing the results. Under these conditions the electroosmotic velocity, which opposes the electrophoretic velocity of the protein, dominated, causing protein to be ejected from the pipette when negative voltage was applied to the outer tip electrode. Throughout these experiments capillary forces were also present, promoting deposition whenever the tip was in contact; however when voltages were applied to promote electrically driven writing, the capillary effects were negligible in comparison [88].

Meanwhile Taha *et al.* tried to extend the use of cantilevered nanopipettes in the Nanonics instrument beyond protein printing [89]. With the target of providing electrical contacts on the nanometric level under ambient conditions,

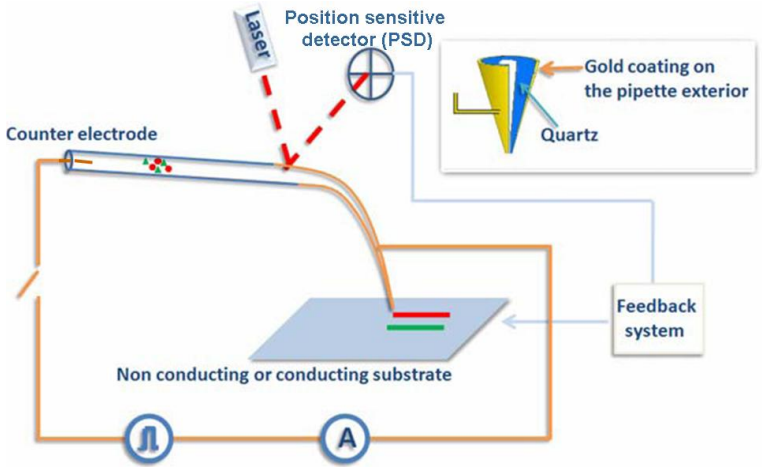

Figure 4.3: Schematic diagram of the ACCEP process, where control of the writing is given by a potential difference between the outer coating of the nanopipette and an electrode inserted into the solution inside the pipette. Adapted from reference [88].

gold nanoparticles suspended in methanol were chosen as the ink in the fountain pen. Gold nanoparticles of diameter of 1.2 nm with attached amino groups were suspended in methanol with a concentration of 0.1 nmol/mL. Results were presented of this suspension being deposited through a 100 nm pipette at a writing speed of 0.1 µm/s, giving a line 100 nm wide and 15 nm high. As before, various parameters were found to affect the writing, in terms of the continuity of the line and the height and width of the line. These parameters included nanopipette aperture size (Figure 4.4), setpoint, suspension concentration and hydrophobicity or hydrophilicity of the surface. The results of the deposition were tested in a number of ways: electron-induced X-ray fluorescence, scanning electron microscopy and atomic force microscopy. The quality of the electrical contact of the writing achieved was tested by writing a line between electrodes 100 nm apart and taking current-voltage measurements. The result was Ohmic behaviour with a resistance of approximately 4000 Ω, which is higher than bulk gold, due to the particulate nature of the gold being deposited, but lower than a previous attempt at putting gold colloids in a metallic gap, or than the resistance obtained with no gold between the electrodes at all. These results relied solely on capillary action to drive the suspension from the pipette. Experiments such as described for proteins above, with electrodes attached to the pipette allowing electrophoretic

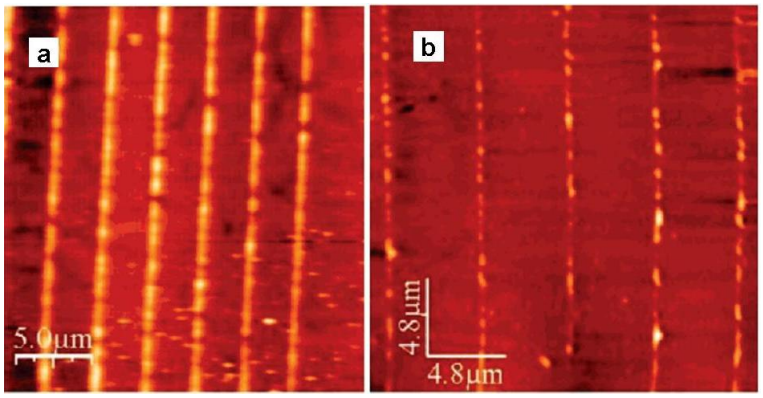

Figure 4.4: AFM images of lines written by FPN with gold nanoparticles on aldehyde-functionalised glass substrates. The dependence on nanopipette aperture size is seen by comparing lines drawn with (a) a 200 nm nanopipette and (b) a 100 nm nanopipette. The average line widths are 550 nm and 350 nm, respectively, and the line heights are 60 nm and 30 nm, respectively. From reference [87].

or electroosmotic control have been performed but not yet published [89].

Thus far the examples given of work using the Nanonics FPN system have been performed in the laboratory of the original developer, Aaron Lewis. Other groups have adopted the technique [85, 90]. Ionescu *et al.* [90] used a nanopipette to administer the proteolytic enzyme trypsin to a protein surface, creating depressions and trenches. Parameters found to be important were the length of time the tip was in contact for, for spots, or the speed of the tip motion, for lines, and the nanopipette aperture size. With a 50 nm nanopipette, a trench with width of approximately 340 nm and depth of approximately 660 nm was etched. Omrane and Papadopoulos [85] used the same technology to write patterns of catalyst for CNT growth. 50 nm and 100 nm nanopipettes were used and the ink was either Al_2O_3-FeMo suspensions in methanol or a cationised ferritin aqueous solution. Writing was performed onto silicon substrates with either a native oxide layer or a 1 μm thermal oxide layer. Al_2O_3-FeMo lines of width 300 nm and height 3 nm were written by the 100 nm pipette (Figure 4.5 a and b) and ferritin lines of width 100 nm and height approximately 20 nm were written by the 50 nm pipette (Figure 4.5 c and d). The smaller width of the ferritin lines was attributed to the larger contact angle of the aqueous solution on the SiO_2 surface, meaning that the liquid did not spread out as much as methanol did. The speed of writing

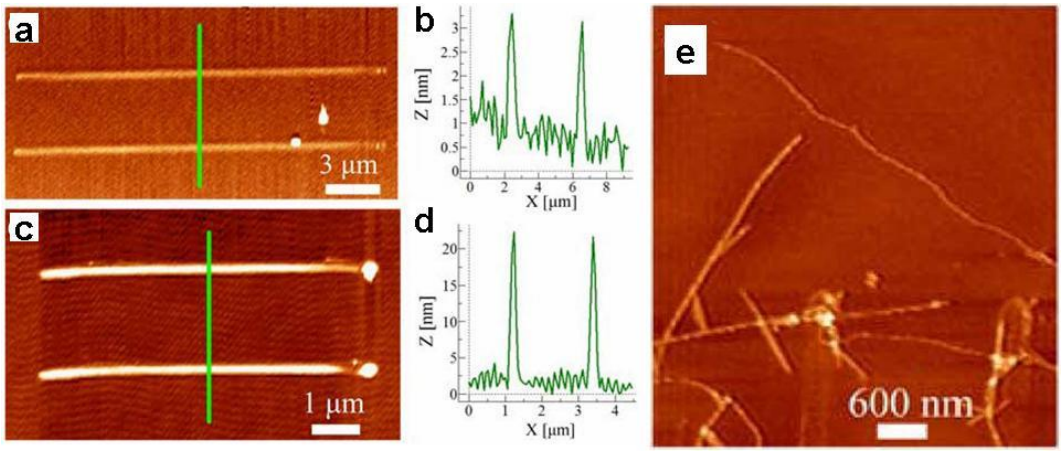

Figure 4.5: AFM images of lines written by FPN of (a) Al_2O_3−FeMo with a 100 nm pipette and (c) ferritin with a 50 nm pipette, with (b and d) the corresponding cross-sections and (e) an AFM image showing CNTs grown from the Al_2O_3−FeMo lines. Adapted from reference [85].

was investigated in the range 50 µm/s to 5 µm/s. The corresponding line heights were 1.25 nm to 3.5 nm for Al_2O_3−FeMo and 11 nm to 21 nm for ferritin. The written patterns were then successfully used to grow SWNTs by the CVD method (Figure 4.5e).

Nanopipettes have been used to deposit small quantities of liquid onto surfaces with different experimental designs. In the work of Hong *et al.* [91] quartz micropipettes were pulled to give apertures of tens or hundreds of nanometres. In contrast to the cantilevered pipettes of Nanonics, these nanopipettes were straight and instead of laser-deflection feedback, shear-force feedback was used to control the distance between the tip and the surface (Figure 4.6). The drawback of this feedback type is that as soon as contact is made between the solution in the nanopipette and the surface the feedback is lost. Single spots of photoresist were made on a gold coated glass substrate by withdrawing after contact was made. In order to write a line, the surface had to be first scanned to map the topography and then a line could be drawn at constant height. The height of the spots was 80 nm but their lateral size could not be resolved with the available instrumentation.

A shear-force microscope was also used by Iwata *et al.* [92] to deposit material through straight pulled-glass nanopipettes. Building on their previous work of

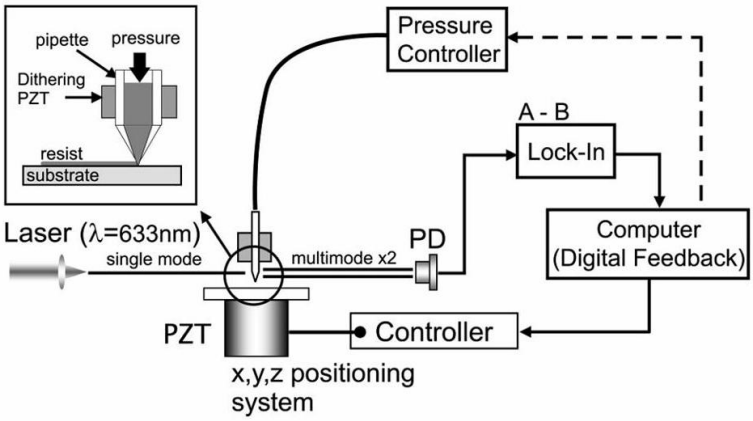

Figure 4.6: Schematic diagram of shear-force feedback for nanopipette writing of photoresist onto a gold-coated glass substrate. From reference [91].

writing with organic solvents on polymer surfaces and writing with ionic metal solutions on silicon surfaces, they then reported writing colloidal gold nanoparticles onto silicon surfaces. The 10 nm gold nanoparticles had a negative charge in water and when a dc bias was applied between the pipette solution and the surface they were deposited onto the surface. By controlling the setpoint carefully, the same pipette could be used for deposition (setpoint 10% of full amplitude of vibration) and for imaging (setpoint 60%) without further deposition. The height of dots increased with a dwell time of 0.2 s to 10 s and with voltage from 10 V to 50 V. The smallest dots produced had a height of 10 nm, corresponding to a monolayer of gold nanoparticles, and a diameter of 95 nm (Figure 4.7). A line was also drawn but was non-uniform due to friction.

Suryavanshi and Yu [93] similarly put an electrode inside a pulled nanopipette and used a bias voltage to control deposition of an aqueous platinum solution onto a Pt/Ir coated surface. Feedback was taken from the ion current to control the pipette height. By applying a potential of -1 V to the surface and withdrawing the pipette at a slow rate of 50 nm/s, a free-standing vertical wire of metallic Pt was produced. From a nanopipette of aperture 100 nm, a platinum wire approximately 150 nm in diameter and 30 μm was grown, which had a resistivity comparable to bulk platinum.

Related to the above work is the work of Klenerman and co-workers [94–100] who developed the use of a scanning ion conductance microscope (SICM) for the

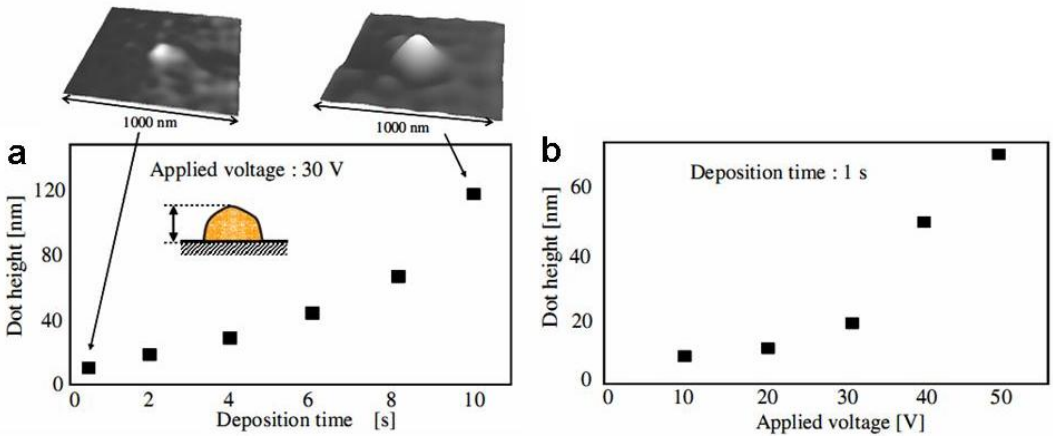

Figure 4.7: Results of nanowriting with shear-force control of gold nanoparticles onto a gold surface. The height of the dot was shown to depend on (a) the deposition time and (b) the applied voltage. Adapted from reference [92].

delivery of material through a nanopipette. SICM is able to image the topography of a soft and non-conducting surface by measuring the drop in current between the contents of the nanopipette and an electrolyte bath that occurs when the pipette tip nears the non-conducting surface. It is particularly well suited to biological applications such as cells, which can be kept alive if the electrolyte bath is a physiological buffer. By application of an electrical potential between the electrode inside the nanopipette and the counter electrode in the bath, the contents of the pipette can be injected into the solution, with control down to very small quantities, as was shown for fluorescently labelled DNA [94]. If a functionalised substrate was positioned under the tip at a distance of approximately 100 nm, then the molecules in the pipette could be drawn onto the substrate as dots or patterns (Figure 4.8). Due to the distance of the pipette and the effects of diffusion in the solution, the features sizes from a pipette with aperture of around 100 nm gave dots of diameter 830 nm (Figure 4.9 a and b) [95]. It was also shown that writing over the same area multiple times could increase the concentration of the molecules adsorbed on the surface so greyscale pictures could be created (Figure 4.9c) [95]. Testing of the parameters for delivery of different types of biomolecules has shown that the DNA is dominated by electrophoretic forces, resulting from the highly negatively charged backbone, whereas delivery of a protein (rabbit immunoglobin G) was shown to be governed primarily by

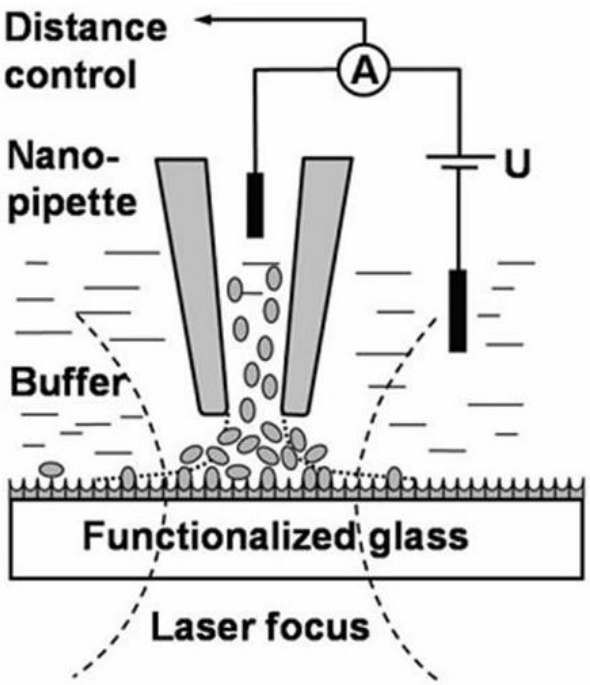

Figure 4.8: Schematic diagram of SICM for deposition of molecules from nanopipette onto a functionalised surface. From reference [96].

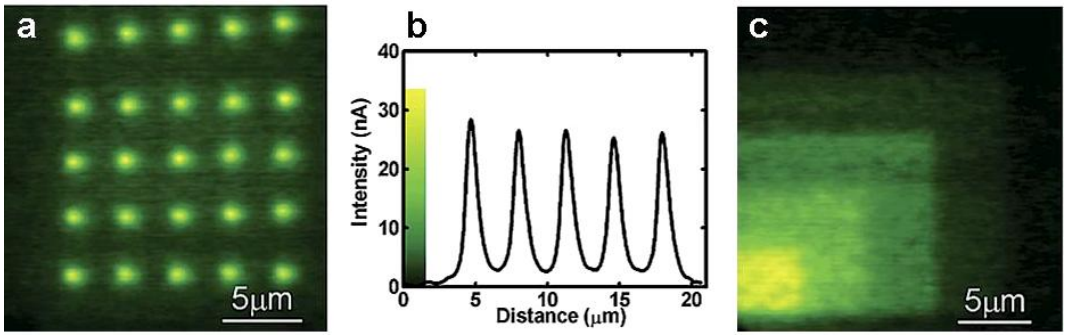

Figure 4.9: Patterns of biotinylated DNA written onto a streptavidin-functionalised glass surface by nanopipette with SICM control. (a) Fluorescence image and (b) corresponding line scan of the dots and (c) boxes showing grey-scale by repeated scanning of the same area. From reference [95].

electroosmotic flow [96]. Moreover, the deposited biomolecules maintained their function, for example as antibodies [97].

An application of the SICM-controlled nanopipette was to investigate biological process in live cells. One example of this involved a small quantity of fluorescently labelled proteins being written onto the surface of a sperm cell with a spot size of 0.9 μm. The diffusion of individual molecules on the cell membrane was

tracked with fluorescence imaging, which gave information about the different diffusion rates of different regions of the cell surface [98]. Another example was where the nanopipette was used to inject alpha toxin molecules inside individual living heart cells. The surrounding cells were untouched by the nanopipette so investigations could be made into inter-cell signalling and how the health of adjacent cells is linked [97]. A third biological application of nanopipette delivery used the brief increased concentration achieved when a solution is injected from the pipette, such as an increase in Na^+ concentration from a nanopipette containing salt solution. The concentrations achieved in the local volume of the bath were calibrated with a fluorescence method, then the effect of increased sodium concentration on the speed of the flagellar motor of a single bacterium was monitored [101].

In the quest to write smaller features on surfaces, Klenerman and co-workers turned to double-barrelled pipettes that allowed the process to be performed without an electrolyte bath [99]. Spots of fluorescent proteins and DNA were made in air, where the deposition occurred within the naturally-occurring meniscus that formed when the nanopipette was brought close to the substrate surface. As with the single-barrelled pipette method, the surface–tip distance was maintained at approximately 100 nm by monitoring the ion current between electrodes. An additional opportunity available with the double-barrelled pipettes was to deposit two different components from the two different barrels by switching the polarity of the potential difference. Sophisticated patterns and pictures were demonstrated with this method, such as the crest of the University of Cambridge made from green and red fluorescent DNA species, Figure 4.10. Since the molecules were now confined to the meniscus instead of having the possibility of diffusing throughout the electrolyte bath, the resolution attainable was superior to previous work on nanowriting. For example, spots of 350 nm diameter (FWHM) of DNA or 430 nm diameter of protein were written [99].

With the double-barrelled pipettes, it was also shown that nanowriting could be performed onto a surface under a bath of organic solvent [100]. Aqueous solution was used inside the nanopipette and an organic liquid such as mineral oil filled the bath. As in the case of writing in air, the aqueous contents of

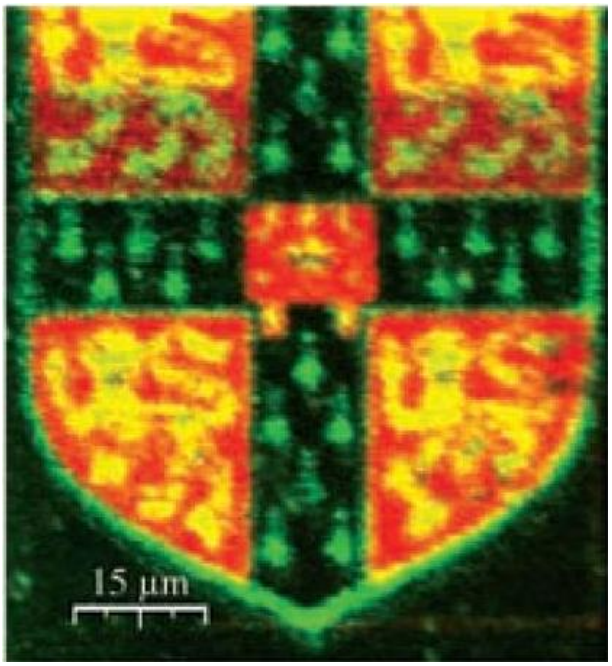

Figure 4.10: Crest of the University of Cambridge made of green and red fluorescent DNA species with yellow representing places where both species are present, created by deposition from double-barrelled nanopipette and imaged with fluorescence. From reference [99].

the pipette formed a meniscus with the surface when the tip of the pipette was brought sufficiently close to the surface, at which point feedback of the distance could be obtained from the ion current (Figure 4.11a). With the nanopipette held at a height of 100 nm a short pulse of a larger voltage could be used to eject more of the aqueous solution and thus create a water droplet on the surface. After ejection, the tip was rapidly raised and the water droplet remained on the substrate surface. If the organic bath is saturated with water then after they have been written the water droplets are prevented from dissolving into the solvent and are thus stable. Good control of droplet size was achieved by altering the pulse voltage and pulse duration. In addition the same drop could be approached several times with more solution being added each time (Figure 4.11b), which means that the droplets could be used to perform and study chemical reactions with extremely small volumes of material, so-called 'attolitre chemistry'.

Instead of using tapered nanopipettes, Meister *et al.* [102, 103] used a conventional AFM probe with the tip hollowed out in a technique labelled Nanoscale

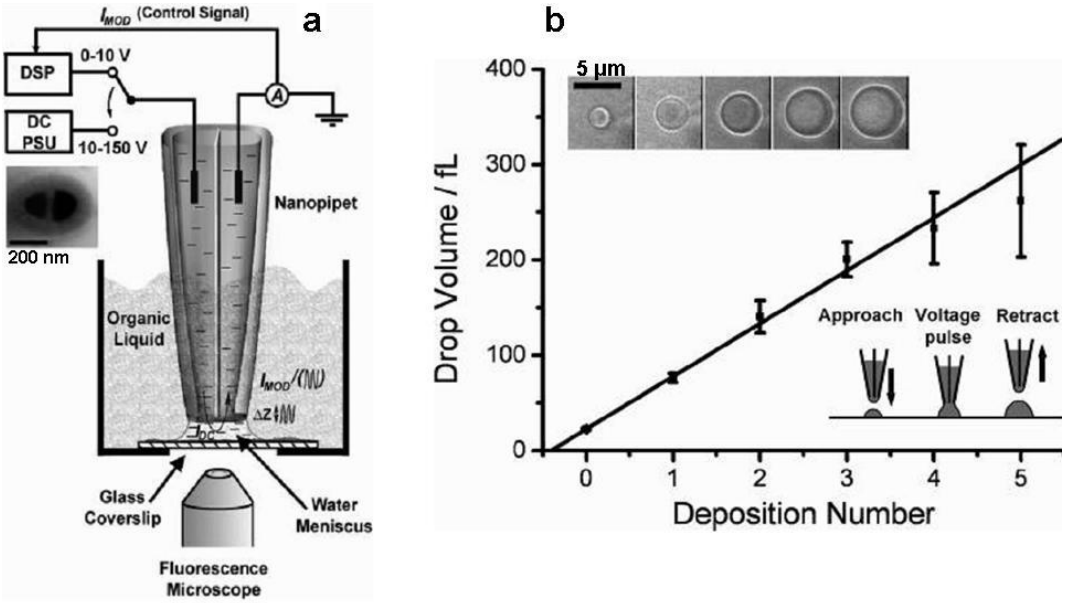

Figure 4.11: (a) Schematic illustration of water droplets being written from a double-barrelled nanopipette in an oil bath. The inset is a SEM image of the pipette tip. (b) Results of addressing the same droplet multiple times (pulse 30 V, 300 ms), where the volume of the drop increases linearly with deposition number. The upper inset is a set of optical images of a drop showing its increase in size. From reference [100].

Dispensing (NADIS). AFM laser-reflection feedback could be used. The hollowed pyramidal probe tips were made in a relatively simple eight-step microfabrication process, starting with a silicon wafer and using reactive ion etching (RIE) and photolithography to create an aperture in the tip and a reservoir on the backside. Early work showed writing of thiols on a gold surface and glycerol on a glass surface but feature sizes exceeded 1 µm in size. Features of less than 500 nm were created with a developed version of NADIS [103], where FIB etching was used to make an aperture size of 200 nm (Figure 4.12). Experiments and simulations explored the influence of hydrophobicity/hydrophilicity of the substrate and the inner and outer surfaces of the tip (Figure 4.13). In both versions of these probes the reservoir was small with a volume of hundreds of femtolitres, which had to be carefully filled by micropipette.

The concept of using a modified version of a standard AFM tip as a nano-fountain pen was taken on and improved by Deladi *et al.* [104] Micromachining techniques were used to create tips with a large reservoir connected to the top of

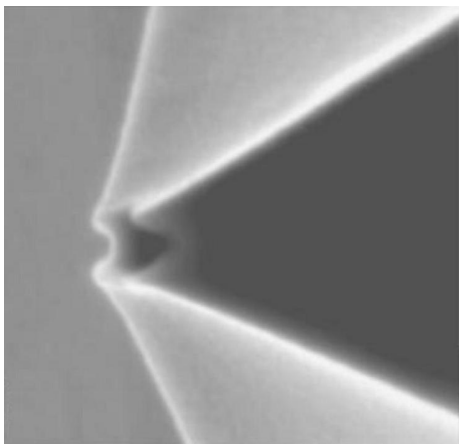

Figure 4.12: NADIS tip with 200 nm aperture fabricated by FIB etching. From reference [103].

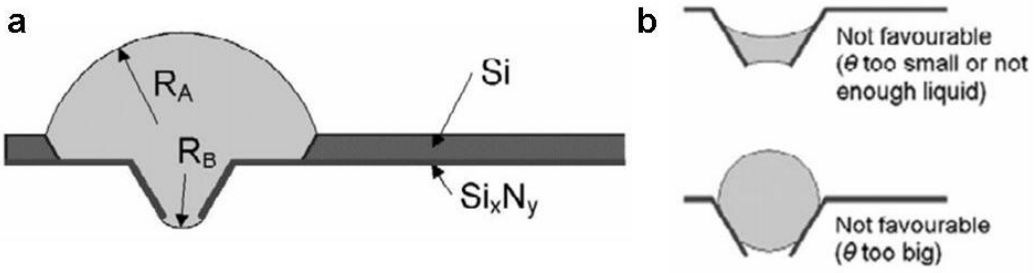

Figure 4.13: Results of simulations on the effect of hydrophobicity/hydrophilicy of the tip, showing that (a) an optimum contact angle, θ, exists and that (b) the cases of too large or too small a contact angle prevent the liquid from flowing out onto the surface. From reference [102].

the tip by microchannels (Figure 4.14). This type of tip was used to write lines of 1-octadecanethiol (ODT) in dichloromethane solvent on a gold surface at a rate of 4 µm/s, going over each line 5 times. The same tip was then used to image the friction of the surface at a speed of 80 µm/s. The lines were observed to have a width of 0.5 µm, which was attributed to diffusion. Thinner lines were predicted for optimised tip sharpness, ink outlet holes, ink velocity and wetting properties. In addition, a chrome surface was etched by a commercial etchant solution. A trench etched by a single 5 µm/s line was 14 nm deep and 0.35 µm wide (at its widest point) [104].

An even more sophisticated development of Meister's NADIS system is the Nanofountain Probe (NFP) [105–110], which incorporates a 'volcano tip' (Figure

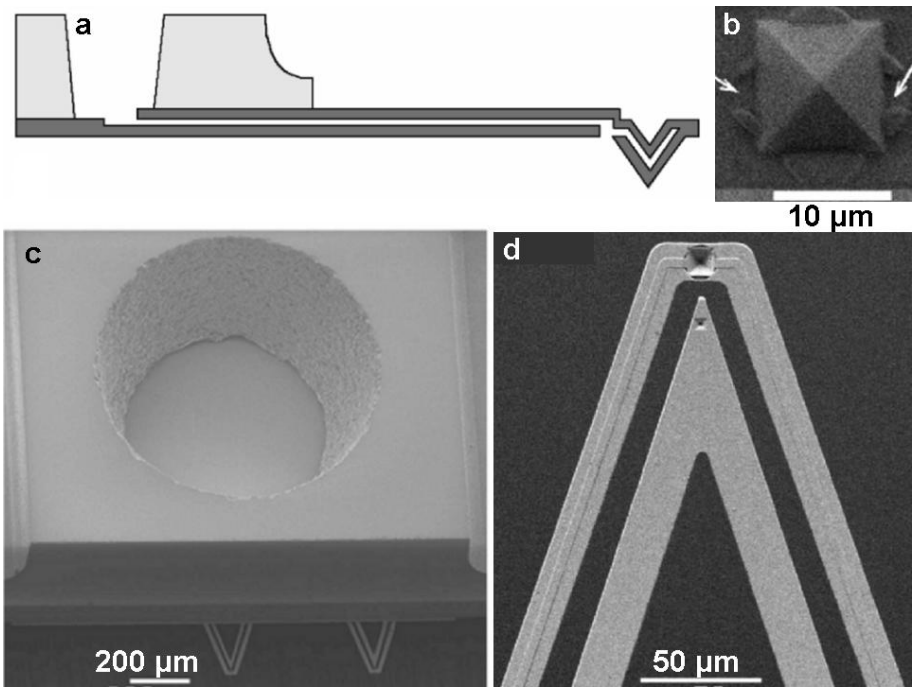

Figure 4.14: (a) Schematic diagram of the modified AFM tip used by Deladi *et al.* SEM images of (b) the tip, (c) the reservoir and (d) the microfluidic channels between reservoir and tip. The arrows in part b indicate the outlet holes from the channels. Adapted from reference [104].

4.15 a and b) on conventional AFM-style probes. Nanofountain probes have a reservoir and microchannels leading to the volcano tip (Figure 4.15c). The design of the tip, which can be see as a hybrid between the DPN and NADIS techniques, aims to give improved resolution of features by creating a sharper point of contact while allowing a continuous supply of solution to the surface. The first-generation design [105, 106] had a single reservoir and a range of cantilever lengths. The complex multi-step microfabrication process resulted in a range of probe qualities, with the best able to repeatably draw lines of sub-100 nm width but many suffering from microchannel clogging, low torsional stiffness and small laser-reflection area, which gave a low feedback signal. The reservoir on these probes is ∼1 mm in length, which is a significant improvement on the reservoirs of the NADIS probes in capacity and ease of filling.

The second-generation NFPs addressed many of the problems of the initial probes by using more sophisticated microfabrication and improved design [111]. In addition, the single operating tip was replaced with an array of twelve tips that

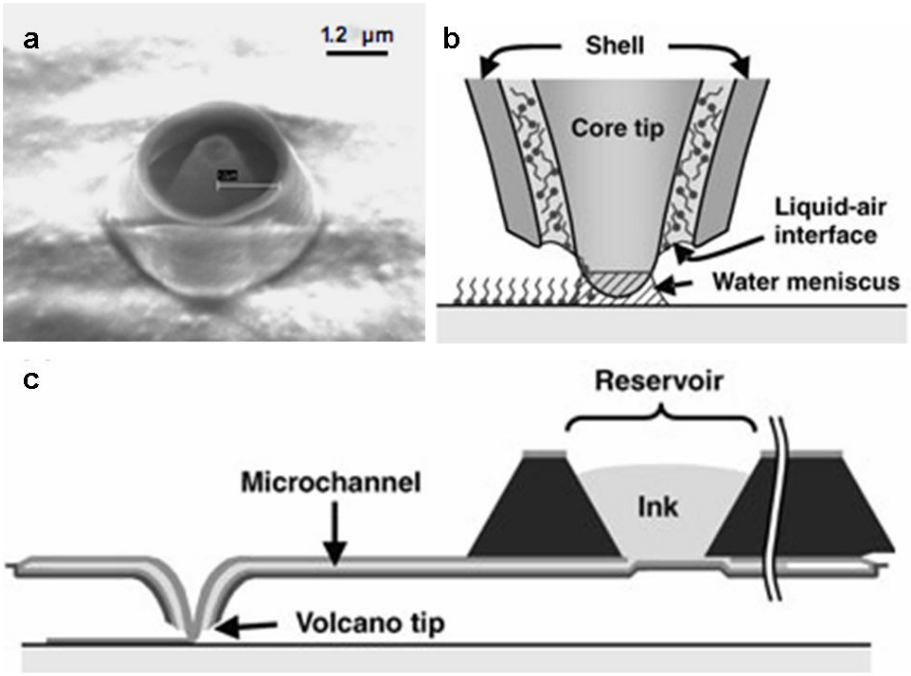

Figure 4.15: (a) SEM image, (b) schematic diagram of the volcano tip and (c) schematic design of the entire nanofountain probe. Part a is from reference [105] and parts b and c are from reference [106].

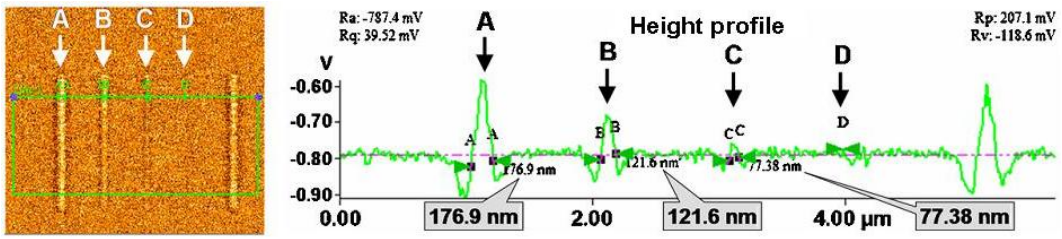

Figure 4.16: Lateral force microscopy image and corresponding profile of lines of MHA written onto a gold substrate. The writing speeds of lines A, B, C and D were 3.2, 6.4, 12.8, 25.6 µm/s, respectively. From reference [111].

would make contact simultaneously, enabling parallel writing. Two reservoirs were used, so writing with two separate inks was made possible. With solutions of 16-mercaptohexadecanoic acid (MHA) in acetonitrile, lines on a gold substrate were reliably produced up to writing speeds of 15 µm/min (0.25 µm/s) with a width of 78 nm (Figure 4.16) [111].

Espinosa and co-workers continued to develop their technique and they manufactured third-generation NFPs [107]. These were more robust and had larger microchannels than their predecessors and were therefore able to transport 15 nm

gold nanoparticles. An aqueous colloid of citrate ion-capped – and thus negatively charged – gold nanoparticles was used as the ink and the substrate was oxidised silicon with a chemically bound APTES monolayer. The amino groups on the surface had a high affinity for gold so the nanoparticles were immobilised on contact with the surface. From 2 s contact time, dots with a height of up to 180 nm and diameters of 600–700 nm were written. After rinsing in water the dot heights were 15–20 nm, corresponding to a monolayer of gold nanoparticles, which could be resolved with high-resolution AFM. On occasion the tips were clogged by nanoparticles so that deposition failed, but the tips could be cleaned with piranha solution and subsequently reused. Factors influencing the spot sizes were the probe tip dimensions, wetting characteristics and evaporation rate but not the contact force. With a range of substrates, an inverse relationship was found between solvent–substrate contact angle and spot size, but only APTES was suitable for binding the gold particles in the washing step [107]. Third-generation NFPs were also used to deliver DNA to a gold surface. Single stranded DNA in a complex solution was used as ink. The diameter of spots was found to increase with increasing contact time, from 180 nm to 422 nm for 0.5 s to 2.0 s, respectively, while the height for all cases was reported as 20 nm. A large range of relative humidity, from 20% to 90% was found to have only a small effect on feature size. Rounder spots were achieved when the volatility of the ink was increased [108].

Loh *et al.* gave another degree of control to deposition with NFPs by the use of electric fields on protein printing [109]. With negatively charged biotin-BSA in aqueous solution as the ink and an MHA-covered gold substrate, deposition without applied electric field was sporadic, giving discontinuous lines of non-uniform width. For electric field controlled writing, the substrate was grounded and the ink reservoir was given an electrostatic bias. With positive bias all deposition was inhibited and with negative bias the writing was assisted by electrophoretic and electroosmotic effects (Figure 4.17a). At large negative voltages (above -3 V), the ink flooded the substrate but at voltages between -1.5 V and -2.5 V writing could be performed with control. Continuous lines of width 170 nm were written at a tip speed of 80 μm/s (Figure 4.17b), considerably faster

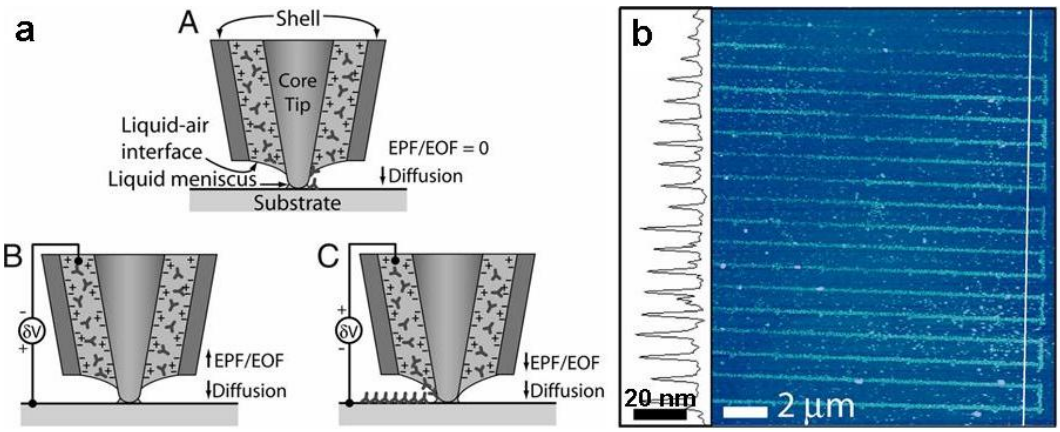

Figure 4.17: (a) Schematic illustration of how electrophoretic flow (EPF) and electroosmotic flow (EOF) aid nanowriting. (b) Lines of biotin-BSA written at high speed on a MHA surface with application of −1.5 V. From reference [109].

than any previously reported writing, with −1.5 V applied. It was predicted that with optimisation of environment and parameters the maximum speed could be further increased. Loh *et al.* also presented a detailed model of the liquid–air interface around the tip that explains why writing was not effective without the application of electric field [109].

Continuing with biological applications of NFPs, Loh *et al.* [110] showed capabilities of single-cell injection of diamond nanoparticles, called nanodiamonds (NDs). The NFP is less damaging to cells and easier to implement than other known techniques for single-cell injection. In addition to the work on cells, the authors demonstrated the NPF's ability to make spots of drug-coated NDs on a glass substrate, from both aqueous and dimethyl sulfoxide (DMSO) solvents. Spot heights and diameters depended on the square root of the dwell time, with smallest spots reported being 7 nm high and 93 nm across [110].

4.2 Experimental

As implied by the name 'nanofountain pen', an analogy can be drawn against macroscopic writing with a fountain pen on a piece of paper. Important materials are the paper and the ink inside the pen, which correspond to the substrate and the CNT dispersion, respectively. Important parameters include the speed of

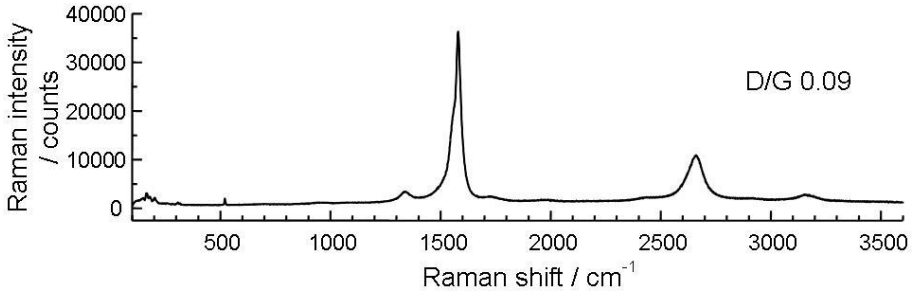

Figure 4.18: Raman spectrum of raw SWNTs, as purchased, deposited on a silicon wafer and measured with 514 nm laser excitation. The ratio of intensities of D and G peaks in this spectrum is 0.09. This measurement was repeated to give an average D/G ratio of 0.12 ± 0.09.

writing and how hard the pen is pressed onto the paper. In the macroscopic case these parameters and others are governed by the hand that holds the pen. In the microscopic case the pen is held by an AFM and these parameters can be set.

4.2.1 Sample preparation

The silicon substrates used were prepared as described in Section 3.4 by cleaning and functionalising with APTES.

SWNT dispersions were produced using HiPco[69] SWNTs purchased from Carbon Nanotechnologies Inc., USA after no purification or processing steps. Raman spectra of the raw SWNTs (Figure 4.18), deposited on a silicon wafer, revealed that the D/G ratio was 0.12 ± 0.09. To form dispersions, the SWNTs (1 mg) were placed in an aqueous solution of either sodium dodecylbenzene-sulfonate (SDBS) (0.2 mg/ml) or sodium dodecyl sulfate (SDS) (0.5 mg/ml) (7 ml). The SWNTs were dispersed into the solution by pulsed horn ultrasonication (Bandelin Sonoplus ultrasonic homogenizer HD 2200 with titanium tip KE76 with a diameter of 6 mm) with an average power of 32 W, a pulse duration of 0.6 s and a repeat rate of 1 s. An ice–water bath surrounded the tube of SWNT dispersion to prevent the SWNTs being damaged by elevated temperatures resulting from the ultrasonication. Ultrasonication was applied for two minutes then paused until the solution felt cool to touch and this was repeated four times so in total ultrasonication was performed for a duration of 8 minutes.

A small portion of this dispersion (1–1.5 ml) was centrifuged (Sigma 2-16

Benchtop Laboratory Centrifuge) at 15000 rpm, equivalent to $\times$20500 g for 30 minutes to one hour to remove large bundles of carbon nanotubes. There was visible dark precipitate and the resulting supernatant had a lighter, grey appearance than the dark, near-black dispersion before centrifugation. The supernatant was pipetted into a clean vial and used for experiments.

In some cases instead of starting by weighing dry SWNTs, a dispersion previously ultrasonicated as described was taken. Some additional ultrasonication was performed, typically 4 or 6 minutes and then it was centrifuged as above.

Raman spectra of the SWNTs after ultrasonication and centrifugation gave a D/G ratio of 0.06 ± 0.02, which indicated that the overall quality was improved by the processing.

4.2.2 Measuring dispersion concentrations

The concentration of SWNTs in the fully prepared dispersions was always lower than the initial concentrations, since SWNTs were lost in the precipitate of the centrifugation step. To determine the actual concentration, Raman spectroscopy of the liquid dispersion was used in a method developed by Andrei Gromov [32] based on earlier work by Salzmann *et al.* [112].

Liquid cells were prepared by Andrei Gromov comprising a base of 1 mm thick glass covered with 2 or 3 mm thick polydimethylsiloxane (PDMS). A hole was made in the PDMS with a volume of approximately 100 µl. The dispersion to be measured was pipetted into the hole until the entire volume was filled. A glass coverslip of thickness 90 µm was placed over the top with no air bubbles trapped inside.

To measure the Raman spectrum, the sample was positioned so that the focus of the laser spot was 120 µm below the lower surface of the coverslip. Raman measurements were made with 514 nm (2.41 eV) excitation light and a power of approximately 2 mW, over a spectral range of 1300–4000 cm^{-1}. Three measurements, each for 20 s acquisition time were made on each dispersion.

The G band and the water (ν_{O-H}) peak were peak-fitted and the G^+ band

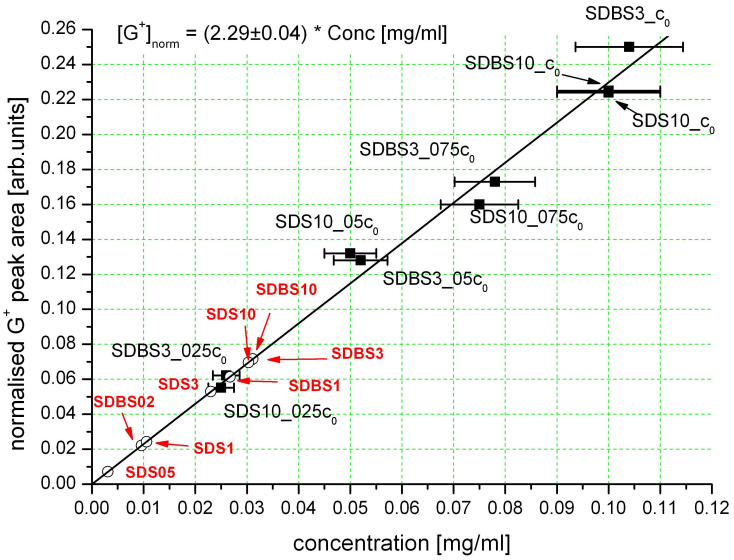

Figure 4.19: Calibration measurements relating normalised G^+ peak intensities to concentration of SWNTs in aqueous dispersions. From reference [32].

intensity was normalised to the water peak. The normalised G^+ intensities from the three measurements were averaged and compared to a calibration plot [32] obtained from dilutions of dispersions from the same SWNT supply and with the same surfactants, SDS and SDBS (Figure 4.19). From these dilutions, the relation between the normalised G^+ intensity, $[G^+]_{\mathrm{norm}}$, and the SWNT concentration, *conc*, is:

$$[G^+]_{\mathrm{norm}} = (2.29 \pm 0.04) * conc[\mathrm{mg/ml}]. \tag{4.1}$$

4.2.3 Nanonics AFM

The basic operation is described in Section 3.2. In this case, the sharp tip normally used to create topographic images of the surface was replaced with a hollow quartz tapered nanopipette. The usual AFM controls and NWS software were used to manage the movement of the tip with respect to the substrate and when the tip was in contact with the surface, the contents of the nanopipette could flow out.

The nanopipettes (Figure 4.20) were made by Nanonics Ltd. by pulling quartz

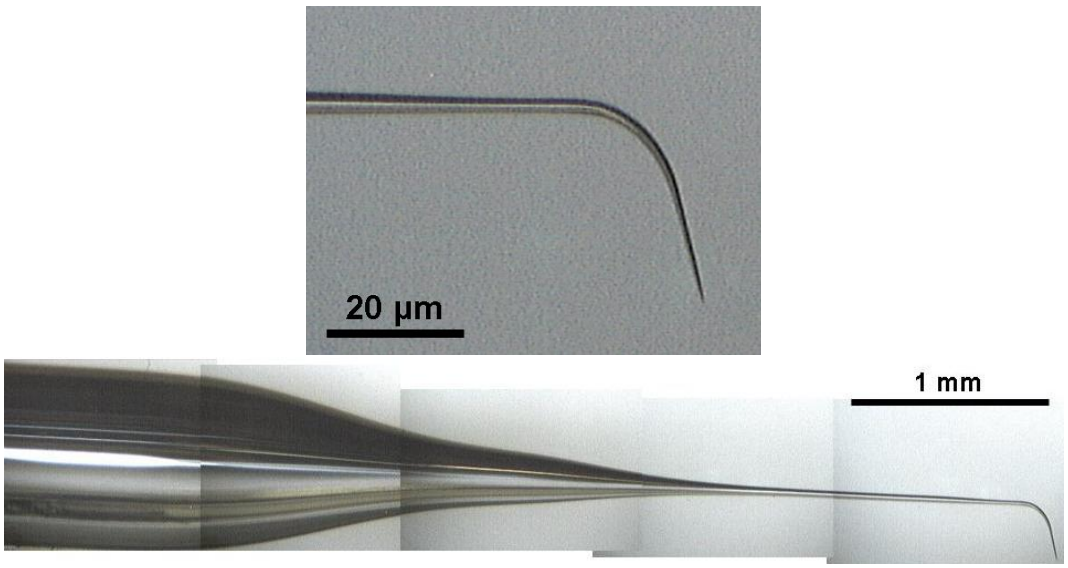

Figure 4.20: Optical microscope picture of tip of nanopipette (top) and composite optical microscope picture of tapered part of nanopipette (bottom).

capillaries. They had a spherical cross-section with an internal diameter at the large end of approximately 400 µm and an aperture at the tip of the tapered end of 50 nm, 100 nm or 150 nm. At the wider end of the nanopipette, the thickness of the quartz walls was 300 µm. The tapered end was coated with gold to provide a reflective surface for the AFM feedback laser. The nanopipette was straight and untapered for a length of approximately 2 cm, while the tapered section was a few millimetres long.

The nanopipettes were filled by touching a small drop of dispersion to the large end of the pipette. Capillary forces drew the solution down the inside of the pipette to fill the end. There was always a large air bubble in the part of the pipette with the maximum diameter but this did not appear to prevent the solution from flowing to the tip. To ensure that there was a large supply of solution and prevent any danger of the solution drying from the open end of the pipette, a reservoir was added. This was a length of plastic tubing 5 mm to 1 cm in length that was completely filled with the dispersion and then pushed onto the large end of the pipette.

There were two different methods of holding the nanopipette in the AFM head. The first method was the same as how standard tips are held, by way of a small magnet (Figure 4.21a). This method had two important disadvantages:

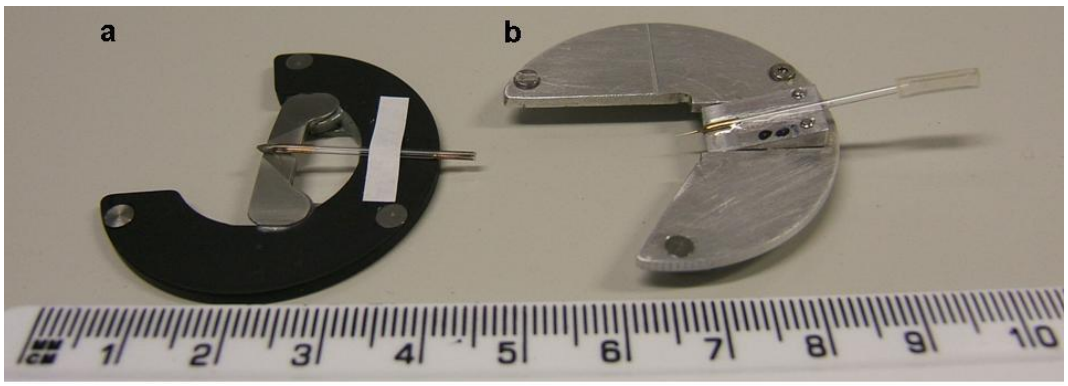

Figure 4.21: Photograph of pipette mounting methods: (a) using a magnet and (b) with glue. In part a the tip is pointing upwards and in part b the tip is pointed downwards, as it would be during operation.

one was that the weight of the nanopipette was considerable and it could not be fully supported by the magnet so sticky tape was also required at another point along its length. The second disadvantage was that the magnet did not hold the pipette in a rigid enough fashion to prevent movement during the process of filling it with the solution. This meant that the time-consuming process of aligning and focussing the laser on the tip had to be done after the pipette had been filled, at which time a delay was detrimental to the experiment. The second and improved method of holding the nanopipette in the AFM head was with a custom-built pipette mount (Figure 4.21b). In this case the pipette was glued into a groove so once fixed it was rigid and thus alignment steps performed before filling with solution did not have to be redone after the pipette was removed, filled and replaced. The glue used was UV-setting, meaning that care could be taken to ensure that the angle the tip points at was good, in the optical microscope, before the glue was exposed to UV light to set it.

The basic principles of the AFM feedback system using laser deflection were the same as if using a standard tip but there were small differences. One advantage was that the size of the pipette in comparison with a normal tip meant that there was a larger area for the laser to reflect from, so the total signal received by the position-sensitive detector was stronger. In the case of the rigid pipette mount there were subtle differences in the angle of the tip and therefore in the position of the laser, mirror and detector (Figure 4.22). It was a significant challenge

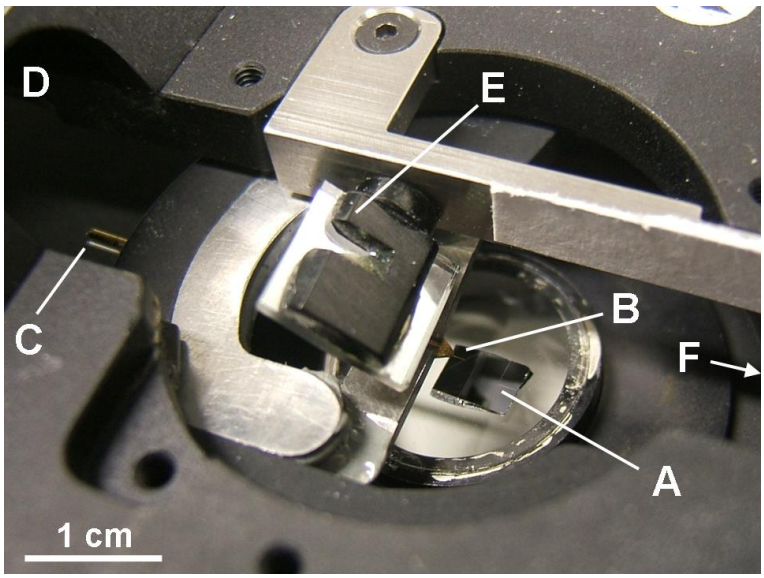

Figure 4.22: Photograph of substrate (A) underneath nanopipette tip (B) inside the Nanonics MV1000 head. C is the large end of the pipette, where solution is added. The optical path of the laser beam used for feedback is from the laser source (D) to the mirror (E), then the tip (B) and finally to the detector (F).

obtaining alignment without the mirror blocking the optical view of the tip from above. Sometimes this challenge was overcome by changing the mirror's vertical position as well as the lateral position and angle, which are advised in the documentation.

The substrate was positioned on a substrate mount underneath the tip. It was stuck onto the substrate mount by either silver paint, nail polish or double-sided tape. The pattern of lines made by a diamond pen on the substrate surface during the preparation of the substrates was used to identify locations.

Before engaging the tip onto the surface, the microscope focal volume, the tip and the desired position on the substrate had to be positioned together laterally. Once this was done then focussing on the surface and engaging the tip allowed the nanowriting process to be monitored in real-time. By saving digital pictures of the optical image of the surface, it was possible to locate the same area afterwards, for example to scan with standard AFM.

In some cases the contents of the pipette started to flow out as soon as the tip made contact with the substrate surface. As the tip moved over the surface, a dark trace was sometimes seen in the optical microscope indicating that material

had been deposited.

4.2.4 Varying parameters

Many of the parameters that can be varied in AFM scanning could be varied during nanowriting experiments.

Nanowriting experiments were performed in both contact and tapping mode regimes. In the case of contact mode, the setpoint was most often fixed at 0.12 V or 0.13 V, where this voltage represents the voltage difference measured between the top and bottom halves of the position-sensitive detector. On occasions, to test the effect of pressing onto the surface with a greater force, the setpoint was increased to 0.2 V or 0.4 V. For tapping mode, the resonance frequency of the pipette was found. Monitoring this peak position before and after filling was found to be an effective method of checking that the pipette was filled to the tip, since in the case of successful filling the resonance position moved to a lower frequency reflecting the additional mass of the contents in place of air. Typical frequencies of filled tips ranged from 25 kHz to 105 kHz and their empty frequencies were on average 2 kHz higher. The lock-in gains were always adjusted so that the resonance peak had a height of 8 V. Setpoints for tapping mode were recorded in terms of a percentage of this total peak height, with the most common being 80%, meaning that the setpoint was input as −6.4 V.

The speed at which the tip moved over the surface was routinely studied. This was easily controlled by the instrument. Speeds used were 1, 2.5, 5, 10, 50 and 100 μm/s.

The tip movement over the surface was controlled in two different ways. The 'manual' method involved typing in the coordinates that the tip was to travel to, then the tip would move at a speed of 10 μm/s to that position. Subsequent steps were entered one-by-one so there was inevitably a delay at each corner point as the next set of coordinates were typed. The alternative to the manual method was to use 'nanochemplotter' scripts. These pre-written scripts contained a list of coordinates and the speeds at which the tip should travel. Initially the scripts used here were those of Yulia Lovsky of Nanonics Ltd., and latterly Yulia's

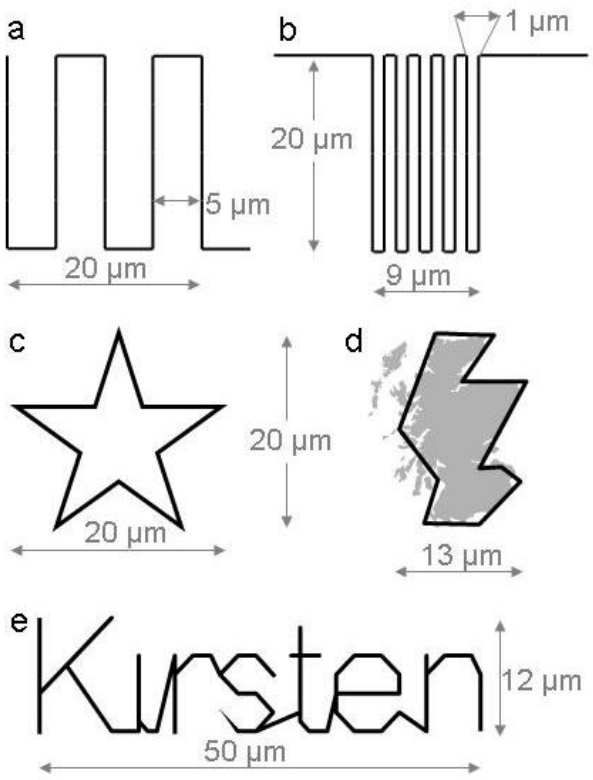

Figure 4.23: Patterns made by scripts for controlling the tip motion over the substrate during nanowriting experiments: (a) sparse snake, (b) dense snake, (c) star, (d) Scotland (shown over map of Scotland) and (e) Kirsten.

scripts were used as a basis for new scripts. A selection of scripted patterns written in Edinburgh is shown in Figure 4.23 and the complete scripts are given in Appendix E. An advantage of using scripts is that the steps follow on from one another immediately so there are no delays at corner points. The only points at which the tip is in contact with the surface waiting for human input is at the start and ends of the script. This is the reason for the long tails at the start and ends of the 'dense snake' script (Figure 4.23b), so the bulk of the pattern can be examined afterwards with the start and end points being cut off from the area being scanned. With other scripts it was beneficial to respond as quickly as possible to the tip making contact or to the script finishing, so the delays at those points were minimised.

4.2.5 Applying voltage during writing

An additional parameter that was sometimes used was the application of a potential difference between the contents of the pipette and the substrate.

The substrate was electrically contacted by making a small scratch with diamond pen and then immediately using silver paint to attach an electrical wire. It was important that this attachment did not affect the samples movement on the piezo scanner, which was achieved by only using a very lightweight electrical wire and making sure that there was spare length so as not to have it ever pull tight as the sample moved. The solution inside the pipette was electrically contacted by placing an electrical wire into the solution at the large end of the pipette.

Typically the pipette was held at 0 V and the voltage on the substrate was ranged between −10 V and +10 V. It is acknowledged that some potential will have been lost within the pipette itself so the values quoted are not representative of the potential between the tip and the surface, however the wire was always placed the same distance into the pipette so there is self-consistency.

In Jerusalem this application of voltage was achieved by connecting the electrical wires directly to the Nanonics AFM controller boxes. The scripts used for controlling the tip movement could also be used to set the voltage to be applied. In Edinburgh the version of controller box was such that the voltage could not be applied in this way. Instead a separate sourcemeter (Keithley 2611 Sourcemeter) was used. The electrical signal was also fed into an input channel on the Nanonics controller boxes, so although the NWS software could not control the voltage, it could monitor and record it. Figure 4.24 illustrates this arrangement.

The ultimate goal of using voltage would be to achieve a switching on and off of the deposition. If 'on' and 'off' voltages had been identified then more care would have been needed to synchronise the voltages with the tip movement, but that was not achieved within this work. As such all experiments using voltage were performed with the voltage switching between two values at a chosen frequency. In Jerusalem the voltage switched four times in each line and in Edinburgh the frequency was most commonly chosen as 1 Hz, which also corresponded to switching four times in a 20 μm line when moving at a speed of 5 μm/s. In most

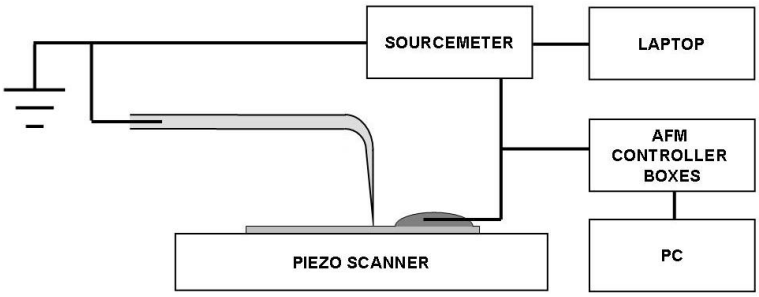

Figure 4.24: Schematic diagram of the experimental setup for voltage-controlled writing. A wire inserted into the contents of the nanopipette is grounded. A second wire, glued to the silicon substrate with silver paint, is connected to the sourcemeter. The laptop controls the output from the sourcemeter and the AFM controller box reads the signal and feeds it to the PC. The AFM feedback controls have been omitted for clarity.

cases the voltage was switched from one bias to the other of the same magnitude, so a voltage stated as ±5 V means 0.5 s of −5 V followed by 0.5 s of +5 V, repeated. The sourcemeter was controlled by LabVIEW, with a simple program developed with assistance from Johan Ek Weis that allowed the user to input the two voltages and the time between switching. The LabVIEW code is included in Appendix F.

4.3 Results and Discussion

4.3.1 Deposition of material

The influence of mode, setpoint, speed, pipette size and voltage on the quality of writing produced from CNT dispersion will now be discussed in turn. Writing was initially evaluated with optical microscopy, in real time during the writing itself and immediately after the tip was withdrawn. Afterwards, AFM (with a Veeco Nanoman VS) was used to test the dimensions of the written lines and check for the existence of any writing that was too small to appear in the optical microscope images.

FPN writing was shown to be possible in both tapping mode and constant contact mode, for example the examples in Figure 4.25.

Changing the setpoint in tapping mode away from the standard 80% did not

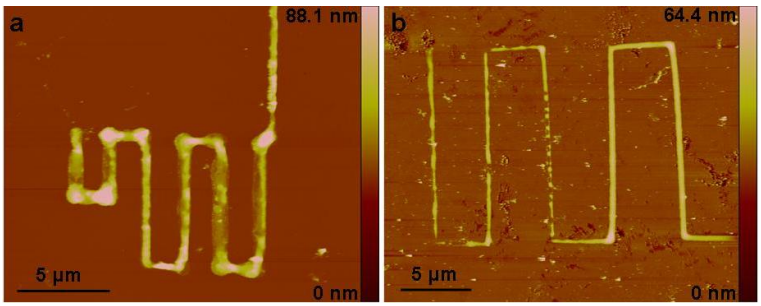

Figure 4.25: AFM images of FPN writing performed in (a) tapping mode and (b) contact mode. Setpoints were 80% and 0.12 V respectively, and the speed of writing was 10 µm/s in each case.

have any noticeable change in the repeatability or quality of the writing. In both tapping and contact modes achieving reliable writing was a difficulty. If no writing was observed in contact mode with setpoint 0.12 V then it could be increased and in some cases writing occurred at 0.2 V or 0.3 V. However, there are two risks associated with higher setpoints. The first risk is that the increased force between the tip and the substrate prevents their correct relative motion. Figure 4.26 illustrates an example of this, where the tip was pressing too hard to allow smooth motion and the result was a skewed pattern. On other occasions the motion was not easy to visualise but the incorrect motion was evident when the scanner returned to the zero position after the writing was completed, and the sample was shifted with respect to the zero position before writing. The second risk is that the tip may be damaged by too high a setpoint. This might be the case in Figure 4.27 where there is a significant increase in the quantity of material deposited with no change in writing parameters while using a high setpoint. The main disadvantage of damaging the tip is increasing its diameter by an unknown amount, which means small features are not possible, parameters that have been optimised will be changed and the resulting tip shape is completely unpredictable. The resultant tip shape thus could be better or could be worse for writing but would not be repeatable. SEM was attempted on nanopipette tips after they had been used for writing to examine the final tip shape, but it proved problematic. The magnet that held the tip to the holder broke off in the strong magnetic field within the SEM and even when the magnet was well glued down and did not

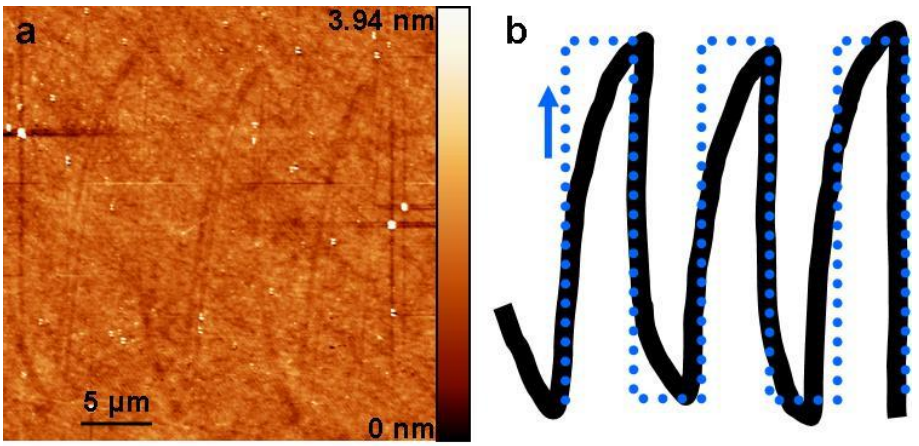

Figure 4.26: (a) AFM image of writing performed with a very high setpoint (2 V) in contact mode. (b) The intended pattern is indicated by the dotted blue line and the path taken by the tip is represented by the black line, which can also be seen as a slight indent on the surface in the AFM image. The tip could not keep up with the sample movement during the long lines so it cut the corner. When the sample changed direction to begin the next long part of the line, the tip would jump to the corner.

break off, the tip was seen to have broken. This could be explained by there being an air cavity within the nanopipette, between the bulk of the liquid in the large end and the tip itself, which is filled with liquid by capillary forces. Thus, when the pipette was put under vacuum within the SEM, the pressure difference resulted in the pipette breaking near the tip.

When the nanopipette tip was in contact with the surface, the speed at which it was moved over the surface was varied. If the tip was not successful at deposition at one speed, changing to a faster or slower speed did not help deposition to occur. If writing did occur then the tip speed did affect the size of the lines written. Figure 4.28 shows the results of a range of speeds from 5 µm/s to 1 µm/s and these are summarised in Figure 4.29. It can be seen that the width is more dependent on tip speed than the height is. In general, a slower tip results in more deposition through the tip, which is consistent with the findings of other nanopipette writing experiments described in Section 4.1. Figure 4.29 also shows the results of nanowriting performed on the same instrument, with the same pipette size and in contact mode, but with an aqueous solution of 0.6 mM $HAuCl_4$ instead of a CNT dispersion, performed by Chaweewan Sapcharoenkun

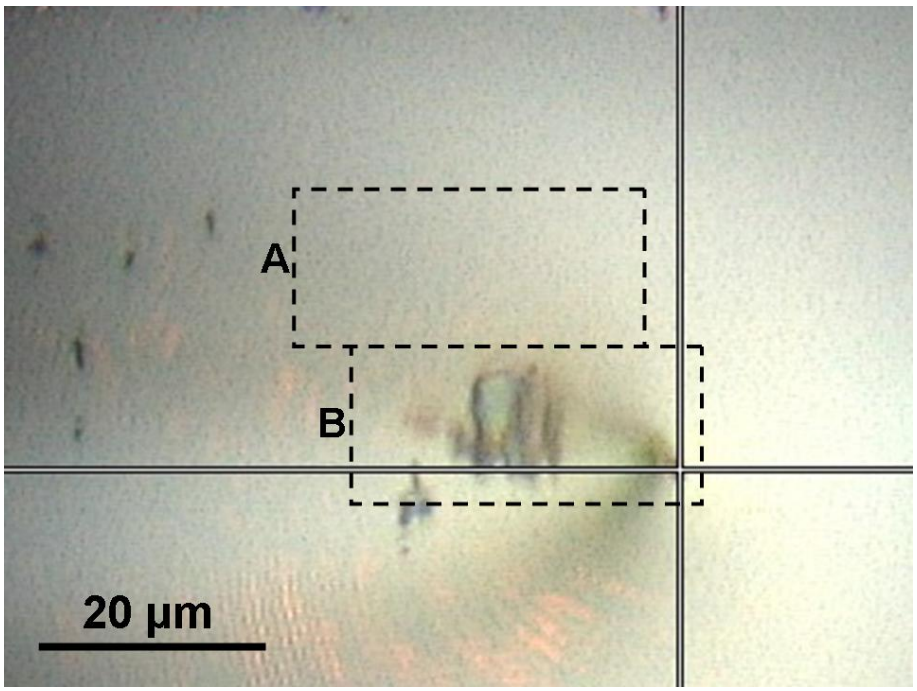

Figure 4.27: Optical microscope image taken during writing, showing a sudden increase in deposition bewteen areas A and B with a setpoint for both of 0.4 V. All parameters were unchanged so the difference is most likely explained by the shape of the tip changing due to damage from the high forces arising from the high setpoint. The shadow leading out from the centre of the crosshairs is the tip of the nanopipette, still in contact with the surface.

[113]. The line sizes are comparable with one another in both height and width except the gold solution lines do not get wider at slower speeds. The maximum speed the CNT dispersion deposition was observed at was 20 µm/s; at 50 µm/s nothing was deposited. A typical AFM topography image might be measured at a rate of one line per second for a 10 µm-wide area, which corresponds to a tip speed of 20 µm/s. Therefore it was predicted that the same tip could not reliably be used for imaging the surface without giving further deposition, though this was not tested experimentally. It can be see in Figure 4.28 and in Figure 4.30 that slower speeds gave more consistent continuous lines.

Related to the correlation between tip speed and line size is the observation of blobs at the start and/or end of many of the nanowriting patterns, as seen in Figure 4.30, for example. When using scripts to control the tip motion these points are the only times that the pipette pauses on a particular spot. In contrast, Figure 4.25a has blobs at every corner because it was written in manual mode,

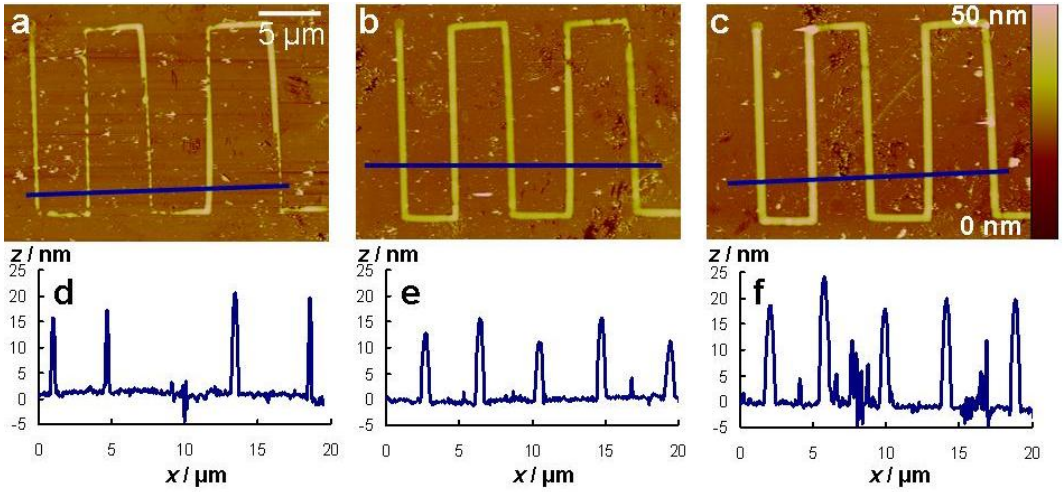

Figure 4.28: AFM images of lines written with line speeds of (a) 5 µm/s, (b) 2 µm/s, (c) 1 µm/s and the corresponding cross-sections (d–f, respectively) of the blue lines on the images. These lines were drawn by a 100 nm nanopipette in contact mode with a setpoint of 0.12 V.

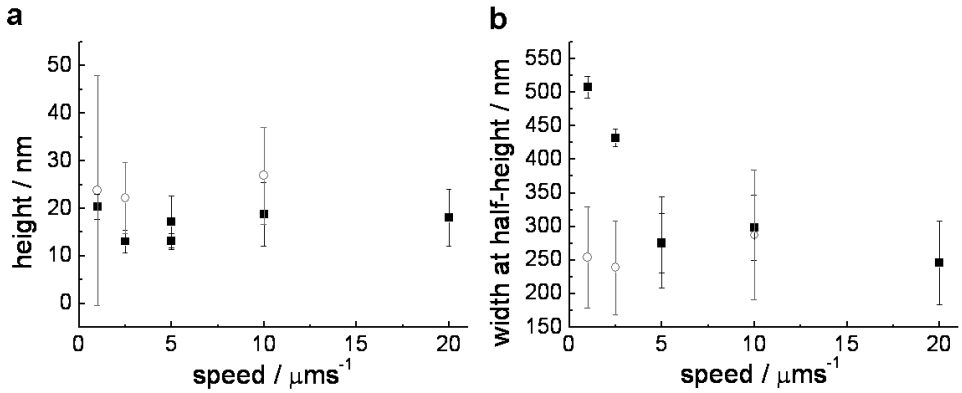

Figure 4.29: Dependence of (a) line height and (b) line width on tip speed from a 100 nm nanopipette operating in contact mode with a FPN dispersion (black squares). Also shown (grey circles) are comparable results for an aqueous solution of 0.6 mM $HAuCl_4$ written with the same conditions on the same instrument by Chaweewan Sapcharoenkun. Data for grey circles used with permission from reference [113].

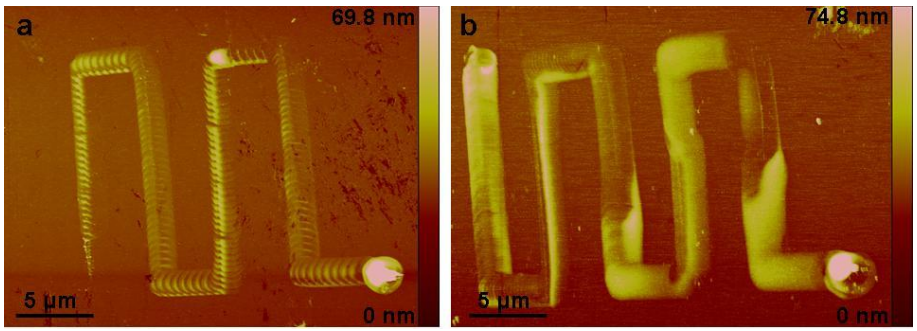

Figure 4.30: AFM images of lines written at two tip speeds (a) 20 µm/s and (b) 10 µm/s, written by a 150 nm nanopipette in contact mode with a setpoint of 0.12 V. The lines written with the faster tip speed show a rippled surface indicating that the tip had a somewhat juddery motion during the writing.

with each line segment being performed after giving separate instructions. Dots or blobs at the start and/or end of a nanowriting pattern were observed far more frequently than successful written lines, but still not on every occasion. The reason for this was not clear.

As expected, the size of the aperture of the pipette influenced the size of lines written with it. Tentative quantitative comparison may be made with awareness of the relevant uncertainties. Importantly, the variation between pipette tips has not been quantified. Nanopipettes are purchased from Nanonics Ltd. and are just given as '100 nm' or '150 nm' with no uncertainty quoted. Older tips from Nanonics Ltd. are perhaps more honest while being less precise, being labelled as '>100 nm', for example. Thus there is no assurance that a 50 nm pipette has an aperture of half the diameter of a 100 nm pipette or even that another 100 nm pipette is the same as the first. The second difficulty in quantifying the relation between pipette aperture size and written line size is the variation in lines written by a given pipette, with the same writing parameters or even within a single writing pattern. Some lines are very dotty, some are consistent for a length and then suddenly stop or diminish for a period, while some are consistent throughout. The cross-sectional shape of lines is also inconsistent and not well understood. It therefore is not clear whether FWHM or the full width at the base is a better measurement. With these unquantified uncertainties in mind, Table 4.1 presents a comparison of a 100 nm and a 150 nm pipette. These

Table 4.1: Dependence of written line height and width on nanopipette aperture size. These measurements were taken on lines written at 5 µm/s with a setpoint of 0.12 V.

Pipette size / nm	Height / nm	Width at base / µm	FWHM / µm
100	15.4	0.56	0.28
150	7.7	1.08	0.77

pipettes were taken to the SEM for accurate analysis of their aperture size but this was unsuccessful due to trapped air expanding, as already described. Writing was also attempted with nanopipettes with an aperture of 50 nm but it was found that without voltage assistance no writing occurred.

The use of voltage to control the deposition has appeal because it would allow the same tip to be used to image an area and then go to the desired place within that area and write a line with very high precision. In addition it could be possible to achieve smaller features by using a smaller pipette than is necessary for writing without voltage. There is the possibility that voltage might help the SWNTs within the dispersion to reach the tip of the pipette with enough alignment to come out instead of causing a blockage. Voltage-controlled writing was performed on the sample shown in Figure 4.31, controlled within the writing script through the Nanonics controller boxes. The voltage applied to the substrate switched between positive and negative four times in each vertical line, at the magnitude indicated. It can clearly be seen in this figure that the quantity of material deposited increased between ±3 V and ±10 V. At the higher voltages, from ±8 V and higher, the dispersion was seen to spurt out of the pipette in big blobs during writing. This gave very little spatial control and precision. In addition, when smaller voltages were used after the high voltages significant deposition was seen (Figure 4.31 area 29), which indicates that the tip aperture was damaged and larger than it was originally. From this experiment and others it was concluded that voltages no higher than ±5 V should be applied.

An example of voltage being used to control the writing is shown in Figure 4.32. This is area 8 from Figure 4.31, written with a voltage of ±3 V. Writing occurred when −3 V was applied to the substrate but did not occur when +3 V

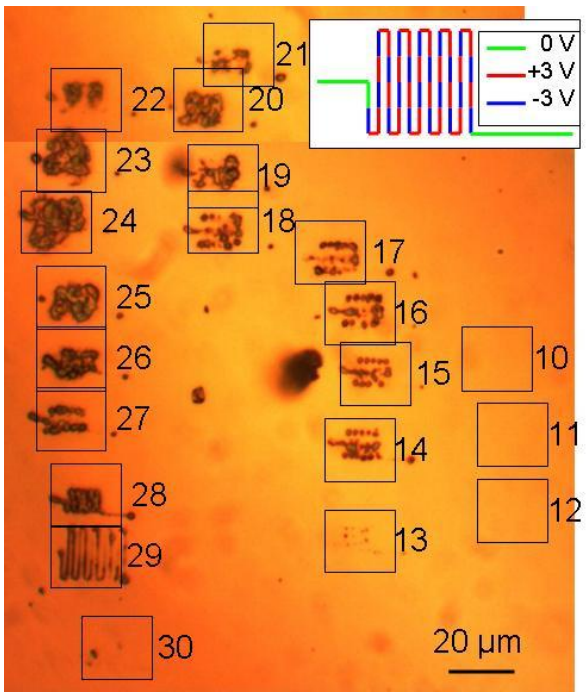

Area	Bias / V
1,2,3	0.5
4,5,6	1
7,8,9	2
10,11,12	3
13,14,15	4
16,17,18	5
19,20,21,22	8
23,24,25	10
26	4
27	3
28	2
29	1
30	0.5

Figure 4.31: Optical microscope image of writing performed with different voltages, as indicated in the table. The inset shows how the voltage is applied throughout the snake pattern. Areas 1–9 are not shown because no writing was visible. There is a steady increase in deposition going from areas 10–12 at ±3 V to areas 23–25 at ±10 V. This writing was performed in contact mode at a setpoint of 0.13 V with a 50 nm pipette at a tip speed of 5 µm/s.

was applied. When voltage was applied in this way the effect could be driven by electrophoresis and/or electroosmosis, depending on the system. In this case the SWNTs had a net negative charge due to the negatively charged surfactant molecules so if electrophoresis was the dominant force then writing would occur when the substrate was positively charged. The observations here are consistent with electroosmosis, which is caused by the quartz walls of the pipette becoming negatively charged and leaving the bulk solution with a net positive charge so that it is then pulled out by the negative bias on the substrate. Very good switching between on and off states was revealed when this sample was examined with AFM after the writing had been performed. Since the lines created during the 'on' state were too small to be visualised in the optical microscope, it was not known at the time that this voltage was best. As Figure 4.31 shows, larger voltages were subsequently used, eventually irreversibly damaging the nanopipette. This illustrates a recurring problem in the quest for control of small, precise writing

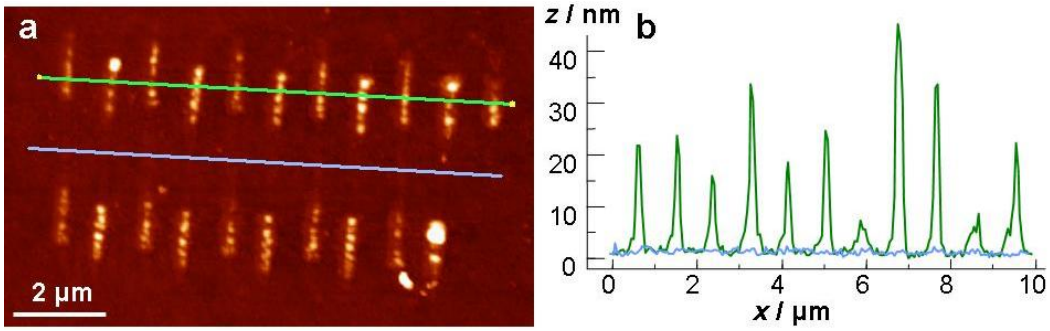

Figure 4.32: (a) AFM image and (b) cross-section of a pattern drawn with the voltage applied to the substrate alternating between +3 V and −3 V. The writing was switched 'off' when a postive voltage was applied to the substrate and it was switched 'on' when the substrate was given a negative bias. This writing was performed in contact mode at setpoint 0.13 V with a 50 nm pipette.

when only optical microscopy is available *in situ* for the evaluation of the deposition. If a dual-probe AFM system was available then a probe AFM tip, installed beside the nanopipette, could immediately scan the writing, allowing a systematic search for optimal parameters for the creation of small features.

Further experiments with application of voltage with the Nanonics system in Jerusalem similarly showed some promise for control of writing but did not produce conclusions about the optimum voltage and parameters. The more complicated Keithley sourcemeter system in Edinburgh brought additional challenges. In particular the lack of synchronisation between script and voltage meant that ambiguity remains about which voltage is applied at what stage in the writing. An example is shown in Figure 4.33, where the red and blue lines representing positive and negative voltage are added as a tentative guide. The rapid changing at 4 Hz resulted in a pulsing of the dispersion, forming a line consisting of overlapping circular blobs. With the slower switching at 0.5 Hz some correlation can be proposed. It may be noted that the lateral dimensions as measured in the Veeco Nanoman VS are approximately 30% smaller than the dimensions of the pattern written by the Nanonics MV1000. This discrepancy could be caused by friction between the static nanopipette and the moving substrate inhibiting the motion of the substrate, slowing down the true lateral speed of the substrate with respect to the tip. Lateral speed was, however, not found to be an important factor in determining whether or not material was

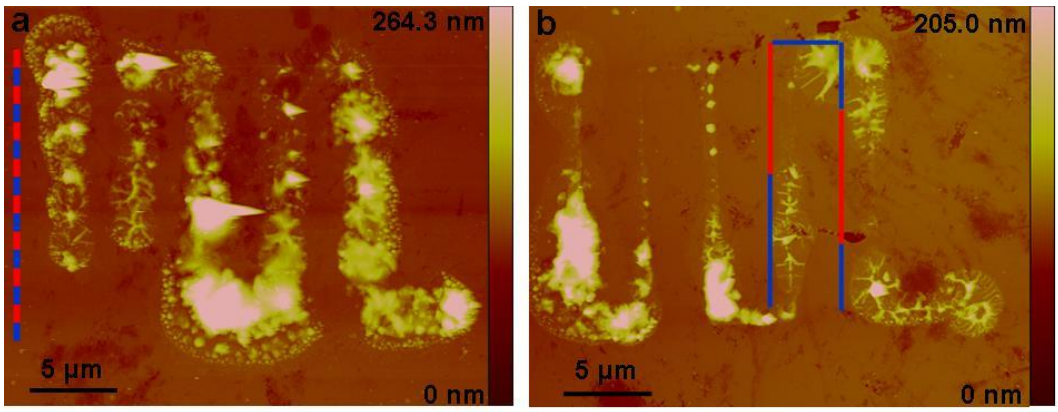

Figure 4.33: AFM images of writing performed with voltage control provided by a Keithley sourcemeter, operating at (a) 4 V at 4 Hz and (b) 3 V at 0.5 Hz. The red and blue lines represent the application of positive and negative bias to the substrate, respectively. The length of these lines approximately represents the length of line written before the bias changed. The positioning of lines is a tentative suggestion to aid interpretation of the results. The writing here was performed with a 100 nm pipette, in contact mode with a setpoint of 0.12 V.

deposited, over a large range of speeds (1, 2.5, 5, 10, 50 and 100 µm/s). When material was deposited, neither extremes of this range were found to be good, so changing the speeds by 30% would still cover a range at which writing could be performed. Thus, this discrepancy does not have a significant impact on the results of nanowriting experiments.

Although Figure 4.33 indicates that the setup developed in Edinburgh for application of voltage was functional, the voltage control was not reliable. Subsequently patterns were written with the same pipette with higher voltages, even up to 10 V, and no deposition was observed. Therefore the use of voltage did not increase the repeatability of nanowriting occurring or not.

As shown so far, nanowriting with SWNT dispersion inside a tapered cantilevered nanopipette can be performed in both tapping and contact mode, at different tip speeds, with different tip sizes and both with and without application of a bias voltage between the substrate and the dispersion inside the pipette. In the best case, small lines were completely switched off with one voltage and on with another. Repeatability remained a challenge throughout these experiments however. The number of patterns creating consistent lines was dwarfed by the number of attempts in which no material at all was deposited from the

nanopipette. Occasions where there was a single drop at either the start or the end but nothing in between were also relatively common. Although different parameters were experimented with, repeatability was not found to improve.

A number of reasons could explain the repeatability problems. It should be remembered that the same technique has been shown to work for deposition of other materials by Lewis and co-workers [78, 87–89]. One factor could be the relative humidity. This would influence the formation of a water meniscus between the tip and the surface. The humidity was not controlled during any of the experiments reported here. On the occasions that it was measured it was always found to be between 30% RH and 40% RH (for a temperature range of 21–25 °C), which is comparatively low for nanowriting experiments. It could also be the case that the SWNTs inside the nanopipette form blockages, preventing the dispersion from flowing out. If the SWNTs are well dispersed, then as long as they are aligned for exiting the nanopipette lengthwise then there should be no problem. If, however, the SWNTs form bundles or tangles then there is the possibility that they would become wedged within the tapered part of the nanopipette. In addition, despite attempts to provide a clean environment for this work there is the possibility of nanometric contaminants being introduced at any stage. In other nanowriting experiments [94] a fine filter (for example 20 nm) was used on the solution before the nanopipette was filled but this approach is not suitable for SWNTs due to their high aspect ratio.

As already mentioned, it is believed that the exact tip shape is critical for successful nanowriting. The tip shape could not be controlled in the experiments here since the nanopipettes were purchased from a commercial source. The angle that the tip makes with the surface was observed to have an effect on the writing. Figure 4.34 shows lines that were written only when the pipette was moving in one direction and no deposition at all when the pipette motion was in the opposite direction. This is most likely caused by the nanopipette not being exactly normal to the surface. This could not be controlled in the earlier work such as the example shown, where the nanopipette was held in place by the magnetic holder, since the angle was set during manufacture. In later work, with the customised rigid pipette holder a lot of care was taken in the orientation of the pipette before the

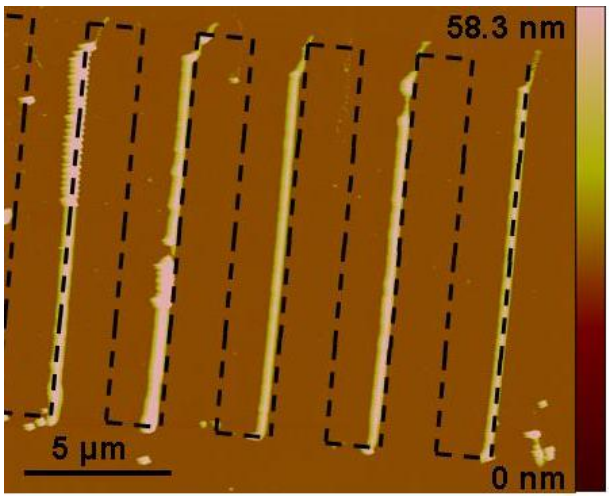

Figure 4.34: AFM image of lines written in tapping mode with a setpoint of 75% at 5µm/s with a 150 nm nanopipette. The complete tip path is indicated by the black dashed line. The writing only occurred when the pipette was moving in one direction and not in the other direction.

UV-setting glue was cured. The orientation of the pipette in the holder controlled the angle in one direction, but the angle in the other direction was dictated by the bend in the pipette, set during manufacture. As with the tip sizes, it was hoped that the bend was set with accuracy and precision but no quantitative information was provided with the tips.

Finally, more understanding is needed about the different surface interactions present in the system and how that affects the deposition. The substrates used in all the experiments detailed above had a SiO_2 surface chemically functionalised with APTES. This functionalisation alters the hydrophilicity in comparison with clean SiO_2. The dispersion within the pipette has surfactant present to keep the SWNTs debundled. Since the concentration of surfactant is below the critical micelle concentration, the surfactant molecules should mostly be on the SWNTs, but there will inevitably be some on the surface of the water, affecting its surface tension. The pipettes are made of quartz with the outside coated with gold. It is not known exactly where the gold coating stops in relation to the pipette aperture. The hydrophobicity or hydrophilicity of the different surfaces – substrate, pipette inner and outer walls – and the properties of the dispersion are likely to be critical to the quality of nanowriting. Computational modelling might be helpful

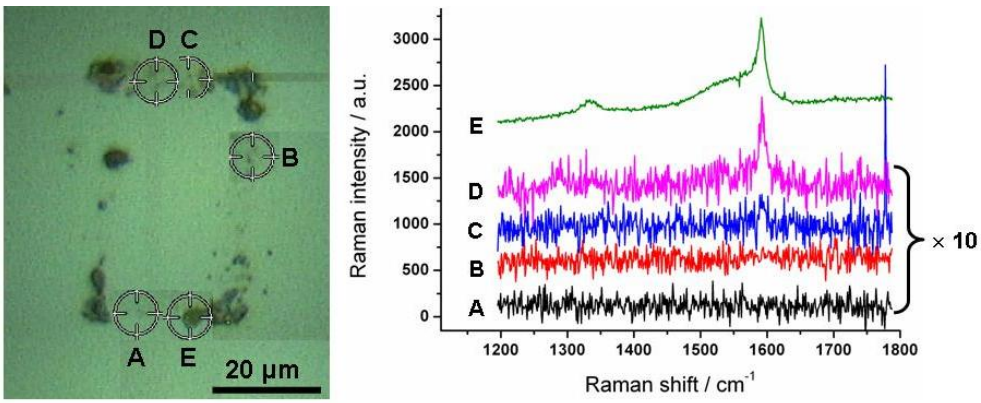

Figure 4.35: Optical microscope picture and corresponding Raman spectra taken with 514 nm laser at different positions on a pattern made by FNP with a CNT-containing ink. Spectra are y–offset for clarity. Point E has a very strong CNT signal and C and D have small hints of CNT signals, while A and B show no evidence of CNTs.

to investigate this, as has been performed for other nanowriting setups [102, 110] but has not been applied to this type of nanopipette.

4.3.2 Deposition of CNTs

While optical microscopy and AFM have been used to test if nanowriting has resulted in material being deposited on the surface, the SWNT content of the deposition was tested with Raman spectroscopy. Successful cases of FPN writing were subject to Raman spectroscopy with either or both 514 nm and 785 nm lasers to check for the characteristic spectral features arising from CNTs, in particular the D and G bands, located around 1300 cm^{-1} and just below 1600 cm^{-1}, respectively.

Of the successful examples of nanowriting, some showed that they contained CNTs while others showed no Raman CNT signal at all. In some cases CNTs were only found to be present in some specific spots, generally where there was a large blob of material rather than during a smooth line. For example, Figure 4.35 shows the results of Raman spectra taken at various points on the same area of writing. One of the five spots measured shows a very large quantity of CNTs while two other positions had a very weak signal and two had none.

The areas shown in Figures 4.35 and Figure 4.25a contain some CNTs while

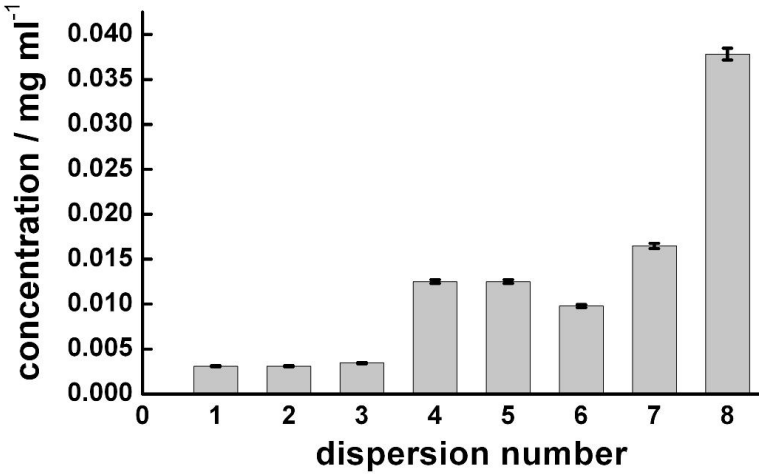

Figure 4.36: Concentrations of dispersions used for FPN writing experiments, measured by Raman spectroscopy.

the writing in Figure 4.34 appeared, from Raman spectroscopy, to be void of CNTs. The concentration of SWNTs in the dispersions was not measured in these examples. The dispersions were made according to the standard procedure, as described in Section 4.2.1, but variations in the dispersion age and the number of times it was repeatedly ultrasonicated mean that the final concentration was not accurately predictable.

For later experiments the dispersion concentrations were measured as described in Section 4.2.2. The concentrations are shown in Figure 4.36. Dispersions 1–3 have a SWNT concentration of approximately 0.003 mg/ml. Assuming an average SWNT length of 0.5 μm, each SWNT will have approximately 50000 carbon atoms and therefore a mass of 1×10^{-15} mg. The concentration of SWNTs in the dispersion is therefore approximately 4×10^{13} SWNT/ml.

One may crudely estimate the volume of dispersion deposited and therefore the expected density of SWNTs in the written lines. Taking the deposited line to have a diameter equal to the diameter of the nanopipette aperture and a semi-cylindrical shape, then a 100 nm nanopipette would write lines with a cross section of $\pi \times (50\text{ nm})^2$, which is 7.9×10^3 nm^2 or 7.9×10^{-21} m^2. Each micron of such a written line would then have a volume of $(1 \times 10^{-6}) \times (7.9 \times 10^{-21})$ m^3 or 7.9×10^{-15} ml. For a dispersion of 0.003 mg/ml (41×10^{13} SWNT/ml), the expected number of SWNTs per micron of line becomes 0.024 SWNT/μm. This

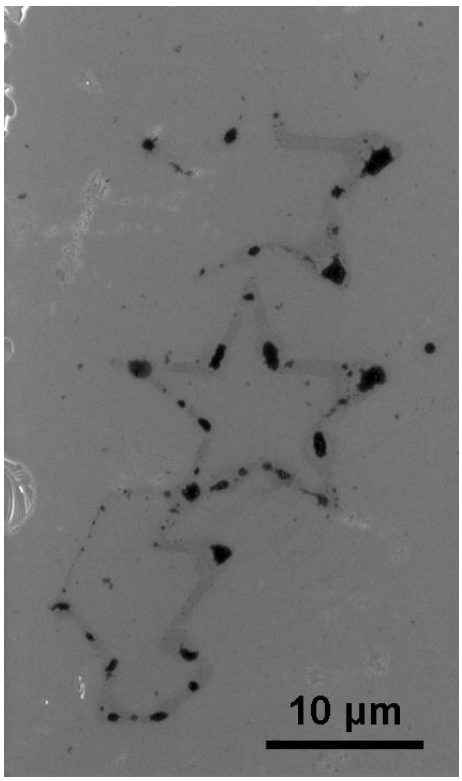

Figure 4.37: SEM image of stars and an outline of Scotland written by nanopipette with a dispersion SWNT concentration of 0.003 mg/ml. The patterns were drawn with a 100 nm pipette, at 5 µm/s in contact mode with a setpoint of 0.12 V.

equates to 1 SWNT per 40 µm

The lines shown in Figure 4.28 and the patterns shown in Figure 4.37 were drawn with dispersion numbers 2 and 3 respectively, thus with concentrations of approximately 0.003 mg/ml. When Raman spectroscopy was performed on them there was no detectable CNT signal.

Efforts were made to increase the concentration of SWNTs in the dispersions, for example, by starting with a greater mass of SWNT or performing ultrasonication for a longer time. As shown in Figure 4.36, the concentration was increased at most by just over a factor of ten, to 0.038 mg/ml. The expected SWNT density from that dispersion would be 0.30 SWNT/µm. However Raman spectroscopy again did not give any evidence of SWNTs. Dispersants that gave a higher concentration of SWNTs but perhaps also a higher degree of bundling were tried in a small number of experiments. In these cases some CNT signal was observed at large blobs, for example at the end of patterns, but still no CNT signal was

observable in lines written by the pipette.

It should be remembered that Raman spectroscopy on SWNTs (in the absence of any plasmonic enhancement) is reliant on the SWNT being in resonance with the excitation laser. The nanotubes used for this work had not been sorted by chirality or any other factor, so it is expected that the dispersions contained a large mixture of SWNTs, only some of which would be resonant with any given excitation wavelength. Therefore with only at most a 30% probability of any SWNT being in the 1 μm laser spot and a lower probability of that SWNT being resonant with the laser, it is unsurprising that in most cases no CNT signal was observed from Raman measurements taken on written lines.

Talia Yeshua has recently performed similar experiments with a Nanonics MV1000 system and a CNT dispersion [114]. The dispersion she used was provided to her from collaborators at Karlsruhe Institute of Technology, Germany, and while the details of the dispersant are unknown, it is believed that polymers are used. The CNTs were length-sorted. Successful writing has been performed at least once with this dispersion onto a clean SiO_2 surface and Raman spectroscopy revealed a CNT signal.

The SWNT dispersion used for this type of nanowriting thus appears to be a critical factor. As already discussed in the previous section, a good understanding of the surface properties of the dispersion would help achieve reliable writing. In addition, it may now be said that the concentration and extent of debundling is also important for getting successful deposition of not just the bulk solution but the SWNTs themselves.

4.3.3 Alignment of deposited CNTs

In one sample that showed a strong Raman CNT signal, indicating that a significant quantity of SWNTs was deposited through the nanopipette, Raman polarisation studies were performed to explore the levels of alignment of SWNTs within the written pattern of lines. The experimental setup for polarised Raman measurements is described in Section 3.1.2 and the theoretical basis is described in the 'Polarisation analysis' part of Section 2.2.1.2. The results presented here

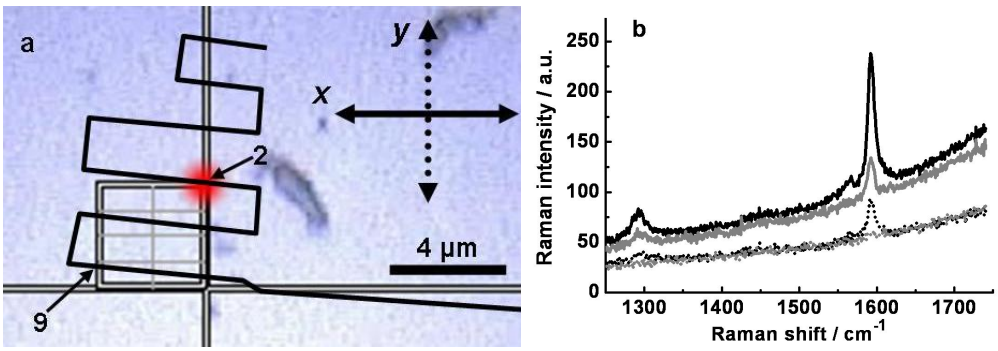

Figure 4.38: Polarised Raman spectroscopy of CNTs within a line written by a nanofountain pen. (a) Optical microscope image showing a measurement grid, the line of nanowriting (black line) and the approximate laser spot size (red spot at position 2), and (b) selected associated Raman spectra. Solid lines: x polarisation; dotted lines: y polarisation; black: grid point 2; grey: grid point 9.

have been published in reference [115].

The first polarisation study was with the sample positioned in the Raman spectrometer with the majority of the written lines orientated approximately in the x direction. A grid over the lines was drawn and Raman measurements were taken at each point (Figure 4.38a). The Raman measurements were made in the parallel configuration, that is, measuring only the light scattered with the same polarisation direction as the incident light, and at each point a spectrum was taken with x-polarised light and y-polarised light. Selected spectra from these measurements are shown in Figure 4.38b, which clearly shows that the measurements taken with polarisation direction approximately parallel to the nanowriting line give a stronger Raman CNT signal than measurements taken with polarisation perpendicular to that. This was an indication that the SWNTs were somewhat aligned within the written line and further study was worthwhile.

A point on the long portion of the written line was chosen and the sample was positioned in the Raman spectrometer with this part of the line exactly aligned in the x direction. Raman spectra were then taken over a 180° range of polarisations. The method described in Section 3.1.2 was used to extract the parallel and perpendicular components of the scattered light at each angle and correct them for instrumental factors by calibration with calcium fluoride. The parallel intensities obtained are plotted in Figure 4.40, where θ is the angle

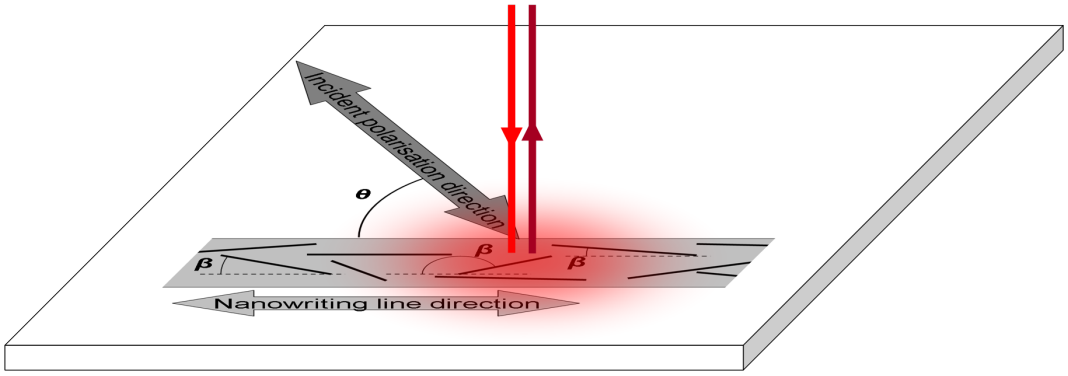

Figure 4.39: Schematic of angles relevant for SWNT alignment studies.

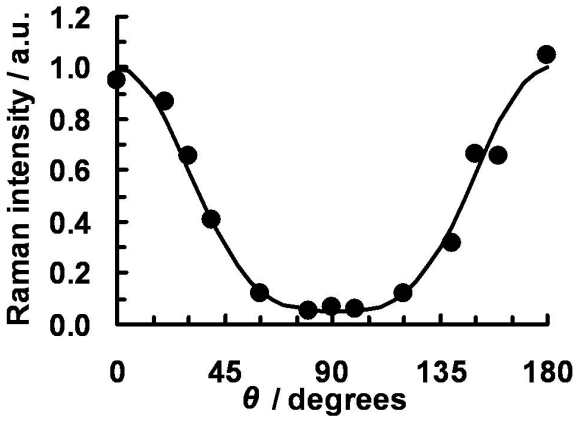

Figure 4.40: Raman intensities measured in the parallel polarisation regime as function of the angle of the incident laser polarisation direction. The solid line represents a fit based on Equation 4.4.

between the polarisation direction of the incident laser light and the x direction or, equivalently, the angle between the polarisation direction and the written line direction (Figure 4.39).

To obtain quantitative information about the distribution of orientations of SWNTs in the deposited line, the analysis method of Liu and Kumar [51], described fully by Perez *et al.* [52], was applied. This method is based on the angle-dependent Raman scattering intensity expected from a SWNT, defined in Equations 2.20 and 2.21. Related expressions may be formulated for a SWNT within an anisotropic medium, such as an aligned SWNT–polymer composite or, in this case, a nanowritten line, where α and β are the Euler angles for the SWNT orientation with respect the direction of the written line (Figure 4.39). Note that

no dependence on α is expected since the SWNTs are all assumed to be lying on the plane. For parallel polarisations of incident and scattered light, the intensity is:

$$I^{VV} \propto [\cos\beta\cos\theta - \sin\beta\sin\theta\cos\alpha]^4, \tag{4.2}$$

and for crossed or perpendicular polarisations of incident and scattered light, the intensity is:

$$I^{VH} \propto [\cos\beta\cos\theta - \sin\beta\sin\theta\cos\alpha]^2[\cos\beta\sin\theta + \sin\beta\cos\theta\cos\alpha]^2. \tag{4.3}$$

In the written line, multiple SWNTs are present, each with a different β. The measured intensity is therefore a result of the sum over all SWNTs within the laser spot. Experimentally measured intensities for parallel polarisations at a range of θ can be plotted and a least-squares fit of the following expression may be applied:

$$\frac{I_\parallel(\theta)}{I_\parallel(\theta = 0°)} \propto \frac{\langle P_4(\cos\beta)\rangle[\cos^4\theta + \frac{6}{7}\cos^2\theta + \frac{3}{35}] + \langle P_2(\cos\beta)\rangle[\frac{6}{7}\cos^2\theta + \frac{2}{7}] + \frac{1}{5}}{\langle P_4(\cos\beta)\rangle\frac{8}{35} + \langle P_2(\cos\beta)\rangle\frac{4}{7} + \frac{1}{5}}, \tag{4.4}$$

using the the order parameters $\langle P_2(\cos\beta)\rangle$ and $\langle P_3(\cos\beta)\rangle$ as fitting parameters, as shown in Figure 4.40.

The averaged Legendre polynomial, $\langle P_2(\cos\beta)\rangle$, is sometimes known as Herman's orientation parameter [52]. In completely random arrangements $\langle P_2(\cos\beta)\rangle$ would have a value of 0, while in a system in which every SWNT was perfectly aligned with the line direction its value would be 1. In the data given in Figure 4.40, the value of Herman's parameter from the least-squares fit is 0.76.

Further information about the alignment of the SWNTs in the deposited line can be obtained by applying the principle of maximum information entropy to define an orientation distribution function (ODF), as discussed by Perez *et al.* [52]. In general, the probability of finding a particle with orientations between

angles (α, β, γ) and $(\alpha + \mathrm{d}\alpha, \beta + \mathrm{d}\beta, \gamma + \mathrm{d}\gamma)$ can be described by:

$$\int_{\gamma=0}^{\gamma=2\pi} \int_{\alpha=0}^{\alpha=2\pi} \int_{\beta=0}^{\beta=\pi} f(\alpha, \beta, \gamma) \sin\beta \, \mathrm{d}\beta \, \mathrm{d}\alpha \, \mathrm{d}\gamma = 1, \tag{4.5}$$

where $f(\alpha, \beta, \gamma)$ is the ODF and α, β and γ are the Euler angles. In the current system α may be disregarded as all of the SWNTs may be considered to be lying on the plane of the surface, in a two-dimensional arrangement. In addition, the cylindrical symmetry of SWNTs removes any dependence on γ. The ODF can then be written in an alternative form:

$$f(\beta) = A \exp[-(\lambda_2 P_2(\cos\beta)) + (\lambda_4 P_4(\cos\beta))], \tag{4.6}$$

where A is a constant and parameters λ_2 and λ_4 are Lagrange multipliers. The ODF is then known once these three parameters are found, which can be done by numerically solving the following set of equations:

$$4\pi^2 \int_{\beta=0}^{\beta=\pi} f(\beta) \sin\beta \, \mathrm{d}\beta = 1, \tag{4.7}$$

$$4\pi^2 \int_{\beta=0}^{\beta=\pi} P_2(\cos\beta) f(\beta) \sin\beta \, \mathrm{d}\beta = \langle P_2(\cos\beta) \rangle, \tag{4.8}$$

$$4\pi^2 \int_{\beta=0}^{\beta=\pi} P_4(\cos\beta) f(\beta) \sin\beta \, \mathrm{d}\beta = \langle P_4(\cos\beta) \rangle, \tag{4.9}$$

where $P_2(\cos\beta)$ and $P_4(\cos\beta)$ are Legendre polynomials of order 2 and 4, respectively. The trapezoidal rule was used to solve these equations to obtain A, λ_2 and λ_4 by least-squares fit to the values of $\langle P_2(\cos\beta) \rangle$ and $\langle P_4(\cos\beta) \rangle$ found earlier from fitting the experimental data with Equation 4.4. The values obtained were: $A = 0.0017$, $\lambda_2 = -0.91$ and $\lambda_4 = -4.8$. The ODF could then be plotted (Figure 4.41a) and used to create a histogram of probability of SWNT orientations within the deposited line (Figure 4.41b). From the ODF it can be calculated that the percentage of SWNTs lying within 30° of the direction of the written line is 98%.

The experimental results from the perpendicular polarisation configuration

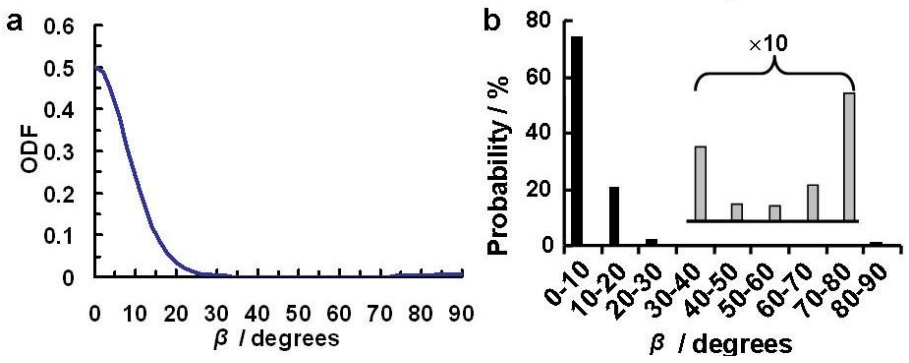

Figure 4.41: (a) ODF, from Equation 4.6, and (b) histogram of probability of SWNT orientation, based on the data shown in Figure 4.40.

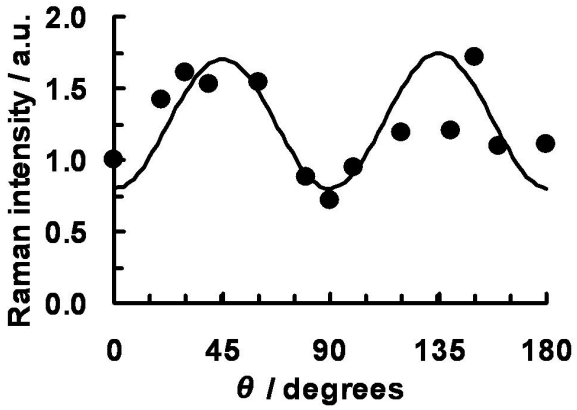

Figure 4.42: Raman intensities measured in the perpendicular polarisation regime as function of the angle of the incident laser polarisation direction. The solid line represents a fit based on Equation 4.10.

were treated in a similar way, using the following equation:

$$\frac{I_\perp(\theta)}{I_\perp(\theta=0°)} \propto \frac{\langle P_4(\cos\beta)\rangle[-\cos^4\theta+\cos^2\theta-\frac{4}{35}]+\langle P_2(\cos\beta)\rangle\frac{1}{21}+\frac{1}{15}}{-\langle P_4(\cos\beta)\rangle\frac{4}{35}+\langle P_2(\cos\beta)\rangle\frac{1}{21}+\frac{1}{15}}, \quad (4.10)$$

which is analogous to Equation 4.4. This equation was fitted to the data to obtain $\langle P_2(\cos\beta)\rangle$ and $\langle P_4(\cos\beta)\rangle$ by a least-squares method (Figure 4.42), then those values were used in Equations 4.7, 4.8 and 4.9 to obtain the ODF. The order parameters $\langle P_2(\cos\beta)\rangle$ and $\langle P_4(\cos\beta)\rangle$ were determined to be 0.7 and 0.3 respectively, giving ODF parameters of $A = 0.0015$, $\lambda_2 = -5.2$ and $\lambda_4 = 0$. Thus, according to these measurements, the percentage of SWNTs lying within 30° of the direction of the written line was 86%.

Table 4.2: Aligment data from repeated polarised Raman measurements showing consistency in SWNT alignment within a line written by FPN.

Measurement	$\langle P_2(\cos\beta)\rangle^a$	$\langle P_4(\cos\beta)\rangle^a$	A^b	${\lambda_2}^b$	${\lambda_4}^b$	Abundance of of SWNT within $-30° < \beta < 30°$
$1_{\parallel}$	0.76	0.70	0.0017	−0.91	−4.8	98%
$1_{\perp}$	0.7	0.3	0.0015	−5.2	0.96	86%
$2_{\parallel}$	0.68	0.24	0.00095	−6.2	1.8	82%
$2_{\perp}$	0.67	0.37	0.0042	−2.8	−0.73	90%
$3_{\parallel}$	0.68	0.42	0.0044	−2.5	−1.2	92%
$3_{\perp}$	0.58	0.32	0.0061	−2.2	−0.84	86%
$4_{\parallel}$	0.32	0.24	0.0098	−0.94	−1.3	76%
$4_{\perp}$	0.56	0.13	0.0040	−3.6	1.0	74%
$5_{\parallel}$	0.4	0.6	0.0059	−1.8	−1.5	90%
$5_{\perp}$	0.6	0.2	0.0040	−3.5	0.55	80%
					Average[c]	$85 \pm 15\%$

[a] As defined in Equations 4.4 and 4.10 for parallel and perpendicular measurements, respectively.
[b] As defined in Equation 4.6.
[c] Uncertainty represents a 95% confidence interval.

The polarised Raman measurements were repeated four more times and the results treated as described in each case. Table 4.2 gives the ODF parameters obtained from each experiment. It is clear from the repeated experiments that there is a high degree of alignment afforded to the SWNTs deposited by FPN.

After the polarised Raman measurements described above, the sample was rinsed in water: 40 hours of immersion in a water bath at room temperature with no agitation, followed by 20 hours at 50 °C with gentle stirring. AFM scanning revealed an 80% decrease in the height of the lines, while the width was unchanged. High-resolution SEM was then able to show bundles of SWNTs inside the written lines (Figure 4.43), with some surfactant still present. The alignment of the SWNTs visible in the SEM images is concurrent with the alignment results from the polarised Raman spectroscopy.

Initial indications of alignment have been seen in SWNTs written through a Nanonics nanofountain pen by Talia Yeshua recently [114]. Alignment was seen when writing was performed with no applied electric field, as was the case for the sample presented here. Writing was also performed by Talia with an electric field, in which case more material flowed from the tip into larger puddles and no

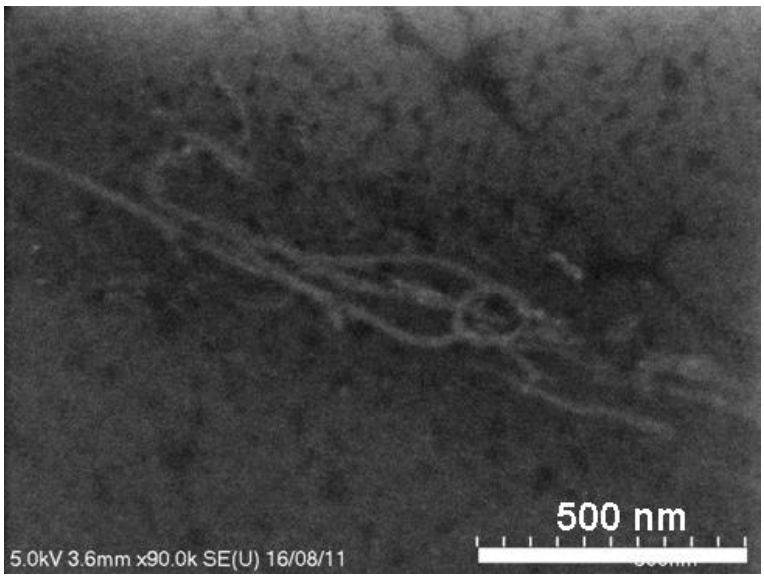

Figure 4.43: High resolution SEM image showing SWNTs mostly aligned with the direction of the line, which can be identified as a darker shadow running from bottom-right to top-left.

alignment was observed.

The alignment of SWNTs occurring during nanowriting can be attributed to the large aspect ratio of the SWNTs and how their size compares to the pipette aperture. While their diameter (∼1 nm) is much thinner than the pipette aperture (∼100 nm), their length (∼1 μm) is larger. Therefore SWNTs must exit the nanopipette with one end first. When the SWNT comes into contact with the surface it forms strong interactions with the surface, particularly when a functionalised surface is used, and then the pipette draws the nanotubes along in the direction of writing as they leave the tip (Figure 4.44).

4.4 Conclusions

This Chapter has described the development of fountain pen nanolithography for the deposition of carbon nanotubes with high spatial precision and with alignment.

This work is a natural progression from prior nanowriting developments, using pulled nanopipettes and modified AFM probes. Much of the work with such pens reported so far has concentrated on biological molecules being deposited in the

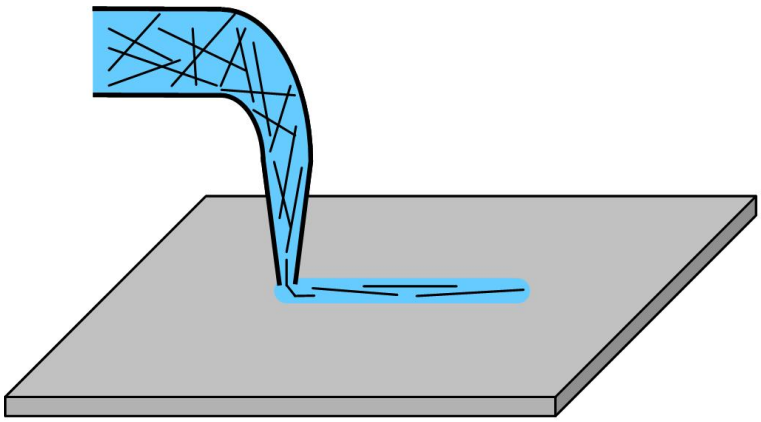

Figure 4.44: Schematic of the process giving alignment of SWNTs in FPN writing. Due to their high aspect ratio, SWNTs exit the nanopipette end-on, they stick to the surface and they are drawn out as the pipette moves along.

ink. In some cases gold nanoparticles have been deposited. Carbon nanotube dispersions have not been shown to be a possible ink until now.

The method presented here has used a cantilevered pulled quartz capillary as a nanopipette held within a Nanonics MV1000 AFM. The SWNT dispersion filled the nanopipette and writing occurred when the nanopipette came into contact with the sample surface, in this case a silicon wafer.

The AFM allowed control of many parameters during the writing process. Tapping and contact mode regimes were both used with success. Standard setpoints of 0.12 V and 80% for contact and tapping modes, respectively, could be used. Increasing the contact-mode setpoint to 0.3 V sometimes helped deposition to occur but risked damage to the tip as well as problems in achieving correct motion of the tip with respect to the surface. Altering the lateral speed of the tip through a range of 1–20 μm/s showed that lines of increased width were drawn at slower speeds. Above 20 μm/s no deposition was observed.

The size of the nanopipette aperture had some influence on the size of features written on the surface but uncertainties in the exact tip shape and size in each case made repeatability and quantification challenging.

Application of voltage between the nanopipette contents and the substrate allowed the deposition to be turned on and off with a substrate bias voltage of −3 V and +3 V, respectively. This is expected to be valuable for enabling

deposition onto features smaller than those visible in optical microscopes, since the nanopipette may first be used to image the surface with deposition switched 'off', locate the desired position and then selectively deposit material there with application of the correct 'on' voltage.

Raman spectroscopy was used to search for the presence of SWNTs in the lines drawn by FPN. In general a strong signal was observed where large spots of dispersion had been deposited but often no SWNT signal was observed within written lines. Measurements of the dispersion concentrations confirmed that the number of SWNTs within the volume of dispersion deposited was expected to be very low. Efforts to increase the SWNT concentration while using standard surfactants (SDBS and SDS) had limited success and did not produce an appreciable difference in the Raman spectra of written lines.

In one case where the measured density of SWNTs in the written line was high, extensive polarised Raman measurements revealed a high degree of alignment, with $85 \pm 15\%$ of SWNTs lying within 30° of the direction of the written line.

Different and improved carbon nanotube dispersions may prove to be key in achieving more consistent and reliable results with this method. This has been indicted by recent initial work with the same method by our collaborators. In addition, a better understanding of the surface interactions in the system, particularly between the solution and the substrate surface, would be of great benefit. Computational methods could be applied to model the interactions of the surfactant solution with the substrate and the nanopipette walls.

Although this technique has not yet been used for the deposition of SWNTs onto nanoantennas for the NANOSPEC project, it has the potential to do so. Since the nanoantennas are not visible in an optical microscope it would require the voltage switching method to be optimised and employed, or the writing to be done within a multi-probe system equipped with a closed-loop scanner, in which the area could first be scanned with a standard imaging AFM tip and then immediately be written on with the nanopipette, loaded as the second probe in the system. Our collaborators in Jerusalem have the necessary instrumentation to allow this.

Beyond the applications for the NANOSPEC project, this technique could

have other future applications in the research of carbon nanotubes. Since it does not rely on the electrical properties of the SWNT, it is believed to work equally well for both metallic and semiconducting SWNTs. Dispersions with sorted SWNTs could therefore be used, for example purely semiconducting or metallic or even chirality-selected SWNTs, and this would allow nanoelectrical systems to be created with semiconducting SWNTs forming transistors and conducting interconnects being written using metallic SWNTs.

Chapter 5

Nanomanipulation of Gold Nanoparticles for SERS of SWNTs

5.1 Literature survey

In the study of carbon nanotubes, Raman spectroscopy is invaluable, providing information about their diameter, conductivity and defectiveness [47]. Individual SWNTs may be measured by conventional Raman spectroscopy only if resonance occurs between the difference in electronic energy levels and the photon energy, that is, by resonance Raman spectroscopy (RRS). The use of surface-enhanced Raman spectroscopy (SERS) to study SWNTs promises benefits in enhancing the signal obtained and allowing non-resonant SWNTs to be detected. In return, the SWNT is an ideal test molecule for learning more about the SERS effect, in particular the interface between the nanostructure and the analyte [4]. The first work on SERS of CNTs was done in 1999 [116] and a number of other studies have been performed since.

5.1.1 SWNTs on bulk SERS substrates

Much of the work with SERS to date has been on so-called 'SERS active substrates', which are usually composed of rough silver or gold layers formed

by evaporation of metal or by drying of colloidal metal nanoparticles on silicon or quartz wafers. On these substrates the enhancement is greatest at hotspots, where the exact morphology of the metal is optimum. If SWNTs are deposited all over these substrates, they can give very strong enhancement and good spectra [116]. However, the fact that the surface comprises bulk coverage with some unpredictability in the formation of nanostructures makes it more difficult to systematically study the SERS effect. Similarly, the use of metal nanoparticles in solution phase can give good average enhancements and some useful measurements but it does not allow the detailed study of specific interactions on individual particles.

Having a single nanostructure interfaced with a single SWNT would be most useful for achieving a better understanding of the SERS effect, such as the nanostructure–SWNT interface. The nanometre-scale of these components makes this a significant challenge, not least because they are too small to visualise with optical microscopy.

5.1.2 Methods of interfacing SWNTs with specific metal nanostructures

When aiming to obtain specific nanostructure–SWNT configurations, often the SWNTs are grown first and then subsequently the plasmonic nanostructures are added. A number of methods has been used to add the plasmonic nanostructures, such as electrodeposition, electroless deposition and AFM nanomanipulation.

Electrodeposition is one of the most common methods used to add gold or silver nanoparticles to surface-supported SWNTs. In this method, after the SWNTs have been grown, a contact electrode is added to the substrate, by EBL or photolithography. The sample is then submersed in an aqueous solution containing the plasmonic metal. Altering the conditions such as solution concentration, deposition potential and time can allow control of the size of the nanoparticles. For example, gold nanoparticles on individual SWNTs have been reported with sizes ranging from 10 nm to 100 nm [117] or 10 nm to 120 nm [118] and silver nanoparticles on a network of SWNTs have been reported with sizes of 30 nm to

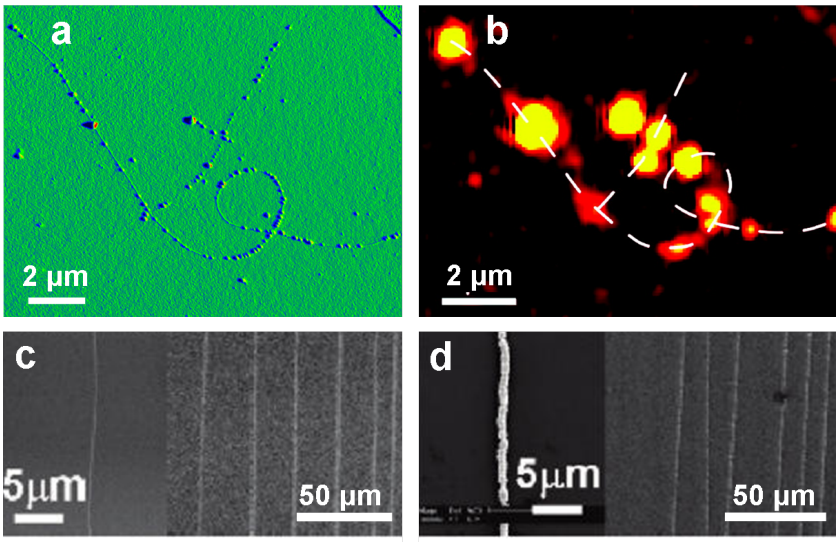

Figure 5.1: (a) AFM and (b) corresponding Raman G band intensity map of gold nanoparticles deposited on SWNTs by electrodeposition and SEM images (c) before and (d) after gold nanoparticles were added to SWNTs by electroless deposition. Parts a and b are adapted from reference [118] and parts c and d are adapted from [121].

150 nm [119, 120]. One disadvantage of this method, as well as the requirement for lithographic steps to create electrodes, is that the nanoparticles preferentially form on defect sites on the CNT. In addition, the nature of electrodeposition is such that the conductivity of the CNT also has some influence on the creation of nanoparticles [117]. An example is shown in Figure 5.1 a and b, where an AFM image reveals AuNPs along the length of a CNT, particularly at the ends, where defects occur.

A similar method which aims to address some of these disadvantages is electroless plating, as described by Chu *et al.* [121]. As in the case of electrodeposition, this method involves submersing a substrate holding SWNTs into a gold solution. In contrast, however, no electrodes are present, and it is instead the inherent electrical properties of the SWNT that causes the gold-containing ions to be reduced to gold metal on the SWNT surface, through a charge-transfer reaction. The method described by Chu *et al.* [121] involves a two-step process, of seed formation and subsequent growth, using two different gold solutions: first higher then lower concentrations of $HAuCl_4$ in ethanol/water. The density of nanoparticles as well as their size could be controlled by adjusting the times of

submersion in each solution. It was shown that every nanotube in the sample was equally decorated with nanoparticles, with no selectivity based on conductivity or defect sites (Figure 5.1 c and d) [121]. Electroless plating has also been shown for SWNTs in dispersion by Wang *et al.* with both gold and silver nanoparticles [122]. These SWNTs were used for biomedical imaging but, as mentioned above, they are not so useful for exploring the SERS effect while they are in solution phase because then the measurements are performed on bulk not on individual SWNTs.

A simpler method than electrochemical or electroless chemical methods is that used by Kumar *et al.* [123]. On a sample already containing carbon nanotubes and lithographic markers, a thin film of silver was deposited by an electron-beam metal evaporator. The film was too thin to allow continuous coverage so the silver formed islands over the surface. Although the carbon nanotubes were individual and lithographic markers allowed the same CNTs to be located before and after silver deposition, there was no consistency in the size, shape or position of the silver islands [123].

In contrast to the methods described already, which involve growing gold or silver nanoparticles directly onto the CNT from solution or gas phase, Tong *et al.* formed nanoparticles separately and then dropped the nanoparticles onto SWNTs lying on substrates. An AFM tip was then used to manipulate the nanoparticles around on the surface to explore the SERS effect at different nanoparticle–CNT separation distances [124].

5.1.3 SERS observations of SWNTs with metal nanostructures

Enhancement factors

The amount by which a signal is enhanced by SERS is important when comparing different configurations of SERS substrates or plasmonic antennas but there is a lack of clarity about how the enhancement factor is defined [68], as mentioned in Section 2.3. In some cases of SERS on CNTs, the without-enhancement signal was too low to measure so it could not be reliably compared to the enhanced

signal to give a value for the enhancement factor [121]. In other cases, where strong signals were obtained from SWNTs deposited onto a rough silver SERS substrate, the signal varied by several orders of magnitude at different positions on the same substrate so the enhancement factor, given as a ratio of the signal from a SERS substrate compared with the same SWNTs deposited on a Si or glass substrate, ranged from 5×10^4 to 1 [116]. For experiments comparing, as near as possible, the same SWNTs with and without nanoparticles, enhancements of 6.4–97 [121], 7.7–12.6 [122] and 5–14 [119] have been reported, with the ranges representing the dependence on laser wavelength. Scolari *et al.* [118] measured on a SWNT with a 70 nm gold nanoparticle and on a bare length of the same SWNT and the Raman intensities increased with the gold nanoparticle by factors of 16 or 37, depending on wavelength. They later described the Raman enhancement factors as 16000 and 37000, although no explanation is given for the additional factor of 1000. Tong *et al.* observed that the G^+ band signal measured on a SWNT at the NP is about three times stronger than the G^+ band of the same SWNT far from the NP, while the RBM of the same SWNT was invisible in non-enhanced Raman but became detectable when the NP was present. The spectra from a SWNT bundle with a NP at different distances was presented and again the signal appears to be approximately three times stronger when the NP is closest (15 nm) to the SWNT compared to when the NP is far (200 nm) from the SWNT [124].

SERS on surface-bound individual SWNTs is slightly different to SERS of molecular species because the location and orientation of the SWNT(s) can be well defined and measured by AFM or SEM. Instead of a consideration of how much of the area of the plasmonic metal structure is covered, it can become a question of how much of the SWNT experiences enhancement. For example, Assmus *et al.*, when describing electrodeposited AuNP–SWNTs, compare the Raman G band intensity on the same SWNT at and away from a single AuNP [117]. The measured intensity increase at the AuNP is a factor of four, however they write that the enhancement only occurs in a space of a few nanometres whereas the non-enhanced signal comes from the entire laser spot, some 500 nm across, so they reasoned that the local enhancement by the AuNP is ‘two or

three orders of magnitude'. They report other enhancement factors of between one and four orders of magnitude, measured and calculated in the same way [117]. Similarly, Scolari *et al.* claim the enhancement factors they give should be increased by at least one order of magnitude because the SERS active region only applies to a short length of the SWNT [118]. Kumar *et al.* also make the claim that the hotspot of high enhancement occurs in a small region, 25 nm, within their laser spot, 500 nm. They claim that this means the measured intensity ratio from the SWNT with and without silver nanoparticles should be multiplied by $[(25\text{ nm})^2/(500\text{ nm})^2] = 400$, that is, the ratio of the areas [123]. However, since there is only one SWNT in their laser spot and this is a one-dimensional object, it would be more appropriate to take the ratio of lengths of SWNT measured, that is (25 nm/500 nm), contrary to their claims.

Resonances

As expected from the theory of plasmonics, the enhancement observed from SERS substrates or plasmonic antennas depends on the wavelength of the excitation laser. An experimental study of this was performed by Chen *et al.* [119, 120] on SWNT networks onto which silver nanoparticles were grown by electro-deposition. A large number of SWNTs were present in the network so the resonance frequencies of the SWNTs cover a broad range. When the metal nanoparticles were formed on the SWNT network, they did so with a dependence on the distance from the contact electrode: near the electrode they formed smaller particles with high density, while further away from the electrode the particles were larger and more spaced out. Dark-field imaging showed that the colour of the particles depended on their distance from the electrode, going from green to red with increasing distance (Figure 5.2a), and dark-field spectroscopy showed resonance peaks at different positions from around 500 nm to just over 700 nm at different distances (Figure 5.2b). As shown in Figure 5.2c, Raman spectra were also measured at a range of distances, with different excitation laser wavelengths. The signal obtained from a green (514 nm) laser decreased with increasing distance from the electrode but the signal obtained from a red

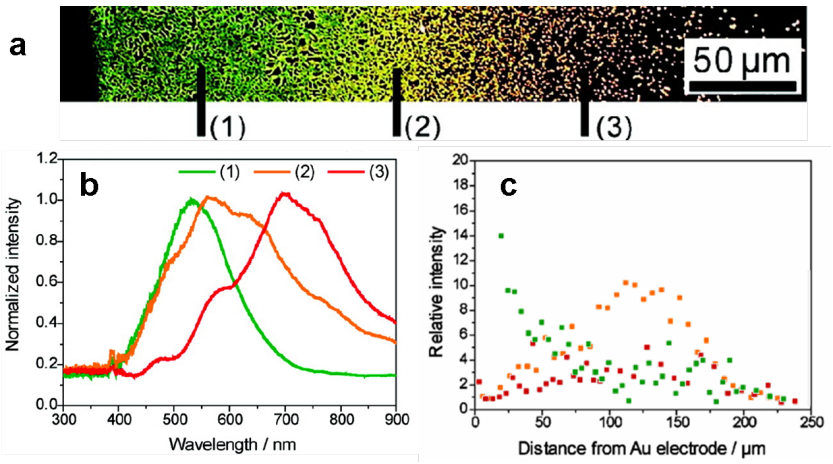

Figure 5.2: (a) Silver particles added to a network of SWNTs by electrodeposition, imaged by dark-field microscopy with the electrode on the left-hand side. (b) LSPR spectra at three points, showing how the resonance frequencies of the particles depend on the distance from the electrode. (c) The SWNT G band Raman intensity measured at various distances from the electrode, showing different behaviour for 514 nm excitation (green points), 633 nm excitation (orange points) and 785 nm excitation (red points). Adapted from reference [119].

(633 nm) laser increased to a maximum at 100 µm from the electrode then decreased with further distance. The distance dependence with a NIR (785 nm) laser was less pronounced, although a slight maximum was observed between 100 µm and 150 µm. These results clearly show that the strength of the Raman signal is dependent on the resonance between the excitation laser frequency and the plasmon resonance of the nanoparticles. The spectra obtained from these AgNP-decorated SWNT networks exhibit the same peaks with the same relative intensities as the SWNT networks without AgNPs, so it is believed that the signals observed arise from surface-enhanced resonance Raman scattering (SERRS) with no significant contribution from non-resonant SWNTs [119]. Enhancements are expected to be multiplicative [68] so SWNTs that are already resonant with the laser energy are likely to contribute more to measurements made on a large number of SWNTs.

Similar wavelength dependence was observed by Wang *et al.* [122]. The absorption spectrum of the AuNPs had a broad background with a very weak peak observed near 600 nm but that of the AgNPs had a very distinct peak

in the absorption spectrum at around 450 nm and the absorption decreased at longer wavelengths. When Raman spectra were taken of the SWNTs, those decorated with AuNPs had enhancement factors of approximately 7.7 and 12.6 for 633 nm and 785 nm excitation respectively. The SWNTs decorated with AgNPs showed a strong dependence on excitation, with an enhancement factor of 26.5 at 633 nm excitation dropping to approximately 8.7 for 785 nm excitation. Thus, the absorption spectrum was a good indicator of the plasmon resonances, upon which the SERS enhancement is strongly dependent [122]. As with the previously described work on SWNT networks, this study was performed on a large number of SWNTs, this time in aqueous dispersion.

Scolari *et al.* [118] studied one SWNT with four wavelengths of excitation laser, at the location of a 70 nm gold nanoparticle, at a 35 nm gold nanoparticle and at a region of pristine SWNT. On the pristine length of SWNT, the strongest signal was obtained with the 568 nm laser, showing the resonance of the SWNT. With this laser, the 70 nm AuNP increased the measured signal by 16 times. At an excitation wavelength of 647 nm, the non-enhanced SWNT Raman signal was weaker, since the SWNT was not in resonance with the laser but the intensity measured at the 70 nm AuNP was 37 times stronger than the non-enhanced, showing that the SERS effect was strongest at that wavelength. The strongest absolute intensity was, however, achieved at 568 nm. At shorter wavelengths, 488 nm and 514 nm, the smaller 35 nm AuNP gave more enhancement than the larger 70 nm AuNP but the enhancement was very small in all cases. Calculated absorption spectra, obtained from Mie theory, were presented for a range of AuNP sizes and showed that the larger particles had a broader resonance that reached as far as 647 nm, while the smallest particle had a sharper resonance closer to 500 nm. The enhancement factors for the 70 nm AuNP therefore correlate well with the presented theory, but the reason for the lack of enhancement from the smaller nanoparticle at shorter wavelength was not fully explained [118].

In their paper on electroless decoration of AuNPs on SWNTs, Chu *et al.* [121] emphasise that their method covers all SWNTs with AuNPs equally, regardless of metallicity, thus enabling the detection of every SWNT in a given sample. AFM and SEM images confirm that all the SWNTs present, horizontally aligned on a

quartz or silicon substrate, are decorated in the process. Before NP decoration, approximately one-third of the SWNTs exhibited a measurable G band in their Raman spectrum. Afterwards, every SWNT gave a measurable G band signal and some RBMs that were not detectable before gold decoration became visible. Semiconducting SWNTs were analysed with two lasers, one at which they were resonant (633 nm) and one at which they were not (785 nm). With the 785 nm laser, AuNP decoration resulted in RBMs appearing that had previously been invisible and the G band intensity went from weak to strong. With the 633 nm laser both RBM and G signals appeared stronger after AuNP decoration than before. Thus, enhancement was seen both in (SERRS) and out (SERS) of resonance. Enhancement factors were estimated at each laser wavelength, although they are lower than the true enhancement because they are based on a comparison of SERRS plus SERS signals to RRS signals, without taking into account non-enhanced non-resonant SWNTs. Average enhancements of 6.4, 54 and 97 were observed for laser wavelengths of 442 nm, 633 nm and 785 nm, respectively. This was compared to the absorption spectrum of the SWNT–AuNP composite, which shows the strongest absorption at 785 nm and decreasing absorption at 633 nm and 442 nm. The absorption spectrum had a sharp peak near 550 nm and a large broad peak near 900 nm, which correspond to the surface plasmon resonances of an individual particle and coupled adjacent particles, respectively, so the SERS enhancement observed at the longer wavelengths is caused primarily by coupled metal nanoparticles [121].

All of these reports show that the strongest signal is obtained when there is resonance between all three components: the excitation laser, the surface plasmon resonance of the metal nanoparticle and the SWNT electronic energy gap, but the enhancement from plasmonic metal structures alone can be sufficient to enable non-resonant SWNTs to be detected.

Polarisation effects

When performing SERS on SWNTs, not only must there be resonance in the frequencies of the laser, nanoparticle and carbon nanotube, there must be the

optimal orientation of the laser polarisation, the nanoparticle geometry and the SWNT axis, if the maximum signal is to be obtained [121].

Raman scattering of SWNTs is highly dependent on the polarisation direction of the incident laser. Both RBM and G modes exhibit a $\cos^2\theta$ dependence with the strongest signal achieved when the laser polarisation is parallel to the SWNT axis [49]. The signal from polarisation perpendicular to the SWNT can go to zero or close to zero depending on the symmetry of the SWNT. This has been described in Section 2.2.1.2.

Plasmonic nanostructures such as gold or silver nanoparticles affect the local electromagnetic field. If linearly polarised light is incident on a plasmonic nanostructure, the field close to the particle has contributions of other polarisations, according to theoretical predictions [68]. The combination of SERS with SWNTs gives a good experimental probe of how polarisation is affected by the plasmonic structure.

The maximum signal is expected to be achieved when the laser polarisation is parallel to the SWNT axis and also parallel to the primary axis of the plasmonic structure. For a single plasmonic metal sphere the second condition is not applicable but for most other plasmonic structures there is one direction that will give the largest enhancement, for example on the longest axis of an ellipsoid or on the dimer axis of a pair of metal spheres.

Chu *et al.* achieved this optimal configuration in their decoration of horizontally aligned SWNTs with AuNPs [121]. The AuNPs formed along the length of the SWNTs so when they grew close enough to couple, they were already aligned parallel to the SWNT axis. Since the SWNTs were all aligned with one another and the AuNPs made them visible in the Raman spectrometer's optical microscope, the sample could easily be orientated to have the SWNTs parallel with the laser polarisation. Strong Raman signals were obtained in this way. No results from other polarisation directions were given [121].

Assmus *et al.* [117] and Tong *et al.* [124] both explored the polarisation effects of a single nanoparticle on an individual SWNT, formed by electrodeposition and AFM nanomanipulation, respectively. Both sets of polarisation measurements used the experimental configuration used in the first polarised Raman spectra of

SWNTs [49], where a $\lambda/2$ waveplate was inserted before the objective lens in the micro-Raman spectrometer and rotated to give different polarisation directions with respect to a stationary SWNT sample. The value of the Raman G^+ peak intensity as a function of angle was given for different SWNT–AuNP distances, as controlled by AFM nanomanipulation (Figure 5.3a). Note that no polarisation filter was placed in the scattered light so the signal represents all the light scattered from that incident light polarisation direction. At 200 nm the SERS effect is negligible and the SWNT displays the expected $\cos^2\theta$ dependence. At smaller AuNP–SWNT distances the signal at all polarisation angles is enhanced, including at $\theta = 90°$ when $\cos^2\theta = 0$. The conclusion reached by Tong *et al.* is that the AuNP induces a non-zero electric field parallel to the SWNT. Contrasting results are presented by Assmus *et al.* from their measurements of SWNTs decorated with AuNPs (Figure 5.3b). They did use a filter in the scattered light, so they were able to extract the scattered light with polarisation parallel (VV configuration) and perpendicular (crossed, VH configuration) to the incident light polarisation, as well as measuring without the filter (V- configuration). The RBM and G^+ peak intensities were plotted against polarisation direction, for a single AuNP as well as agglomerates of AuNPs on individual SWNTs. Both the bare SWNT and the SWNT with a single AuNP were said to exhibit the expected $\cos^4\theta$ behaviour in the VV configuration and $\cos^2\theta\sin^2\theta$ behaviour in the VH configuration. The values presented do appear to go to zero in the VV configuration but not quite to zero for the V- configuration, which might explain the discrepancy between their conclusions and that of Tong *et al.*, which was based solely on V- data.

The effect on polarisation of an agglomerate of AuNPs on an individual SWNT is also presented in Figure 5.3b. In this case there is no doubt that the expected $\cos^4\theta$ and $\cos^2\theta\sin^2\theta$ behaviours were not exhibited. This result indicates that the polarisation dependence is highly influenced by the plasmonic nanostructure geometry. However, no information was available about the precise structure of the agglomerates [117].

In the case of the undefined agglomerates, no further analysis was performed. Insufficient information was available about their structures to allow computa-

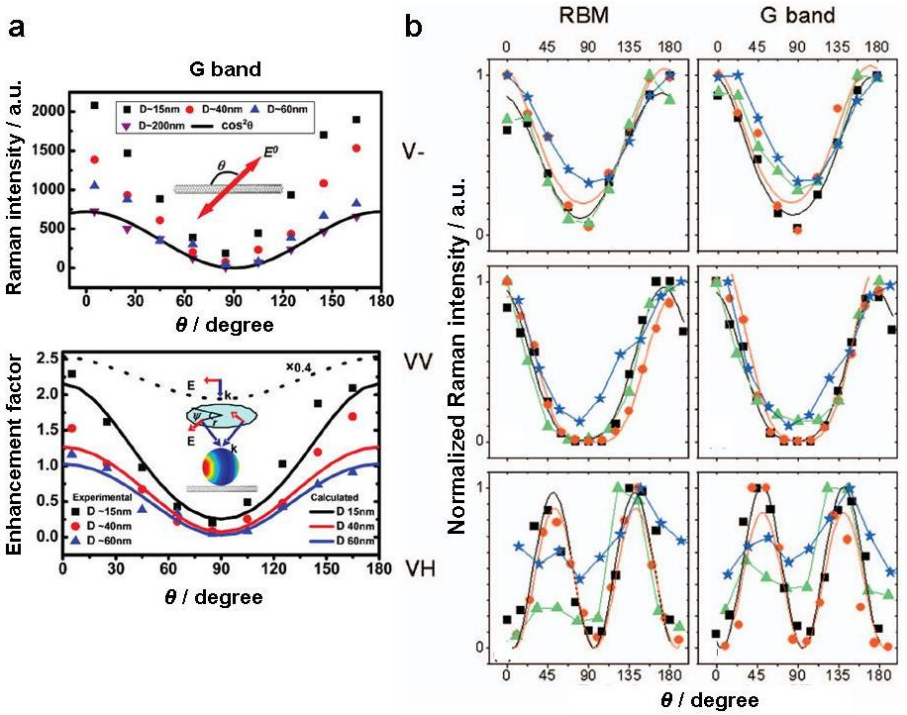

Figure 5.3: (a, top) Incident polarisation-direction dependence of the SWNT G band intensity with different AuNP–SWNT separation distances, D, and (a, bottom) incident polarisation-direction dependence of the Raman enhancement factor for theory (lines) and experiment (points) at different separation distances. (b) Incident polarisation direction dependence of RBM and G band intensities for unfiltered (V-), parallel (VV) and crossed (VH) polarisation configurations for a bare SWNT (black squares), a SWNT with a single AuNP (red circles) and two different SWNTs with AuNP agglomerates (green triangles and blue stars). Part a is adapted from reference [124] and part b is adapted from reference [117].

tional modelling to be applied for the comparison of theory to experiment. For the single nanoparticle, Tong *et al.* did compare generalised Mie theory to their results. They showed that the total induced electric field, E_{loc}, was not relevant when looking at one-dimensional SWNTs, but instead only the component of E_{loc} parallel to the SWNT axis, E_x, should be used in calculations. Using this modification of the standard model, theoretical results showed a good match to the experimental data [124].

5.1.4 AFM nanomanipulation

AFM probes were first used to controllably manipulate nanometric objects on a surface when Junno *et al.* manipulated GaAs nanoparticles in 1995 [125], which

built on work performed with STM instruments to controllably manipulate single atoms [126]. Since then the technique has been developed and applied to different types of nanoparticles [127–129].

Recent research into AFM nanomanipulation has been to increase the level of automation with a view to improving on the time-consuming manual iterations that are normally required [130]. Commercial systems offering the conventional nanomanipulation function have been available for approximately ten years.

5.2 Experimental

5.2.1 Materials

Two different types of gold nanoparticle (AuNP) were used for this work.

The first had a total diameter of 150 nm in a core–shell structure. The core was a 125 nm-diameter sphere of silica and the gold shell was 12.5 nm thick. These were purchased from Nanospectra Biosciences Inc. (US) from several production batches. These nanoparticles are provided in pure water with no surface coating. Their optical resonance peak should be in the range 780–820 nm. The concentration was on the order of 10^9 NPs per millilitre of water.

The second type of AuNP was a solid gold sphere of diameter 50 nm. Again these were in water. Since these particles were purchased some time previous to their application in this project, information is not available about their source, their concentration and the presence of any additives to the water.

The substrates used were prepared as described in Section 3.4. For basic deposition and nanomanipulation experiments, cleaned silicon wafer chips were used. Thereafter, microfabricated samples with CNTs grown and electrodes patterned by lithography were used for experiments involving nanomanipulation of AuNPs onto CNTs. Although the electrodes were not used for electrical contacts, they provided useful reference points with which to accurately identify locations, especially when switching between Raman and AFM instruments.

The AFM tips used for nanomanipulation were standard tapping mode probes. Most commonly used were NSG10 tips from NT-MDT (Russia). These silicon

probes had a force constant, k, of 3.1–37.6 N/m, a resonance frequency, f, of 140–390 kHz and a tip curvature radius, r, of 10 nm. Other similar probes that were used were RTESP silicon probes from Veeco (US) (k = 20–80 N/m, f = 253–326 kHz) or Tap300Al-G silicon probes from BudgetSensors (Bulgaria) (k = 40 N/m, f = 300 kHz).

5.2.2 Deposition methods

When depositing the AuNPs onto the substrate, the ultimate desire is for the nanoparticles to be well dispersed, giving separate individual NPs, while having a high enough density that the distances between the AuNPs and the CNT are not too large, ideally less then 10 μm.

To create well-dispersed AuNPs, they were placed in an ultrasonic bath for periods of 5 minutes, typically three or four times. Initially the solutions would appear clear and a black precipitate was observed at the bottom of the vial. After ultrasonication, the precipitate was not observed. In the case of the 50 nm particles, the dispersion had a pink colour, while the 150 nm particles formed a colourless dispersion.

Several methods were investigated for depositing the NP dispersions onto the substrate. A small spot was desired, to allow NPs to be put into one part of a chip while leaving other areas on the chip clean.

In a quest to create small drops, Pasteur pipettes were melted and pulled to form a small capillary, by Andrei Gromov. Placing the sharp tip into the AuNP dispersion caused the capillary to fill but it was found that when the tip was placed onto the substrate the dispersion did not flow out. This was understandable because the end of the tip was generally a rough shape and therefore the pipette contents could not make good contact with the substrate surface. Instead, a syringe was attached to the pipette and this was used to provide a slight increase in air pressure down the pipette, forcing a drop to form outside the pipette tip. When this drop was touched onto the substrate it would spread according to the wetting of the surface. At best, a drop on the surface with a diameter of approximately 1 mm could be achieved with this method, but it was highly

dependent on manual control so larger spots were frequently created. Attaching the pipette to a micropositioner could have enabled improved spatial precision but the attachment methods used were not rigid enough to be unaffected by the process of attaching and pushing the syringe, and micro-scale precision was not necessary as the drop was on the millimetre scale. The preferred method was to hold the pipette by hand.

Alternatively, a micropipette was used instead of a pulled Pasteur pipette. The micropipette was set to deliver the smallest volume possible, 2 µl. If this volume was used and dropped on the surface it would create a drop 2–3 mm in diameter. However the mechanism of the micropipette allowed easier control of smaller drops by only partially depressing the plunger. As such this method was adopted as the easiest way to create small drops on the substrate.

Once the drop was created on the surface, it would immediately begin to dry. On the open bench it would appear to be dry within tens of seconds. It was observed several times that this kind of drying created inhomogeneity in the density of deposited particles, with boundaries appearing within the total drop area.

To give more homogeneous drying within the area of the deposited drop, measures were taken to prevent the drop from drying for a set period of time, using the setup shown in Figure 5.4. This was prepared in advance, allowing the atmosphere inside the makeshift chamber to equilibrate at saturated humidity. When the drop was added to the sample it was slid inside the chamber with minimal opening. In this setup the drop would not dry for several hours. Typically a period of 30 minutes or 1 hour was used and then the sample was put in a commercial spinner: SPS SPIN150 Single Substrate Spin Processor – v3, Semiconductor Production Systems, Europe. Spinning at 3000 rpm caused the drop to spread out thinly over the surface and dry. After this process was complete a relatively homogeneous density of NPs was observed in the area of the drop. There was still some increase of density at the drop edges, due to surface effects and drying during the few seconds of being in the lab atmosphere before and after being in the chamber. Negligible AuNP density was observed outside of the drop area, showing that nanoparticles did not stick to the substrate during

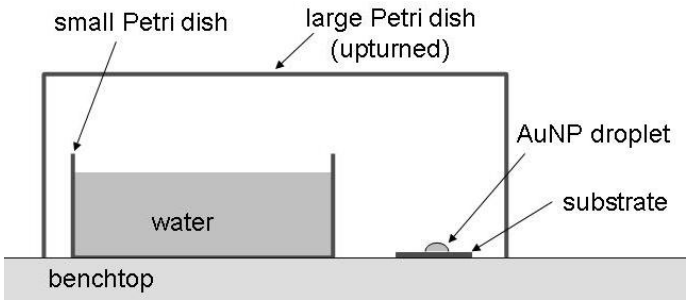

Figure 5.4: Schematic representation of the method used for homogeneous AuNP deposition. By creating a saturated humid atmosphere, this arrangement enables the AuNP dispersion droplet to sit on the substrate without drying until it is removed by spinning.

the spinning process. While this procedure was a big improvement on bench air drying, in the case of substrates with electrodes and other lithographic features, uneven deposition sometimes still occurred, presumably because these features acted as a barrier preventing the dispersion from spinning off the substrate.

The density of deposited AuNP was examined by optical microscopy and AFM. With a 100× lens, 150 nm particles could just be identified, although it was not possible to distinguish between a single particle and two or more particles clustered together. The smaller, 50 nm, particles appeared as a grey covering over the surface. AFM, when working optimally, could identify separate particles of either size.

5.2.3 Nanomanipulation

Nanomanipulation was carried out with the Nanoman function of the 7.20 or 7.30 software on the Veeco Nanoman VS with Dimension 3100 controller.

The process of nanomanipulation begins with scanning the area in tapping mode to identify the particle to be moved and the desired location it is to finish at. The deposited nanoparticles were identified primarily by measurement of their height, being within the range 150 ± 26 nm or 52 ± 10 nm, as expected from AFM measurements of distributions of particles deposited on clean silicon. In addition, where it was available, comparison of the same area before and after nanoparticle deposition helped identify spots that arose from the deposition.

Once the overview was established, the scan area was reduced to a square of length ranging from 1–3 μm, containing the nanoparticle. Closed-loop control was used throughout the nanomanipulation process. When this small scan area was completed the 'plane correct' option was engaged, meaning that instead of taking only the height at the centre of the area as a reference, the computer calculated heights based on a plane fit to the completed scan data.

With the Nanoman function, paths were drawn on the scan image, representing the route to be taken by the tip during the nanomanipulation process. To move a nanoparticle, a path would be drawn from one side of the NP, through its centre, to a chosen position on its other side. The software allowed the user to choose several parameters for this stage, most notably the height as well as the lateral speed. In between paths and before and after the first and last paths the 'connect' parameters were applied. As with the 'path' parameters, the height and speed were set by the operator.

Nanomanipulation was performed in fixed-height mode. This means that the feedback control that normally acts in AFM to maintain a constant force between tip and surface was switched off. Instead heights, in nanometres, were chosen and these were applied with respect to a reference height, such as the height of the central pixel or the average height of the scan area. Note that the tip path would not take into account the surface topography, only – if plane correct was activated – the average slope of the surface.

Once the path(s) were drawn and the parameters set, the user commanded the computer to 'Do it' and the tip completed the directed route before returning to the centre. The scan area was then refreshed, in tapping mode, to identify the new location of the NP. In an ideal case the NP was then located at the end of the path. Figure 5.5 gives an example of the Nanoman function and the result of one step of nanomanipulation.

Nanomanipulation was found to be an iterative process. Even if the NP was found to move the full distance of a path, several steps would be required to move the NP the entire way from where it was initially deposited to the desired location, such as exactly placed on top of a carbon nanotube. With larger scan areas, longer paths could be drawn but the accuracy was reduced so the likelihood

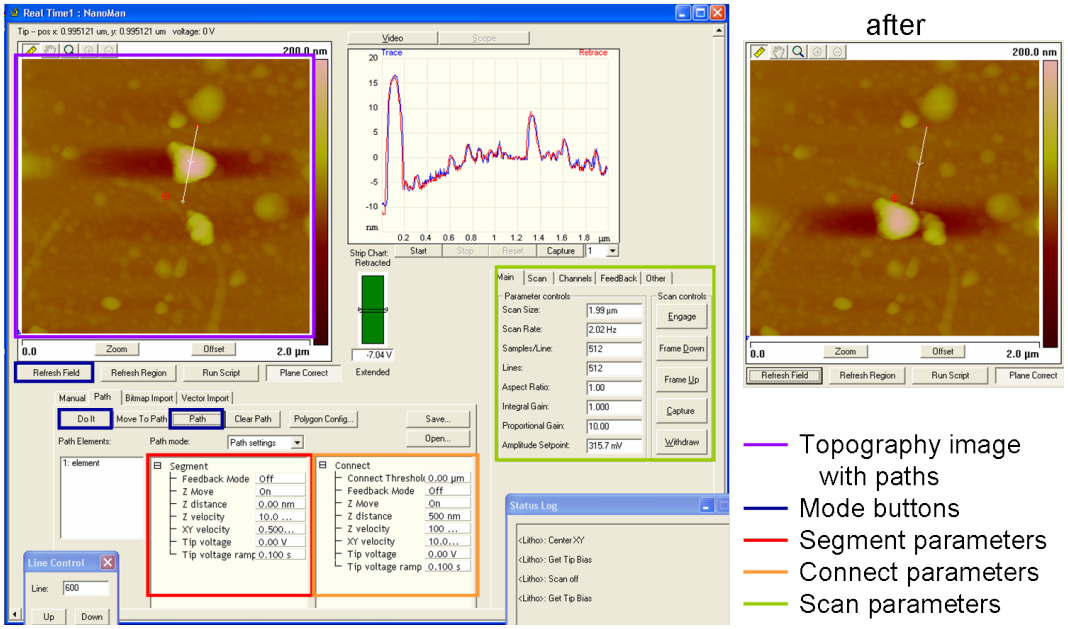

Figure 5.5: Nanoman function in Veeco's 7.20 software showing one step of the nanomanipulation process. The area is scanned and appears in the topography image, and paths for the tip to take are drawn onto this image (white lines with arrows). The mode buttons switch between refreshing the image (Refresh Field), drawing paths onto the image (Paths) and executing the paths (Do It). The segment parameters apply during the paths and control tip movement such as z height, and xy speed. The connect parameters apply while the tip moves to the start of the path and after the tip has finished the path and, if applicable, between consecutive paths. As with the segment parameters, the z height, and xy speed can be set. Once the paths have been completed, the field is refreshed according to the scan parameters, which set the resolution, speed, setpoint and feedback gains. The refreshed image (also shown, labelled 'after') keeps the arrows representing the paths, which allows easy reference of how the particle moved in comparison to the tip movements.

was increased of the tip failing to accurately hit the NP to push it. When the NP was close to the CNT, a small area, such as 1 μm^2, was used and in most cases several iterations were made to position the NP exactly so that its highest point was placed over the top of the CNT.

The main parameters that were varied during nanomanipulation were the height of the paths and the number and position of paths. In addition, the parameters used for the tapping mode scans had a significant impact on the speed of the process, which was important if thermal drift occurred over time. As an example, the path shown in Figure 5.5 would take (0.5 $\mu m \times 0.5$ $\mu m/s$) = 1 s plus

a little time for the connects, and area would be refreshed in (512 lines$\times\frac{1}{2\text{ Hz}}$) = 256 s, so the total time for one iteration would be between 4 and 5 minutes.

The results section will describe some of the challenges encountered during nanomanipulation and the solutions found or measures taken to minimise problems. One that was a regular occurrence was that the tip would become contaminated and/or damaged during the process and therefore scans decreased in clarity by the end. Typically it was very useful to have a good image at the end of the nanomanipulation, showing the final location of the NP with respect to the CNT and any other reference features, both for the sake of reporting results and for aiding analysis of the following Raman results. If the tip was in too bad a condition after the nanomanipulation was completed then a new tip was inserted and the area was scanned with good resolution and quality. At this stage in particular, care was taken to minimise the risk of accidental movement of the NP, for example tapping mode was used and the setpoint was kept as high as possible.

5.2.4 Raman mapping of SERS enhancement

Once a nanoparticle was positioned on a carbon nanotube, the enhancement brought by the nanoparticle was measured by Raman spectroscopy. This was performed with a Nanonics piezo scanner within a Renishaw micro-Raman spectrometer as described in Section 3.1.3. Raman maps were usually made with x and y steps of 200 nm. In this case, if the NP offered a large enhancement then the spectra of several points of the Raman map will show a stronger signal, with the very strongest located at the centre of the enhanced region. If the intensities are plotted as a colour map, the enhanced region will appear brighter and the very centre of this bright region would contain the pixel with highest intensity. This could be taken as a measure of the enhanced Raman signal from the NP. For these Raman maps, a $\lambda/4$ waveplate was placed in the laser beam to create circularly polarised light to minimise any effect of the the orientation of CNT and/or NP with respect to the incident polarisation direction. Scattered light of all polarisations was detected.

The Raman spectra forming these maps were almost always measured for 60 s each, with the spectrum centred at 1500 cm^{-1}. When using 150 nm NPs, a laser wavelength of 785 nm was used with a 1200 l/mm grating, giving a full range of 1248 cm^{-1} to 1740 cm^{-1}. When using 50 nm NPs a laser wavelength of 514 nm was used with a 2400 l/mm grating, giving a full range of 1195 cm^{-1} to 1790 cm^{-1}. These respective wavelengths were most appropriate for creating a resonance between the laser light and the plasmon resonances of the NPs.

In order to compare intensities measured from different days, a calibration was required, since the measured magnitude of Raman scattering is highly dependent on laser power and system alignment, which can vary substantially. For calibration, the (111) surface of a calcium fluoride crystal was used, on the same sample stage with the same objective lens and laser as the sample measurement. After being measured three times, its Raman peak at 322 cm^{-1} was fitted with a Gaussian function and the average of the three peak areas was taken as a measure of the spectrometer's response on that day of measurement. When making comparison of sample results on different days, the sample intensities were divided by the calcium fluoride intensity from the corresponding day.

The spectra obtained in the Raman mapping were saved in QuartzSpec as text files, which were then processed in MATLAB Version 7.8.0.347 (R2009a). The programs written and used for this analysis procedure will be summarised here and are replicated in full in Appendix G. The first analysis to be performed was to integrate the area of the total spectrum at each point in the map and to plot all the spectra in a grid, both of which proved useful for identifying reference points such as electrodes or nanoparticle clusters and aligning AFM or optical microscope images with the Raman map. The second analysis was to integrate just the region of the spectrum where a characteristic CNT signal was expected, to check for enhancement of the CNT signal by a NP.

The first analysis (script: `nanonics_map`) began with the file containing all the spectral data being read into MATLAB. With a simple 'zapping' algorithm (function: `zap`), each spectrum was checked for spikes, which were removed and replaced with a linear connection between the start and end of the spike. The user must choose the threshold values for recognising a spike so some manual

iterations were often required to find suitable values for removing spikes while not cutting true spectral peaks. The area between the first and last points was integrated by the trapezoidal rule (function: `peak_area`). Each spectrum in turn was displayed to the user as this was performed to allow verification of suitable zapping. Once all the spectra had been processed, the integrated areas were plotted as a colour map with the map dimensions as chosen in Quartz when setting up the measurement and manually entered into MATLAB. In addition, a mini replica of each spectrum was plotted on a grid of the same dimensions. The spectra were too small to allow detailed interpretation but presented in this way they allowed an overview of the map, showing regions of characteristic spectral shape such as electrodes in contrast to bare silicon.

The second analysis (script: `nanonics_map_Iat1595_baseline`) began in the same way as the first with the spectral data being read and each spectrum being checked for spikes. In this case, after the spectrum was zapped it was also baseline corrected, using a polynomial fit to the spectrum, ignoring regions chosen by the user such as those where real spectral peaks were expected, which was subtracted from the whole spectrum (function: `baseline_correct`). Then the area of the peak of interest was found by trapezoidal integration between user-defined end-points. As in the first analysis, this peak area information was presented in the form of a colour map. Although the colour maps generally had a linear colour scale, it was sometimes found that the peak areas were more easily interpreted when plotted on a logarithmic colour scale. If a particular region of the map was of interest then that selection of the spectra could then be plotted as a grid either with or without axes (function: `plotsection`). In almost all cases, this second analysis used the G band of the CNT Raman spectrum as a characteristic signal, so the peak would be integrated from 1580–1605 cm^{-1}, or similar, as chosen based on manual examination of the spectra.

The Raman maps of the total spectral integrated intensity and the selected peak integrated intensity, and the image of all the spectra plotted on a grid were then combined with AFM images and optical microscope images in Microsoft Office PowerPoint 2003. Careful comparison was made to correlate the location of the Raman map with the optical and AFM images, taking into account drift

that almost always occurred during the Raman mapping measurement, acting to stretch the Raman maps in x and/or y directions. Once the maps were correlated with the use of large features such as electrodes, checks were made that any observed CNT Raman signals correlated with the expected locations of CNTs from AFM images. In the case that plasmonic enhancement of the Raman signal of a CNT occurred then this would be observed in the position that the AFM image shows the NP to be.

To quantify the enhancement, the G peak integrated area of the spectrum exhibiting the strongest signal in the region of the nanoparticle was taken. This could be compared either with the same CNT in the same map at a spot away from the enhancing NP or with the same CNT without the NP measured previously. In the latter case, the intensities would be scaled according to calcium fluoride measurements as described above.

In some cases, particularly when correlation of small-step Raman maps and optical or AFM images proved too difficult, larger Raman maps were measured with WiRE software and the Prior mechanical stage. MATLAB was also used for interpreting the data obtained in this way. The analysis (script: `map_code`) involved reading the file of data, converting its format from a long list of consecutive spectra to a three-dimensional matrix (function: `separate_4_column_data`) then zapping and baseline correcting each spectrum as before. The D and G regions were both integrated and a map was plotted of the G/D ratio as well as one of the G peak intensities. Also as previously, all the spectra could be plotted on a grid or a selection of the spectra could be plotted on a grid with or without axes. This type of larger lower-resolution map was useful to learn the characteristic spectral shapes associated with different features present on the sample and for aiding correlation of small-step Raman maps with optical or AFM images. To distinguish between maps measured with the Nanonics piezo scanner and those with the Prior stage, the term 'finemap' was used for the former and 'roughmap' for the latter.

5.2.5 Measurement of laser spot size

In order to quantify the enhancing effect of the plasmonic nanoparticle an accurate measure of the laser spot size is necessary. If this is known then the proportion of the overall laser spot that is affected by the small nanoparticle may be estimated and a value may be given for the enhancement of the small enhanced region, rather than for the whole laser spot area, which will contain a significant proportion of non-enhanced surface.

The beam width was measured by making a linear small-step Raman map across a SWNT, perpendicular to its axis. As with the previously described small-step Raman maps, a Nanonics scanner was used with Quartz and QuartzSpec software and the data analysis was performed in MATLAB.

An appropriate SWNT was picked for having a good Raman signal and being straight and therefore having a well-defined direction. With the use of AFM images and with reference to features such as electrodes, the sample was orientated in the Raman spectrometer so that the SWNT was orientated in the y direction. The Raman spectra along a single line or a set of lines were then measured across the SWNT with steps of 50 or 100 nm. The G band intensities were integrated in MATLAB and plotted against lateral position. The cross-sections were then fitted with Gaussian functions and the average FWHM was taken as a measure of the laser width.

Figure 5.6 shows this for the 514 nm laser, where three cross-sections were measured, each on a different SWNT. This gave a laser spot width of 770 ± 90 nm.

For the 785 nm laser ten lines across one SWNT were used (Figure 5.7). Each line was processed as above and the eight resulting values of FWHM were averaged to give a final measure of the laser spot width of 1.0 ± 0.2 μm.

5.2.6 Polarisation analysis

When a strong CNT Raman signal was observed by SERS from a gold nanoparticle, the nature of that signal could be further characterised with a polarisation study.

To do this, the sample was placed in the Raman spectrometer with a

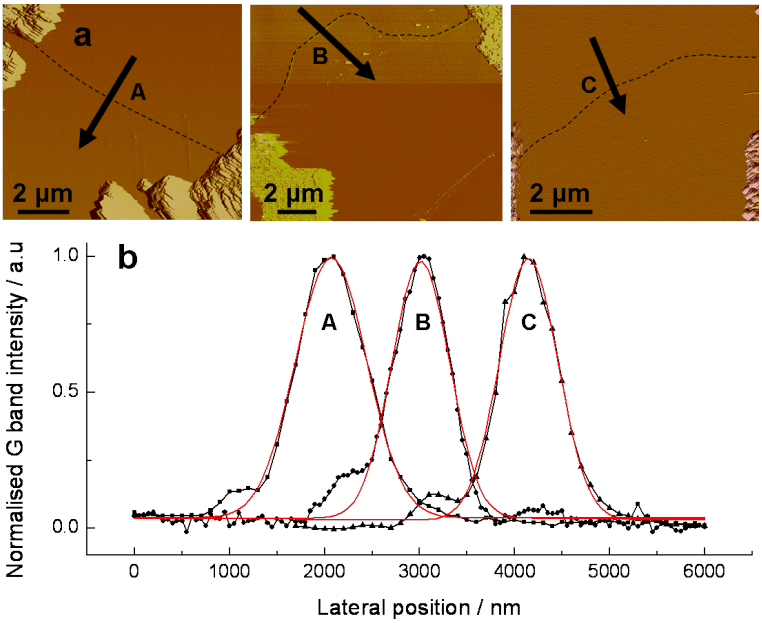

Figure 5.6: The spot size of the 514 nm laser measured on three SWNTs (A-C). (a) AFM identifying SWNTs that had straight regions and revealing their orientation so a Raman line map could be made perpendicular to the SWNT axis. (b) Raman line maps with steps of 100 nm (A, C) or 50 nm (B), made over the SWNT and the G band area was integrated. Cross sections in the x direction were extracted and fitted with Gaussian profiles. An average of the width from three lines was taken. The dashed lines highlight the locations of the SWNTs.

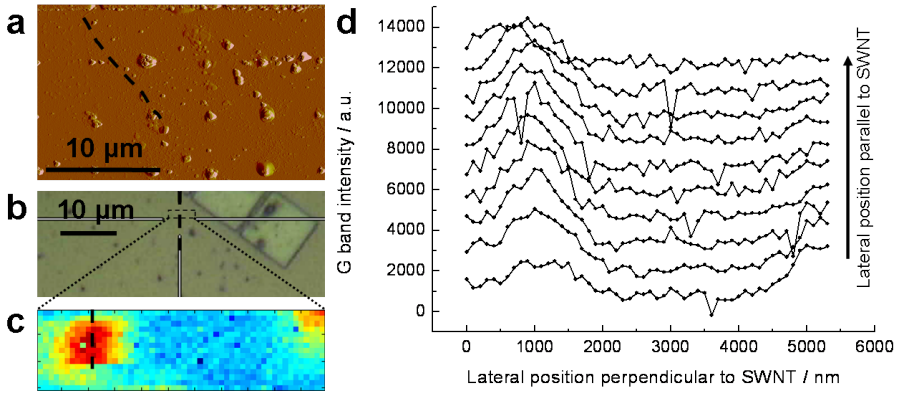

Figure 5.7: The method used to measure the spot size of the 785 nm laser: (a) AFM was used to identify a straight SWNT and its orientation, (b) the optical microscope was used to position the sample in the spectrometer, using grid markers, so that the SWNT was orientated in the y direction, then (c) a Raman map with steps of 100 nm was made over the area containing the SWNT and the G band area was integrated at each point. Finally, (d) cross sections in the x direction were extracted and fitted with Gaussian profiles and an average of the width from ten lines was made. The dashed line highlights the location of the SWNT.

known orientation. Polarisation studies were performed as already described in Section 3.1.2, using a $\lambda/2$ waveplate in the laser path and a $\lambda/2$ waveplate and an analyser in the scattered light path, with calcium fluoride being used to correct for instrument polarisation dependence.

When this was performed on a 150 nm NP positioned on top of a CNT, the NP was visible with a 100× short working distance objective lens. It could therefore be positioned in the centre of the laser spot using the optical microscope.

5.3 Results and Discussion

5.3.1 Nanomanipulation

Although nanomanipulation is an established method and was performed in a commercial instrument, the successful application to the manipulation of gold nanoparticles onto carbon nanotubes took some experimenting and some useful lessons were learned. Here, the challenges faced and the solutions found will be described, some discussion will be given on the z heights used, then examples of successful manipulation of both 150 nm and 50 nm AuNPs will be shown.

5.3.1.1 Challenges and solutions

Drift

When performing the nanomanipulation process, one of the most common problems faced arose from thermal drift. If, during the time between the image being refreshed and the path being executed, the sample moved with respect to the tip by more than the tip width then the tip would not hit the particle optimally for pushing it along. An example of this occurring is shown in Figure 5.8a, where the sample drifted upwards to the point that the particle was completely clear of the paths of the tip and did not move at all as directed. In some cases the drift was less severe and the particle was still in the tip path but not as directly as intended. Often this would cause the particle to move some distance but not reach the end of the path, as if the tip was pushing the side of the particle and

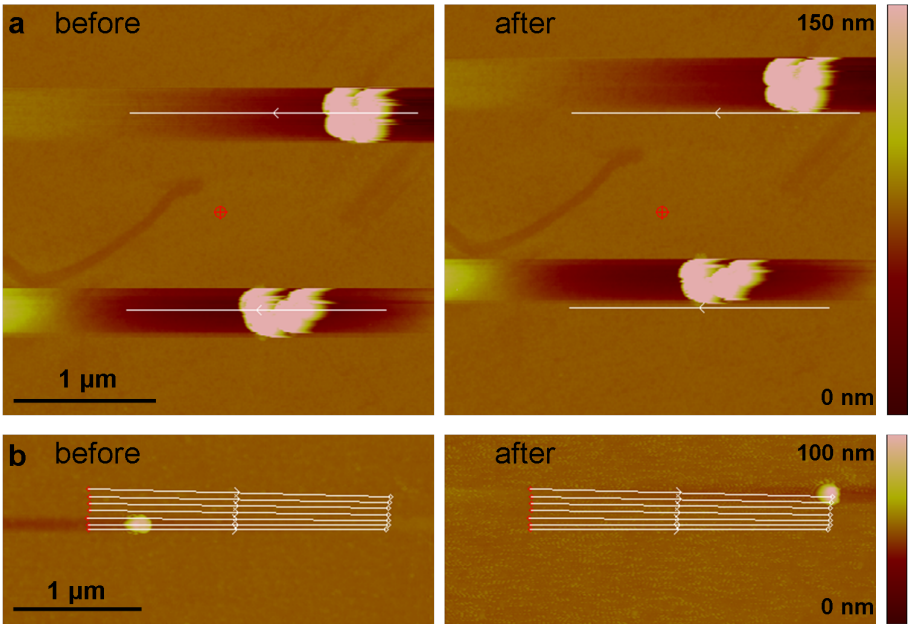

Figure 5.8: Drift occurring during manomanipulation, with (a) single paths, where the tip misses the particles during the paths and therefore does not cause the desired movement and with (b) multiple paths, where the particle does reach the target position.

after a certain point the tip slid past the particle, leaving it at the side of the path.

One solution to the problem of thermal drift is illustrated in Figure 5.8b: multiple paths. If the drift direction is known then a series of paths can be programmed, covering a range from the initial position of the particle through to the expected position of the particle resulting from drift. The tip is likely to 'catch' the particle during at least one of the paths and push it the full desired distance. In addition to this method of taking into account the drift, measures can be taken to effectively minimise it. Since drift is approximately linear with time, minimising the time between refreshing the pane and executing the paths reduces the drift distance. This is achieved by reducing the resolution of the scan, increasing its speed, only refreshing the relevant part of the pane and switching immediately from one to the other with no pause. Finally, where possible, positioning the sample in the AFM in advance of attempting nano-manipulation, for example the previous day, seemed to give a lower rate of drift.

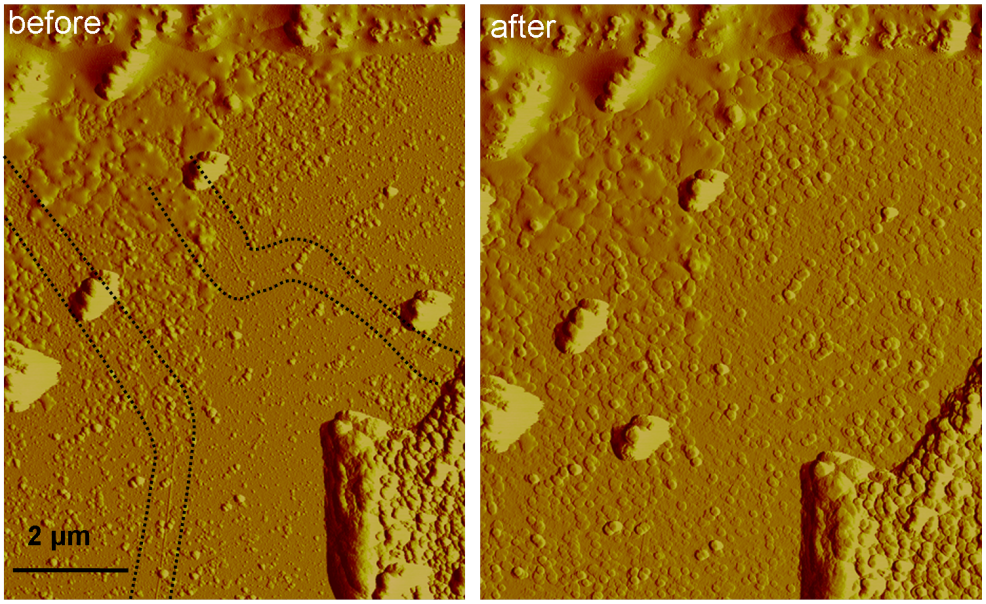

Figure 5.9: AFM amplitude error images of a sample with CNTs and NPs before and after a multi-step nanomanipulation process. Initially the tip was good and the two CNTs could be imaged (seen between the dotted lines). After nanomanipulation the tip was damaged or contaminated and the resolution required to see CNTs was not available. The final NP position was chosen with reference to the features that were still visible, giving an estimate of the CNT position.

Tip deterioration

Another difficulty that was encountered during nanomanipulation experiments was contamination or damage of the AFM tip, as illustrated in Figure 5.9. If a good tip was used at the start of the process then the sample could be scanned to show where the larger features (other NPs, electrodes) and the small CNT were in relation to one another. Commonly, the tip quality deteriorated during the process due to contamination or damage and the available resolution dropped, to the point that the CNT could not be directly observed. In this case, the final position of the NP had to be chosen with careful reference to the earlier, better AFM images, using the larger features. Replacing the tip would enable an improved image and greater accuracy but it was not appropriate to do so immediately after it deteriorated, due to the time and financial cost of replacing the tip and the chances of the new tip also quickly reducing in quality.

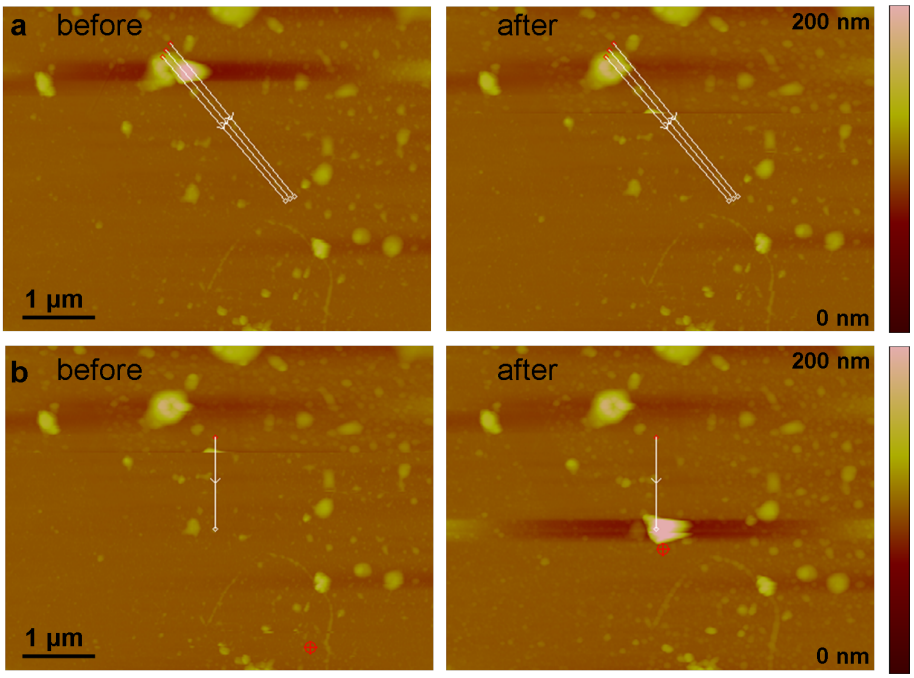

Figure 5.10: An example of a NP being (a) 'lost' during manipulation and (b) 'found' in a subsequent manipulation step on a bare area of the substrate.

NP removal

A particularly frustrating disadvantage of using an AFM probe to manipulate NPs was that they would sometimes stick to the tip instead of to the surface after being pushed. This would effectively mean they were lost, as seen in Figure 5.10a. Sometimes the NP could be 'found' again if it could be made to stick once more to the surface instead of the tip. Figure 5.10b gives an example of this occurring. Executing a path on a clean region of the surface, with a reduced z height, caused the particle to reappear and it could continue on its journey. There is a risk that the particle that appeared is in fact something other than the lost NP, but this has a low probability. Unfortunately it was often impossible to redeposit a lost NP once it was stuck on the tip, even through trying the method described here with a range of z heights and path orientations. In this case, if the tip quality was not adversely affected then the same tip could continue to be used and another NP manipulated. If proceeding in this way then one had to remember that the first NP could reappear at any point, albeit with a low probability, which did occur a small number of times.

Identification of individual NPs

Probably the biggest challenge in the process of manipulating gold nanoparticles onto carbon nanotubes was identifying individual gold nanoparticles, rather than an unknown contaminant or an agglomerate of nanoparticles.

AFM scans only reveal the topography of a sample without providing information about the materials present. Therefore AFM cannot unambiguously distinguish between a gold nanoparticle and a similar-sized contaminant of another material. The most reliable approach was to compare AFM scans from before and after the gold nanoparticles were deposited. Any new features that appeared were then caused by the deposition, which meant they were likely to be NPs, although other contaminants could possibly also have been deposited or moved around on the surface during the process. As already mentioned, a particle was primarily chosen from among features appearing only after NP deposition based on its height falling in the expected range, which was 127–178 nm (95% confidence interval) for the 150 nm particles.

Examining particle heights in comparison to earlier AFM images did not help distinguish between a single, individual NP and a dimer or trimer or even a planar agglomerate of more NPs. It was found that distinguishing such structures was very challenging. Standard AFM tips could only resolve separate particles when in very good condition, which was not the case if much imaging or any manipulation had been performed. With a slightly blunt or contaminated tip, if a non-circular shape was observed it might infer an agglomerate rather than a spherical particle, but it could also be attributed to the tip shape. Generally, contaminated tips can be identified when they give the same repeated shape for all features on a surface. This might, however, not apply when relatively large nanoparticles are compared to features two orders of magnitude smaller, if the contamination is not at the very apex of the AFM tip. Thus, non-circular features observed in the AFM image could indicate multiple NPs or may be the result of a contaminated tip measuring single NPs. It is generally not clear which case accounts for non-spherical shapes so the identification of individual NPs is questionable. In principle an ultra-sharp AFM tip would allow improved

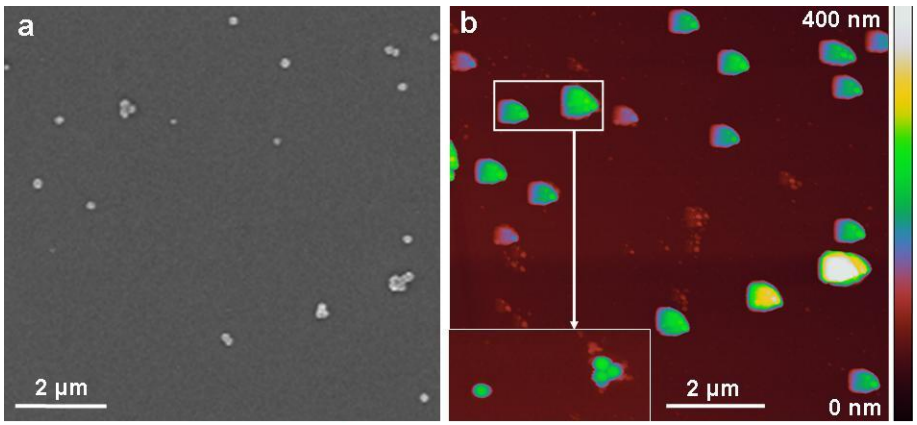

Figure 5.11: A comparison of the resolution of (a) SEM and (b) AFM when imaging agglomerates of AuNPs. With a normal AFM tip, after some use, the separate NPs may not be resolved, although they may be with a brand new tip (b, inset). The colour scheme used for the AFM image allows easy differentiation between the heights of single particles (green), two layers of particles (yellow) and more than two layer of particles (white).

resolution and the structures of agglomerates should then be resolvable, but the sharpness of such tips decreases rapidly as they are used, so by the time the agglomerate is located the tip may not be any more useful than a standard tip. SEM is able to quickly and easily resolve individual NPs but its use should be avoided on samples that could be damaged due to the electron energies or carbon contamination. Figure 5.11 gives a comparison of AFM and SEM in their ability to resolve the structures of NP agglomerates.

One might think that if the AFM tip is pushed into an agglomerate of NPs, they would be split up, and this could be repeated until separate NPs are obtained. This is, in fact, not usually the case. Figure 5.12 shows an example of a manipulation experiment where a 'particle' was moved over 5 µm as one entity then it split into two particles of different sizes. The height of the initial particle was 50 nm, which indicated that it could have been a single particle. When it split, the smaller part had a height of 50 nm and the larger part had a height of 90 nm, the height expected for a NP sitting on top of three other NPs, in a pyramidal structure. The lateral resolution available did not allow these structures to be identified.

Moreover, Figure 5.13 shows an example of a dimer comprised of two initially

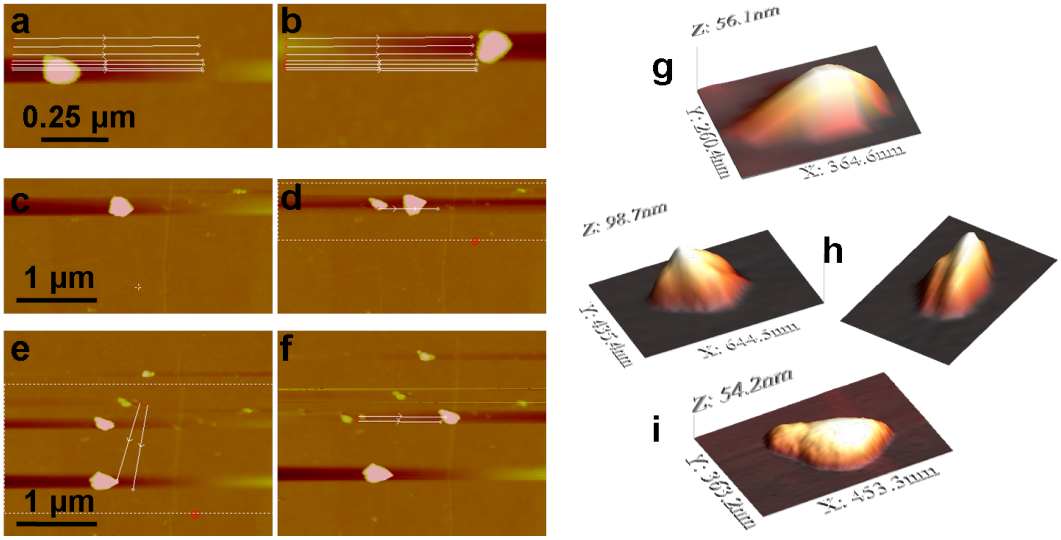

Figure 5.12: An agglomerate of NPs appearing to move (a & b) as one particle then (c & d) splitting into two, of which (e) the larger was pushed out of the way and (f) the smaller was pushed onto the CNT. Also shown are 3-D visualisations of the (g) initial, (h) larger (from two angles) and (i) smaller particles. Note that the heights indicated on the z axes in parts g–i are from the minimum point to the maximum so are slightly greater than the height of the particle above the average surface height.

separate particles forming irreversibly during the nanomanipulation process.

Ultimately, the uncertainty about choosing and manipulating individual nanoparticles was not satisfactorily resolved. After all other experiments had been completed on a sample, SEM could be performed to give certainty about the particle's composition. During manipulation, careful interpretation of AFM images was the best approach. An alternative approach that might have helped, but was not used here, is to compare the Raman spectra of particles after deposition.

5.3.1.2 Choice of z height

As described in Section 5.2, nanomanipulation paths were run in fixed-height mode. The z height to be used was entered into the segment parameters list, as nanometres above a reference point (Figure 5.14). The reference height should be the height of the surface at the central pixel of the field, but there is evidence that this is not completely true. A CNT on a flat surface was used in an experiment of

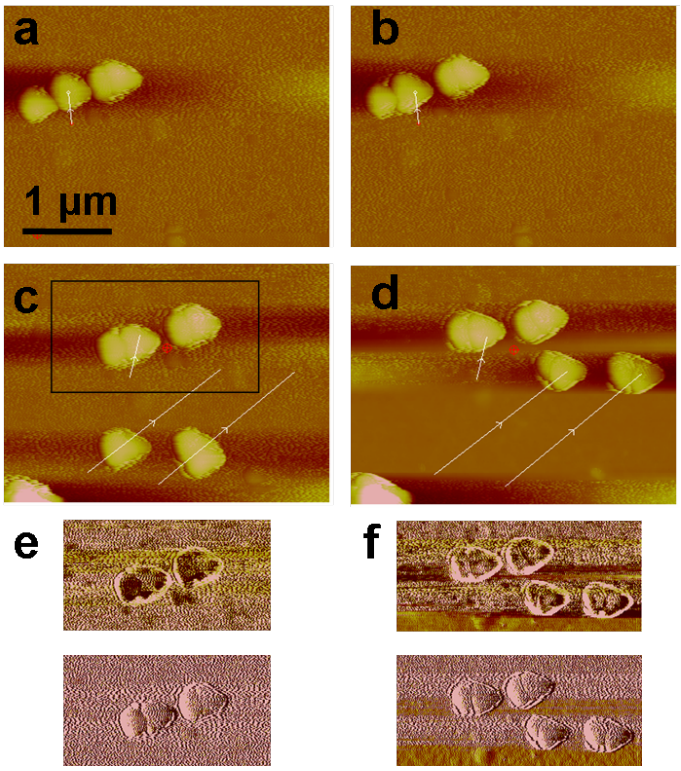

Figure 5.13: (a) Two separate particles, to the left of a dimer, were moved slightly closer (b) after one step of nanomanipulation. Later, (c) the tip tried to push the right-hand NP further away from the left-hand one, but (d) the two particles both moved as one and had the same appearance as the other NP dimers present (e) before and (f) after the final manipulation step, both in topography and phase (upper) and amplitude error (lower) images.

different tip heights following paths across the CNT. At heights above −20 nm no change was observed at all, then at −30 nm the whole sample, not just the CNT, moved according to the path, thus the true height of the surface was between −20 nm and −30 nm. Note that drawing a path over the same CNT with the (rigid, tapping-mode) tip operating with contact-mode feedback caused the CNT to be moved and broken. On another occasion where paths were drawn over a bare surface with no CNT, there was no observed effect until heights as low as −50 nm were used, at which point the whole sample moved. On a third sample low-lying contaminants were moved at −45 nm but not at −40 nm. When such low heights were used, the tip was almost always damaged, evidenced by a drop in the resolution of scans afterwards. Because the sample would move if the tip pressed too hard, there was actually very little risk to the CNT, with a range

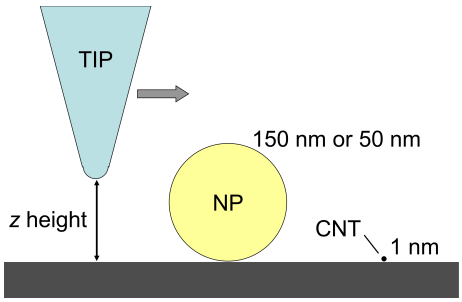

Figure 5.14: Schematic illustration of z heights in the nanomanipulation process.

of only a few nanometres where the tip would be low enough to touch the CNT but not low enough to push the whole sample. CNT damage from the tip during manipulation was never experimentally observed.

It was discovered from extensive experimentation that heights of 0 nm or -20 nm provided the most consistent successful manipulation results. When manipulating NPs onto CNTs, a disposable piece of CNT, such as near an end, was used to check that the tip at that height did not move or break the CNT. Then the final stages of NP positioning were performed over a good region of the CNT at that height. At 0 nm or -20 nm no problems were encountered.

5.3.1.3 Nanomanipulation of 150 nm nanoparticles

An example of a 150 nm AuNP that was successfully manipulated onto the end of a CNT is given in Figure 5.15. This nanomanipulation was performed at a z height of -10 nm and a lateral speed during paths of 0.5 µm/s. In total 21 iterations of nanomanipulation followed by AFM scanning were used to obtain the optimal AuNP position. Although this particle came from a batch of 150 nm diameter particles, it actually has a smaller diameter, close to 90 nm. This particle did not split into two pieces at any point, its height did not change during the process and it remained circular in appearance throughout, all of which indicate that it was probably a single particle rather than an agglomerate.

Another example is given in Figure 5.16, where two nanoparticles were manipulated independently over a distance of 11 µm onto a CNT and then were pushed together to form a dimer. This nanomanipulation was performed at a lateral speed during paths of 0.5 µm/s and a z height of 0 nm except the final

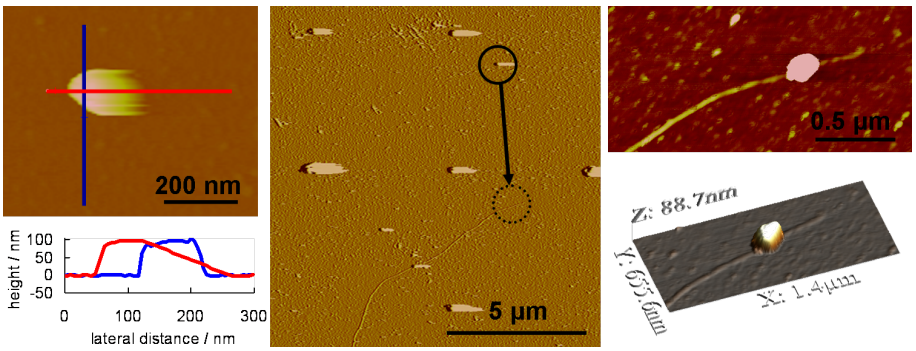

Figure 5.15: An example of manipulation of a particle from its initial position (shown on left) over a distance of 5 µm (shown in centre as amplitude error image) to its new position on top of a CNT (shown on right). The topography images and cross-section show that the AuNP was approximately 90 nm in height before and after manipulation.

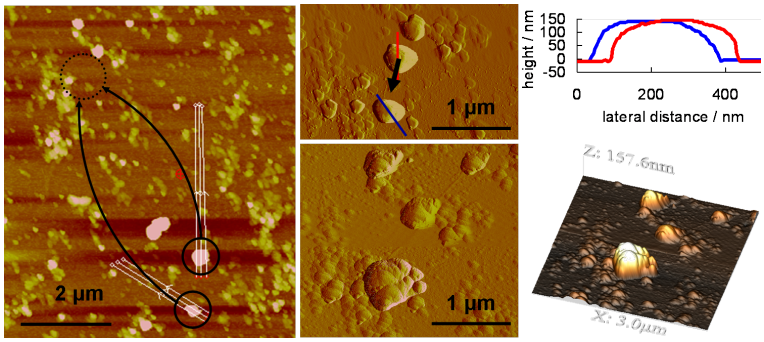

Figure 5.16: An example of manipulation of two particles over a total distance of 11 µm (partially shown on left) onto the CNT (centre top) and then pushed together to form a dimer (centre bottom). The final topography image (right bottom) and earlier cross-section (right top) show that both AuNPs were approximately 150 nm in height.

step, which was at 10 nm. In total 13 iterations were necessary with multiple paths in each iteration. The other particles that are seen to be on or near to the CNT have a smaller height so they are not 150 nm AuNPs. They may be much smaller gold nanoparticles or they may be contaminants from other sources. The target had been to have a dimer orientated parallel with the CNT axis. From the final AFM image it appears that this was not quite achieved, with the dimer axis rotated approximately 40° anticlockwise from the CNT axis.

Figure 5.17 gives two more results of AuNPs from the 150 nm batch after they were nanomanipulated onto CNTs. In both cases the same tip that was used for the manipulation was also used to make the final AFM image and the tip quality

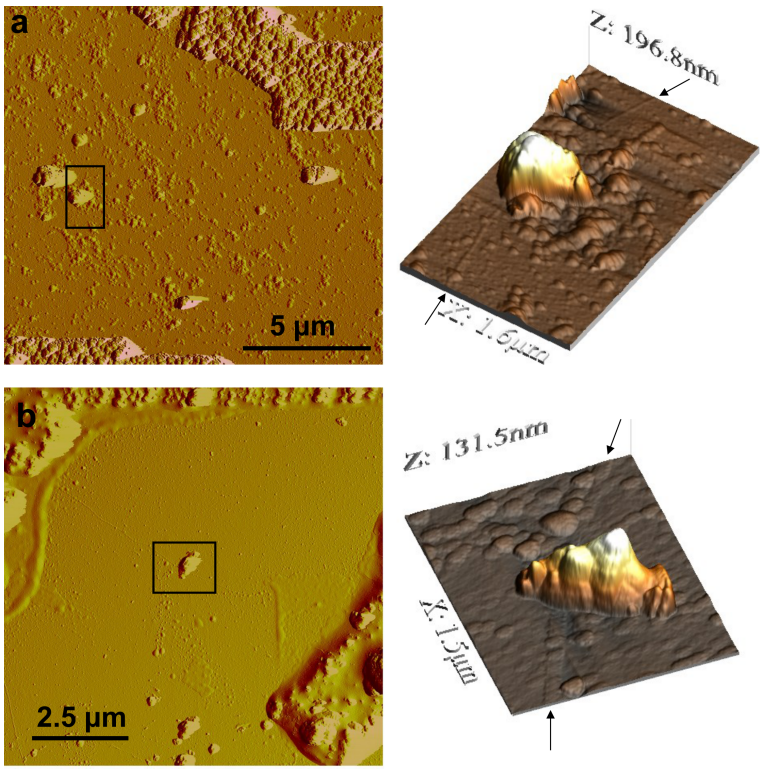

Figure 5.17: Two further results of manipulation of particles onto the CNTs. Left is the amplitude error showing the location of the NP in the context of the other features such as electrodes. Right is the topography of the particle, showing its position with respect to the CNT (indicated with arrows).

was low. Whether the particles are individual AuNPs or agglomerates cannot be reliably stated since the irregular shape could be attributed to the poor tip quality. The particle in Figure 5.17a was difficult to move and required a z height of -30 nm; -20 nm was not able to move it. The particle in Figure 5.17b was moved with a z height of 0 nm.

A final example of 150 nm NP nanomanipulation is given in Figure 5.18. Although the initial appearance was of a single particle, it was then observed to change shape and split into two parts during the process. After this occurred, first one of the parts was manipulated onto the CNT and then, after Raman analysis had been completed, the second part was also manipulated onto the CNT. A total of 11 iterations were used in the first manipulation and 10 in the second. The complete record of each step of the process is given in Appendix H. At the start of the process the particle was difficult to move, showing no change at z heights of -20 nm down to -50 nm. To achieve initial movement, contact-mode feedback

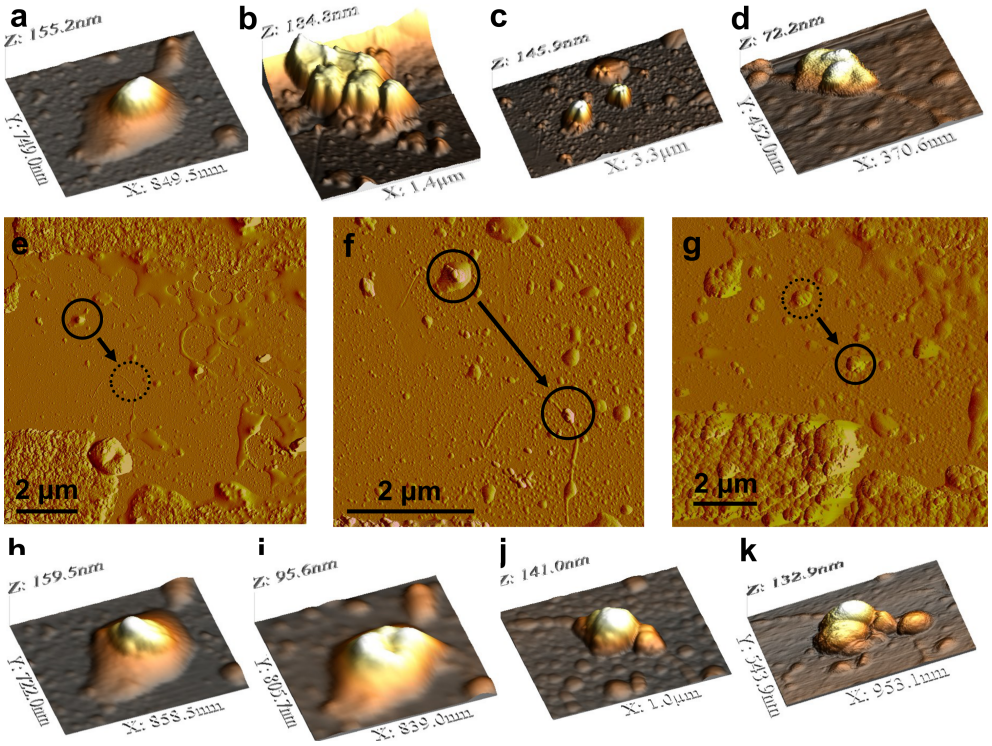

Figure 5.18: Nanomanipulation of (a) what initially appeared as a single particle onto a CNT, which (b) changed shape and then (c) split into two distinct parts. (d) The right-hand part was manipulated onto the CNT. The complete move is shown on the amplitude error images (e) before and (f) after this stage of manipulation. (g) In a second manipulation process the remaining particle (h) was manipulated, (i) leaving some material behind until (j) it was positioned on top of the CNT. (k) Finally, an ultrasharp AFM tip was used to obtain a higher resolution image of the particles on the CNT, some time later.

was switched on. While the setpoint was low, the tip was a tapping-mode tip with a high force constant so the forces would be higher than expected for normal contact-mode AFM. Once the particle started to move, paths were performed at a height of -50 nm until the last few near the CNT which were at -20 nm. The second manipulation used z heights of 0 nm after beginning at 20 nm and decreasing until effective movements were achieved.

5.3.1.4 Nanomanipulation of 50 nm nanoparticles

When gold nanoparticles of diameter 50 nm were deposited on samples containing carbon nanotubes, it was was done with the method of putting a drop of NP dispersion on the sample in a humid environment and then spinning after a given

length of time. This meant that the NPs were more dispersed than they were in some of the examples using 150 nm NPs. Whether the particles observed in AFM were composed of one or more NPs was still a matter of doubt, but appearances suggest that more individual NPs are obtained.

The 50 nm NPs could be manipulated in exactly the same way as the larger particles as already described. Their smaller size meant there was a smaller range of effective z heights. On a number of occasions a height of 0 nm was found to be either completely unsuccessful or partially successful but -20 nm was effective in all cases. Examples of good manipulation are given in Figure 5.19, where one particle was moved onto the CNT and then a second particle was moved onto another position on the CNT. The first particle was moved with 12 iterations of AFM scans and nanomanipulation paths and the second particle used 9 iterations. Both particles took approximately 35 minutes for the manipulation, discounting the time before and afterwards to obtain higher resolution AFM images for comparison and reporting purposes.

On another CNT one NP was first positioned, shown already in Figure 5.12. To this, a second particle was added, seen in Figure 5.20. This second particle was moved over a distance of 4.5 µm and once it was positioned on top of the CNT it was pushed together with the first particle to form a dimer. As far as can be measured by AFM, this dimer was orientated exactly parallel to the CNT axis.

5.3.2 Enhancement of Raman scattering

Once nanomanipulation had been successfully performed to place a gold nanoparticle on top of a CNT, Raman mapping was used to study how the Raman signal from the CNT was affected by the presence of the AuNP, as described in Section 5.2.4. A full example of this analysis process will be given here before other results are presented more briefly.

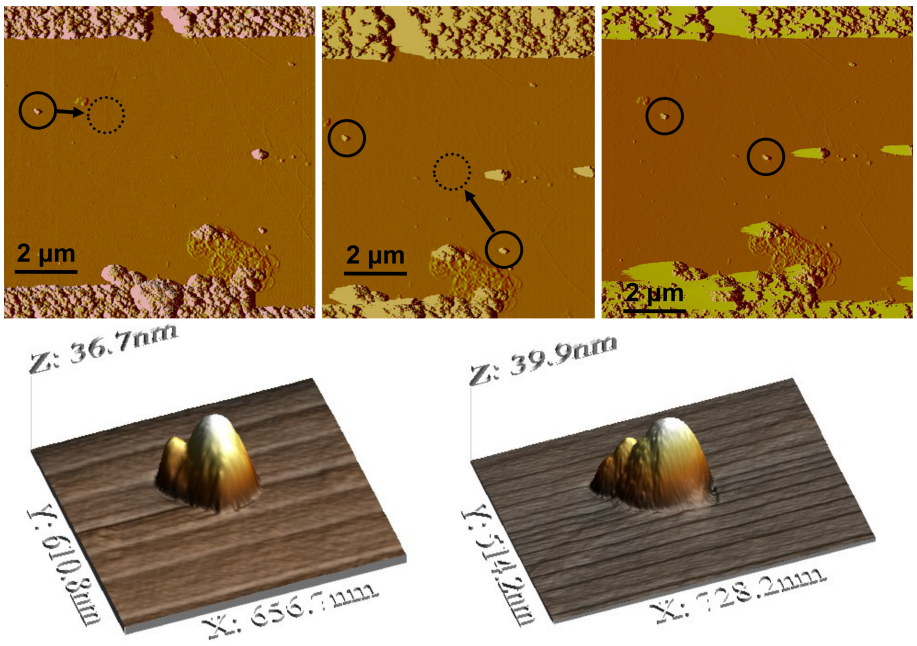

Figure 5.19: An example of manipulation of 50 nm NPs. The first was moved a distance of 1.9 µm (shown top left and top centre) and the second was moved 2.8 µm (shown top centre and top right). The topographies for the particles' final positions on the CNTs are represented in the bottom line. Note that the CNT has a very small height and is difficult to distinguish from the noise of the AFM measurement and the roughness of the sample. In addition, where the CNT lies parallel with the fast scan axis (x direction) it is nearly invisible in the amplitude error image but it is in fact no smaller at this point than any other.

5.3.2.1 Example of full analysis process

An example of the process of interpreting the Raman mapping data is given for the sample described already in Figure 5.18. Since this particle was from the batch with a diameter of 150 nm AuNPs, the 785 nm laser was used in all the Raman measurements.

A Raman finemap was made after the first stage of manipulation but before the second manipulation with the larger particle was completed. This map, made using the Nanonics piezo scanner, had points at which Raman spectra were taken spaced 200 nm apart in both x and y directions and a total size of 40 × 40 points. The total area mapped was therefore 8 µm by 8 µm, disregarding the contribution of drift occurring during the measurement. As each spectrum was measured for one minute, this map took in excess of 27 hours to measure.

Figure 5.21 shows the first step of the Raman-map analysis, where the total

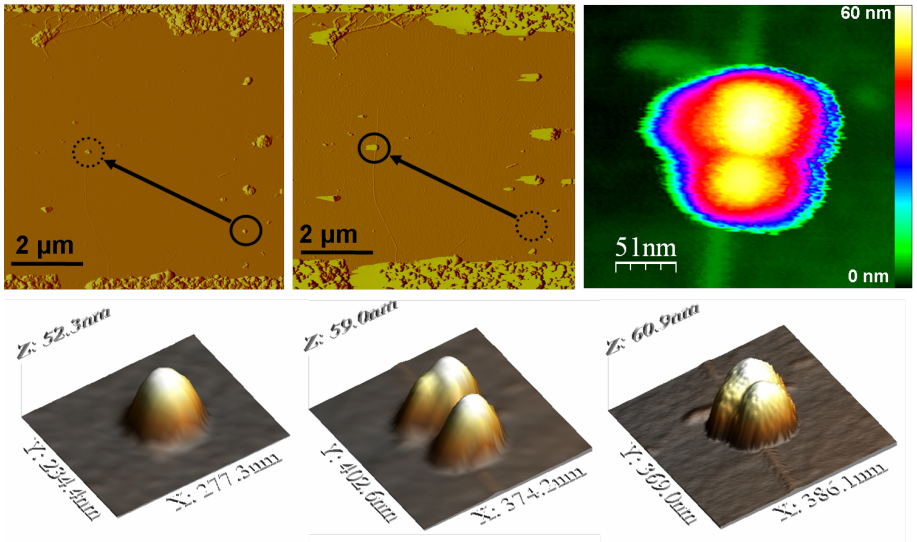

Figure 5.20: An example of a second 50 nm NP being manipulated to the same position on a CNT as first 50 nm NP had already been placed. The amplitude error images (top left and centre) illustrate the total move, over 4.5 µm. The topography images are given for the particle initially (bottom left), the two particles on the CNT with a clear separation (bottom centre) and the two particles after being pushed together while still on top of the CNT (bottom right). The topography of the final dimer is also given in a 2-D representation with a different colour scale, allowing both the CNT and the NPs to be observed (top right).

spectrum at each point was integrated and plotted as a colour map. Along with examination of the actual spectra at each point, looking for characteristic spectral shapes of electrodes or bare surface, this allowed the area of the map to be correlated with an AFM image of the same sample.

The next stage of the analysis is represented in Figure 5.22, involving the integration of only the G band region of the Raman spectra at each point. Using the correlation between the AFM image and the Raman map assigned from the previous stage of analysis, the Raman points corresponding to the CNT were identified. The spectra from that region were selected and plotted. The spectra show only a very weak signal in the region of the G band. The AFM image indicates that the CNT is probably a small bundle of CNTs rather than a single one, due to the height being between 5 nm and 10 nm along its length. The fact that no strong G band signal appeared in any of these Raman spectra meant that none of the CNTs present are resonant with the laser and the fact that the signal did not increase at one particular point meant that the enhancement from the

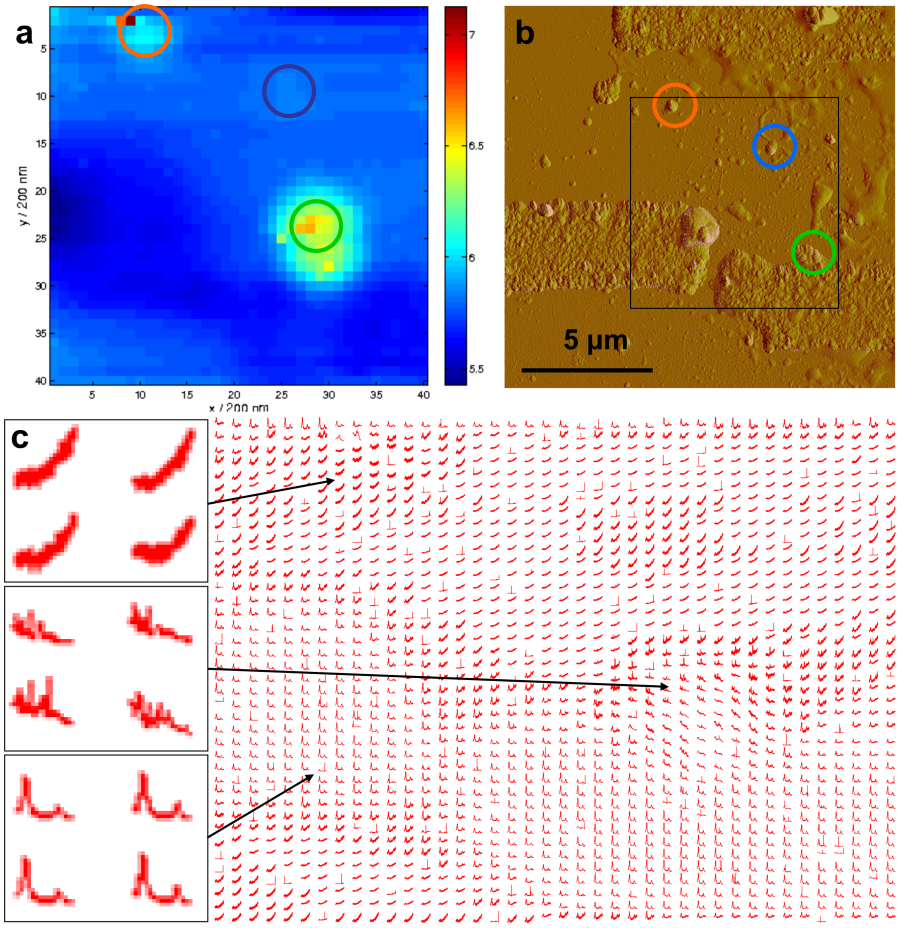

Figure 5.21: The result of a Raman finemap with steps of 200 nm and total dimensions of 40 × 40 points. The intensity of the whole spectrum was integrated and (a) plotted as a colour map with a logarithmic colour scale. (b) An amplitude error AFM image of the same sample, with the approximate area of the Raman map indicated by the black rectangle. The coloured circles relate particles that are identifiable in both images. (c, right) A mini image of each spectrum plotted in a grid of the same dimensions. This allows regions with characteristic spectral shapes to be identified, such as (c, top left) bare silica, (c, middle left) NP agglomerate and metal (c, bottom left) electrode.

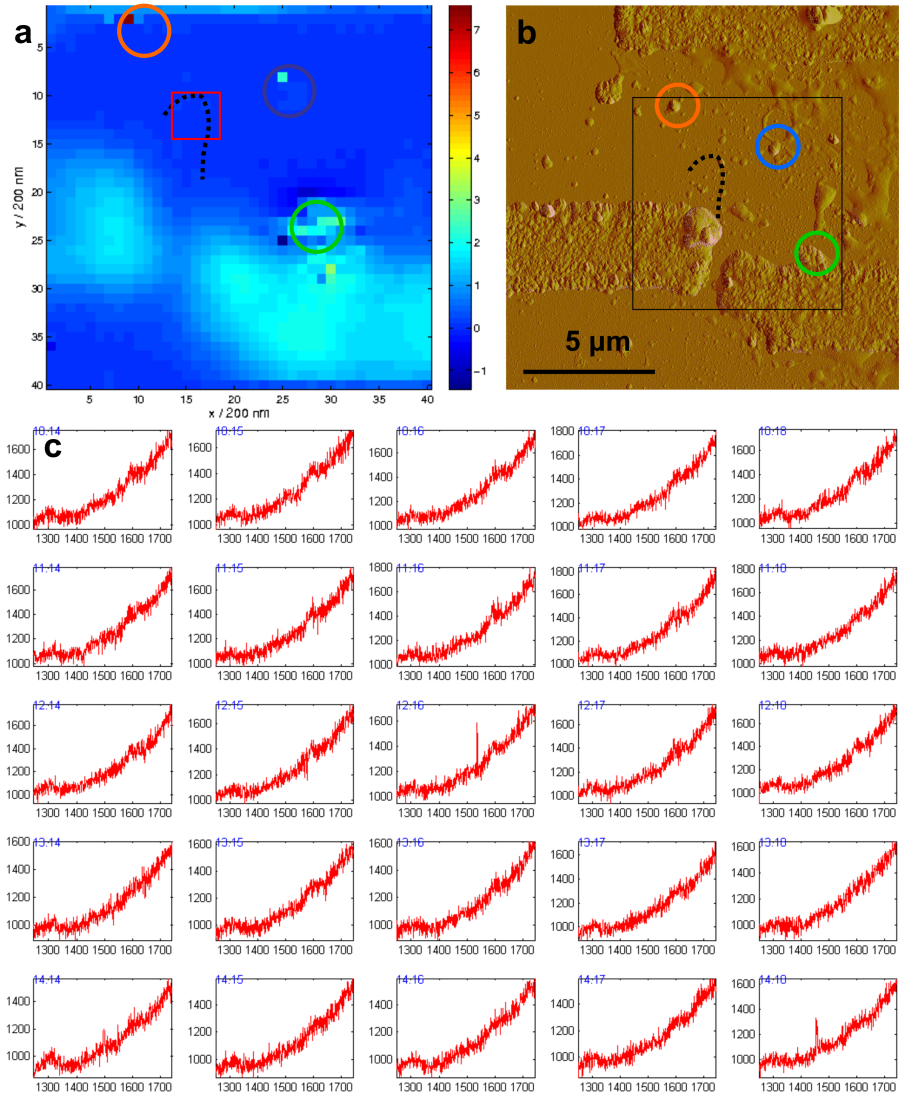

Figure 5.22: The second step of analysis of the Raman map shown in Figure 5.21, this time only integrating the area of each spectrum between 1560 cm^{-1} and 1590 cm^{-1}, corresponding to the G band of the CNT. (a) A colour map of the G band region and (b) the AFM amplitude error image, with the CNT position highlighted on both with a dotted black line. The red box on the colour map indicates the area that has been selected and (c) each spectrum within plotted on a grid. To maximise the space given for the spectra, the axes are not all labelled. The spectra are all plotted as Raman intensity (a.u.) against Raman shift (cm^{-1}).

manipulated nanoparticle was negligible.

Continuing with the same sample, Raman mapping was performed again after a second particle had been manipulated onto the CNT, as described in Figure 5.18. The analysis is shown in Figure 5.23. In contrast with the previous

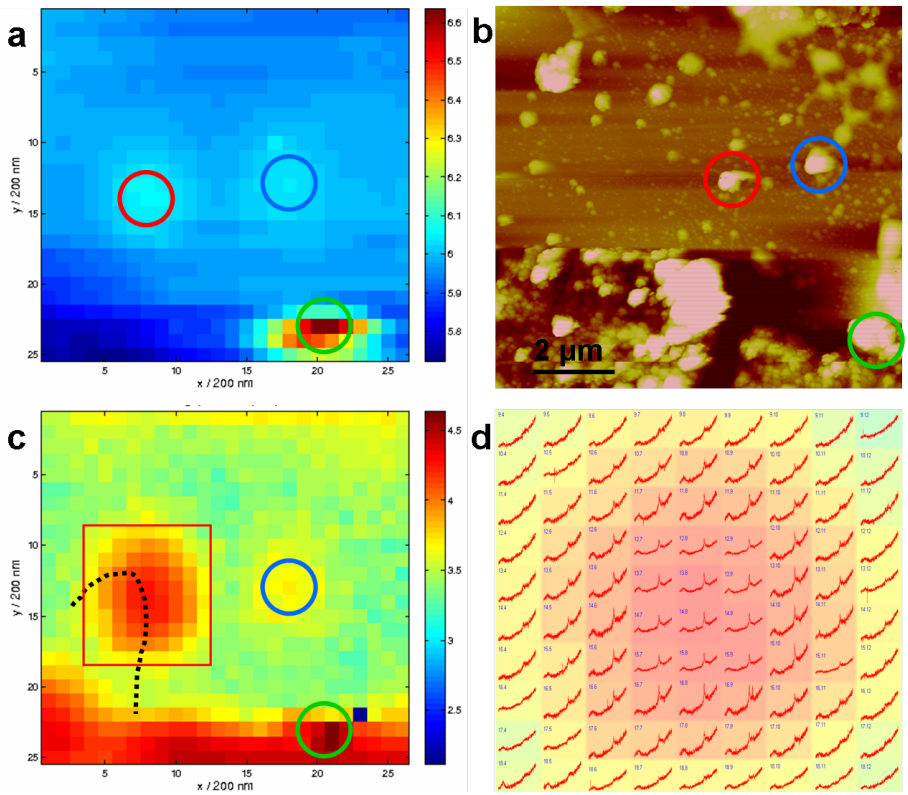

Figure 5.23: Analysis of a second Raman map on the same sample as shown in Figures 5.21 and 5.22, after manipulation of a particle from the position previous circled in orange to the position now circled in red in (a) the colour map of the total spectral area and (b) the AFM topography image. (c) The colour map showing the G band intensity shows a very clear region of higher signal where the NP was manipulated to. (d) The spectra taken from the enhanced region (red square) are shown superimposed over the colour map. Although the axes are not shown, the Raman shift axis is identical to that of Figure 5.22c and the intensities of the spectra are normalised according to their highest point. Note that drift, primarily in the y direction, during the Raman mapping measurement results in the Raman map (a and c) appearing squashed in the y direction with respect to the AFM image (b).

map, some of the spectra now do show a very clear CNT G band signal. The intensities of this G band are maximal at points at the centre of the the bright region, which corresponds to where the particle was moved to. The intensities decrease with distance from the particle, as expected for enhancement at a point, convoluted with a laser spot with a Gaussian profile.

The most intense spectrum in this Raman finemap is shown in Figure 5.24, along with the spectrum from the corresponding position in the previous Raman map, before the particle was manipulated. Integrating the G band areas of these

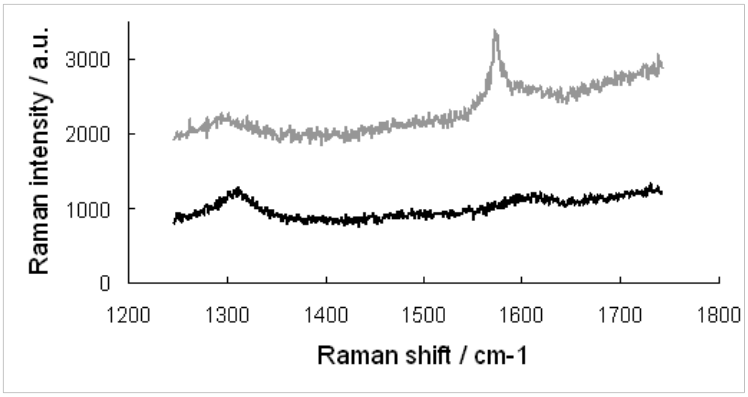

Figure 5.24: Raman spectra before (black) and after (grey) the second nanoparticle was placed on the CNT by nanomanipulation. No correction, other than removal of spikes, has been made to these spectra.

two spectra gives intensities of 1.0×10^3 counts and 2.3×10^4 counts for before and after the final nanomanipulation, respectively. The ratio of these numbers gives a 'raw' enhancement factor of 23. The calcium fluoride spectra indicate that the instrument detection was slightly more efficient for the second map, so the corrected enhancement factor is 20. This figure represents the increase in CNT signal intensity from the whole laser spot without and with the particle. The near-field enhancement may be crudely estimated by attributing the increased signal to arise only from the region close to the NP, for example a region of 150 nm in length, in comparison with the total length of CNT in the laser spot, 1 μm. In this case this shorter length of CNT is exhibiting an enhancement of 130×.

The strong plasmonic enhancement occurring in this sample allowed further investigations on the polarisation dependence of the Raman scattering, which will be presented in Section 5.3.2.4.

5.3.2.2 Enhancement from 150 nm nanoparticles

In addition to the example shown in detail in the previous section, plasmonic enhancement was observed on other samples containing 150 nm gold nanoparticles on CNTs. The first of these is presented in Figure 5.25. The AFM image revealed several possible CNTs, so the nanoparticle was initially manipulated

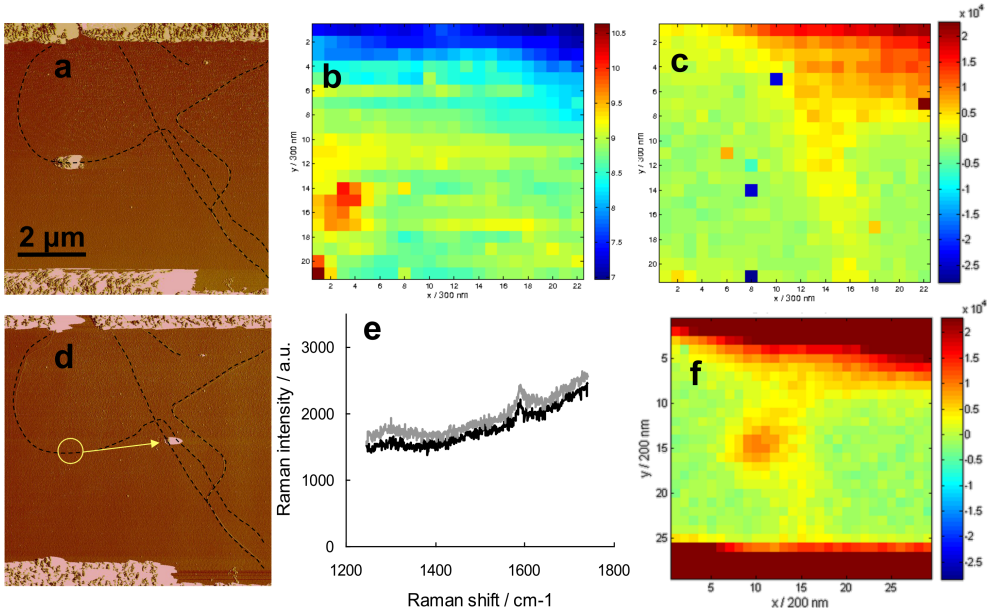

Figure 5.25: (a) An AFM (phase) image showing several CNTs with a AuNP positioned on one, on which a Raman finemap was measured and plotted as (b) the intensity of the total spectral range and (c) the G peak intensity. (d) An AFM (phase) image showing the AuNP positioned on a different CNT, on which a second Raman finemap was measured and (f) G peak intensities plotted. (e) Raman spectra from equivalent points before (black) and after (grey) the second nanomanipulation step.

onto what looked like an individual CNT (Figure 5.25a). A Raman finemap was measured, which showed the position of the AuNP (stronger intensity on the map of total spectral area, due to an enhanced background) and spectra containing CNT G peaks but there were no G peaks at or near the AuNP. There are two reasons for this: either the CNT is out of resonance with the laser and the AuNP enhancement is too small to make it measurable; or the feature that AFM suggests is a CNT is actually the 'ghost' of where a CNT once grew that has now been lost. Raman maps with 514 nm excitation show some very small CNT signals in the region of this CNT, suggesting that the former explanation is correct. The AuNP was then manipulated onto another CNT, where the G peaks had appeared in the first Raman map (Figure 5.25d). A second Raman finemap at this stage showed that the G peak of the CNT was enhanced at the position of the AuNP. The maximum measured G peak intensity in the second map was approximately 3.6× stronger than the G peak observed at the same point on the

first map, before the AuNP was in position. When considering the enhancement to be on a 150 nm length of the CNT, this implies a local SERS enhancement factor of 24.

In another case, a single 150 nm AuNP was manipulated onto a CNT bundle (Figure 5.26a), which was not resonant with 785 nm light. A Raman finemap on the area with the usual parameters did not reveal any CNT G peak signal. Nanomanipulation was performed a second time, putting a single particle further up the CNT bundle and adding to the first particle with a second (Figure 5.26b). The height of the latter became greater but the AFM was not capable or resolving the structure to identify whether it was a dimer or more than two AuNPs, nor any associated orientation that the structure might have. Another Raman finemap was measured but once again no CNT signal was observed.

However, switching to a 100× lens and measuring with longer acquisition times on isolated spots did reveal some peaks in the Raman spectrum. The 100× could resolve the positions of the 'dimer' and the single particle, and it was known from AFM that the CNT bundle followed a straight line between, so spectra could be measured at the 'dimer' and on the bare CNT bundle between the particles (Figure 5.26 c and d). Of the two peaks present in the G band region, the lower energy one, at 1587 cm^{-1}, has no change in size and the higher energy one, at 1614 cm^{-1}, has just over twice the intensity in the spectra measured at the plasmonic structure. The intensity of the D peak is approximately double in strength on the plasmonic structure compared to off it. While this does indicate that enhancement is being exhibited by this plasmonic structure, it does not enable the quantification of the enhancement factor, because the measurement positions were chosen by manual examination of the microscope image rather than by use of a systematic Raman finemap. Finally, it should be noted that the peak observed at 1614 cm^{-1} in both enhanced and non-enhanced spectra is somewhat blue-shifted out of the normal range for a CNT G peak. Possible reasons for this could be that the peak originates with something other than the CNT or that the CNT is heavily doped, which has been shown to blue-shift the G peaks in SWNTs [131].

On two occasions, when Raman spectroscopy was used to look for enhance-

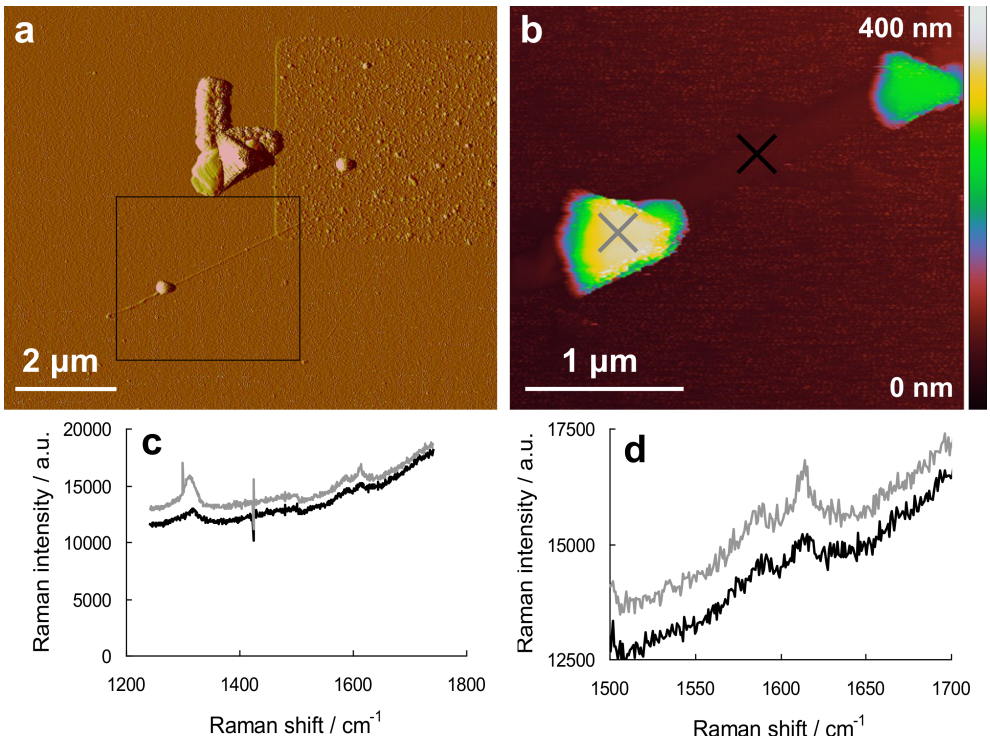

Figure 5.26: (a) An AFM (amplitude error) image showing a CNT bundle together with a AuNP. (b) An AFM (height) image showing the same CNT bundle now with a second AuNP added to the first, increasing its height (bottom left), and another single AuNP at another point on the CNT (top right). (c) Raman spectra from single, long-acquisition-time measurements on a bare part of the CNT bundle (black) and at the AuNP dimer (grey). (d) The same spectra as in part c, showing only the G band region.

ment from a AuNP on a CNT, the spectra obtained differed significantly from the expected CNT spectrum. In the region of the AuNP, the spectra contained large peaks at a range of Raman shifts covering the whole measured spectrum, which varied from point to point. Since the spatial distance between points in the finemap is less than the laser spot diameter, it was unexpected to see large, sudden differences between consecutive spectra. The reason for these extra peaks and possible strategies for minimising them were investigated and the findings are presented in Appendix I. No way of eliminating the anomalous peaks was found and they often had an intensity that dominated the spectrum, rendering any CNT undetectable. The ultimate outcome was that samples exhibiting these intense, fluctuating peaks were not of any use in studying SERS on CNTs.

Although several other samples with AuNPs positioned on CNTs were created

by nanomanipulation, the enhancement from them could not be identified. This was because of difficulties in correlating the AFM images to the Raman maps. Despite their long acquisition times (typically between 8 and 15 hours), the Raman maps often did not cover a large enough area to give reliable positioning information from obvious features such as electrodes. In addition, sample drift was very frequently observed after the Raman map was finished so, despite care being taken in the initial positioning, the region containing the AuNP was not always in the mapped area.

Switching from the 50× objective lens to the 100× lens could help overcome some of these difficulties but would bring disadvantages of its own. The improved spatial resolution of the optical image means positioning can be more precise and smaller features can be used, such as the AuNPs themselves, rather than just the big substrate markers and electrodes. However, the depth of field of the 100× lens is very much smaller than that of the 50×, so the sample height needs to be readjusted to compensate for z drift more frequently. This is not compatible with long Raman mapping measurements, which run for many hours without giving any opportunities for focussing to be performed. Future work may involve the development of an improved methodology for measuring Raman spectra on AuNP–CNT structures.

5.3.2.3 Enhancement from 50 nm nanoparticles

A single 50 nm nanoparticle was manipulated onto an individual CNT, which was not in resonance with either 514 nm or 785 nm lasers. Raman finemaps were measured with both lasers after the AuNP was in position and the electrode and the catalyst area were used to correlate the Raman map to the AFM image. The CNT was long enough to have a clear length several microns away from the AuNP, so the spectra at and far from the AuNP could be compared. However, no signal from the CNT was observed in the Raman spectra on either position with either laser.

On another location, a single 50 nm was manipulated onto the top of a small CNT bundle and a Raman finemap was measured with the 514 nm laser. Again,

the CNT bundle gave no Raman signal away from the AuNP, which indicates that none of its constituent CNTs were resonant with 514 nm light. The spectra from the position of the AuNP also showed no CNT signal, but the intensity of the spectral background increased at the AuNP to approximately three times its intensity on other places on the silicon oxide surface. Where clusters of AuNPs lay on the electrode surface, the signal measured there had the same peaks as other areas of the electrodes but the intensity was over three times stronger. Thus, the particles do have plasmonic properties and the ability to give a small enhancement but the enhancement factor is not large enough to allow a non-resonant CNT to be measured.

A second AuNP was added to the single AuNP already on the CNT bundle with the dimer axis parallel to the CNT, which should give the strongest enhancement (Figure 5.20). However, the Raman finemap measured with the 514 nm laser on the dimer still did not observe any Raman signal from the CNT. There was again an increase in the background intensity at the AuNPs. This time it was only double, possibly due to the resonance of the dimer moving slightly away from 514 nm or possibly due to the experimental conditions.

Finally, a single AuNP was positioned on a CNT that was resonant with 514 nm light. The Raman finemap that was measured with the 514 nm laser could be correlated with the AFM image using the positions of CNTs, electrodes and plasmonic particles. Figure 5.27 presents the results of the Raman map, which shows that the single AuNP was enhancing the Raman signal of the CNT. A comparison of the spectra from the AuNP–CNT position and the spectra from the same CNT with no plasmonic particle reveals an increase in intensity of 1.7×. No correction for instrument dependence is necessary in this case. If we assume that the enhanced length of CNT is 50 nm and the the spot size of the 514 nm laser was 770 nm, then the local SERS enhancement is approximately 26×, which is very comparable to the enhancement achieved from a single 150 nm AuNP under 785 nm illumination.

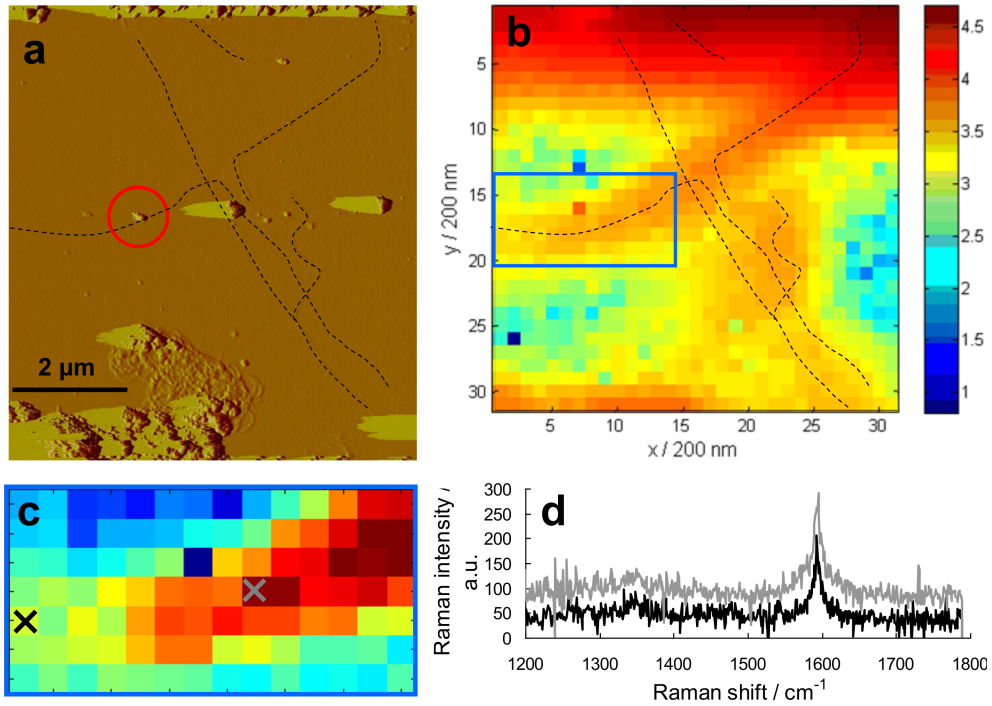

Figure 5.27: (a) An AFM (amplitude error) image showing a 50 nm AuNP (red circle) positioned on top of an individual CNT (black dashed lines. (b) The G peak intensity Raman map of the same location, where the positions of the CNTs correlate to areas of higher intensity. The colour scale is in $\log_{10}$(counts). (c) Part of G peak intensity Raman map containing the AuNP and a bare length of CNT, corresponding to the blue box in part b. (d) The spectra measured on a bare length of CNT (black) and at the AuNP–CNT position (grey), with the intensity axis offset for clarity.

5.3.2.4 Polarisation effects

Polarisation studies were performed where the SERS enhancement of the CNT signal was observed to be significant. One such sample was that described at length in Section 5.3.2.1. It was discovered that the location of the particle on the CNT could be identified in the Raman spectrometer's optical microscope when a 100× short working distance objective lens was used. This meant that the spectra of the enhanced signal could be measured without the time-consuming Raman mapping process.

The first measurements were made with simple orthogonal arrangements, as shown in Figure 5.28. The sample was orientated so that the CNT axis was lying in the x direction. Measurements were taken with the incident laser light linearly polarised in the x direction and the y direction and with filters in the

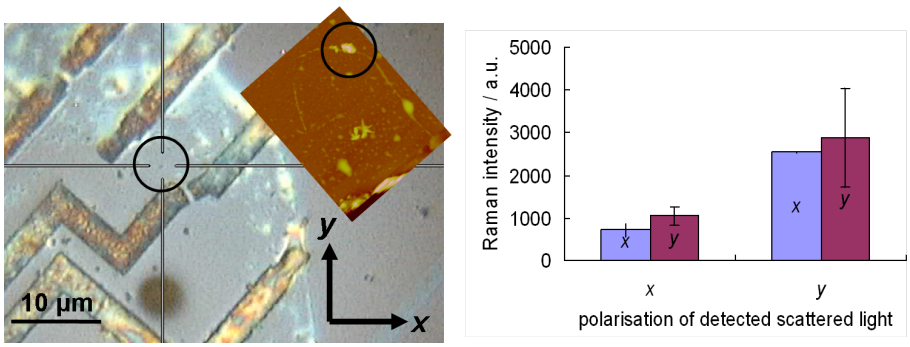

Figure 5.28: Preliminary polarised Raman measurements of CNT with SERS enhancement. The optical image (left) indicates the sample orientation with respect to the CNT direction, as seen by AFM (inset). The graph (right) shows the results from x-polarised incident light in lilac and those from y-polarised light in pink. No correction for instrument dependence has been applied. The error bars represent the standard deviation, from approximately eight repeated measurements.

scattered light path so that only the light scattered with polarisations in the x and y directions were measured. The results are not what would be expected of a bare CNT orientated in the same direction. As described previously, the Raman signal from a CNT is strongest with light polarised parallel to its axis: in this case in the x direction. However, for this sample the strongest signal is obtained when both incoming and scattered light polarisations are perpendicular to the CNT axis. It is also notable that the polarisation direction of the incident light is of lesser importance than the polarisation direction of the scattered light.

To fully test the polarisation-direction dependence of the Raman scattering from this sample, spectra were taken at each incident polarisation direction over 180° in 10° steps. Figure 5.29a illustrates the orientation of the sample with respect to the x and y directions. As described in Section 5.3.2.1, the x- and y-polarised scattered light was detected. The spectra obtained from one such set of measurements are given in Figure 5.29b.

To analyse the dependence of the CNT G band on the polarisation direction, the G band area in each spectrum was integrated, after a linear background had been subtracted. These integrated intensities were corrected for the instrument polarisation dependence using measurements made on calcium fluoride and then the parallel, $I_{\parallel}$, and perpendicular, $I_{\perp}$, components of the scattered light were

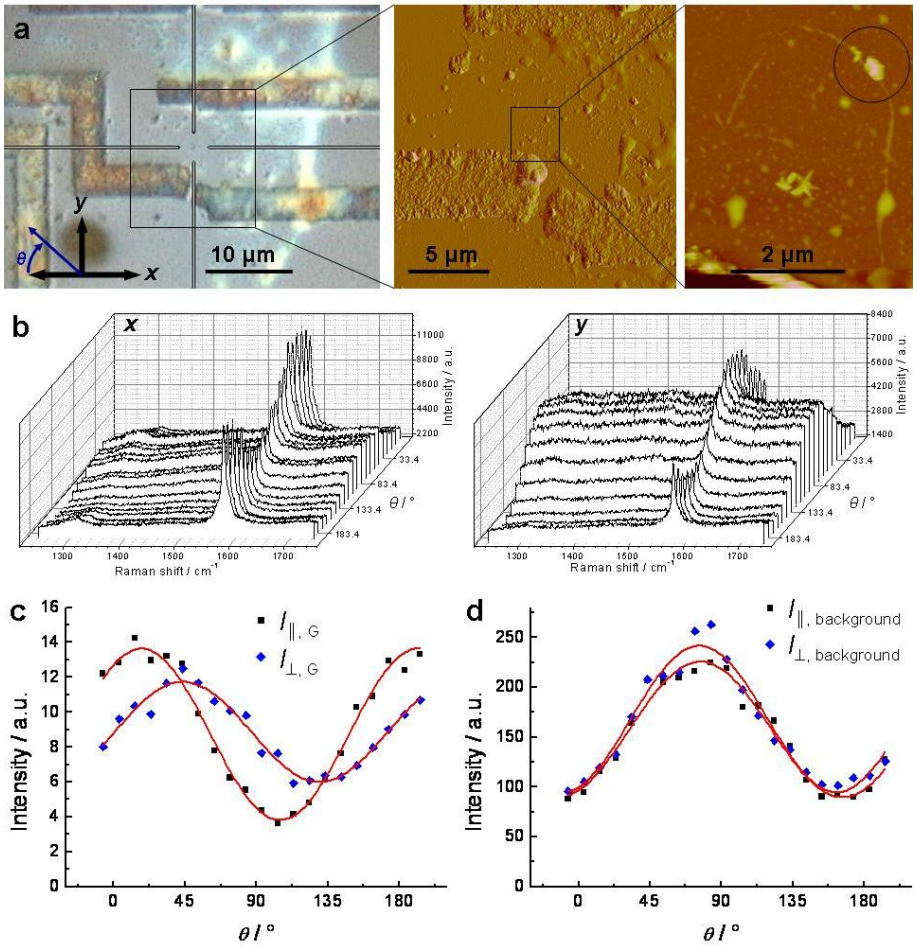

Figure 5.29: Results of polarised Raman measurements on a CNT bundle decorated with a plasmonic gold nanoparticle structure by nanomanipulation. The nanoparticle is visible in (a, left) the optical microscope image and (a, right) the AFM image, which also reveals the position and orientation of the CNT bundle. The x and y directions and θ are indicated in the optical microscope image. The spectra measured with x- and y-polarised scattered light are presented (b) without any correction. The intensities $I_{\parallel}$ (black squares) and $I_{\perp}$ (blue diamonds) for (c) the G band and (d) the background are plotted, along with a sine wave fit for each set.

calculated. Figure 5.29c shows these intensities as a function of the polarisation angle. The points were fit with a sine wave with no restraints, which gave a reasonable fit (adjusted $R^2 = 0.98$ and 0.95 for $I_{\parallel}$ and $I_{\perp}$, respectively). Several more sets of data were collected and analysed in the same way. The different sets showed a similar trend and the sine waves were all fit with a period of between 175° and 187° and an adjusted R^2 range of 0.60–0.98.

The $I_{\parallel}$ points shown in Figure 5.29c have a maximum at $\theta = 17°$ and a minimum at $\theta = 105°$. This is typical of all measurements: the mean over five sets was $\theta = 19(9)°$ for the maximum and $\theta = 109(8)°$ for the minimum. According to Figure 5.29a, it would appear that the CNT lies at an angle of $\sim \theta = 45°$. For an isolated CNT, one would expect the strongest $I_{\parallel}$ intensity to be parallel with the CNT axis. However, where the CNT signal in this sample is experiencing plasmonic enhancement, this is not what we see. It is likely that within the plasmonic structure, a hotspot occurs, giving a large enhancement to a highly localised region of space. Since the AFM-measured height of the CNT suggests that it is a bundle, one or more CNTs could have separated (perhaps during the nanomanipulation) from the rest of the bundle and could now be located in the hotspot, orientated at a different angle to the rest of the bundle. This would explain the observed results.

The $I_{\perp}$ points shown in Figure 5.29c have a slightly smaller difference in magnitude between the maximum and minimum. From the fit, the maximum and minimum were slightly shifted compared to the $I_{\parallel}$ points, at $\theta = 44°$ and $\theta = 130°$, respectively, while the period of the sine wave was very similar. Again, this was typical of other measurements, which had a mean of $\theta = 44(16)°$ for the maximum and $\theta = 131(12)°$ for the minimum. These observations are not yet well understood.

It is clear from Figure 5.29b that not only the G peak but also the background showed a polarisation-dependent response. To investigate this, the area of the background was measured by integrating the entire spectrum and subtracting the G peak area. These values, for five sets, were also corrected using calcium fluoride and converted to $I_{\parallel}$ and $I_{\perp}$. Figure 5.29d shows these intensities from one set, to which sine waves were also fitted. In this case the $I_{\parallel}$ and $I_{\perp}$ intensities were

equal, which indicates that the radiation causing the background signal was not polarised. There was, however, clearly a dependence on the incident polarisation direction, θ. From the fits, for $I_{\parallel}$ the average maximum was at $\theta = 79(3)^{\circ}$ and the average minimum was at $\theta = 168(2)^{\circ}$. $I_{\perp}$ was only slightly shifted from this with an average maximum at $\theta = 70(5)^{\circ}$ and an average minimum at $\theta = 160(3)^{\circ}$.

The polarisation dependence of the background signal was evidence that the plasmonic structure was acting as an antenna, harvesting the light that was incident on it with an efficiency proportional to the strength of its resonance in that direction. The maximum at $\theta = 79(3)^{\circ}$ suggested that the strongest plasmon resonance of the structure had a primary axis in that direction.

To test whether the background signal was the result of other Raman scattering events, luminescence or radiative emission arising from heating, the dependence on incident laser power was tested. Neutral density filters were used to reduce the laser power, to 10%, 5%, 1% and 0.5% of the total power ($\sim$1 mW). The results shown above all used 10% power. The background intensity was integrated, corrected for instrument dependence and converted to $I_{\parallel}$ and $I_{\perp}$, as previously. These intensities are shown as a function of polarisation angle in Figure 5.30a. The same data are shown in Figure 5.30b, presented for different polarisation angles as a function of laser power. This plot clearly shows that the dependence on power is non-linear. Both Raman scattering and luminescence would give intensities directly proportional to incident power, so this result indicates that heating is occurring and the background signal is the result of blackbody radiation, possibly from the substrate immediately surrounding the plasmonic antenna.

Another method of testing whether or not heating was occurring was by looking at the positions of the G peaks. The CNT G peak is known to downshift with increasing temperature at a rate of between -0.022 and -0.044 cm^{-1}/K [132], and therefore can be used as a local probe of temperatures where the Raman spectrum is measured. This will be discussed again in Section 6.2.

Spectra corresponding to the highest and lowest background intensities in several of the sets of measurements were peakfitted with one Lorentzian and two smaller mixed Lorentzian–Gaussian peaks. Taking an average of all

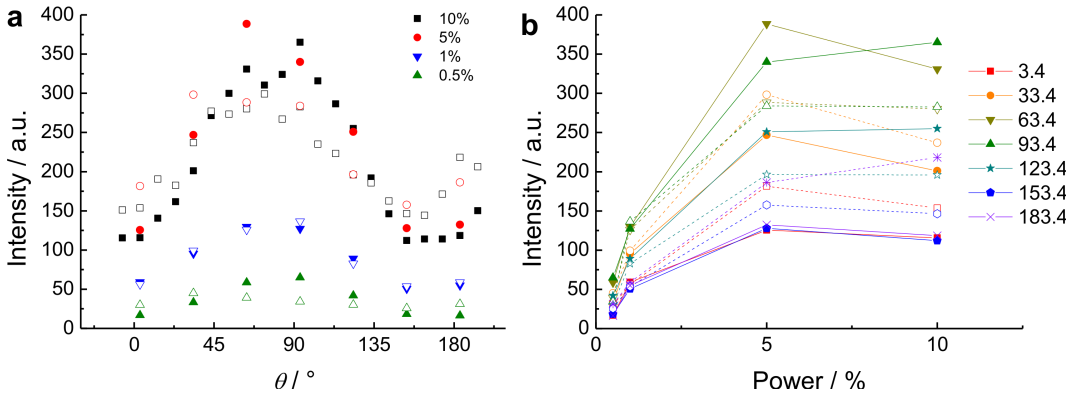

Figure 5.30: Spectrum background intensities from Raman measurements made on a AuNP structure interfaced with a CNT bundle with different laser powers, plotted (a) as a function of angle for different powers, and (b) as a function of power for each of the angles.

the Lorentzian peak positions of the the low-background measurements gave 1578.6(3) cm^{-1} and the high-background measurements gave 1579.0(4) cm^{-1}. These results correspond to a temperature decrease associated with the higher background of between 0 and 36 K, taking into account the experimental uncertainties and the range of values in the literature for temperature calibration. This finding is inconsistent with the proposed interpretation of the power-dependent results, so a conclusive statement of the cause of the background cannot be made.

To summarise the results of polarised Raman spectroscopy on a AuNP structure positioned on a CNT bundle, both the G band and background intensities are dependent on the polarisation angle. The G band shows a maximum approximately 20° anticlockwise of the CNT bundle axis, which could be due to a fragment of CNT orientated in that direction while being located in a plasmonic hotspot. The background intensity has a maximum approximately 30° clockwise of the CNT bundle axis, which may correspond to the strongest plasmon resonance of the structure made of AuNPs. The structure of the gold particles was not well defined, even when measured with high-resolution AFM, because the different parts had different heights, none of which matched the expected height of a 150 nm nanoparticle. As such it could not be directly confirmed that the direction of the strongest resonance corresponded to the principle axis of the

structure.

It was interesting to study this sample to find out what information could be gained from polarised Raman spectroscopy but it would be more useful to perform similar experiments on well-defined plasmonic structures, such as single AuNPs or AuNP dimers with different orientations, created by nanomanipulation, or more sophisticated structures created by other methods. In that case, comparisons could be made with the polarisation results reported in the literature.

5.4 Conclusions

This chapter has described an approach using AFM nanomanipulation for creating devices with carbon nanotubes interfaced with plasmonic antennas to enable surface-enhanced Raman spectroscopy. Colloidal gold nanoparticles were deposited onto substrates containing CNTs and an AFM tip was used to push the nanoparticles into position, precisely on top of the CNTs.

The AFM nanomanipulation process was optimised for controlling AuNPs without damaging the CNTs that were also present. Tip z heights of -20–0 nm were most effective and multiple paths were found to counteract the effect of thermal drift, meaning that particles could routinely be manipulated over tens of microns. Some challenges persisted, however, such as the loss of the NP onto the tip and the deterioration of tip sharpness and cleanliness, which decreased the resolution so that separate AuNPs could not be resolved and the CNTs were not identifiable from the surface roughness.

150 nm gold nanoparticles were successfully manipulated onto CNTs on at least ten occasions (not all shown here) and 50 nm gold nanoparticles were successfully manipulated onto CNTs at least five times.

A method was developed to use a piezo scanner within a micro-Raman spectrometer to create Raman maps with points separated by 200 nm, 300 nm or 500 nm. The spectra measured were presented as colour maps of the total intensity of the spectrum, which allowed the AuNP position to be identified, and of the CNT Raman G band intensity, which allowed the the strength of the enhancement to be quantified. It was found to be difficult to correlate AFM images, optical

microscope images and the Raman maps. Despite this, in some cases there was unambiguous enhancement of the Raman signal from the same CNT before and after a AuNP or AuNP-based structure was manipulated on to it.

Enhancements from the 150 nm particles were obtained using 785 nm laser excitation, with which the particles were resonant. A single AuNP increased the measured G band intensity by a factor of 3.6, which indicated a local SERS enhancement factor of at least 24. A 150 nm AuNP-based structure on a CNT bundle increased the measured G band intensity by a factor of 26, indicating a local SERS enhancement factor of at least 130.

Similar experiments with 50 nm AuNPs, manipulated onto CNTs and measured with 514 nm laser excitation, indicated that an enhancement of 1.7× could be achieved by a single particle. This suggests a local SERS enhancement factor of approximately 26. Non-resonant CNTs, which were not observed by Raman spectroscopy without plasmonic particles, remained undetectable by Raman spectroscopy when decorated with a single particle or a dimer orientated parallel to the CNT axis.

Raman spectroscopy with controlled polarisation was used to study the sample that showed the largest SERS enhancement. By rotating the polarisation direction of the linearly polarised incident light and separately collecting orthogonal components of the scattered light independently, the dependence of the parallel and crossed polarised scattered light intensities could be measured. The G peak showed a maximum intensity that differed from the CNT bundle axis, which may arise from a small portion of CNT being located in a plasmonic hotspot with a different orientation to the rest of the bundle. The background intensity also exhibited a polarisation dependence, with a maximum occurring at a completely different direction to the maximum G peak intensity. It is proposed that the background is strongest when the incident light is polarised parallel to the plasmonic structure's strongest resonance.

It is hoped that using this method it should be possible to study CNTs interfaced with a range of plasmonic structures formed from colloidal nanoparticles, including single nanoparticles, dimers parallel to the CNT axis, dimers perpendicular to the CNT axis and larger structures comprising three or more

particles. Since the Raman scattering intensity of CNTs is very dependent on the polarisation of the excitation light, they are excellent probes for reaching a better understanding of plasmonic structures and the interface between plasmonic structures and one-dimensional molecules.

In addition, nanomanipulation could be used to create a plasmonic antenna on a CNT that was electrically contacted. If this was achieved then experiments could be performed with plasmonically enhanced Raman spectroscopy simultaneously with electrical transport measurements, as was the overall aim of the NANOSPEC project.

Chapter 6

Combined Raman–transport measurements

6.1 Introduction

The electrical properties of SWNTs have already been described briefly in Section 2.1.3. There, it was stated that approximately two thirds of SWNTs are semiconducting and the remaining third are metallic or quasi-metallic, depending on their (n, m) indices. In addition, Section 2.1.3 explained that the conductance of a SWNT can be modelled with the Landauer formula, which describes the measured resistance of a SWNT device, R_{tot}, as the sum of resistances from the SWNT itself, R_{SWNT}, scattering, R_{S}, and contacts, R_{C}:

$$R_{\mathrm{tot}} = R_{\mathrm{SWNT}} + R_{\mathrm{C}} + R_{\mathrm{S}}. \tag{6.1}$$

Although the theoretical resistance of the SWNT is ∼6.5 kΩ, most measured resistances are of the order of 1 MΩ [133]. Interesting behaviour can be seen in devices specifically designed to have low contact resistances. For example, Yao *et al.* reported resistances as low as 17 kΩ and they were able to achieve a very high current density of more than 10^9 A/cm^2, with an applied bias voltage of 5 V on SWNTs deposited from dispersion onto a SiO_2 surface between Ti/Au electrodes. At high bias, the current in the SWNT saturated, implying non-Ohmic behaviour [134]. Moreover, Pop *et al.* showed that in suspended SWNTs

between Pt electrodes in vacuum, negative differential conductance (NDC) was observed, whereby the current decreases with an increase of the bias voltage, above a certain voltage [135].

The reason for current saturation and NDC has been attributed to electron–phonon scattering [134, 135]. If a high bias voltage is applied to a SWNT device with low contact resistances, then the electrons are accelerated until they have sufficient energy to emit an optical phonon. This scattering event prevents the current from increasing beyond the saturation limit. If the phonons created by the high-energy electrons are not dissipated by thermal conduction to the contacts, substrate or gases, then the increased phonon population itself increases the resistance of the SWNT, through the increased probability of scattering between an electron and an existing phonon. This results in the observed NDC [134, 135]. At low biases the electron does not have the energy for optical phonon scattering and, due to the 1-D nature of the SWNT, acoustic phonon scattering is suppressed, so ballistic electron transport can occur.

Although this explanation accounts qualitatively for the observed phenomena, further research is needed to understand more fully the behaviour at high bias voltages, the limits of current density, the factors affecting current saturation and NDC, the coupling between electrons and phonons, the coupling between phonons that leads to thermal conductivity and heat dissipation and the structural changes occurring at the point of electrical breakdown. Since Raman spectroscopy can probe phonon modes in SWNTs, experiments combining electrical transport and Raman spectroscopy on SWNTs provide a route to furthering our knowledge and understanding of this subject. Increased understanding could aid successful application of SWNTs in integrated circuits, where they could be used as conducting interconnects or as field-effect transistors [136, 137].

6.2 Example of Raman–transport study

Almost all the recent research into electrical transport with Raman spectroscopy has been performed by Cronin and co-workers [6, 132, 136–142]. Their work provides an example of the types of things that were aimed to be investigated

within the NANOSPEC project, while some important aspects are different.

6.2.1 Comparison of approaches

One of the differences between the work of Cronin and co-workers and the NANOSPEC work is that the NANOSPEC project would have an interest in both metallic and semiconducting SWNTs, while Cronin and co-workers are almost exclusively interested in metallic or quasi-metallic SWNTs. A second difference is that Cronin and co-workers work on suspended SWNTs, while the NANOSPEC project would also look at surface-supported SWNT, meaning that longer SWNTs could be studied, four-probe electrical measurements could be made and heat would be dissipated to the surface, which may change the current-carrying capacity of the SWNT. Finally, the NANOSPEC project's aims were based on the use of plasmonic antennas to enhance the Raman scattering so a stronger and clearer signal could be obtained irrespective of resonance between the SWNT and the laser. Although Cronin has also shown an interest in plasmonics [143–145], he has not yet combined it with Raman–transport experiments on SWNTs.

One area that the NANOSPEC project's approach would be more able to explore than the approach taken by Cronin and co-workers is the behaviour at higher bias voltages, up to the point of electrical breakdown. While, if current saturation or NDC occur, increasing the voltage does not increase the current, it does increase the temperature of the SWNT. As described previously, the raised temperature decreases the intensity of the Raman spectrum, but the use of plasmonic antennas should allow the continued monitoring of the Raman spectrum at these increased temperatures. The changes in phonon population and the structural changes occurring in the SWNT as it approaches electrical breakdown could be studied. This could be done in different gas environments and with both surface-supported and suspended SWNTs, since these conditions influence heat dissipation and phonon populations.

Another subtly different study that may also be performed more effectively with NANOSPEC's approach would be to explore the maximum current that a

SWNT may transport. Although a considerable body of knowledge has already been gathered on the limits of current in SWNTs, the use of plasmonically enhanced Raman spectroscopy on samples tailored for high-current experiments would contribute further understanding in this area. Cronin and co-workers have reported more results from SWNTs that were tuned to show NDC but they have not reported Raman spectra from SWNTs carrying a current higher than 10 μA. Again, surface-supported SWNTs may be more appropriate for this study due to the improved heat dissipation and the use of plasmonic enhancement should help provide clear Raman spectra.

6.2.2 Device design and experimental setup

The general device design used by Cronin and co-workers comprised a silicon wafer with a thick insulating SiO_2 layer, platinum electrodes separated by a trench of width 2–5 μm and SWNTs grown by CVD over the trench from catalyst particles located on top of the electrodes. As the SWNT growth was the final step in device creation, the SWNTs were not damaged or contaminated during post-processing steps. A bias voltage, V_b, could be applied between the platinum electrodes and the source–drain current, I, was measured. Additionally, a gate voltage, V_g, could be applied to the silicon wafer, allowing it to act as a global backgate. Before use in Raman–transport studies, devices were screened for having the electrical properties of a single, individual, suspended SWNT. Raman spectroscopy was carried out using lasers of wavelength 532 nm, 633 nm and 785 nm. Measurements were performed in a controlled environment, either vacuum (pressure not stated) or in Ar, CO_2 or He gases, so as to prevent the SWNTs burning at high applied voltages [132, 136–138, 140, 141, 146, 147].

6.2.3 Experimental observations

Of the considerable body of work that Cronin and co-workers have completed on suspended, electrically-connected SWNTs, only a selection is presented here. It is presented under three categories: studies focusing on the electrical response of SWNTs in different conditions; studies primarily interested in probing the phonon

populations while using electrical current to heat the SWNTs; and studies concentrating on the effect of gate voltage on the Raman signal. This distinction is rather arbitrary, however, since there is much overlap in their fundamental outcomes, such as the observation and understanding of electron–phonon coupling.

Electrical measurements of suspended SWNTs

Bushmaker *et al.* performed Raman–transport experiments on devices of individual, suspended, quasi-metallic SWNTs, produced as described above [132]. The current through the SWNT, I, was measured while applying a bias voltage and a gate voltage. With respect to the gate voltage two regimes were used: 1) $V_\mathrm{g} = \frac{1}{2}V_\mathrm{b}$, which ensured the Fermi energy was always in the bandgap so the SWNT was undoped, and 2) $V_\mathrm{g} = 2$ V, which meant the SWNT was p-doped. Striking differences were observed between these two regimes. The I/V_b curve for the undoped SWNT was linear, indicating Ohmic behaviour, while for the p-doped SWNT current saturation and NDC were observed. Raman spectra taken at a range of V_b in each of the two gating regimes provided information about the phonon populations. In the undoped SWNT the G^+ and G^- peak positions downshifted by similar amounts as the current through the nanotube was increased. The peak downshifts were calibrated against temperature by measurements using a temperature-controlled stage, then the downshifts observed from electrically heated SWNTs could be converted to temperatures. For the p-doped SWNT, the G^+ and G^- downshifts, and therefore effective temperatures, differed. The G^+ downshift indicated a higher temperature, especially at high bias voltages. This difference in temperature was interpreted as non-equilibrium phonon populations, in comparison with the equilibrium phonon populations that were observed in the undoped SWNT. The electrical measurements were interpreted with a Landauer model, fitted to the data in both regimes with parameters of electron and hole transmission coefficients, capacitance and bandgap. The transition between Ohmic and NDC behaviour was explained by the presence or absence of a bandgap at the Fermi energy and how that affects the response to increased temperature. These findings were consistent with other

reports of optical phonon emission causing self-heating in suspended conducting SWNTs [132].

Amer *et al.* continued the Raman–transport studies on suspended SWNTs, in particular turning their attention to the point at which NDC occurs on the I/V_b curve [139]. Careful observation showed them that the current, after reaching its peak, dropped suddenly before continuing to decrease gradually as V_b was increased. At the same point, the G^+ and G^- downshifts deviated from one another, indicating that non-equilibrium phonon populations had been created. The bias voltage that this 'kink' occurred at varied with V_g and with different gases (Ar, He and CO_2), while in vacuum it was not present. A range of temperatures (88–373 K) was tested and the position of the kink upshifted and downshifted within this range, with a maximum occurring at 233 K. At the lowest temperatures, the kink was not observed. The Landauer formula was applied to the electrical data and it enabled calculation of the voltage drop across the SWNT resulting from optical phonon scattering, V_{op}, separately from the other contributors to resistance. In this case, the kink consistently appeared at $V_{op} = 0.2$ V. This corroborates the belief that conducting electrons in SWNTs scatter optical phonons when they reach a threshold energy. Amer *et al.* used the Landauer formula to fit the data from above and below the kink, changing only one parameter, the non-equilibrium factor, between the two regions. This factor was observed to depend on the gas environment so it allowed gases to be ordered by how effectively they couple vibronically to the phonons in the SWNT [139].

Non-equilibrium phonon populations

Bushmaker *et al.* first reported non-equilibrium phonon populations in 2007 when they compared the positions of the Raman G^- and G^+ peaks of suspended SWNTs under high electrical bias [138]. In approximately one third of the devices studied, the G^+ peak moved to a lower Raman shift by a greater extent than the G^- peak moved. As described above, these downshifts could be converted to effective temperatures, using a calibration based on a temperature-controlled stage. Thus in these devices the G^+ was preferentially heated. The anti-Stokes

/Stokes intensity for the G^+ peak gave a comparable temperature estimate. The G^+ peak also increased its width as its position changed. In a small number of devices the G^- peak instead was preferentially heated, while in others either the peaks were not resolvable or both peaks downshifted equally. It is not clear how the intensities of the Raman peaks were affected by V_b because the authors showed that the intensity of the shifting peak decreased but regarding the same device they also wrote that the integrated areas of both G peaks remained constant. The fact that the integrated areas were constant was presented as evidence that the resonance conditions had not changed. In metallic SWNTs, as in these experiments, the broadened, BWF-shaped G^- peak represents a longitudinal optical (LO) phonon and the G^+ represents a transverse optical (TO) phonon. Bushmaker *et al.* explain the preferential heating as arising from the two Kohn anomalies in metallic SWNTs: one of higher energy at the Γ point on the LO phonon branch and one of lower energy at the $2k_F$ point on the TO phonon branch. Electron–phonon coupling at the $2k_F$ point is stronger than at the Γ point and the electrons reach the energy of the TO phonons first, so the TO phonon is preferentially heated. The electrical measurements were fitted with a Landauer formula. It was discovered that not only the emission of optical phonons but also their absorbance must be considered as scattering events in the formula to achieve a good fit to the data. In this study the highest current density that was reported was 5.3×10^8 A/cm^2 [138].

After this first report of preferential heating leading to non-equilibrium phonon populations, several other studies have been performed by Cronin and co-workers [6, 132, 136, 137, 139]. Much of this work was aimed at reaching a better understanding of phonon relaxation processes, as phonon–phonon coupling, thermal transport to the ends of the SWNT and thermal conduction to the surrounding gas environment. For example, Deshpande *et al.* measured Raman spectra at different locations along an electrically heated, suspended SWNT [136]. They saw in shorter (2 μm) SWNTs the phonons remained in thermal non-equilibrium, with the G^+ peak having a maximum temperature in the centre of the SWNT and the temperature of the G^- peak being approximately constant throughout its length. In contrast, longer (5 μm) SWNTs showed an approximately equal

increase in the temperature of both G^+ and G^- peaks, with both cooling towards the contacts compared to the centre. Thus, they proposed a model in which hot phonons become thermalised if the length of the SWNT is sufficient [136]. While Deshpande *et al.* performed their study only in an argon atmosphere, Hsu *et al.* compared the temperatures measured in the centre of the suspended SWNTs in different gas environments [137]. They showed that the electrical powers required to reached comparable temperatures in a vacuum were far smaller than the powers needed in gases at ambient pressure. A comparison of different gases revealed that their ability to remove heat from the SWNT, known as thermal boundary conductance, g, was ordered $g_{Ar} < g_{He} < g_{N_2} < g_{CO_2}$ [137]. In addition to these results of dissipation of heat from electrically heated SWNTs, Cronin and co-workers performed measurements using laser heating to explore how the heat was conducted along the SWNT, either by using a laser in the centre and microthermometers as contacts on the ends [140], or by using one laser to heat and a second laser to measure Raman spectra at points along the tube [141]. These studies all contributed knowledge towards the goal of reaching a full understanding of the electron–phonon and phonon–phonon scattering processes within SWNTs.

Dependence of Raman scattering on gate voltage

Devices containing individual suspended quasi-metallic SWNTs, as described in Section 6.2.2, were studied by Raman spectroscopy while the voltage applied to the gate electrode, V_g, was varied [146–148]. Bushmaker *et al.* paid particular attention to the appearance of the G^- peak as the gate electrode potential was changed, effectively moving the Fermi energy of the SWNT [147]. The Raman shift of the G^- peak initially decreased and then increased as $|V_g|$ increased, typically from 0 to 6 V, making a "W"-shaped curve. At the same time, the G^- peak became less broad. These observations were explained in terms of a Kohn anomaly at the Γ point, which normally causes an upshift in the phonon frequency due to phonon softening, but which is suppressed when the Fermi energy is in the bandgap. The results showed that the Kohn anomaly in these suspended quasi-metallic SWNTs was nonadiabatic [147].

In a separate study, Bushmaker *et al.* reported a change in Raman intensity as the gate voltage was varied, on the same type of devices as the previous study [146]. They showed that the intensities of all Raman bands (RBM, G^-, G^+ and G′) increased significantly, by nearly two orders of magnitude, as $|V_g|$ increased from 0 to 2.5 V. This intensity modulation was not explained by a change in resonance condition because it was not dependent on the excitation laser wavelength and the anti-Stokes/Stokes ratio was constant over the V_g range. Instead, since the intensity drop occurred when the Fermi energy was zero, the reason appeared to be related to the cause of the small bandgap. The authors claim that the bandgap is not caused by the tube curvature or a Peierls distortion, as other reports have claimed, but it is caused by a Mott insulator transition, which causes electrons to become strongly correlated and localised to their parent atom [146].

Further investigation of these effects was performed by Dhall *et al.* [148]. As in the previous study, pristine, suspended, quasi-metallic SWNTs were studied with Raman spectroscopy while the gate voltage was varied. Again, the G^- peak first downshifted then upshifted with increasing $|V_g|$, giving a W-shaped relationship, and the intensity of the G^- peak reduced in the region of V_g near 0 V. In contrast to the previous report, Dhall *et al.* did not see any change in position or intensity of the G^+ peak as V_g was varied. The experimentally measured maximum G^- downshift was linearly related to the ratio of Raman intensities at $V_g = 0$ V and at larger V_g (where the intensity became constant). On at least one device, the maximum downshift (15 cm^{-1}) was larger than predicted by theory (3 cm^{-1}), due to strong electron–phonon coupling. The range of strengths of electron–phonon coupling between the SWNT devices could be explained by chirality dependence, although the full mechanism is not yet well understood. The behaviour described here was exhibited by approximately half of the suspended, quasi-metallic SWNTs, while the other half showed no change in the position of the G^- peak and and a slight decrease in its intensity as $|V_g|$ was increased. The first case was explained by strong electron–phonon coupling due to the nonadiabatic Kohn anomaly and the alternative by weaker electron–phonon coupling and the Kohn anomaly being unimportant. Dhall *et al.* performed these

measurements at a range of temperatures (4–400 K) [148] and it was observed that devices switched from the latter to the former types of behaviour as the temperature was lowered. Moreover, within the set of SWNTs that showed nonadiabatic (W-shaped shift *vs* V_g) behaviour, the maximum downshift was larger at lower temperatures for some and was independent of temperatures for others. Comparison with calculations indicated that the presence of a small bandgap, arising from curvature or electron–electron interactions, was important in determining whether the temperature affected the maximum downshift or not [148].

6.3 Progress and prospects

Over the course of the NANOSPEC project, of which the work presented in this thesis is part, progress was made towards measurements of Raman spectra during electrical transport, in particular with plasmonic enhancement of the Raman scattering. The creation of devices containing SWNTs with electrical contacts and plasmonic antennas proved challenging and an optimal device configuration has yet to be realised. The setup for electrical transport experiments also needed to be developed, as appropriate for different device designs. The progress made in devices and experimental setup will be discussed in the following two sections.

6.3.1 Preparation of devices

As described in Section 2.4, a number of approaches were made within the NANOSPEC project towards creating devices suitable for plasmonically enhanced Raman–transport measurements on SWNTs.

In particular, the sample described in detail in Section 5.3.2.1, was selected as having promise, if conducting AFM probes are used within a Raman spectrometer. This sample contained a long bundle of SWNTs lying on a SiO_2 surface with 150 nm gold particles manipulated onto it, giving a strong Raman signal when irradiated with 785 nm light. Equipment available in Jerusalem has the capability required for these measurements so Talia Yeshua and Christian Lehmann plan to

perform them imminently.

Other devices that can be studied with the use of conducting AFM are those created by dielectric deposition. These samples, made by Aravind Vijayaraghavan in collaboration with Sebastian Heeg, have a large array of positions on which SWNTs may be deposited from dispersion to positions between pairs of electrodes. One electrode may be contacted macroscopically with the other requiring conducting AFM. If a multi-probe AFM is available then a second probe with a plasmonic particle at the end could provide plasmonic enhancement (tip-enhanced Raman spectroscopy, TERS) while a current is passed through the SWNT. Alternatively, samples were prepared with simple plasmonic structures present between the electrode pairs, so plasmonically enhanced Raman–transport could be performed with only one conducting AFM probe inside a Raman spectrometer.

A sample design not requiring the use of conducting AFM was to use the local heating method [28] to grow SWNTs from the heater electrode to a counter electrode, with plasmonic antennas pre-patterned by lithographic techniques between the electrodes. This sample was initially created by Niklas Lindahl with additional lithography for the antennas and counter electrode performed by Roberto Fernández-García. Unfortunately, extensive experiments on test samples (without the second lithography step) performed in Edinburgh revealed that SWNT growth was not possible due to sample degradation, so SWNTs were not successfully grown over the antennas between electrodes in this way.

Finally, long surface-supported SWNTs as those described in Chapter 5 would be suitable for plasmonically enhanced Raman–transport experiments if the SWNT was successfully contacted to the electrodes and the gold nanoparticles manipulated onto the SWNT provided sufficient enhancement. Although this has not been achieved yet, there is no reason to believe it is not attainable in the near future.

6.3.2 Preparation of experimental setup

Two systems were developed for enabling Raman–transport measurements for the NANOSPEC project: Jerusalem's multiprobe AFM–Raman and Edinburgh's

Raman with controlled gas chamber.

The system in Jerusalem was developed by the staff of Nanonics Imaging Ltd. under the direction of Prof. Aaron Lewis. Its application to Raman–transport on SWNTs was performed by Christian Lehmann along with Talia Yeshua. It uses the Nanonics MV4000 AFM, which can operate two AFM probes with nanometre precision either together or independently. It was positioned within a Renishaw micro-Raman spectrometer equipped with 532 nm and 785 nm lasers. The main advantage of this system is that the SWNT need not be connected to macroscopic electrical contact pads. Instead, the conducting probe can make contact with small electrode pads or directly to the SWNT itself, although the latter is difficult due to the poor spatial resolution available from the conducting probe. Another advantage is that the sample is positioned on a piezo scanner, which may aid alignment of the sample in the centre of the laser spot. The main disadvantage of this system is that it does not give any opportunity to control the gas environment so all measurements must be performed in air. As such, the currents passed through the SWNT must be limited to prevent the SWNT burning.

The system in Edinburgh is also based on a Renishaw micro-Raman spectrometer but this system aims to provide a controlled gas environment in which to perform the Raman–transport measurements. Existing equipment included a vacuum chamber with electrical feedthrough and optical window and simple micropositioners. However, the electrical contact pads on the sample that were expected to be studied were too small to be reliably contacted with the simple micropositioners, which only had one degree of freedom and had non-linear tip motion. Improved micropositioners were purchased, which had linear motion in three dimensions, but these were too large to fit in the existing vacuum chamber.

Thus, a new gas chamber was designed which had to fulfil several requirements. Firstly, for electrical measurements to be made on samples with small (200 μm square) contact pads, there needed to be an electrical feedthrough and micropositioners holding electrically-connected sharp tungsten needles. Secondly, the requirement for *in situ* Raman spectroscopy introduced several restrictions in the chamber geometry. The chamber required an optical window close enough to the sample to allow light to focus through a long-distance 50× objective lens.

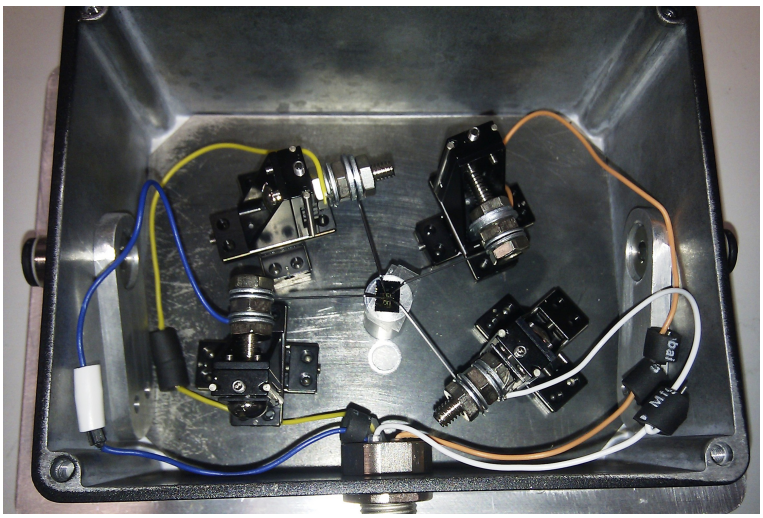

Figure 6.1: Photograph of chamber for electrical measurements with a sample installed and micropositioners holding contact needles onto the sample contact pads. The electrical feedthrough is at the bottom of the picture and the gas inlet and outlets are at the sides.

The overall size and weight of the chamber could not exceed the limits imposed by the Raman spectrometer's hood and mechanical stage. Finally the nature of it being a gas chamber means there was a requirement for a gas inlet and outlet and the lid and all connections must be sufficiently air-tight. The chamber was designed with help from Oleg Nerushev and produced by the Mechanical Workshop in the School of Chemistry, the University of Edinburgh. It was not able to go to vacuum. This would have been desirable, since vacuum measurements are reported in several related publications, however it was not possible to design a chamber suitable for evacuating which was compatible with the other requirements, in particular fitting inside the Raman spectrometer. The initial optical window, which was made of sapphire 5 mm thick, was not good because it made the focal length very wavelength dependent and it was not possible to get a clear enough picture from while light illumination to position the sample correctly. Changing the material or reducing its thickness should allow improved clarity, important for positioning in the Raman microscope and for obtaining Raman spectra. Figure 6.1 shows a picture of the completed chamber and the micropositioners.

To measure the very small currents that flow through a nanotube when voltage

is applied, highly precise instruments are required. The instruments used came from Keithley Instruments Inc. and include Sourcemeters 2410, 2611 and 2612 and Picoammeter 6485. These devices could be controlled either manually or by a laptop using either LabVIEW or TSP. David Machray developed the methods of controlling the sourcemeters during his MChem honours project.

Although Raman–transport measurements were not achieved with this setup during this project, it is ready to be used and measurements could be made in the future.

Chapter 7

Overall Conclusion

This thesis has presented progress made towards interfacing carbon nanotubes with plasmonic nanoantennas. One aim of this work was to improve the fundamental understanding of the interface between plasmonic nanostructures and nearby molecules, such as carbon nanotubes. Another aim was to use plasmonically enhanced Raman spectroscopy during electrical transport experiments on SWNTs to learn more about the reasons for current saturation and the changes leading to electrical breakdown.

The planned experiments combining plasmonically enhanced Raman spectroscopy and electrical transport required devices with carbon nanotubes interfaced with electrical connections and plasmonic structures. Creating these devices was a challenge that was approached in two methods described in this thesis: fountain pen nanolithography of carbon nanotubes and atomic force nanomanipulation of gold nanoparticles.

Fountain pen nanolithography is a technique for delivering small quantities of a material though a nanopipette onto a spatially precise location on a surface. The use of a carbon nanotubes dispersion inside the nanopipette has been shown for the first time. The important parameters controlling the deposition were investigated, such as the nanopipette speed and the voltage between the substrate and the dispersion. It was found that the quality of the carbon nanotube dispersion was very important: it required a high concentration of individual carbon nanotubes. Where carbon nanotubes were deposited by a nanopipette

along a line, there was a very high degree of alignment, according to polarised Raman spectroscopy.

Nanomanipulation was performed with an atomic force microscope to push colloidal gold nanoparticles onto carbon nanotubes, from where they landed after drop- or spin-coating. Gold nanoparticles with a diameter of 50 nm and a plasmonic resonance near 514 nm were used, as were particles with a spherical core of silica and a shell of gold with a total diameter of 150 nm, which had a plasmonic resonance near 785 nm. Both types of particle were successfully manipulated onto carbon diameters to give single particles and dimers. The enhancement of the Raman scattering was measured with the use of Raman mapping with a piezo scanner. Measured enhancements of 1.7× and 3.6× from individual 50 nm and 150 nm nanoparticles, respectively, indicated a local enhancement at the particle of approximately 26× and 24×. When a structure containing more then one nanoparticle was positioned on top of a carbon nanotube bundle, a measured enhancement of 26× suggested a local enhancement of at least 130×. In this case, polarised Raman revealed that the polarisation dependence of the carbon nanotube Raman scattering deviated from that expected from the bare carbon nanotube bundle. In addition, the background intensity was polarisation-direction dependent. This gives a method of probing the orientation of a plasmonic structure's strongest resonance.

Experiments combining electrical transport with plasmonically enhanced Raman spectroscopy were not completed within the scope of this thesis but are the primary focus of the future outlook. Combined measurements on a sample containing nanomanipulated plasmonic particles and carbon nanotubes will be made imminently, using multi-probe conducting atomic force microscopy. It is also possible that in the near future gold nanoparticles could be manipulated onto electrically contacted carbon nanotubes, which would allow plasmonically enhanced Raman spectroscopy to be performed in conjunction with electrical transport measurements in a controlled gas environment.

As well as combined Raman–transport experiments, it would also be interesting to study the enhancement and polarisation dependence of specific structures of gold nanoparticles, such as dimers and trimers, on carbon nanotubes

to get a better understanding of the plasmonic structures and their interaction with a one-dimensional structure such as a carbon nanotube. A continuation of the work presented in this thesis would be to achieve this by atomic force nano-manipulation. Other participants of the NANOSPEC project recently published a similar study based on dielectrophoretic deposition of SWNTs onto plasmonic structures [149].

Bibliography

[1] S. Reich, C. Thomsen and J. Maultzsch, *Carbon Nanotubes: basic concepts and physical properties*, Wiley-VCH, Berlin, 2003.

[2] S. Ilani and P. L. McEuen, *Annu. Rev. Condens. Matter Phys.*, 2010, **1**, 1–25.

[3] S. A. Maier, *Plasmonic: Fundamentals and Applications*, Springer, 2007.

[4] K. Kneipp, H. Kneipp, M. S. Dresselhaus and S. Lefrant, *Philos. T. Roy. Soc. A*, 2004, **362**, 2361–2373.

[5] C.-W. Liang, W.-Y. Lee, C.-H. Tsai and S. Roth, *Phys. Status Solidi B*, 2008, **245**, 2209–2211.

[6] Z. Liu, A. W. Bushmaker, M. Aykol and S. B. Cronin, *ACS Nano*, 2011, **5**, 4634–4640.

[7] Z. Zhou, X. Dou, L. Ci, L. Song, D. Liu, Y. Gao, J. Wang, L. Liu, W. Zhou, S. Xie and D. Wan, *J. Phys. Chem. B*, 2006, **110**, 1206–1209.

[8] L. Radushkevich and V. Lukyanovich, *Sov. J. Chem. Phys.*, 1952, **26**, 88–95.

[9] M. Monthioux and V. L. Kuznetsov, *Carbon*, 2006, **44**, 1621–1623.

[10] S. Iijima, *Nature*, 1991, **354**, 56–58.

[11] S. Iijima and T. Ichihashi, *Nature*, 1993, **363**, 603–605.

[12] D. S. Bethune, C. H. Kiang, M. S. Devries, G. Gorman, R. Savoy, J. Vazquez and R. Beyers, *Nature*, 1993, **363**, 605–607.

[13] P. J. F. Harris, *Carbon Nanotubes Related Structures: New Materials for the Twenty-first Century*, Cambridge University Press, 1999.

[14] X. Wang, Q. Li, J. Xie, Z. Jin, J. Wang, Y. Li, K. Jiang and S. Fan, *Nano Lett.*, 2009, **9**, 3137–3141.

[15] M. Dresselhaus, Y. Lin, O. Rabin, A. Jorio, A. S. Filho, M. Pimenta, R. Saito, G. Samsonidze and G. Dresselhaus, *Mat. Sci. Eng. C*, 2003, **23**, 129–140.

[16] T. Hertel, www.phys-chemie.uni-wuerzburg.de/fileadmin/08050200/user_upload/index_explained.jpg, Accessed July 2013.

[17] A. Javey and J. Kong, *Carbon Nanotube Electronics*, Springer London, Limited, 2009.

[18] J. Svensson, *Ph.D. thesis*, Department of Physics, Unversity of Gothenburg, 2010.

[19] B. Xu, J. Yin and Z. Liu, in *Physical and Chemical Properties of Carbon Nanotubes*, ed. S. Suzuki, InTech, 2013, ch. Phonon Scattering and Electron Transport in Single Wall Carbon Nanotube, pp. 373–393.

[20] R. Saito, M. Fujita, G. Dresselhaus and M. S. Dresselhaus, *Appl. Phys. Lett.*, 1992, **60**, 2204–2206.

[21] A. Szabó, C. Perri, A. Csató, G. Giordano, D. Vuono and J. B. Nagy, *Materials*, 2010, **3**, 3092–3140.

[22] J. Prasek, J. Drbohlavova, J. Chomoucka, J. Hubalek, O. Jasek, V. Adam and R. Kizek, *J. Mater. Chem.*, 2011, **21**, 15872–15884.

[23] H. Lai, M. Lin, M. Yang and A. Li, *Mat. Sci. Eng. C*, 2001, **16**, 23–26.

[24] M. Jose-Yacaman, M. Miki-Yoshida, L. Rendon and J. Santiesteban, *Appl. Phys. Lett.*, 1993, **62**, 657–659.

[25] Y. Fan, B. R. Goldsmith and P. G. Collins, *Nat. Mater.*, 2005, **4**, 906–911.

[26] P. Nikolaev, M. Bronikowski, R. Bradley, F. Rohmund, D. Colbert, K. Smith and R. Smalley, *Chem Phys Lett*, 1999, **313**, 91–97.

[27] M. J. Bronikowski, P. A. Willis, D. T. Colbert, K. A. Smith and R. E. Smalley, *The 47th international symposium: Vacuum, thin films, surfaces/interfaces, and processing NAN06*, 2001, **19**, 1800–1805.

[28] S. Dittmer, J. Ek-Weis, O. A. Nerushev and E. E. B. Campbell, *J. Nanosci. Nanotechnol.*, 2010, **10**, 4015–4022.

[29] R. Jasti and C. R. Bertozzi, *Chem. Phys. Lett.*, 2010, **494**, 1–7.

[30] C. Backes and A. Hirsch, in *Noncovalent Functionalization of Carbon Nanotubes*, John Wiley & Sons, Ltd, 2010, pp. 1–48.

[31] M. S. Strano, V. C. Moore, M. K. Miller, M. J. Allen, E. H. Haroz, C. Kittrell, R. H. Hauge and R. Smalley, *J. Nanosci. Nanotechnol.*, 2003, **3**, 81–86.

[32] P. Angelikopoulos, A. Gromov, A. Leen, O. Nerushev, H. Bock and E. E. B. Campbell, *J. Phys. Chem. C*, 2010, **114**, 2–9.

[33] K. Yurekli, C. A. Mitchell and R. Krishnamoorti, *J. Am. Chem. Soc.*, 2004, **126**, 9902–9903.

[34] S. D. Bergin, Z. Sun, P. Streich, J. Hamilton and J. N. Coleman, *J. Phys. Chem. C*, 2010, **114**, 231–237.

[35] K. D. Ausman, R. Piner, O. Lourie, R. S. Ruoff and M. Korobov, *J. Phys. Chem. B*, 2000, **104**, 8911–8915.

[36] S. Fogden, C. A. Howard, R. K. Heenan, N. T. Skipper and M. S. P. Shaffer, *ACS Nano*, 2012, **6**, 54–62.

[37] S. A. Hodge, S. Fogden, C. A. Howard, N. T. Skipper and M. S. P. Shaffer, *ACS Nano*, 2013, **7**, 1769–1778.

[38] M. C. Hersam, *Nat. Nanotechnol.*, 2008, **3**, 387–394.

[39] T. Tanaka, H. Jin, Y. Miyata, S. Fujii, H. Suga, Y. Naitoh, T. Minari, T. Miyadera, K. Tsukagoshi and H. Kataura, *Nano Lett.*, 2009, **9**, 1497–1500.

[40] A. A. Green and M. C. Hersam, *ACS Nano*, 2011, **5**, 1459–1467.

[41] S. Ghosh, S. M. Bachilo and R. B. Weisman, *Nat. Nanotechnol.*, 2010, **5**, 443–450.

[42] C. V. Raman and K. S. Krishnan, *Nature*, 1928, **121**, 501–502.

[43] A. Smekal, *Naturwissenschaften*, 1923, **43**, 873–875.

[44] A. Fadini and F.-M. Schnepel, *Vibrational Spectroscopy methods and applications*, Ellis Horwood Limited, Chichester, 1989.

[45] M. Diem, *Introduction to Modern Vibrational Spectroscopy*, John Wiley & Sons, New York, 1993.

[46] *Handbook of Raman Spectroscopy: From the Research Laboratory to the Process Line*, ed. I. R. Lewis and H. Edwards, CRC Press, 2001.

[47] A. Jorio, M. A. Pimenta, A. G. Souza, R. Saito, G. Dresselhaus and M. S. Dresselhaus, *New J. Phys.*, 2003, **5**, 139.

[48] M. Dresselhaus, G. Dresselhaus, R. Saito and A. Jorio, *Phys. Rep.*, 2005, **409**, 47–99.

[49] G. S. Duesberg, I. Loa, M. Burghard, K. Syassen and S. Roth, *Phys. Rev. Lett.*, 2000, **85**, 5436–5439.

[50] H. H. Gommans, J. W. Alldredge, H. Tashiro, J. Park, J. Magnuson and A. G. Rinzler, *J. Appl. Phys.*, 2000, **88**, 2509–2514.

[51] T. Liu and S. Kumar, *Chem. Phys. Lett.*, 2003, **378**, 257–262.

[52] R. Perez, S. Banda and Z. Ounaies, *J. Appl. Phys.*, 2008, **103**, 074302.

[53] G. Shmaltz, *Zeitchrift des Verein Deutscher Ingenieure*, 1929, 1461–1467.

[54] G. Binnig, H. Rohrer, C. Gerber and E. Weibel, *Phys. Rev. Lett.*, 1982, **49**, 57–61.

[55] *The Nobel Prize in Physics 1986*, http://www.nobelprize.org/nobel_prizes/physics/laureates/1986/, accessed July 2013.

[56] G. Binnig, C. F. Quate and C. Gerber, *Phys. Rev. Lett.*, 1986, **56**, 930–933.

[57] E. Meyer, H. J. Hug and R. Bennewitz, *Scanning Probe Microscopy: The Lab on a Tip*, Springer, 2004.

[58] P. Eaton and P. West, *Atomic Force Microscopy*, Oxford University Press, 2010.

[59] I. T. Clark and M. Yoshimura, in *Electronic Properties of Carbon Nanotubes*, ed. J. M. Marulanda, InTech, 2011, ch. Fabrication of Carbon Nanotubes for High-Performance Scanning Probe Microscopy, pp. 91–104.

[60] Nanonics Imaging, Ltd., *MultiView 1000^{TM} User Guide*, 2007.

[61] S. L. Flegler, J. W. J. Heckman and K. L. Klomparens, *Scanning and Transmission Electron Microscopy: An Introduction*, W. H. Freeman and Company, New York, 1993.

[62] P. W. Atkins, *Physical Chemistry*, Oxford University Press, 4th edn., 1992.

[63] K. Shimizu and T. Mitani, *New horizons of applied scanning electron microscopy*, Springer Berlin Heidelberg, 2010.

[64] K. Kalantar-zadeh and B. Fry, *Nanotechnology-Enabled Sensors*, Springer, 2008.

[65] J. Li and J. Liu, in *Scanning Microscopy for Nanotechnology*, ed. W. Zhou and Z. Wang, Springer New York, 2007, pp. 237–280.

[66] J. Ek Weis, *Ph.D. thesis*, School of Chemistry, the University of Edinburgh, 2011.

[67] S. Suzuki, in *Electronic Properties of Carbon Nanotubes*, ed. J. M. Marulanda, InTech, 2011, ch. 15.

[68] E. C. Le Ru and P. G. Etchegoin, *Principles of surface-enhanced Raman spectroscopy and related plasmonic effects*, Elsevier, 2009.

[69] J. Aizpurua and R. Hillenbrand, in *Plasmonics: From basics to adavanced topics*, ed. S. Enoch and N. Bond, Springer, 2012, ch. 5, pp. 151–176.

[70] G. Mie, *Annalen der Physik*, 1908, **330**, 377–445.

[71] N. Halas, *MRS Bulletin*, 2005, **30**, 362–367.

[72] R. Fernández-García, personal communication, 2010.

[73] E. E. B. Campbell, A. Lewis, S. A. Maier and S. Reich, *NanoScience Europe Transnational Call for Collaborative Proposals: Application Form*, 2008.

[74] E. E. B. Campbell, *NANOSPEC: Interfacing Carbon Nanotubes with Nanoantennas for Simultaneous Multifunctional Spectroscopy and Electrical Nanocharacterisation*, NanoSciE+: End of Project Report, 2013.

[75] E. Hecht, *Optics*, Addison-Wesley, 4th edn., 2002.

[76] M. Cardona and G. Güntherodt, *Light scattering in solids II: basic concepts and instrumentation*, Springer, 1982.

[77] I. Horcas, R. Fernandez, J. M. Gomez-Rodriguez, J. Colchero, J. Gomez-Herrero and A. M. Baro, *Rev. Sci. Instrum.*, 2007, **78**, 013705.

[78] A. Lewis, Y. Kheifetz, E. Shambrodt, A. Radko, E. Khatchatryan and C. Sukenik, *Appl. Phys. Lett.*, 1999, **75**, 2689–2691.

[79] T. P. Burgin, J. C. Lewenstein and D. Werho, *Langmuir*, 2005, **21**, 6596–6602.

[80] M. Wilson, K. Kannangara, G. Smith, M. Simmons and B. Raguse, *Nanotechnology: basic science and emerging technologies*, Chapman & Hall/CRC, 2002.

[81] N. Lindahl, *Ph.D. thesis*, Department of Physics, Unversity of Gothenburg, 2012.

[82] K. Yamamoto, S. Akita and Y. Nakayama, *J. Phys. D: Appl. Phys.*, 1998, **31**, L34.

[83] M. Ganzhorn, A. Vijayaraghavan, A. A. Green, S. Dehm, A. Voigt, M. Rapp, M. C. Hersam and R. Krupke, *Adv. Mater.*, 2011, **23**, 1734–1738.

[84] R. Krupke, F. Hennrich, H. B. Weber, M. M. Kappes and H. v. Lhneysen, *Nano Lett.*, 2003, **3**, 1019–1023.

[85] B. Omrane and C. Papadopoulos, *IEEE Transactions on Nanotechnology*, 2010, **9**, 375–380.

[86] R. D. Piner, J. Zhu, F. Xu, S. H. Hong and C. A. Mirkin, *Science*, 1999, **283**, 661–663.

[87] H. Taha, R. S. Marks, L. A. Gheber, I. Rousso, J. Newman, C. Sukenik and A. Lewis, *Appl. Phys. Lett.*, 2003, **83**, 1041–1043.

[88] Y. Lovsky, A. Lewis, C. Sukenik and E. Grushka, *Anal. Bioanal. Chem.*, 2010, **396**, 133–138.

[89] H. Taha, A. Lewis and C. Sukenik, *Nano Lett.*, 2007, **7**, 1883–1887.

[90] R. E. Ionescu, R. S. Marks and L. A. Gheber, *Nano Lett.*, 2003, **3**, 1639–1642.

[91] M. H. Hong, K. H. Kim, J. Bae and W. Jhe, *Appl. Phys. Lett.*, 2000, **77**, 2604–2606.

[92] F. Iwata, S. Nagami, Y. Sumiya and A. Sasaki, *Nanotechnology*, 2007, **18**, 105301.

[93] A. P. Suryavanshi and M.-F. Yu, *Nanotechnology*, 2007, **18**, 105305.

[94] L. Ying, A. Bruckbauer, A. M. Rothery, Y. E. Korchev and D. Klenerman, *Anal. Chem.*, 2002, **74**, 1380–1385.

[95] A. Bruckbauer, L. Ying, A. M. Rothery, D. Zhou, A. I. Shevchuk, C. Abell, Y. E. Korchev and D. Klenerman, *J. Am. Chem. Soc.*, 2002, **124**, 8810–8811.

[96] A. Bruckbauer, D. Zhou, L. Ying, Y. E. Korchev, C. Abell and D. Klenerman, *J. Am. Chem. Soc.*, 2003, **125**, 9834–9839.

[97] L. Ying, A. Bruckbauer, D. Zhou, J. Gorelik, A. Shevchuk, M. Lab, Y. Korchev and D. Klenerman, *Phys. Chem. Chem. Phys.*, 2005, **7**, 2859–2866.

[98] A. Bruckbauer, P. James, D. Zhou, J. W. Yoon, D. Excell, Y. Korchev, R. Jones and D. Klenerman, *Biophys. J.*, 2007, **93**, 3120–3131.

[99] K. T. Rodolfa, A. Bruckbauer, D. Zhou, Y. E. Korchev and D. Klenerman, *Angew. Chem., Int. Ed.*, 2005, **44**, 6854–6859.

[100] K. T. Rodolfa, A. Bruckbauer, D. Zhou, A. I. Schevchuk, Y. E. Korchev and D. Klenerman, *Nano Lett.*, 2006, **6**, 252–257.

[101] J. D. Piper, C. Li, C.-J. Lo, R. Berry, Y. Korchev, L. Ying and D. Klenerman, *J. Am. Chem. Soc.*, 2008, **130**, 10386–10393.

[102] A. Meister, S. Jeney, M. Liley, T. Akiyama, U. Staufer, N. de Rooij and H. Heinzelmann, *Microelectron. Eng.*, 2003, **6768**, 644–650.

[103] A. Meister, M. Liley, J. Brugger, R. Pugin and H. Heinzelmann, *Appl. Phys. Lett.*, 2004, **85**, 6260–6262.

[104] S. Deladi, N. R. Tas, J. W. Berenschot, G. J. M. Krijnen, M. J. de Boer, J. H. de Boer, M. Peter and M. C. Elwenspoek, *Appl. Phys. Lett.*, 2004, **85**, 5361–5363.

[105] K.-H. Kim, N. Moldovan, C. Ke and H. D. Espinosa, *MRS Proceedings*, 2004, **782**, http://dx.doi.org/10.1557/PROC–782–A5.56.

[106] K.-H. Kim, N. Moldovan and H. D. Espinosa, *Small*, 2005, **1**, 632–635.

[107] B. Wu, A. Ho, N. Moldovan and H. D. Espinosa, *Langmuir*, 2007, **23**, 9120–9123.

[108] K.-H. Kim, R. Sanedrin, A. Ho, S. Lee, N. Moldovan, C. Mirkin and H. Espinosa, *Adv. Mater.*, 2008, **20**, 330–334.

[109] O. Y. Loh, A. M. Ho, J. E. Rim, P. Kohli, N. A. Patankar and H. D. Espinosa, *Proc. Nat. Acad. Sci. U.S.A.*, 2008, **105**, 16438–16443.

[110] O. Loh, R. Lam, M. Chen, N. Moldovan, H. Huang, D. Ho and H. D. Espinosa, *Small*, 2009, **5**, 1667–1674.

[111] N. Moldovan, K.-H. Kim and H. D. Espinosa, *J. Micromech. Microeng.*, 2006, **16**, 1935–1942.

[112] C. G. Salzmann, B. T. Chu, G. Tobias, S. A. Llewellyn and M. L. Green, *Carbon*, 2007, **45**, 907–912.

[113] C. Sapcharoenkun, *Ph.D. thesis*, School of Chemistry, the University of Edinburgh, 2013.

[114] T. Yeshua, C. Lehmann and A. Lewis, personal communication, 2013.

[115] K. M. Strain, T. Yeshua, A. V. Gromov, O. Nerushev, A. Lewis and E. E. B. Campbell, *Mater. Express*, 2011, **1**, 279–284.

[116] G. S. Duesberg, W. J. Blau, H. J. Byrne, J. Muster, M. Burghard and S. Roth, *Chem. Phys. Lett.*, 1999, **310**, 8–14.

[117] T. Assmus, K. Balasubramanian, M. Burghard, K. Kern, M. Scolari, N. Fu, A. Myalitsin and A. Mews, *Appl. Phys. Lett.*, 2007, **90**, 173109.

[118] M. Scolari, A. Mews, N. Fu, A. Myalitsin, T. Assmus, K. Balasubramanian, M. Burghard and K. Kern, *J. Phys. Chem. C*, 2008, **112**, 391–396.

[119] Y.-C. Chen, R. J. Young, J. V. Macpherson and N. R. Wilson, *J. Phys. Chem. C*, 2007, **111**, 16167–16173.

[120] Y.-C. Chen, R. J. Young, J. V. Macpherson and N. R. Wilson, *J. Raman Spectrosc.*, 2011, **42**, 1255–1262.

[121] H. B. Chu, J. Y. Wang, L. Ding, D. N. Yuan, Y. Zhang, J. Liu and Y. Li, *J. Am. Chem. Soc.*, 2009, **131**, 14310–14316.

[122] X. Wang, C. Wang, L. Cheng, S.-T. Lee and Z. Liu, *J. Am. Chem. Soc.*, 2012, **134**, 7414–7422.

[123] R. Kumar, H. Zhou and S. B. Cronin, *Appl. Phys. Lett.*, 2007, **91**, 223105.

[124] L. M. Tong, Z. P. Li, T. Zhu, H. X. Xu and Z. F. Liu, *J. Phys. Chem. C*, 2008, **112**, 7119–7123.

[125] T. Junno, K. Deppert, L. Montelius and L. Samuelson, *Appl. Phys. Lett.*, 1995, **66**, 3627–3629.

[126] D. M. Eigler and E. K. Schweizer, *Nature*, 1990, **344**, 524–526.

[127] L. T. Hansen, A. Khle, A. H. Srensen, J. Bohr and P. E. Lindelof, *Nanotechnology*, 1998, **9**, 337.

[128] S. Decossas, F. Mazen, T. Baron, G. Brmond and A. Souifi, *Nanotechnology*, 2003, **14**, 1272–1278.

[129] F. Rubio-Sierra, W. Heckl and R. Stark, *Adv. Eng. Mater.*, 2005, **7**, 193–196.

[130] C. Onal, O. Ozcan and M. Sitti, *IEEE Transactions on Nanotechnology*, 2011, **10**, 472–481.

[131] K. De Blauwe, C. Kramberger, W. Plank, H. Kataura and T. Pichler, *Phys. Status Solidi B*, 2009, **246**, 2732–2736.

[132] A. W. Bushmaker, V. V. Deshpande, S. Hsieh, M. W. Bockrath and S. B. Cronin, *Nano Lett.*, 2009, **9**, 2862–2866.

[133] B. S. Yeo, T. Schmid, W. H. Zhang and R. Zenobi, *Appl. Spectrosc.*, 2008, **62**, 708–713.

[134] Z. Yao, C. L. Kane and C. Dekker, *Phys. Rev. Lett.*, 2000, **84**, 2941.

[135] E. Pop, D. Mann, J. Cao, Q. Wang, K. Goodson and H. J. Dai, *Phys. Rev. Lett.*, 2005, **95**, 155505.

[136] V. V. Deshpande, S. Hsieh, A. W. Bushmaker, M. Bockrath and S. B. Cronin, *Phys. Rev. Lett.*, 2009, **102**, 105501.

[137] I.-K. Hsu, M. T. Pettes, M. Aykol, L. Shi and S. B. Cronin, *J. Appl. Phys.*, 2010, **108**, 084307.

[138] A. W. Bushmaker, V. V. Deshpande, M. W. Bockrath and S. B. Cronin, *Nano Lett.*, 2007, **7**, 3618–3622.

[139] M. Amer, A. W. Bushmaker and S. B. Cronin, *Nano. Res.*, 2012, **5**, 172–180.

[140] I.-K. Hsu, M. T. Pettes, A. W. Bushmaker, M. Aykol, L. Shi and S. B. Cronin, *Nano Lett.*, 2009, **9**, 590–594.

[141] I.-K. Hsu, M. T. Pettes, M. Aykol, C.-C. Chang, W.-H. Hung, J. Theiss, L. Shi and S. B. Cronin, *J. Appl. Phys.*, 2011, **110**, 044328.

[142] M. Aykol, W. Branham, Z. Liu, M. R. Amer, I.-K. Hsu, R. Dhall, S.-W. Chang and S. B. Cronin, *J. Micromech. Microeng.*, 2011, **21**, 085008.

[143] P. Pavaskar and S. B. Cronin, *Appl. Phys. Lett.*, 2009, **94**, 253102.

[144] J. Theiss, P. Pavaskar, P. M. Echternach, R. E. Muller and S. B. Cronin, *Nano Lett.*, 2010, **10**, 2749–2754.

[145] P. Pavaskar, I.-K. Hsu, J. Theiss, W. H. Hung and S. B. Cronin, *J. Appl. Phys.*, 2013, **113**, 034302.

[146] A. W. Bushmaker, V. V. Deshpande, S. Hsieh, M. W. Bockrath and S. B. Cronin, *Phys. Rev. Lett.*, 2009, **103**, 067401.

[147] A. W. Bushmaker, V. V. Deshpande, S. Hsieh, M. W. Bockrath and S. B. Cronin, *Nano Lett.*, 2009, **9**, 607–611.

[148] R. Dhall, S.-W. Chang, Z. Liu and S. B. Cronin, *Phys. Rev. B*, 2012, **86**, 045427.

[149] S. Heeg, A. Oikonomou, R. Fernandez-Garcia, C. Lehmann, S. A. Maier, A. Vijayaraghavan and S. Reich, *Nano Lett.*, XXXX, **XXX**, XXX–XXX.

[150] A. Kudelski and B. Pettinger, *Chem. Phys. Lett.*, 2000, **321**, 356–362.

[151] P. J. Moyer, J. Schmidt, L. M. Eng, A. J. Meixner, G. W. Sandmann, H. Dietz and W. Plieth, *J. Am. Chem. Soc.*, 2000, **122**, 5409–5410.

[152] A. Otto, *J. Raman Spectrosc.*, 2002, **33**, 593–598.

[153] K. Itoh, I. Kudryashov, J. Yamagata, T. Nishizawa, M. Fujii and N. Osaka, *J. Phys. Chem. B*, 2005, **109**, 271–276.

[154] M. R. Goncalves, F. Enderle and O. Marti, *J. Nanotechnol.*, 2012, **2012**, 15.

[155] N. P. W. Pieczonka and R. F. Aroca, *ChemPhysChem*, 2005, **6**, 2473–2484.

[156] Y. Maruyama, M. Ishikawa and M. Futamata, *J. Phys. Chem. B*, 2004, **108**, 673–678.

[157] E. J. Bjerneld, F. Svedberg, P. Johansson and M. Kall, *J. Phys. Chem. A*, 2004, **108**, 4187–4193.

[158] K. L. Norrod and K. L. Rowlen, *Anal. Chem.*, 1998, **70**, 4218–4221.

Appendices

Appendix A

Whit's this a' aboot?

Single walled carbon nanotubes (SWNTs) are a guid wee way that you can git carbon in. They hae a cylinder shape but are teeny weenie - wi' a diameter of aboot yin nanometre (a hunner-thousan' times wee-er than yer hair!). If a' goes weel then these wee things'll make the computer o' the future - wee-er and lighter and faster an' a' that, bit we arnae quite there yit - there's a couple o' wee things to wirk oot first. Here ye'll see a braw way o' pittin' these SWNT whatsits whereaboots we want them - called fountain pen nanolithography - an' we'll talk aboot ways o' tryin' tae understand them better usin' a laser.

Fountain pen nanolithography lets ye draw wee lines an' pictures wi' the SWNTs by pittin' them as the ink intae a wee bitty pen. When ye go tae draw a line, the ink comes oot an' there ye are wi' them lying jist where ye want them, a' lined up nicely.

If ye shine a laser oan these wee carbon tubes ye cun find oot some useful stuff, but sometimes it doesnae work that well at a'. We cun make it better if we hae wee dots o' gold biding oan the wee tube at the same bit that we pit the laser oan. Wi' a muckle machine we can gie the teeny gold dots a ride ower the place until they're sittin' jist right. The laser thing wirked twenty times better efter that.

Once a' o' that's done, we cun send electricity along the SWNT whatsit at the same time as daein' the laser thing an' we'll end up kennin' mair than we did aboot these wee SWNTs at the start.

Appendix B

Publications, conferences and exchanges

Publications

- Direct Deposition of Aligned Single Walled Carbon Nanotubes by Fountain Pen Nanolithography.
  K. M. Strain, T. Yeshua, A. V. Gromov, O. Nerushev, A. Lewis, E.E.B. Campbell, *Mater. Express*, 2011, **1**, 279-284.

Conferences

- EuCheMS Chemistry Congress
  Nürnberg, Germany, August 2010
  Oral presentation "Nanofountainpen Deposition of Carbon Nanotubes"

- Nano-ERA Review conference
  Dublin, Ireland, June 2011
  Poster presentation "Interfacing Carbon Nanotubes with Nanoantennas for Simultaneous Multifunctional Spectroscopy and Electrical Nanocharacterization"

- NT11
  Cambridge, UK, July 2011
  Poster presentation "Deposition of Aligned Carbon Nanotubes Using Fountain Pen Nanolithography"

- NT12
  Brisbane, Australia, June 2012
  Oral presentation "AFM Nanomanipulation of Gold Nanoparticles for Plasmonically Enhanced Raman Spectroscopy on Electrically Contacted SWNTs"

Exchanges

- Hebrew University, Jerusalem, under supervision of Prof. Aaron Lewis
  10 January – 20 February 2010
  Purpose "Introduction to nanofountain pen deposition"

- Free University, Berlin, under supervision of Prof. Stephanie Reich
  19 – 21 May 2010
  Purpose "Polarised Raman spectroscopy"

- Hebrew University, Jerusalem, under supervision of Prof. Aaron Lewis
  7 – 14 October 2010
  Purpose "Nanofountain pen deposition"

Appendix C

Instructions for making Raman fine maps

These instructions describe the process of setting up and making a mapping Raman measurement where the Nanonics piezo scanner is used to provide sub-micron steps.

Setting up

1. Turn on Raman microscope in the normal way.
2. Put silver-coloured stage inset onto Prior stage, screw in.
3. Place Nanonics scanner onto stage, with the hinge at LHS.
4. Plug the cable labelled 'scanner' into the back of the scanner.
5. Ensure that the three light-grey cables going from Nanonics controller boxes are connected to the computer that controls the Raman microscope (not into the Nanonics computer).
6. Turn on the Nanonics controller boxes using the power switch at the back-right of the bottom box.
7. Place sample on sample mount in centre of scanner (optionally with added weights to assist friction).
8. Push Nanonics scanner into corner formed by gold-coloured bars on the stage, then fix in place with clips (see Figure C.1).

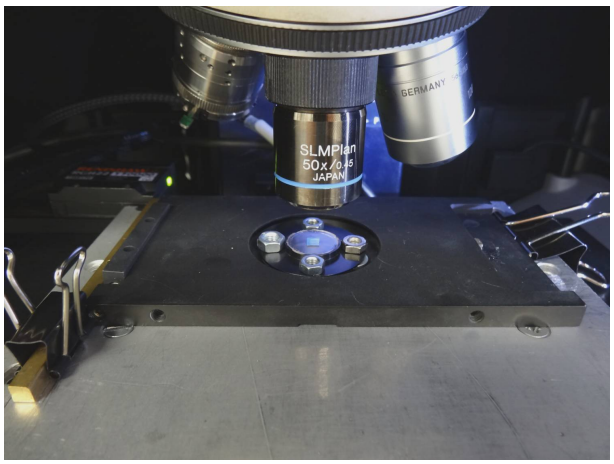

Figure C.1: Photo of Nanonics scanner on Raman stage.

Preparing the measurement

1. Open WiRE, Quartz, QuartzSpec and Paint on the computer.
2. In WiRE,
   (a) perform normal laser alignment steps,
   (b) locate the sample in the centre of the crosshairs, using the camera in WiRE and the Prior stage controls.
3. In Quartz (click 'OK' on the message saying 'Please ensure mode is set to...'),
   (a) go to Scan > Dimensions (or click Scan Dimensions button) to open the Scan Settings window (Figure C.2),
      i. unless a resolution of less than 100 nm is required, leave X and Y size as 128 pixels, and X and Y range as 12 800 nm,
      ii. scan rotation 'Left to right' at 0 degrees,
      iii. click 'OK' - no other settings are important here.
4. In QuartzSpec,
   (a) open Spectral Acquisition setup window by clicking on the button with red axes and a blue spectrum near the top of the window (Figure C.3),
      i. put in spectral settings just as in WiRE,
      ii. uncheck 'Close laser shutter on completion' and 'Restore instrument state on completion' (or else measurement will take much longer than the predicted time),
      iii. click 'OK' when settings are all correct,
   (b) click the button with a single blue spectrum to take a single spectrum with the given settings. This checks that the communications between QS and WiRE are working.

5. In Quartz,
   (a) go to Scan > Select Points to open the new window,
      i. chose the desired resolution, *i.e.* 'Select every 2 points' will give 200 nm steps between spectra,
      ii. chose whether a line or rectangle is desired then draw onto the grid where those points should be,
      iii. when satisfied click 'Close'.
6. In WiRE and Paint,
   (a) check that the sample is positioned exactly as desired,
   (b) take a screenshot of the sample position, paste into Paint and Save As,
   (c) focus laser on sample surface,
   (d) take a second screenshot, paste into Paint and Save As with a different name.
7. When completely ready (pause to check all steps have been completed!), in Quartz, click the button for 'Spectral Scan' to start the measurement. It will take (length of each spectral acquisition) × (number of points selected) × ∼1.15.

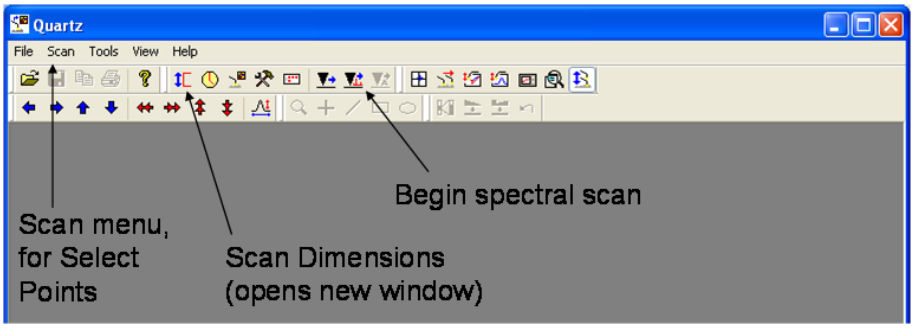

Figure C.2: Quartz window.

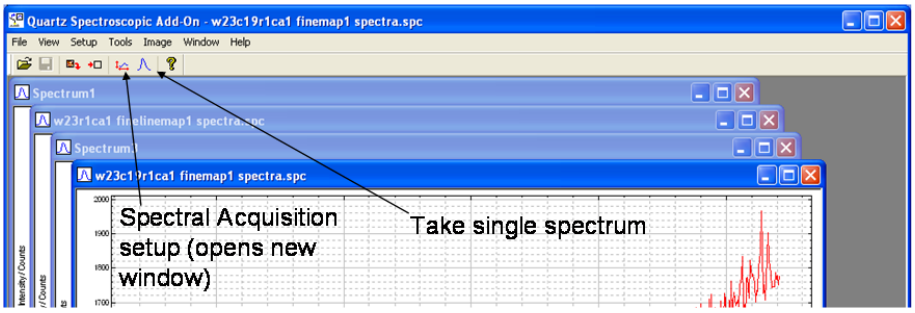

Figure C.3: QuartzSpec window.

After the measurement is complete

1. In QuartzSpec,
   (a) save spectra in File > Save As, to save .spc file,
   (b) can also File > Export to ASCII > All Spectra, to save as .dat (equivalent to .txt).
2. In WiRE and Paint,
   (a) take a screenshot of the sample with the laser on (comparable to the before-measurement 'laser focus' picture to be used to detect z drift), paste into Paint and Save As,
   (b) focus on the sample
   (c) take a second screenshot (to compare to the before-measurement 'sample focus' picture to be used to detect drift in the x–y plane), paste into Paint and Save As with a different name.
3. Turn off Nanonics controller boxes before unplugging cable from scanner.
4. Turn off Raman spectrometer in the normal way.

Appendix D

Details of microfabrication process

The following steps were used in the microfabrication of samples with electrically-contacted CNTs. Replicated from reference [18].

Pads for electrical probing

This photolithography process is used for large features that do not require good alignment to any previous pattern.

1. Spin LOR3A at 3000 rpm for a thickness of 380 nm. Bake at 180 °C for 3 min.
2. Spin S1813 at 4000 rpm for a thickness of 1.3 μm. Bake at 110 °C for 2 min.
3. Expose with an intensity of 1.5 mW/cm^2 for 50 s through a photomask.
4. Develop in MF319 for 35 s.
5. Oxygen plasma at 50 W for 15 s.
6. Deposit 5 nm Ti / 120 nm Au.
7. Lift-off in Shipley 1165 remover.

Marks and catalyst

This EBL process is mainly used to make alignment marks and also for contacts to CNTs with sizes down to 400 nm.

1. Spin LOR3A at 3000 rpm for a thickness of 280 nm. Bake 3 min at 180 °C.

2. Spin UV5-0.6 at 4000 rpm for a thickness of 650 nm. Bake 1 min at 130 °C.
3. Expose marks and electrodes using EBL with a current of 10 nA and a dose of 45 $\mu C/cm^2$.
4. Postbake for 1.5 min at 130 °C.
5. Develop in MF24A for 35 s and ash in O_2 plasma at 50 W for 15 s.
6. Deposit 5 nm Ti / 100 nm Mo using e-gun evaporation.
7. Lift-off in Shipley 1165 remover heated to 60 °C. Rinse in IPA and water, blow dry.
8. Pattern catalyst areas using the same recipe as for the electrodes and deposit 5 nm Al_2O_3 / 0.5 nm Fe using e-gun evaporation.

Contacts to CNTs

This EBL process is used for features with sizes smaller than 400 nm.

1. Locate CNTs using SEM and design electrodes according to their positions.
2. Spin copolymer MMA(8.5)MAA EL4 at 3000 rpm for a thickness of 80 nm. Bake at 170 °C for 5 min.
3. Spin ZEP520 (1:1 Anisole) at 3000 rpm for a thickness of 120 nm. Bake at 170 °C for 5 min.
4. Expose at 1 nA and a dose of 370 $\mu C/cm^2$.
5. Develop in hexylacetate for 1 min, rinse in IPA, develop in MIBK/IPA (1:2) for 2 min, rinse in water and blow dry.
6. Deposit 0.5 nm Ti / 30 nm Pd using e-gun evaporation.
7. Lift-off in Shipley 1165 remover.

Appendix E

Nanochemplotter scripts

The following pages contain the 'nanochemplotter' scripts used within the Nanonics NWS software to direct the tip during nanowriting experiments.

The 'Original snake from Jerusalem' was obtained from Yulia Lovsky and exists with bias voltages of 0 V, ±0.5 V, ±1 V, ±2 V, ±3 V, ±4 V, ±5 V, ±8 V and ±10 V. These voltages are only relevant for experiments performed in Jerusalem; if these scripts were used with the instrument in Edinburgh then the voltages in the script have no significance at all. Similarly, the 'Sparse snake' shown here has a bias voltage of ±10 V and the 'Dense snake' has a bias voltage of ±1 V but there is no meaning to these values. The 'Speed' corresponding to steps involving a change in voltage should have a value of 5 (units unknown) to ensure a sharp step rather than a triangular voltage waveform.

Table E.1: Headings used in the tables of scripts.

Name	Description	Units (if applicable)
#	Number of step	
Speed	Lateral speed of tip	µm/ms
Res	Time it takes for scanner to move one pixel	ms
STMBias	Bias voltage (if system allows)	V
STMBiasA	Is STMBias applied?	Values T or F
SetPoint	Setpoint	V
SetPointA	Is SetPoint applied?	Values T or F
XPos	X coordinate	µm
XPosA	Is XPos applied?	Values T or F
YPos	Y coordinate	µm
YPosA	Is YPos applied?	Values T or F
ZPos	Z height	nm
ZposA	Is ZPos applied?	Values T or F
Wait	Pause for a time	ms
WaitA	Is Wait applied?	Values T or F
Trigger	Standard trigger waveforms	Values 1, 2 or 3
TriggerA	Is Trigger applied?	Values T or F

Headings not defined here are not relevant to any work presented in this thesis.

Original snake from Jerusalem (shown: ±3 V, other voltages also used)

#	Speed	Res	STMBias	STMBiasA	SetPoint	SetPointA	XPos	XPosA	YPos	YPosA	ZPos	ZposA	Wait	WaitA	Trigger	TriggerA	Channel	Calc	Polarity	Value	StopStepA	FB	HVReset	SPMA	Path	SubVIA
0	0.005	8	3	F	0	F	5	T	0	T	0	F	0	F	0	F	0	R	>	0	F	F	F	F		F
1	0.005	8	3	F	0	F	5	T	2.5	T	0	F	0	F	0	F	0	R	>	0	F	F	F	F		F
2	5	8	-3	T	0	F	5	T	2.5	T	0	F	0	F	0	F	0	R	>	0	F	F	F	F		F
3	0.005	8	-3	F	0	F	5	T	5	T	0	F	0	F	0	F	0	R	>	0	F	F	F	F		F
4	5	8	3	T	0	F	5	T	5	T	0	F	0	F	0	F	0	R	>	0	F	F	F	F		F
5	0.005	8	3	F	0	F	6	T	5	T	0	F	0	F	0	F	0	R	>	0	F	F	F	F		F
6	0.005	8	3	F	0	F	6	T	2.5	T	0	F	0	F	0	F	0	R	>	0	F	F	F	F		F
7	5	8	-3	T	0	F	6	T	2.5	T	0	F	0	F	0	F	0	R	>	0	F	F	F	F		F
8	0.005	8	-3	F	0	F	6	T	0	T	0	F	0	F	0	F	0	R	>	0	F	F	F	F		F
9	5	8	3	T	0	F	6	T	0	T	0	F	0	F	0	F	0	R	>	0	F	F	F	F		F
10	0.005	8	3	F	0	F	6	T	-3	T	0	F	0	F	0	F	0	R	>	0	F	F	F	F		F
11	5	8	-3	T	0	F	6	T	-3	T	0	F	0	F	0	F	0	R	>	0	F	F	F	F		F
12	0.005	8	-3	F	0	F	6	T	-5	T	0	F	0	F	0	F	0	R	>	0	F	F	F	F		F
13	5	8	3	T	0	F	6	T	-5	T	0	F	0	F	0	F	0	R	>	0	F	F	F	F		F
14	0.005	8	3	F	0	F	7	T	-5	T	0	F	0	F	0	F	0	R	>	0	F	F	F	F		F
15	0.005	8	3	F	0	F	7	T	-3	T	0	F	0	F	0	F	0	R	>	0	F	F	F	F		F
16	5	8	-3	T	0	F	7	T	-3	T	0	F	0	F	0	F	0	R	>	0	F	F	F	F		F
17	0.005	8	-3	F	0	F	7	T	0	T	0	F	0	F	0	F	0	R	>	0	F	F	F	F		F
18	5	8	3	T	0	F	7	T	0	T	0	F	0	F	0	F	0	R	>	0	F	F	F	F		F
19	0.005	8	3	F	0	F	7	T	2.5	T	0	F	0	F	0	F	0	R	>	0	F	F	F	F		F
20	5	8	-3	T	0	F	7	T	2.5	T	0	F	0	F	0	F	0	R	>	0	F	F	F	F		F
21	0.005	8	-3	F	0	F	7	T	5	T	0	F	0	F	0	F	0	R	>	0	F	F	F	F		F
22	5	8	3	T	0	F	7	T	5	T	0	F	0	F	0	F	0	R	>	0	F	F	F	F		F
23	0.005	8	0	F	0	F	8	T	5	T	0	F	0	F	0	F	0	R	>	0	F	F	F	F		F
24	0.005	8	0	F	0	F	8	T	2.5	T	0	F	0	F	0	F	0	R	>	0	F	F	F	F		F
25	5	8	-3	T	0	F	8	T	2.5	T	0	F	0	F	0	F	0	R	>	0	F	F	F	F		F
26	0.005	8	-3	F	0	F	8	T	0	T	0	F	0	F	0	F	0	R	>	0	F	F	F	F		F
27	5	8	3	T	0	F	8	T	0	T	0	F	0	F	0	F	0	R	>	0	F	F	F	F		F
28	0.005	8	3	F	0	F	8	T	-3	T	0	F	0	F	0	F	0	R	>	0	F	F	F	F		F
29	5	8	-3	T	0	F	8	T	-3	T	0	F	0	F	0	F	0	R	>	0	F	F	F	F		F
30	0.005	8	-3	F	0	F	8	T	-5	T	0	F	0	F	0	F	0	R	>	0	F	F	F	F		F
31	5	8	3	T	0	F	8	T	-5	T	0	F	0	F	0	F	0	R	>	0	F	F	F	F		F
32	0.005	8	3	F	0	F	9	T	-5	T	0	F	0	F	0	F	0	R	>	0	F	F	F	F		F
33	0.005	8	3	F	0	F	9	T	-3	T	0	F	0	F	0	F	0	R	>	0	F	F	F	F		F
34	5	8	-3	T	0	F	9	T	-3	T	0	F	0	F	0	F	0	R	>	0	F	F	F	F		F
35	0.005	8	-3	F	0	F	9	T	0	T	0	F	0	F	0	F	0	R	>	0	F	F	F	F		F
36	5	8	3	T	0	F	9	T	0	T	0	F	0	F	0	F	0	R	>	0	F	F	F	F		F
37	0.005	8	3	F	0	F	9	T	2.5	T	0	F	0	F	0	F	0	R	>	0	F	F	F	F		F
38	5	8	-3	T	0	F	9	T	2.5	T	0	F	0	F	0	F	0	R	>	0	F	F	F	F		F
39	0.005	8	-3	F	0	F	9	T	5	T	0	F	0	F	0	F	0	R	>	0	F	F	F	F		F
40	5	8	3	T	0	F	9	T	5	T	0	F	0	F	0	F	0	R	>	0	F	F	F	F		F
41	0.005	8	3	F	0	F	10	T	5	T	0	F	0	F	0	F	0	R	>	0	F	F	F	F		F
42	0.005	8	3	F	0	F	10	T	2.5	T	0	F	0	F	0	F	0	R	>	0	F	F	F	F		F
43	5	8	-3	T	0	F	10	T	2.5	T	0	F	0	F	0	F	0	R	>	0	F	F	F	F		F
44	0.005	8	-3	F	0	F	10	T	0	T	0	F	0	F	0	F	0	R	>	0	F	F	F	F		F
45	5	8	3	T	0	F	10	T	0	T	0	F	0	F	0	F	0	R	>	0	F	F	F	F		F
46	0.005	8	3	F	0	F	10	T	-3	T	0	F	0	F	0	F	0	R	>	0	F	F	F	F		F
47	5	8	-3	T	0	F	10	T	-3	T	0	F	0	F	0	F	0	R	>	0	F	F	F	F		F
48	0.005	8	-3	F	0	F	10	T	-5	T	0	F	0	F	0	F	0	R	>	0	F	F	F	F		F

49	5	8	3	T	0	F	10	T	-5	T	0	F	0	F	0	F	0	R	>	0	F	F	F	F
50	0.005	8	3	F	0	F	11	T	-5	T	0	F	0	F	0	F	0	R	>	0	F	F	F	F
51	0.005	8	3	F	0	F	11	T	-3	T	0	F	0	F	0	F	0	R	>	0	F	F	F	F
52	5	8	-3	T	0	F	11	T	-3	T	0	F	0	F	0	F	0	R	>	0	F	F	F	F
53	0.005	8	-3	F	0	F	11	T	0	T	0	F	0	F	0	F	0	R	>	0	F	F	F	F
54	5	8	3	T	0	F	11	T	0	T	0	F	0	F	0	F	0	R	>	0	F	F	F	F
55	0.005	8	3	F	0	F	11	T	2.5	T	0	F	0	F	0	F	0	R	>	0	F	F	F	F
56	5	8	-3	T	0	F	11	T	2.5	T	0	F	0	F	0	F	0	R	>	0	F	F	F	F
57	0.005	8	-3	F	0	F	11	T	5	T	0	F	0	F	0	F	0	R	>	0	F	F	F	F
58	5	8	3	T	0	F	11	T	5	T	0	F	0	F	0	F	0	R	>	0	F	F	F	F
59	0.005	8	3	F	0	F	12	T	5	T	0	F	0	F	0	F	0	R	>	0	F	F	F	F
60	0.005	8	3	F	0	F	12	T	2.5	T	0	F	0	F	0	F	0	R	>	0	F	F	F	F
61	5	8	-3	T	0	F	12	T	2.5	T	0	F	0	F	0	F	0	R	>	0	F	F	F	F
62	0.005	8	-3	F	0	F	12	T	0	T	0	F	0	F	0	F	0	R	>	0	F	F	F	F
63	5	8	3	T	0	F	12	T	0	T	0	F	0	F	0	F	0	R	>	0	F	F	F	F
64	0.005	8	3	F	0	F	12	T	-3	T	0	F	0	F	0	F	0	R	>	0	F	F	F	F
65	5	8	-3	T	0	F	12	T	-3	T	0	F	0	F	0	F	0	R	>	0	F	F	F	F
66	0.005	8	-3	F	0	F	12	T	-5	T	0	F	0	F	0	F	0	R	>	0	F	F	F	F
67	5	8	3	T	0	F	12	T	-5	T	0	F	0	F	0	F	0	R	>	0	F	F	F	F
68	0.005	8	3	F	0	F	13	T	-5	T	0	F	0	F	0	F	0	R	>	0	F	F	F	F
69	0.005	8	3	F	0	F	13	T	-3	T	0	F	0	F	0	F	0	R	>	0	F	F	F	F
70	5	8	-3	T	0	F	13	T	-3	T	0	F	0	F	0	F	0	R	>	0	F	F	F	F
71	0.005	8	-3	F	0	F	13	T	0	T	0	F	0	F	0	F	0	R	>	0	F	F	F	F
72	5	8	3	T	0	F	13	T	0	T	0	F	0	F	0	F	0	R	>	0	F	F	F	F
73	0.005	8	3	F	0	F	13	T	2.5	T	0	F	0	F	0	F	0	R	>	0	F	F	F	F
74	5	8	-3	T	0	F	13	T	2.5	T	0	F	0	F	0	F	0	R	>	0	F	F	F	F
75	0.005	8	-3	F	0	F	13	T	5	T	0	F	0	F	0	F	0	R	>	0	F	F	F	F
76	5	8	3	T	0	F	13	T	5	T	0	F	0	F	0	F	0	R	>	0	F	F	F	F
77	0.005	8	3	F	0	F	14	T	5	T	0	F	0	F	0	F	0	R	>	0	F	F	F	F
78	0.005	8	3	F	0	F	14	T	2.5	T	0	F	0	F	0	F	0	R	>	0	F	F	F	F
79	5	8	-3	T	0	F	14	T	2.5	T	0	F	0	F	0	F	0	R	>	0	F	F	F	F
80	0.005	8	-3	F	0	F	14	T	0	T	0	F	0	F	0	F	0	R	>	0	F	F	F	F
81	5	8	3	T	0	F	14	T	0	T	0	F	0	F	0	F	0	R	>	0	F	F	F	F
82	0.005	8	3	F	0	F	14	T	-3	T	0	F	0	F	0	F	0	R	>	0	F	F	F	F
83	5	8	-3	T	0	F	14	T	-3	T	0	F	0	F	0	F	0	R	>	0	F	F	F	F
84	0.005	8	-3	F	0	F	14	T	-5	T	0	F	0	F	0	F	0	R	>	0	F	F	F	F
85	5	8	3	T	0	F	14	T	-5	T	0	F	0	F	0	F	0	R	>	0	F	F	F	F
86	0.005	8	3	F	0	F	15	T	-5	T	0	F	0	F	0	F	0	R	>	0	F	F	F	F
87	0.005	8	3	F	0	F	15	T	-3	T	0	F	0	F	0	F	0	R	>	0	F	F	F	F
88	5	8	-3	T	0	F	15	T	-3	T	0	F	0	F	0	F	0	R	>	0	F	F	F	F
89	0.005	8	-3	F	0	F	15	T	0	T	0	F	0	F	0	F	0	R	>	0	F	F	F	F
90	5	8	3	T	0	F	15	T	0	T	0	F	0	F	0	F	0	R	>	0	F	F	F	F
91	0.005	8	3	F	0	F	15	T	2.5	T	0	F	0	F	0	F	0	R	>	0	F	F	F	F
92	5	8	-3	T	0	F	15	T	2.5	T	0	F	0	F	0	F	0	R	>	0	F	F	F	F
93	0.005	8	-3	F	0	F	15	T	5	T	0	F	0	F	0	F	0	R	>	0	F	F	F	F
94	0.005	8	0	T	0	F	15	T	5	T	0	F	0	F	0	F	0	R	>	0	F	F	F	F
95	0.005	8	5	F	0	F	25	T	5	T	0	F	0	F	0	F	0	R	>	0	F	F	F	F

Star

#	Speed	Res	STMBias	STMBiasA	SetPoint	SetPointA	XPos	XPosA	YPos	YPosA	ZPos	ZposA	Wait	WaitA	Trigger	TriggerA	Channel	Calc	Polarity	Value	StopStepA	FB	HVReset	SPMA	Path	SubVIA
0	0.005	8	0	F	0	F	8	T	0	T	0	F	0	F	0	F	0	R	>	0	F	F	F	F		F
1	0.005	8	0	F	0	F	10	T	-8	T	0	F	0	F	0	F	0	R	>	0	F	F	F	F		F
2	0.005	8	0	F	0	F	12	T	0	T	0	F	0	F	0	F	0	R	>	0	F	F	F	F		F
3	0.005	8	0	F	0	F	20	T	0	T	0	F	0	F	0	F	0	R	>	0	F	F	F	F		F
4	0.005	8	0	F	0	F	14	T	5	T	0	F	0	F	0	F	0	R	>	0	F	F	F	F		F
5	0.005	8	0	F	0	F	16	T	12	T	0	F	0	F	0	F	0	R	>	0	F	F	F	F		F
6	0.005	8	0	F	0	F	10	T	8	T	0	F	0	F	0	F	0	R	>	0	F	F	F	F		F
7	0.005	8	0	F	0	F	4	T	12	T	0	F	0	F	0	F	0	R	>	0	F	F	F	F		F
8	0.005	8	0	F	0	F	6	T	5	T	0	F	0	F	0	F	0	R	>	0	F	F	F	F		F
9	0.005	8	0	F	0	F	0	T	0	T	0	F	0	F	0	F	0	R	>	0	F	F	F	F		F

Scotland

#	Speed	Res	STMBias	STMBiasA	SetPoint	SetPointA	XPos	XPosA	YPos	YPosA	ZPos	ZposA	Wait	WaitA	Trigger	TriggerA	Channel	Calc	Polarity	Value	StopStepA	FB	HVReset	SPMA	Path	SubVIA
0	0.005	8	0	F	0	F	4	T	-10	T	0	F	0	F	0	F	0	R	>	0	F	F	F	F		F
1	0.005	8	0	F	0	F	10	T	-10	T	0	F	0	F	0	F	0	R	>	0	F	F	F	F		F
2	0.005	8	0	F	0	F	7	T	-5	T	0	F	0	F	0	F	0	R	>	0	F	F	F	F		F
3	0.005	8	0	F	0	F	13	T	-5	T	0	F	0	F	0	F	0	R	>	0	F	F	F	F		F
4	0.005	8	0	F	0	F	8	T	4	T	0	F	0	F	0	F	0	R	>	0	F	F	F	F		F
5	0.005	8	0	F	0	F	10	T	4	T	0	F	0	F	0	F	0	R	>	0	F	F	F	F		F
6	0.005	8	0	F	0	F	12	T	6	T	0	F	0	F	0	F	0	R	>	0	F	F	F	F		F
7	0.005	8	0	F	0	F	8	T	10	T	0	F	0	F	0	F	0	R	>	0	F	F	F	F		F
8	0.005	8	0	F	0	F	3	T	10	T	0	F	0	F	0	F	0	R	>	0	F	F	F	F		F
9	0.005	8	0	F	0	F	4	T	5	T	0	F	0	F	0	F	0	R	>	0	F	F	F	F		F
10	0.005	8	0	F	0	F	0	T	0	T	0	F	0	F	0	F	0	R	>	0	F	F	F	F		F

Kirsten

#	Speed	Res	STMBias	STMBiasA	SetPoint	SetPointA	XPos	XPosA	YPos	YPosA	ZPos	ZposA	Wait	WaitA	Trigger	TriggerA	Channel	Calc	Polarity	Value	StopStepA	FB	HVReset	SPMA	Path	SubVIA
0	0.005	8	0	F	0	F	0	T	0	T	0	F	0	F	0	F	0	R	>	0	F	F	F	F		F
1	0.005	8	0	F	0	F	0	F	-12	T	0	F	0	F	0	F	0	R	>	0	F	F	F	F		F
2	0.005	8	0	F	0	F	0	F	-8	T	0	F	0	F	0	F	0	R	>	0	F	F	F	F		F
3	0.005	8	0	F	0	F	8	T	0	T	0	F	0	F	0	F	0	R	>	0	F	F	F	F		F
4	0.005	8	0	F	0	F	3	T	-5	T	0	F	0	F	0	F	0	R	>	0	F	F	F	F		F

5	0.005	8	0	F	0	F	8	T	-12	T	0	F	0	F	0	F	0	R	>	0	F	F	F	F
6	0.005	8	0	F	0	F	8	F	-12	F	0	F	0	F	0	F	0	R	>	0	F	F	F	F
7	0.005	8	0	F	0	F	11	T	-12	F	0	F	0	F	0	F	0	R	>	0	F	F	F	F
8	0.005	8	0	F	0	F	11	F	-4	T	0	F	0	F	0	F	0	R	>	0	F	F	F	F
9	0.005	8	0	F	0	F	11	F	-4	F	0	F	0	F	0	F	0	R	>	0	F	F	F	F
10	0.005	8	0	F	0	F	11	F	-1	T	0	F	0	F	0	F	0	R	>	0	F	F	F	F
11	0.005	8	0	F	0	F	11	F	-1	F	0	F	0	F	0	F	0	R	>	0	F	F	F	F
12	0.005	8	0	F	0	F	15	T	-4	T	0	F	0	F	0	F	0	R	>	0	F	F	F	F
13	0.005	8	0	F	0	F	15	F	-12	T	0	F	0	F	0	F	0	R	>	0	F	F	F	F
14	0.005	8	0	F	0	F	15	F	-6	T	0	F	0	F	0	F	0	R	>	0	F	F	F	F
15	0.005	8	0	F	0	F	17	T	-4	T	0	F	0	F	0	F	0	R	>	0	F	F	F	F
16	0.005	8	0	F	0	F	19	T	-4	F	0	F	0	F	0	F	0	R	>	0	F	F	F	F
17	0.005	8	0	F	0	F	19	F	-4	F	0	F	0	F	0	F	0	R	>	0	F	F	F	F
18	0.005	8	0	F	0	F	20	T	-10	T	0	F	0	F	0	F	0	R	>	0	F	F	F	F
19	0.005	8	0	F	0	F	22	T	-12	T	0	F	0	F	0	F	0	R	>	0	F	F	F	F
20	0.005	8	0	F	0	F	24	T	-12	F	0	F	0	F	0	F	0	R	>	0	F	F	F	F
21	0.005	8	0	F	0	F	26	T	-10	T	0	F	0	F	0	F	0	R	>	0	F	F	F	F
22	0.005	8	0	F	0	F	24	T	-8	T	0	F	0	F	0	F	0	R	>	0	F	F	F	F
23	0.005	8	0	F	0	F	22	T	-8	F	0	F	0	F	0	F	0	R	>	0	F	F	F	F
24	0.005	8	0	F	0	F	20	T	-6	T	0	F	0	F	0	F	0	R	>	0	F	F	F	F
25	0.005	8	0	F	0	F	22	T	-4	T	0	F	0	F	0	F	0	R	>	0	F	F	F	F
26	0.005	8	0	F	0	F	24	T	-4	F	0	F	0	F	0	F	0	R	>	0	F	F	F	F
27	0.005	8	0	F	0	F	26	T	-6	T	0	F	0	F	0	F	0	R	>	0	F	F	F	F
28	0.005	8	0	F	0	F	26	F	-6	F	0	F	0	F	0	F	0	R	>	0	F	F	F	F
29	0.005	8	0	F	0	F	29	T	-1	T	0	F	0	F	0	F	0	R	>	0	F	F	F	F
30	0.005	8	0	F	0	F	29	F	-4	T	0	F	0	F	0	F	0	R	>	0	F	F	F	F
31	0.005	8	0	F	0	F	28	T	-4	F	0	F	0	F	0	F	0	R	>	0	F	F	F	F
32	0.005	8	0	F	0	F	31	T	-4	F	0	F	0	F	0	F	0	R	>	0	F	F	F	F
33	0.005	8	0	F	0	F	29	T	-4	F	0	F	0	F	0	F	0	R	>	0	F	F	F	F
34	0.005	8	0	F	0	F	29	F	-11	T	0	F	0	F	0	F	0	R	>	0	F	F	F	F
35	0.005	8	0	F	0	F	30	T	-12	T	0	F	0	F	0	F	0	R	>	0	F	F	F	F
36	0.005	8	0	F	0	F	32	T	-12	F	0	F	0	F	0	F	0	R	>	0	F	F	F	F
37	0.005	8	0	F	0	F	32	F	-12	F	0	F	0	F	0	F	0	R	>	0	F	F	F	F
38	0.005	8	0	F	0	F	33	T	-8	T	0	F	0	F	0	F	0	R	>	0	F	F	F	F
39	0.005	8	0	F	0	F	40	T	-8	F	0	F	0	F	0	F	0	R	>	0	F	F	F	F
40	0.005	8	0	F	0	F	40	F	-6	T	0	F	0	F	0	F	0	R	>	0	F	F	F	F
41	0.005	8	0	F	0	F	38	T	-4	T	0	F	0	F	0	F	0	R	>	0	F	F	F	F
42	0.005	8	0	F	0	F	35	T	-4	F	0	F	0	F	0	F	0	R	>	0	F	F	F	F
43	0.005	8	0	F	0	F	33	T	-6	T	0	F	0	F	0	F	0	R	>	0	F	F	F	F
44	0.005	8	0	F	0	F	33	F	-10	T	0	F	0	F	0	F	0	R	>	0	F	F	F	F
45	0.005	8	0	F	0	F	35	T	-12	T	0	F	0	F	0	F	0	R	>	0	F	F	F	F
46	0.005	8	0	F	0	F	38	T	-12	F	0	F	0	F	0	F	0	R	>	0	F	F	F	F
47	0.005	8	0	F	0	F	40	T	-10	T	0	F	0	F	0	F	0	R	>	0	F	F	F	F
48	0.005	8	0	F	0	F	40	F	-10	F	0	F	0	F	0	F	0	R	>	0	F	F	F	F
49	0.005	8	0	F	0	F	43	T	-12	T	0	F	0	F	0	F	0	R	>	0	F	F	F	F
50	0.005	8	0	F	0	F	43	F	-4	T	0	F	0	F	0	F	0	R	>	0	F	F	F	F
51	0.005	8	0	F	0	F	43	F	-6	T	0	F	0	F	0	F	0	R	>	0	F	F	F	F
52	0.005	8	0	F	0	F	45	T	-4	T	0	F	0	F	0	F	0	R	>	0	F	F	F	F
53	0.005	8	0	F	0	F	48	T	-4	F	0	F	0	F	0	F	0	R	>	0	F	F	F	F
54	0.005	8	0	F	0	F	49	T	-6	T	0	F	0	F	0	F	0	R	>	0	F	F	F	F
55	0.005	8	0	F	0	F	49	F	-12	T	0	F	0	F	0	F	0	R	>	0	F	F	F	F
56	0.005	8	0	F	0	F	49	F	-12	F	0	F	0	F	0	F	0	R	>	0	F	F	F	F
57	0	0	0	F	0	F	-1	F	-12	F	0	F	0	F	0	F	0	C	>	0	F	F	F	F
58	0.005	0	0	F	0	F	-1	F	-12	F	0	F	0	F	0	F	0	C	>	0	F	F	F	F
59	5	0	0	F	0	F	-1	F	-12	F	0	F	0	F	0	F	0	C	>	0	F	F	F	F

Sparse snake (shown: 0.001 µm/ms, other speeds also used)

#	Speed	Res	STMBias	STMBiasA	SetPoint	SetPointA	XPos	XPosA	YPos	YPosA	ZPos	ZposA	Wait	WaitA	Trigger	TriggerA	Channel	Calc	Polarity	Value	StopStepA	FB	HVReset	SPMA	Path	SubVIA
0	0.001	8	10	F	0	F	0	T	5	T	0	F	0	F	0	F	0	R	>	0	F	F	F	F		F
1	0.001	8	10	F	0	F	0	T	10	T	0	F	0	F	0	F	0	R	>	0	F	F	F	F		F
2	5	8	10	T	0	F	0	T	10	T	0	F	0	F	0	F	0	R	>	0	F	F	F	F		F
3	0.001	8	10	F	0	F	0	T	15	T	0	F	0	F	0	F	0	R	>	0	F	F	F	F		F
4	5	8	-10	T	0	F	0	T	15	T	0	F	0	F	0	F	0	R	>	0	F	F	F	F		F
5	0.001	8	-10	F	0	F	0	T	20	T	0	F	0	F	0	F	0	R	>	0	F	F	F	F		F
6	5	8	10	T	0	F	0	T	20	T	0	F	0	F	0	F	0	R	>	0	F	F	F	F		F
7	0.001	8	10	F	0	F	5	T	20	T	0	F	0	F	0	F	0	R	>	0	F	F	F	F		F
8	0.001	8	10	F	0	F	5	T	15	T	0	F	0	F	0	F	0	R	>	0	F	F	F	F		F
9	5	8	-10	T	0	F	5	T	15	T	0	F	0	F	0	F	0	R	>	0	F	F	F	F		F
10	0.001	8	-10	F	0	F	5	T	10	T	0	F	0	F	0	F	0	R	>	0	F	F	F	F		F
11	5	8	10	T	0	F	5	T	10	T	0	F	0	F	0	F	0	R	>	0	F	F	F	F		F
12	0.001	8	10	F	0	F	5	T	5	T	0	F	0	F	0	F	0	R	>	0	F	F	F	F		F
13	5	8	-10	T	0	F	5	T	5	T	0	F	0	F	0	F	0	R	>	0	F	F	F	F		F
14	0.001	8	-10	F	0	F	5	T	0	T	0	F	0	F	0	F	0	R	>	0	F	F	F	F		F
15	5	8	10	T	0	F	5	T	0	T	0	F	0	F	0	F	0	R	>	0	F	F	F	F		F
16	0.001	8	10	F	0	F	10	T	0	T	0	F	0	F	0	F	0	R	>	0	F	F	F	F		F
17	0.001	8	10	F	0	F	10	T	5	T	0	F	0	F	0	F	0	R	>	0	F	F	F	F		F
18	5	8	-10	T	0	F	10	T	5	T	0	F	0	F	0	F	0	R	>	0	F	F	F	F		F
19	0.001	8	-10	F	0	F	10	T	10	T	0	F	0	F	0	F	0	R	>	0	F	F	F	F		F
20	5	8	10	T	0	F	10	T	10	T	0	F	0	F	0	F	0	R	>	0	F	F	F	F		F
21	0.001	8	10	F	0	F	10	T	15	T	0	F	0	F	0	F	0	R	>	0	F	F	F	F		F
22	5	8	-10	T	0	F	10	T	15	T	0	F	0	F	0	F	0	R	>	0	F	F	F	F		F
23	0.001	8	-10	F	0	F	10	T	20	T	0	F	0	F	0	F	0	R	>	0	F	F	F	F		F
24	5	8	10	T	0	F	10	T	20	T	0	F	0	F	0	F	0	R	>	0	F	F	F	F		F
25	0.001	8	0	F	0	F	15	T	20	T	0	F	0	F	0	F	0	R	>	0	F	F	F	F		F
26	0.001	8	0	F	0	F	15	T	15	T	0	F	0	F	0	F	0	R	>	0	F	F	F	F		F
27	5	8	-10	T	0	F	15	T	15	T	0	F	0	F	0	F	0	R	>	0	F	F	F	F		F
28	0.001	8	-10	F	0	F	15	T	10	T	0	F	0	F	0	F	0	R	>	0	F	F	F	F		F
29	5	8	10	T	0	F	15	T	10	T	0	F	0	F	0	F	0	R	>	0	F	F	F	F		F
30	0.001	8	10	F	0	F	15	T	5	T	0	F	0	F	0	F	0	R	>	0	F	F	F	F		F
31	5	8	-10	T	0	F	15	T	5	T	0	F	0	F	0	F	0	R	>	0	F	F	F	F		F
32	0.001	8	-10	F	0	F	15	T	0	T	0	F	0	F	0	F	0	R	>	0	F	F	F	F		F
33	5	8	10	T	0	F	15	T	0	T	0	F	0	F	0	F	0	R	>	0	F	F	F	F		F
34	0.001	8	10	F	0	F	20	T	0	T	0	F	0	F	0	F	0	R	>	0	F	F	F	F		F
35	0.001	8	10	F	0	F	20	T	5	T	0	F	0	F	0	F	0	R	>	0	F	F	F	F		F
36	5	8	-10	T	0	F	20	T	5	T	0	F	0	F	0	F	0	R	>	0	F	F	F	F		F
37	0.001	8	-10	F	0	F	20	T	10	T	0	F	0	F	0	F	0	R	>	0	F	F	F	F		F
38	5	8	10	T	0	F	20	T	10	T	0	F	0	F	0	F	0	R	>	0	F	F	F	F		F
39	0.001	8	10	F	0	F	20	T	15	T	0	F	0	F	0	F	0	R	>	0	F	F	F	F		F
40	5	8	-10	T	0	F	20	T	15	T	0	F	0	F	0	F	0	R	>	0	F	F	F	F		F
41	0.001	8	-10	F	0	F	20	T	20	T	0	F	0	F	0	F	0	R	>	0	F	F	F	F		F
42	5	8	0	T	0	F	20	T	20	T	0	F	0	F	0	F	0	R	>	0	F	F	F	F		F
43	0.001	8	0	F	0	F	25	T	20	T	0	F	0	F	0	F	0	R	>	0	F	F	F	F		F

Dense snake (shown: 0.001 µm/ms, other speeds also used)

#	Speed	Res	STMBias	STMBiasA	SetPoint	SetPointA	XPos	XPosA	YPos	YPosA	ZPos	ZposA	Wait	WaitA	Trigger	TriggerA	Channel	Calc	Polarity	Value	StopStepA	FB	HVReset	SPMA	Path	SubVIA
0	0.001	8	1	F	0	F	10	T	0	T	0	F	0	F	0	F	0	R	>	0	F	F	F	F		F
1	5	8	1	F	0	F	10	T	0	T	0	F	0	F	0	T	0	R	>	0	F	F	F	F		F
2	0.001	8	1	F	0	F	10	T	5	T	0	F	0	F	0	F	0	R	>	0	F	F	F	F		F
3	5	8	1	F	0	F	10	T	5	T	0	F	0	F	0	T	0	R	>	0	F	F	F	F		F
4	0.001	8	1	F	0	F	10	T	10	T	0	F	0	F	0	F	0	R	>	0	F	F	F	F		F
5	5	8	1	F	0	F	10	T	10	T	0	F	0	F	0	T	0	R	>	0	F	F	F	F		F
6	0.001	8	1	F	0	F	10	T	15	T	0	F	0	F	0	F	0	R	>	0	F	F	F	F		F
7	5	8	-1	F	0	F	10	T	15	T	0	F	0	F	0	T	0	R	>	0	F	F	F	F		F
8	0.001	8	-1	F	0	F	10	T	20	T	0	F	0	F	0	F	0	R	>	0	F	F	F	F		F
9	5	8	1	F	0	F	10	T	20	T	0	F	0	F	0	T	0	R	>	0	F	F	F	F		F
10	0.001	8	1	F	0	F	11	T	20	T	0	F	0	F	0	F	0	R	>	0	F	F	F	F		F
11	0.001	8	1	F	0	F	11	T	15	T	0	F	0	F	0	F	0	R	>	0	F	F	F	F		F
12	5	8	-1	F	0	F	11	T	15	T	0	F	0	F	0	T	0	R	>	0	F	F	F	F		F
13	0.001	8	-1	F	0	F	11	T	10	T	0	F	0	F	0	F	0	R	>	0	F	F	F	F		F
14	5	8	1	F	0	F	11	T	10	T	0	F	0	F	0	T	0	R	>	0	F	F	F	F		F
15	0.001	8	1	F	0	F	11	T	5	T	0	F	0	F	0	F	0	R	>	0	F	F	F	F		F
16	5	8	-1	F	0	F	11	T	5	T	0	F	0	F	0	T	0	R	>	0	F	F	F	F		F
17	0.001	8	-1	F	0	F	11	T	0	T	0	F	0	F	0	F	0	R	>	0	F	F	F	F		F
18	5	8	1	F	0	F	11	T	0	T	0	F	0	F	0	T	0	R	>	0	F	F	F	F		F
19	0.001	8	1	F	0	F	12	T	0	T	0	F	0	F	0	F	0	R	>	0	F	F	F	F		F
20	0.001	8	1	F	0	F	12	T	5	T	0	F	0	F	0	F	0	R	>	0	F	F	F	F		F
21	5	8	-1	F	0	F	12	T	5	T	0	F	0	F	0	T	0	R	>	0	F	F	F	F		F
22	0.001	8	-1	F	0	F	12	T	10	T	0	F	0	F	0	F	0	R	>	0	F	F	F	F		F
23	5	8	1	F	0	F	12	T	10	T	0	F	0	F	0	T	0	R	>	0	F	F	F	F		F
24	0.001	8	1	F	0	F	12	T	15	T	0	F	0	F	0	F	0	R	>	0	F	F	F	F		F
25	5	8	-1	F	0	F	12	T	15	T	0	F	0	F	0	T	0	R	>	0	F	F	F	F		F
26	0.001	8	-1	F	0	F	12	T	20	T	0	F	0	F	0	F	0	R	>	0	F	F	F	F		F
27	5	8	1	F	0	F	12	T	20	T	0	F	0	F	0	T	0	R	>	0	F	F	F	F		F
28	0.001	8	0	F	0	F	13	T	20	T	0	F	0	F	0	F	0	R	>	0	F	F	F	F		F
29	0.001	8	0	F	0	F	13	T	15	T	0	F	0	F	0	F	0	R	>	0	F	F	F	F		F
30	5	8	-1	F	0	F	13	T	15	T	0	F	0	F	0	T	0	R	>	0	F	F	F	F		F
31	0.001	8	-1	F	0	F	13	T	10	T	0	F	0	F	0	F	0	R	>	0	F	F	F	F		F
32	5	8	1	F	0	F	13	T	10	T	0	F	0	F	0	T	0	R	>	0	F	F	F	F		F
33	0.001	8	1	F	0	F	13	T	5	T	0	F	0	F	0	F	0	R	>	0	F	F	F	F		F
34	5	8	-1	F	0	F	13	T	5	T	0	F	0	F	0	T	0	R	>	0	F	F	F	F		F
35	0.001	8	-1	F	0	F	13	T	0	T	0	F	0	F	0	F	0	R	>	0	F	F	F	F		F
36	5	8	1	F	0	F	13	T	0	T	0	F	0	F	0	T	0	R	>	0	F	F	F	F		F
37	0.001	8	1	F	0	F	14	T	0	T	0	F	0	F	0	F	0	R	>	0	F	F	F	F		F
38	0.001	8	1	F	0	F	14	T	5	T	0	F	0	F	0	F	0	R	>	0	F	F	F	F		F
39	5	8	-1	F	0	F	14	T	5	T	0	F	0	F	0	T	0	R	>	0	F	F	F	F		F
40	0.001	8	-1	F	0	F	14	T	10	T	0	F	0	F	0	F	0	R	>	0	F	F	F	F		F
41	5	8	1	F	0	F	14	T	10	T	0	F	0	F	0	T	0	R	>	0	F	F	F	F		F
42	0.001	8	1	F	0	F	14	T	15	T	0	F	0	F	0	F	0	R	>	0	F	F	F	F		F
43	5	8	-1	F	0	F	14	T	15	T	0	F	0	F	0	T	0	R	>	0	F	F	F	F		F
44	0.001	8	-1	F	0	F	14	T	20	T	0	F	0	F	0	F	0	R	>	0	F	F	F	F		F
45	5	8	1	F	0	F	14	T	20	T	0	F	0	F	0	T	0	R	>	0	F	F	F	F		F
46	0.001	8	1	F	0	F	15	T	20	T	0	F	0	F	0	F	0	R	>	0	F	F	F	F		F
47	0.001	8	1	F	0	F	15	T	15	T	0	F	0	F	0	F	0	R	>	0	F	F	F	F		F
48	5	8	-1	F	0	F	15	T	15	T	0	F	0	F	0	T	0	R	>	0	F	F	F	F		F

49	0.001	8	-1	F	0	F	15	T	10	T	0	F	0	F	0	F	0	R	>	0	F	F	F	F
50	5	8	1	F	0	F	15	T	10	T	0	F	0	F	0	T	0	R	>	0	F	F	F	F
51	0.001	8	1	F	0	F	15	T	5	T	0	F	0	F	0	F	0	R	>	0	F	F	F	F
52	5	8	-1	F	0	F	15	T	5	T	0	F	0	F	0	T	0	R	>	0	F	F	F	F
53	0.001	8	-1	F	0	F	15	T	0	T	0	F	0	F	0	F	0	R	>	0	F	F	F	F
54	5	8	1	F	0	F	15	T	0	T	0	F	0	F	0	T	0	R	>	0	F	F	F	F
55	0.001	8	1	F	0	F	16	T	0	T	0	F	0	F	0	F	0	R	>	0	F	F	F	F
56	0.001	8	1	F	0	F	16	T	5	T	0	F	0	F	0	F	0	R	>	0	F	F	F	F
57	5	8	-1	F	0	F	16	T	5	T	0	F	0	F	0	T	0	R	>	0	F	F	F	F
58	0.001	8	-1	F	0	F	16	T	10	T	0	F	0	F	0	F	0	R	>	0	F	F	F	F
59	5	8	1	F	0	F	16	T	10	T	0	F	0	F	0	T	0	R	>	0	F	F	F	F
60	0.001	8	1	F	0	F	16	T	15	T	0	F	0	F	0	F	0	R	>	0	F	F	F	F
61	5	8	-1	F	0	F	16	T	15	T	0	F	0	F	0	T	0	R	>	0	F	F	F	F
62	0.001	8	-1	F	0	F	16	T	20	T	0	F	0	F	0	F	0	R	>	0	F	F	F	F
63	5	8	1	F	0	F	16	T	20	T	0	F	0	F	0	T	0	R	>	0	F	F	F	F
64	0.001	8	1	F	0	F	17	T	20	T	0	F	0	F	0	F	0	R	>	0	F	F	F	F
65	0.001	8	1	F	0	F	17	T	15	T	0	F	0	F	0	F	0	R	>	0	F	F	F	F
66	5	8	-1	F	0	F	17	T	15	T	0	F	0	F	0	T	0	R	>	0	F	F	F	F
67	0.001	8	-1	F	0	F	17	T	10	T	0	F	0	F	0	F	0	R	>	0	F	F	F	F
68	5	8	1	F	0	F	17	T	10	T	0	F	0	F	0	T	0	R	>	0	F	F	F	F
69	0.001	8	1	F	0	F	17	T	5	T	0	F	0	F	0	F	0	R	>	0	F	F	F	F
70	5	8	-1	F	0	F	17	T	5	T	0	F	0	F	0	T	0	R	>	0	F	F	F	F
71	0.001	8	-1	F	0	F	17	T	0	T	0	F	0	F	0	F	0	R	>	0	F	F	F	F
72	5	8	1	F	0	F	17	T	0	T	0	F	0	F	0	T	0	R	>	0	F	F	F	F
73	0.001	8	1	F	0	F	18	T	0	T	0	F	0	F	0	F	0	R	>	0	F	F	F	F
74	0.001	8	1	F	0	F	18	T	5	T	0	F	0	F	0	F	0	R	>	0	F	F	F	F
75	5	8	-1	F	0	F	18	T	5	T	0	F	0	F	0	T	0	R	>	0	F	F	F	F
76	0.001	8	-1	F	0	F	18	T	10	T	0	F	0	F	0	F	0	R	>	0	F	F	F	F
77	5	8	1	F	0	F	18	T	10	T	0	F	0	F	0	T	0	R	>	0	F	F	F	F
78	0.001	8	1	F	0	F	18	T	15	T	0	F	0	F	0	F	0	R	>	0	F	F	F	F
79	5	8	-1	F	0	F	18	T	15	T	0	F	0	F	0	T	0	R	>	0	F	F	F	F
80	0.001	8	-1	F	0	F	18	T	20	T	0	F	0	F	0	F	0	R	>	0	F	F	F	F
81	5	8	1	F	0	F	18	T	20	T	0	F	0	F	0	T	0	R	>	0	F	F	F	F
82	0.001	8	1	F	0	F	19	T	20	T	0	F	0	F	0	F	0	R	>	0	F	F	F	F
83	0.001	8	1	F	0	F	19	T	15	T	0	F	0	F	0	F	0	R	>	0	F	F	F	F
84	5	8	-1	F	0	F	19	T	15	T	0	F	0	F	0	T	0	R	>	0	F	F	F	F
85	0.001	8	-1	F	0	F	19	T	10	T	0	F	0	F	0	F	0	R	>	0	F	F	F	F
86	5	8	1	F	0	F	19	T	10	T	0	F	0	F	0	T	0	R	>	0	F	F	F	F
87	0.001	8	1	F	0	F	19	T	5	T	0	F	0	F	0	F	0	R	>	0	F	F	F	F
88	5	8	-1	F	0	F	19	T	5	T	0	F	0	F	0	T	0	R	>	0	F	F	F	F
89	0.001	8	-1	F	0	F	19	T	0	T	0	F	0	F	0	F	0	R	>	0	F	F	F	F
90	5	8	1	F	0	F	19	T	0	T	0	F	0	F	0	T	0	R	>	0	F	F	F	F
91	0.001	8	1	F	0	F	30	T	0	T	0	F	0	F	0	F	0	R	>	0	F	F	F	F

Appendix F

LabVIEW program for voltage-assisted writing

The following pages contain the LabVIEW program used for applying a bias voltage during the nanofountain pen writing process. This program was run on a laptop, which was connected to the Keithley sourcemeter (see Figure 4.33) through a USB–RS232 converter. The user must select the correct channel for communications to the sourcemeter and then enter the parameters for the experiment: the length of time to hold each voltage for and the two voltages to be applied in an alternating fashion. When the user runs the program the two voltages will continue to be alternately applied until the user stops the LabVIEW program.

switch_1.vi

Front panel

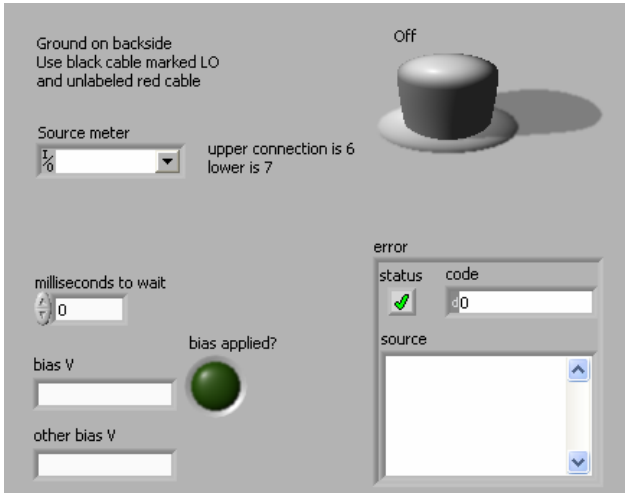

Sequential structure
1st pane

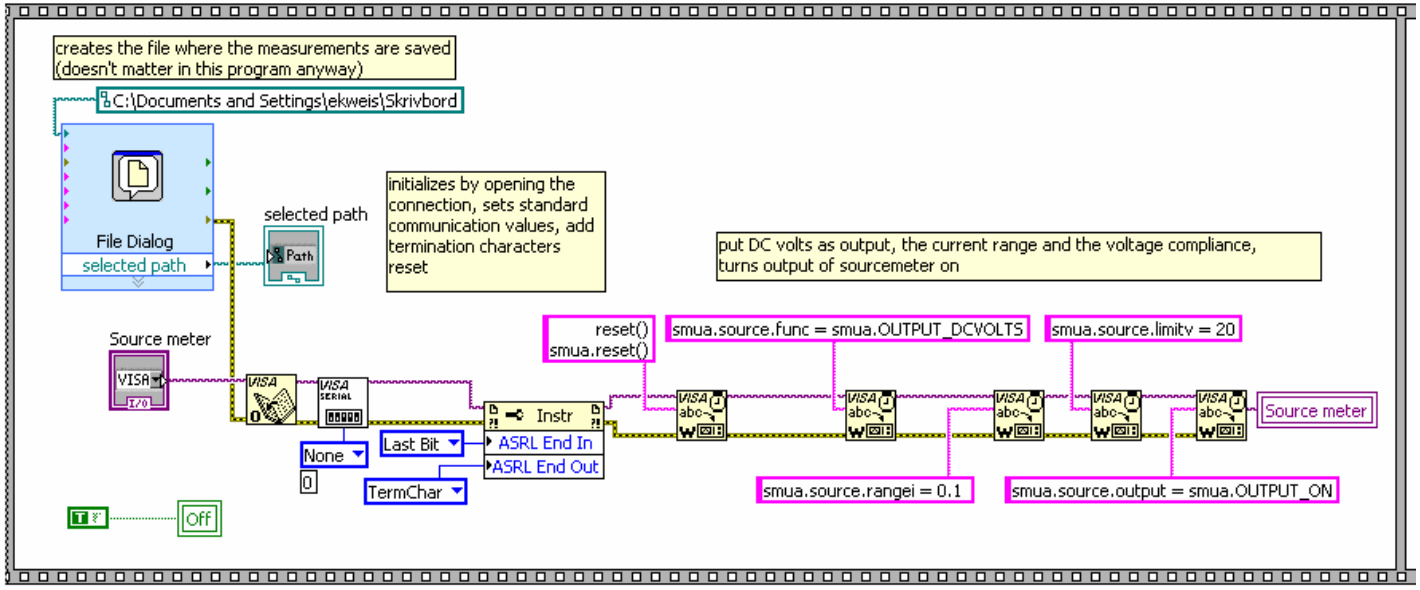

Sequential structure 2nd pane

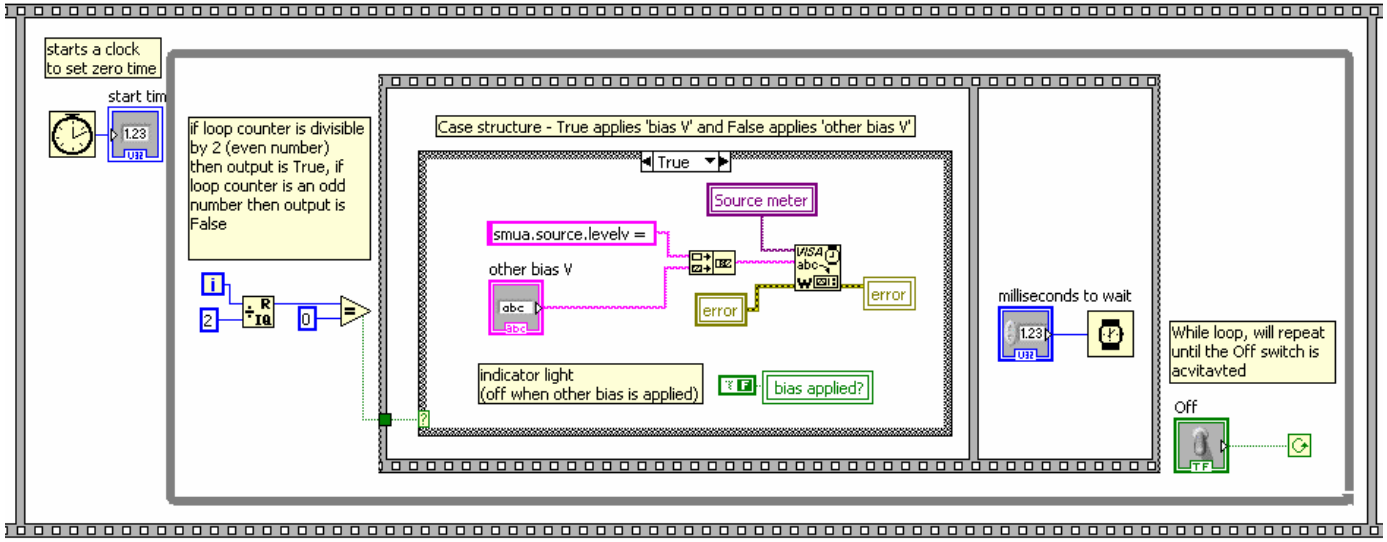

Case structure alternative case

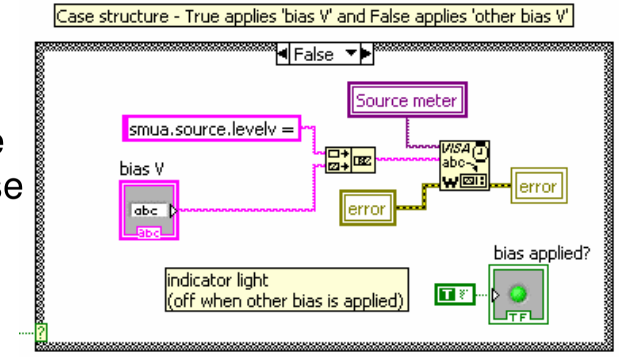

Sequential structure 3rd pane

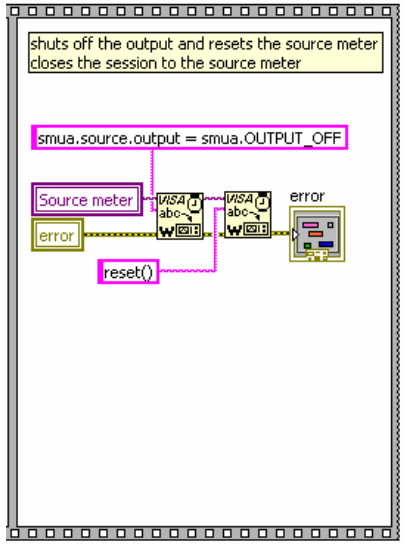

Appendix G

MATLAB programs

The following pages contain the MATLAB scripts and functions used for the analysis of Raman maps. In colour in electronic version.

Name of program	Type	Description
`nanonics_map`	script	Analyses maps made with Nanonics scanner with Quartz/QuartzSpec software to integrate the total spectral area
`nanonics_map_Iat1595_baseline`	script	Analyses Quartz/QuartzSpec maps, integrating a selected spectral region *e.g.* the G band
`zap`	function	Searches for, identifies and removes spikes such as those caused by cosmic rays
`baseline_correct`	function	Removes the background by subtraction of a polynomial fit to the spectrum, ignoring regions where peaks are expected
`peak_area`	function	Integrates the area between two points on the spectrum using the trapezoidal rule
`plotsection`	function	Plots the spectra of a selected region of the Raman map
`map_code`	script	Analyses maps made with the Prior stage and WiRE software
`separate_4_column_data`	function	Restructures the data from WiRE into a three-dimensional matrix

nanonics_map.m

```
% Takes .dat file from QuartzSpec, takes each spectrum and removes spikes
%  then integrates whole spectrum.
% Outputs: plots of all spectra, intensity colour map, selected area

clear all
close all

%% User inputs

folder = 'D:\Kirsten''s documents\PhD\my research\CS5 samples\c11\2013
514nm maps\1.3 g5 finemap3 130516\';
name = 'cs5c11r1c3g5 514nm finemap3 spectradata';
xsize = 24; % needs to be counted during experiment
ysize = 24;
xstep = '300 nm'; % needs to be noted during experiment
ystep = '300 nm';

%% Load data

spectralfile = load ([folder name '.dat']); %file has x values in first
column and spectral data in subsequent columns
sizeoffile = size(spectralfile);
noofxpoints = sizeoffile(1);
noofspectra = sizeoffile(2); %actually number +1 because of x values
x_data = spectralfile(:,1);
filename = strcat(folder,name);

%% Find total integrated area

areas = zeros(noofspectra, 1);
zappedspectra = zeros(sizeoffile);

for i = 2:noofspectra %should be 2 to noofspectra

%manual counter for use when not using loop
%i=105;

%% Remove spikes

%y_data for each spectrum is in spectralfile(:,i) i.e. 'i'th column
zappedspectra(:,i) = zap(spectralfile(:,i)', 500, 100, 15);

%plot spectra raw (green), zapped (blue)
figure(i)
plot (x_data, spectralfile(:,i), ':g')
hold on
plot (x_data, zappedspectra(:,i), '--');
title('Raman spectrum with background')
legend('raw data', 'zapped data', 'Location', 'Northwest')
xlabel('Raman shift / cm^-^1')
ylabel('Intensity / a.u.')
grid on


%% define and integrate G peak
```

```
areas(i) = peak_area(x_data, zappedspectra(:,i), 1248, 1740); %full is
1248-1740

pause(0.2); %pause time in seconds

if  mod(i,50) == 0                    %i == 80
    close all    %stops java memory heap problems
end


end         %end loop through spectra

close all

%% Plot areas against spectrum number as 2D graph

figure(1)
plot(areas, '-ok', 'LineWidth', 2)
title('integrated intensities as function of spectrum number')
xlabel('spectrum number')
ylabel('G peak intensity / a.u.')

%% Plots as 3D image

%counts desired size of ratio data matrix, then puts data into matrix that
%size

shaped_areas = (reshape(areas(2:noofspectra), xsize, ysize))';

%creates image
map = figure('NumberTitle', 'on','Name', 'Map');
image(shaped_areas, 'CDataMapping', 'scaled');
axis image
%title()
title(sprintf(['Full integrated area \n' name]), 'fontsize', 12)
xlabel(['x / ' xstep], 'fontsize', 12)
ylabel(['y / ' ystep], 'fontsize', 12)
%caxis([209000 1170000]) %fixes min and max of colour scale
colorbar

%% Saves outputs: data from map and bitmap file of map

save([filename 'Full areas data.txt'],'shaped_areas','-ASCII');
print('-dbmp16m', '-r1000', [filename ' map.bmp']);
hgexport(map, [filename ' exported map']);

%% Optional plot section of all spectra

%will plot all spectra with no moo axes

for i = 2: noofspectra %should be 2 to noofspectra

%manual counter for use when not using loop
%i=105;
```

```
figure(100)
subaxis(ysize, xsize, (i-1),'Spacing', 0, 'Padding', 0, 'Margin', 0)
plot (x_data, zappedspectra(:,(i)), 'r')
axis off

end

saveas(100, [folder 'all spectra plotted.bmp']); %uncomment to save

%% Create variable with all spectra in grid

%can then select individual spectra by using shaped_spectra(:, xposition,
%yposition)

shaped_spectra = reshape(zappedspectra(:,2:noofspectra), noofxpoints,
xsize, ysize);

%will plot spectra with axes in Figure 10 and without axes in Figure 11

xstart = 20;
xend = 23;
ystart = 8;
yend = 12;

plotsection(shaped_spectra, x_data, xstart, xend, ystart, yend);

%saveas(10, [folder 'spectra selection.bmp']); % uncomment if desired
%saveas(11, [folder 'spectra selection2.bmp']);
```

nanonics_map_Iat1595_baseline.m

```
% Takes .dat file from QuartzSpec, takes each spectrum and removes spikes
% and background, then integrates chosen region (eg G band).
% Outputs: plots of all spectra, G band colour map, selected area

clear all
close all

%% User inputs

folder = 'D:\Kirsten''s documents\PhD\my research\transport
measurements\CS5 samples\c11\2013 514nm maps\1.3 g5 finemap2\';
name = 'cs5c11r1c3g5 514nm finemap2 spectradata.dat';
xsize = 19; % needs to be counted during experiment
ysize = 20;
xstep = '500 nm'; % needs to be noted during experiment
ystep = '500 nm';
G_start = 1575; % define limits of area to be integrated, cm-1
G_end = 1605;

%% Load data

filename = strcat(folder,name);
spectralfile = load ([folder name]); %file has x values in first column and
spectral data in subsequent columns
```

```
sizeoffile = size(spectralfile);
noofxpoints = sizeoffile(1);
noofspectra = sizeoffile(2); %actually number +1 because of x values
x_data = spectralfile(:,1);
G_range = strcat(sprintf('%-4.4d', G_start), '-' , sprintf('%-4.4d',
G_end)); %puts G range into a string for future use


%% Find total integrated area

areas = zeros(noofspectra, 1);
zappedspectra = zeros(sizeoffile);
baselinespectra = zeros(sizeoffile);

for i = 2:noofspectra %should be 2 to noofspectra

%manual counter for moo use when not using loop
%i=504;

%% Remove spikes

%y_data for each spectrum is in spectralfile(:,i) i.e. 'i'th column
zappedspectra(:,i) = zap(spectralfile(:,i)', 400, 400, 15);

%% Baseline correct

%corrected_y_data = baseline_correct(x_data, new_y, 2);
baselinespectra(:,i) = baseline_correct(x_data, zappedspectra(:,i), 2);

%plot spectra raw (green), zapped (blue) and baselined (red)
figure(i)
plot (x_data, spectralfile(:,i), ':g')
hold on
plot (x_data, zappedspectra(:,i), '--');
plot (x_data, baselinespectra(:,i), 'r');
title('Raman spectrum with background')
legend('raw data', 'zapped data', 'baseline-corrected data', 'Location',
'Northwest')
xlabel('Raman shift / cm^-^1')
ylabel('Intensity / a.u.')
grid on


%% define and integrate G peak

areas(i) = peak_area( x_data, baselinespectra(:,i), G_start, G_end);

pause(0.05); %pause time in seconds

if  mod(i,50) == 0                    %i == 80
    close all    %stops java memory heap problems
end


end         %end loop through spectra

close all
```

```
%% Plot areas against spectrum number as 2D graph

figure(1)
plot(areas, '-ok', 'LineWidth', 2)
title('integrated intensities as function of spectrum number')
xlabel('spectrum number')
ylabel('G peak intensity / a.u.')

%% Plots as 3D image

%counts desired size of ratio data matrix, then puts data into matrix that
%size

shaped_areas = (reshape(areas(2:noofspectra), xsize, ysize))';

%creates image
map = figure('NumberTitle', 'on','Name', 'Map');
%image(shaped_areas, 'CDataMapping', 'scaled');
image(log10(abs(shaped_areas)), 'CDataMapping', 'scaled');
axis image
%title()
title(sprintf(['Integrated area '  G_range ' cm^-^1 logscale\n' name]),
'fontsize', 12)
xlabel(['x / ' xstep], 'fontsize', 12)
ylabel(['y / ' ystep], 'fontsize', 12)
%caxis([-2000 13000]) %fixes min and max of colour scale
colorbar

saveas(map, [filename ' I ' G_range ' logscale map.bmp']);

%% Saves outputs: data from map and bitmap file of map

save([filename ' integrated area ' G_range '
data.txt'],'shaped_areas','-ASCII');
%print('-dbmp16m', '-r1000', [filename ' I ' G_range ' map.bmp']);
hgexport(map, [filename 'I ' G_range ' exported map']);
save([filename ' zappedspectra.txt'],'zappedspectra','-ASCII');
save([filename ' baselinespectra.txt'],'baselinespectra','-ASCII');

%% Plot areas against spectrum number as 2D graph in rows

%used for plotting cross-sections, e.g. for measuring lasr spot size

%figure(1)
%plot(areas(361:420), '-ok', 'LineWidth', 2)
%title('row7 integrated intensities')
%xlabel('x distance / 100 nm')
%ylabel('G peak intensity / a.u.')
%saveas(1, [folder 'row 7 Gpeak (1570-1590cm-1).bmp']);


%% Create variable with all spectra in grid

%can then select individual spectra by using shaped_spectra(:, xposition,
%yposition)
```

```
shaped_spectra = reshape(zappedspectra(:,2:noofspectra), noofxpoints,
xsize, ysize);

%will plot spectra with axes in Figure 10 and without axes in Figure 11

xstart = 8;
xend = 11;
ystart = 14;
yend = 22;

plotsection(shaped_spectra, x_data, xstart, xend, ystart, yend);

%saveas(11, [folder 'spectra selection2.bmp']);
```

zap.m

```
function zapped_spectral_data = zap(spectral_data, thresholdstep1,
thresholdstep2, thresholdwidth)

%function to return zapped spectral data

%variables list:
%spectral_data         input  [many]x1 matrix of spectral intensity data
%thresholdstep        input  checking for sharp enough to define as spike
%thresholdstep2        input  checking for flat enough to define as flat
%thresholdwidth       input  checking for narrow enough to define as spike
%zapped_spectral_data  output [many]x1 zapped matrix of spectral intensity
data

if nargin < 2, thresholdstep1 = 500; end %sets value if user doesn't specify
if nargin < 3, thresholdstep2 = 500; end %sets value if user doesn't specify
if nargin < 4, thresholdwidth = 15; end %sets value if user doesn't specify

sizeoffile = size(spectral_data);
noofxpoints = sizeoffile(1);

y_data = spectral_data;
new_y = y_data;

%% find spikes
for c = 1:3 %do the spike removal procedure 3 times incase of multiple spikes

    %initialise markers
    start_spike = 1;
    end_spike = 1;

    movingmean = zeros(noofxpoints);
    forwardstep = zeros(noofxpoints);
    backwardstep = zeros(noofxpoints);

    %calculate moovingmean for each point, and difference between the
    %movingmean and point before or point after
    for s = 3:(noofxpoints-3)
        movingmean(s) = mean(new_y((s-1):(s+1)));
        forwardstep(s) = new_y(s+2)-movingmean(s);
```

```
        backwardstep(s) = new_y(s-2)-movingmean(s);
    end

    %set start and end points of spikes based on thresholds
    for s = 3:(noofxpoints-3)
        if forwardstep(s) > thresholdstep1 %tests for big enough step to
be spike
            if abs(forwardstep(s-1)) < thresholdstep2 %test for previous
step to be not spike
                start_spike = (s+1); %sets start value
            elseif abs(forwardstep(s-2)) < thresholdstep2 %tests for more
previous step being not spike
                start_spike = (s); %sets start value
            end
        end
        if backwardstep(s) > thresholdstep1 %tests for big enough step to
be spike
            if abs(backwardstep(s+1)) < thresholdstep2 %test for next step
to be not spike
                end_spike = (s-1); %sets end value
            elseif abs(backwardstep(s+2)) < thresholdstep2 %tests for next
but one step being not spike
                end_spike = (s); %sets end value
            end
        end
    end

    %replaces spike with line between end points
    if (end_spike - start_spike)< thresholdwidth %checks that start and end
are close enough to be a spike
        delta_s = end_spike - start_spike; %difference in s between start
and end
        delta_y = new_y(end_spike) - new_y(start_spike); %difference in y
between start and end
        for s=(start_spike+1):(end_spike-1)
            new_y(s) =
delta_y*((s-start_spike)/delta_s)+y_data(start_spike);
        end
    end
end

zapped_spectral_data = new_y;  %returns corrected data into function output
variable
```

baseline_correct.m

```
function baselineddata = baseline_correct(x_data, y_data, order,
D_start_shift, D_end_shift, G_start_shift, G_end_shift)

%function to take spectral data and remove polynomial background, ignoring
%areas of D or G peaks

%variable list:
%x_data          input          Raman shift values for the spectrum
%y_data          input          Raman intensity values for the spectrum
%order         optionalinput  order of polynomial used to fit background,
%default is 5
%D/G_start/end   optionalinput  Raman shifts of starts and end of D and G
%peak, default 1300-1400 and 1520-1650 cm-1
%baselineddata   output         Raman intensity data after baseline
%subtraction

sizeoffile = size(x_data);
noofxpoints = sizeoffile(1);

%% Find nonpeak part of spectrum

%define where the D and G peaks start and end, in terms of Raman shift
if nargin < 7, G_end_shift = 1650; end %sets value if user doesn't specify
if nargin < 6, G_start_shift = 1520; end %sets value if user doesn't specify
if nargin < 5, D_end_shift = 1400; end %sets value if user doesn't specify
if nargin < 4, D_start_shift = 1300; end %sets value if user doesn't specify

%define where D and G peaks start and end, in terms of matrix indices
D_start_index = find(x_data>=D_start_shift,1,'first');
D_end_index = find(x_data>=D_end_shift,1,'first');
G_start_index = find(x_data>=G_start_shift,1,'first');
G_end_index = find(x_data>=G_end_shift,1,'first');

%creates variables containing only the spectral data not including peaks
nonpeak_x_data = x_data([1:D_start_index, D_end_index:G_start_index,
G_end_index:noofxpoints]);
nonpeak_y_data = y_data([1:D_start_index, D_end_index:G_start_index,
G_end_index:noofxpoints]);

%% Polyfit nonpeak part of spectrum

if nargin < 3, order = 5; end %sets value if user doesn't specify
nonpeak_polycoeff = polyfit(nonpeak_x_data, nonpeak_y_data, order);
nonpeak_fit = polyval(nonpeak_polycoeff, x_data);

%% Subtract baseline from moo data
baselineddata = y_data - nonpeak_fit;
```

peak_area.m

```
function area_of_peak = peak_area ( x_data, y_data, peak_start_position,
peak_end_position)

%function taking Raman intensity vs shift data and integrating the area
%under the curve between two given points

%variable list:
%x_data               input         Raman shift data
%y_data               input         Raman intensity data
%peak_start_position  input         Raman shift of start of peak
%peak_end_position    input         Raman shift if end of peak
%area_of_peak         output        integrated area under curve

if x_data(2)-x_data(1) > 0 %checks for the shift numbers being acending
    peak_start_index = find(x_data>=peak_start_position,1,'first');
    peak_end_index = find(x_data>=peak_end_position,1,'first');
else %applies if Raman shift numbers are decreasing in the moo matrix
    peak_start_index = find(x_data<peak_start_position,1,'first');
    peak_end_index = find(x_data<peak_end_position,1,'first');
end

peak_x_data = x_data([peak_start_index : peak_end_index]);
peak_y_data = y_data([peak_start_index : peak_end_index]);
area_of_peak = trapz(peak_x_data, peak_y_data);
```

plotsection.m

```
function output = plotsection(shaped_spectra, x_data, xstart, xend, ystart,
yend)

%function to plot only a chosen section of the map as minispectra

%variables list:
%shaped_spectra      input  [xpoints]x[xsize]x[ysize] matrix of spectral
intensity data
%x_data               input  spectral shift data
%xstart               input  number of x point at start of selected area
%xend                 input  number of x point at end of selected area
%ystart               input  number of y point at start of selected area
%yend                 input  number of y point at end of selected area
%output               output gridnumber - integer


% (not needed now) shaped_spectra = reshape(zappedspectra(:,2:noofspectra),
noofxpoints, xsize, ysize); moo

columns = xend - xstart + 1;
rows = yend - ystart + 1;

label_position = x_data(1);

figure(10)
```

```
for currentrow = ystart : yend

    rowno = currentrow - ystart +1;

    for currentcolumn = xstart : xend

        columnno = currentcolumn - xstart +1;

        gridposition = (rowno-1)*columns + columnno;
        xposition = xstart + columnno -1;
        yposition = ystart + rowno -1;

        subplot (rows, columns, gridposition)
        plot(x_data, shaped_spectra(:, xposition, yposition), 'color',
'r')
        %legend([xposition], 'location', 'northwest')
        %title([num2str(yposition) '.' num2str(xposition)])
        axis tight
        if x_data(1) == 1248
            set(gca,'XTick',[1300 1450 1600])
        else
            set(gca,'XTickLabel')
        end
        text(label_position, (max(shaped_spectra(:, xposition,
yposition))-10),[num2str(yposition) '.' num2str(xposition)], 'color',
'b')
    end

end

for currentrow = ystart : yend

    rowno = currentrow - ystart +1;

    for currentcolumn = xstart : xend

        columnno = currentcolumn - xstart +1;

        gridposition = (rowno-1)*columns + columnno;
        xposition = xstart + columnno -1;
        yposition = ystart + rowno -1;

        figure(11)
        subaxis(rows, columns, (gridposition), 'Spacing', 0, 'Padding', 0,
'Margin', 0)
        plot(x_data, shaped_spectra(:, xposition, yposition), 'color',
'r')
        axis off
        %title([num2str(yposition) '.' num2str(xposition)])
        text(label_position, max(shaped_spectra(:, xposition,
yposition)),[num2str(yposition) '.' num2str(xposition)], 'color', 'b')
    end

end

output = gridposition;
```

map_code.m

```
% Takes .txt file from Wire:
%   columns 1 and 2 are x and y positions, respectively
%   columns 3 and 4 contain Raman shift and intensity, respectively
% Selects only the desired region, removes spikes and background,
% then integrates chosen region (eg RBM peak).
% Outputs: plots of all spectra, peak intensity colour map, selected area

clear all
close all

%% User inputs

folder = 'D:\Kirsten''s documents\PhD\my research\CS5 samples\c11\2013
514nm maps\1.3 g5-6 roughmap0 130221\';
name = 'cs5c11r1c3 gap5-6 roughmap 514nm';
D_start = 1300; % define limits of area to be integrated, cm-1
D_end = 1400; % need not be G, just the peak of interest
G_start = 1570; % define limits of area to be integrated, cm-1
G_end = 1600; % need not be G, just the peak of interest

%% Load data

scrsz = get(0,'ScreenSize'); %measures screensize for use when making
figures
filename = strcat(folder, name);
spectralfile = load ([folder name '.txt']);
D_range = strcat(sprintf('%-4.4d', D_start), '-' , sprintf('%-4.4d',
D_end)); %puts G range into a string for future use
G_range = strcat(sprintf('%-4.4d', G_start), '-' , sprintf('%-4.4d',
G_end)); %puts G range into a string for future use

%% Separate data from one very long column into multiple layers in 3rd
dimension

spectraldata = separate_4_column_data(spectralfile);
noofspectra = size(spectraldata, 3);
zappedspectraldata = spectraldata; %initiates variable to give correct x,
y and shift values
baselineddata = spectraldata;     %initiates variable to give correct x,
y and shift values

%% Zaps and baselinecorrects and plots each stage of data's history

for spectrumnumber = 1 : noofspectra %puts values into each spectrum slot
in turn
    zappedspectraldata(:, 4, spectrumnumber) = zap(spectraldata(:, 4,
spectrumnumber), 500, 100, 15);
    baselineddata(:, 4, spectrumnumber) =
baseline_correct(spectraldata(:,3,spectrumnumber),zappedspectraldata(:,
4,spectrumnumber),2);
    figure('NumberTitle','on', 'OuterPosition',[1 1 scrsz(3)/2
scrsz(4)/2])
    plot ( spectraldata(:, 3, spectrumnumber) , spectraldata(:, 4,
spectrumnumber) , ':g' );
```

```
    hold on
    plot (spectraldata(:, 3, spectrumnumber) , zappedspectraldata(:, 4,
spectrumnumber) , '--');
    plot (spectraldata(:, 3, spectrumnumber) , baselineddata(:, 4,
spectrumnumber), 'r');
    grid on
    pause(0.2);

    if  mod(spectrumnumber,50) == 0                    %i == 80
    close all    %stops java memory heap problems
    end
end

%% Measures peak areas and calculate G/D ratio

%initialise variables so loop is efficient
x_data = baselineddata(:, 3, 1);
D_peak_area = zeros(noofspectra);
G_peak_area = zeros(noofspectra);
G_D_ratio = zeros(noofspectra);

for spectrumnumber = 1 : noofspectra %meaures each spectrum in turn
    y_data = baselineddata(:, 4, spectrumnumber);
    D_peak_area(spectrumnumber) = peak_area(x_data, y_data , D_start,
D_end);
    G_peak_area(spectrumnumber) = peak_area(x_data, y_data , G_start,
G_end);
    G_D_ratio(spectrumnumber) = G_peak_area(spectrumnumber) /
D_peak_area(spectrumnumber);
end

%% Plot absolute peak areas and G/D ratio vs spectrum number

G_areas = G_peak_area;     %transpose row vector to column vector
D_areas = D_peak_area;     %transpose row vector to column vector
figure('OuterPosition',[1 scrsz(4)/2 scrsz(3) scrsz(4)/2])
subplot(1,2,1)
plot(G_areas, '-ok', 'LineWidth', 2)
hold on
plot(D_areas, '-or', 'LineWidth', 2)
title(['G and D peak intensities for ' name], 'fontsize', 14)
xlabel('spectrum number', 'fontsize', 12)
%YTickLabel('fontsize', 14)
ylabel('peak intensity / a.u.', 'fontsize', 12)
legend('G peak areas', 'D peak areas', 'fontsize', 12)

subplot(1,2,2)
plot(G_D_ratio, '-ob', 'LineWidth', 2)
title([' '])
xlabel('spectrum number')
ylabel('peak intensity / a.u.')
legend('G/D ratio')

print('-dbmp16m', '-r1000', [filename  ' map dataplot.bmp']);

%% 3D map

%create map_data
```

```
    %columns: x position, y position, G/D ratio
    %rows: each spectrum

    map_data = zeros(noofspectra, 3); %creates matrix of correct size

for spectrumnumber = 1 : noofspectra %meaures each spectrum in turn
    map_data(spectrumnumber, :) = [ baselineddata(1, 2, spectrumnumber)
baselineddata(1, 1, spectrumnumber) G_D_ratio(spectrumnumber)];
end

%extract x values into vector xpositions in acending order
mapdatayx = sortrows(map_data, [2 1]); %sort rows by y then by x values
xpositions(1)= mapdatayx(1,1); %puts first x value into first place
i=2; %starts counter
while i <= noofspectra && mapdatayx(i,1)>mapdatayx(i-1,1) %while the x
value is larger than the previous one
    xpositions(i) = mapdatayx(i,1); %put the x value into the xpositions
vector
    i = i+1; %increase loop counter
end %end once each of the x values has been taken

%extract y values into vector ypositions in acending order
mapdataxy = sortrows(map_data, [1 2]); %sort by x then by y
ypositions(1)= mapdataxy(1,2); %puts first y value into first place
i=2; %starts counter
while i <= noofspectra && mapdataxy(i,2)>mapdataxy(i-1,2)
    ypositions(i) = mapdataxy(i,2); %put the y value into the ypositions
vector
    i = i+1; %increase loop counter
end

%counts desired moo size of ratio data matrix,
%then puts G/D ratio into matrix that size
xsize = size(xpositions, 2);
ysize = size(ypositions, 2);
ratio = reshape(mapdataxy(:, 3), ysize, xsize);

%creates image
map = figure('NumberTitle', 'on','Name', 'Map',
'OuterPosition',[scrsz(4)/2+120 1 scrsz(3)/2 scrsz(4)/2]);
image(xpositions, ypositions, ratio, 'CDataMapping', 'scaled');
axis image
title(['Map of G/D ratio for ' name], 'fontsize', 12)
xlabel('x / um', 'fontsize', 12)
ylabel('y / um', 'fontsize', 12)
%caxis([0 10]) %fixes min and max of colour scale
colorbar

%% Saves outputs: data from G/D ratio map and bitmap file of map

%save([filename ' GD map data.txt'],'map_data','-ASCII');
%print('-dbmp16m', '-r1000', [filename ' map.bmp']);
%hgexport(map, [filename ' exported map']);

%% Creates map of G peak areas

Gmap = reshape(G_peak_area(:,1), xsize, ysize)';
```

```
%creates image
map = figure('NumberTitle', 'on','Name', 'Map',
'OuterPosition',[scrsz(4)/2+120 1 scrsz(3)/2 scrsz(4)/2]);
image(xpositions, ypositions, Gmap, 'CDataMapping', 'scaled');
axis image
title(['Map of G ' G_range ' intensity for ' name], 'fontsize', 12)
xlabel('x / um', 'fontsize', 12)
ylabel('y / um', 'fontsize', 12)
%caxis([500 4000]) %fixes min and max of colour scale
colorbar

%saveas(map,[folder name 'Gpeak (' G_range 'cm-1) map.bmp']);

%% Prints spectra as grid

figure('NumberTitle', 'on','Name', 'Spectra', 'OuterPosition',[1 30
scrsz(3) scrsz(4)]); %[scrsz(4)/2+120 1 scrsz(3)/2 scrsz(4)/2] left bottom
width height
figurenumber = gcf;

for i = 1: noofspectra %should be 2 to noofspectra
    figure(figurenumber)
    subaxis(ysize, xsize, i,'Spacing', 0, 'Padding', 0, 'Margin', 0)
    plot (x_data, baselineddata(:,4,i), 'r')
    axis off
end

%saveas(figurenumber,[filename 'spectragrids.bmp']);


%% Create variable with all spectra in grid

%can then select individual spectra by using shaped_spectra(:, xposition,
%yposition)

noofxpoints = size(x_data, 1);
shaped_spectra = reshape(baselineddata(:,4,1:noofspectra), noofxpoints,
xsize, ysize);

%will plot spectra with axes in Figure 10 and without axes in Figure 11

xstart = 13;
xend = 17;
ystart = 19;
yend = 24;

plotsection(shaped_spectra, x_data, xstart, xend, ystart, yend);

%saveas(10, [filename 'spectra selectionA.bmp']); % uncomment if desired
saveas(11, [filename 'spectra selection6.bmp']);
```

separate_4_column_data.m

```
function [spectraldata] = separate_4_column_data(spectralfile)
% Function to separate data into spectra

% variable list:
% spectralfile    input     [manymany]x4 matrix with many spectra appended
in list, shift
% values in column 3
% spectraldata    output    [many]x4x[many] matrix with separated spectra

%the created 3-dimensional matrix is as follows:
%dimension 1 (rows) - each data point
%dimension 2 (columns) - y-spacial-position, x-spacial-position,
%Raman-shift, Raman-Intensity
%dimension 3 (layers) - spectra

%% Counts size of file
sizeoffile = size(spectralfile); %count how many points there are
noofpoints = sizeoffile(1); %put how many points into variable noofpoints

%% Identify the start of each new spectrum
for c = 1 : (noofpoints-1)
    if spectralfile(c,3) < spectralfile((c+1),3)
        testnewspectrum(c) = c;
    %else
    %   testnewspectrum(c) = 0;
    end
end

testnewspectrumcolumn = testnewspectrum';
ind = find(testnewspectrumcolumn); %the indices of the last point of each
spectrum (ignoring last spectrum)

sizeofind = size(ind);              %counts the moo number of spectra
numberofspectra = sizeofind(1);  %puts the number of spectra into variable

ind(numberofspectra+1) = noofpoints; %adds in the last point of the last
spectra
numberofspectra = numberofspectra +1; %adds the last spectra to the count

%% Put the spectral data into separate layers of spectraldata (3D) matrix
spectraldata(:,:,1) = spectralfile(1:ind, :); %puts values into the first
spectrum slot

for spectrumnumber = 2 : numberofspectra %puts values into each spectrum
slot in turn
    startno = ind(spectrumnumber-1)+1;
    endno = ind(spectrumnumber);
    spectraldata(:,:,spectrumnumber) = spectralfile(startno:endno, :);
end                 %ends when all spectra are in their place

%% Ensures that spectrum data is in acending shift order

if spectraldata(1, 3, 1) > spectraldata(2, 3, 1)
    spectraldata = flipdim(spectraldata, 1);
end
```

Appendix H

Nanomanipulation example

Figures H.1 and H.2 show each step of the manipulation that appears in Figure 5.18 in Section 5.3.

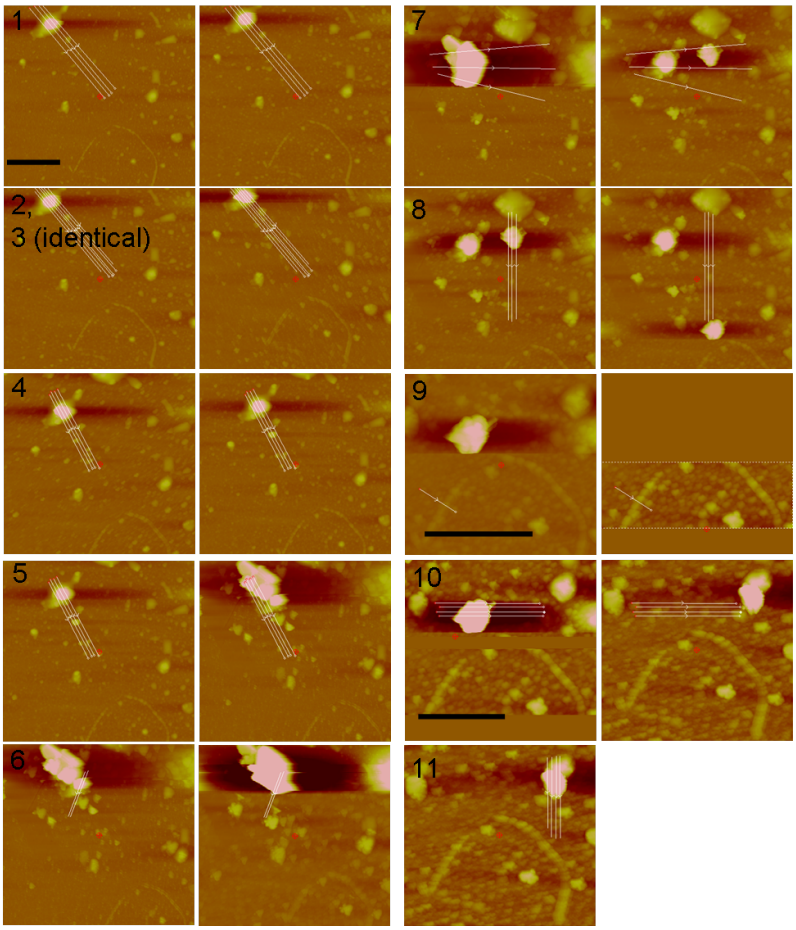

Figure H.1: A complete sequence of nanomanipulation steps for the first part of the manipulation of an agglomerate of nanoparticles onto a CNT. The scale bar represents 1 µm.

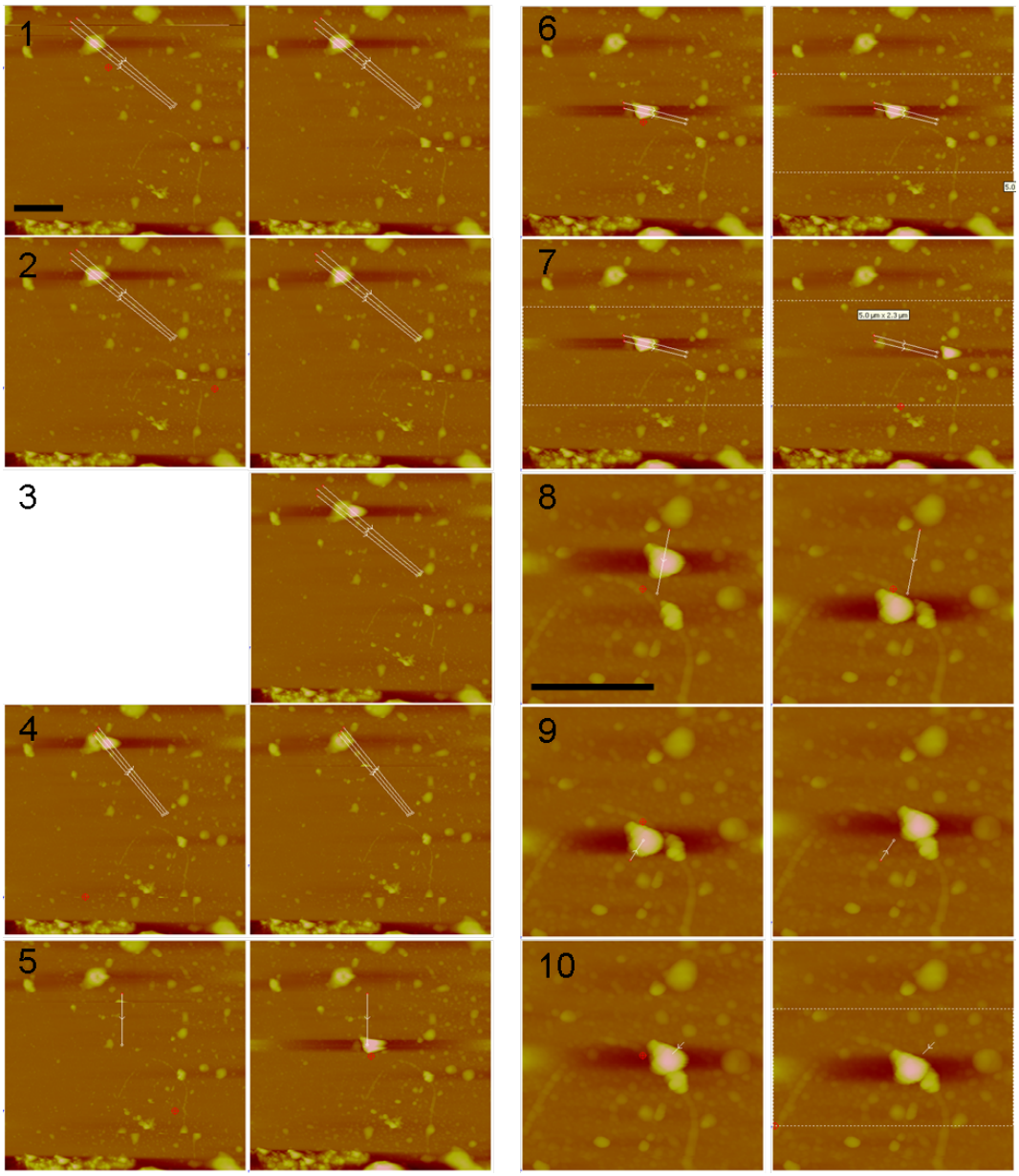

Figure H.2: A complete sequence of nanomanipulation steps for the second part of the manipulation of an agglomerate of nanoparticles onto a CNT. The scale bar represents 1 µm.

Appendix I

SERS fluctuations

Observations of spectral fluctuations

Anomalous peaks were first observed where nanomanipulation had been performed on a particle to place it onto a SWNT (Figure I.1a). When attempting to quantify the enhancement of the SWNT Raman signal given by the nanoparticle, it was impossible to distinguish the SWNT signal from other signals, some of which appeared at a similar spectral position (Figure I.1b). This was repeated on another sample with a particle pushed onto a SWNT (Figure I.1c) where the Raman spectra at the particle showed many intense peaks at all positions within the measured spectral range (Figure I.1d). The spatial steps between measurements was 200 nm and the diameter of the laser spot was 1 μm, so consecutive measurements were expected to have very similar spectra. Repeated Raman measurements on the particle revealed that the intensity and position of these extra peaks fluctuated rapidly (faster than the 1 s time resolution of the Raman spectrometer).

Such large-intensity fluctuating peaks were also observed in other areas of Raman maps, where agglomerates of nanoparticles were located (Figure I.2). Measurements at different positions on a sample showed that the extra peaks were not observed on clean areas of SiO_2 and they sometimes did and sometimes did not appear where nanoparticles were observed, whether they appeared as isolated particles or as a "puddle" of gold. On electrodes they also sometimes did

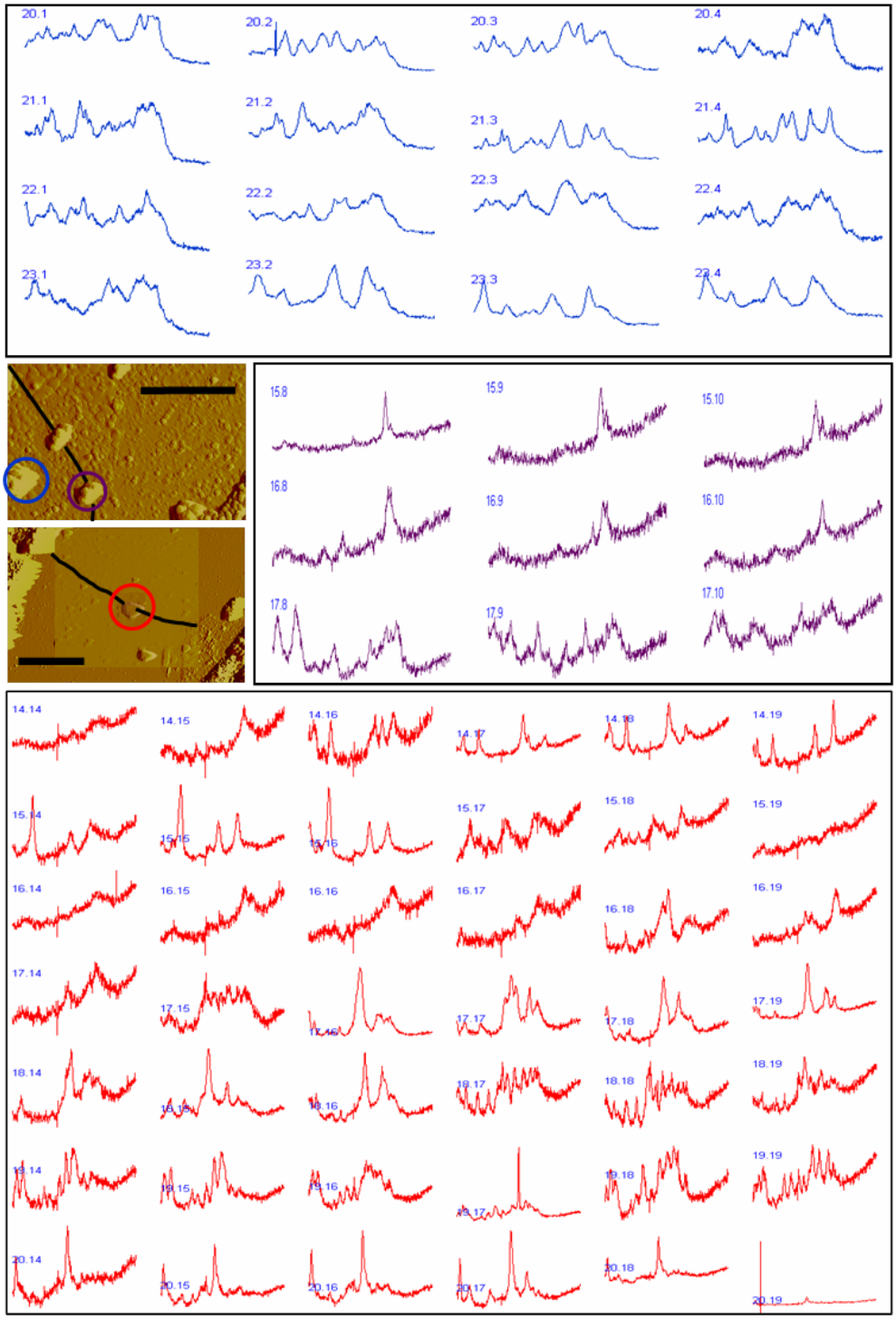

Figure I.1: Raman spectra from fine maps of nanoparticles and carbon nanotubes, showing fluctuations between adjacent points. AFM images show the locations of the carbon nanotubes (highlighted with black lines) and nanoparticles (circled in the colour corresponding to the associated spectra). The Raman spectra all have a range of 1248–1740 cm^{-1} and are normalised to the point of maximum intensity. The scale bars on the AFM images are 3 μm.

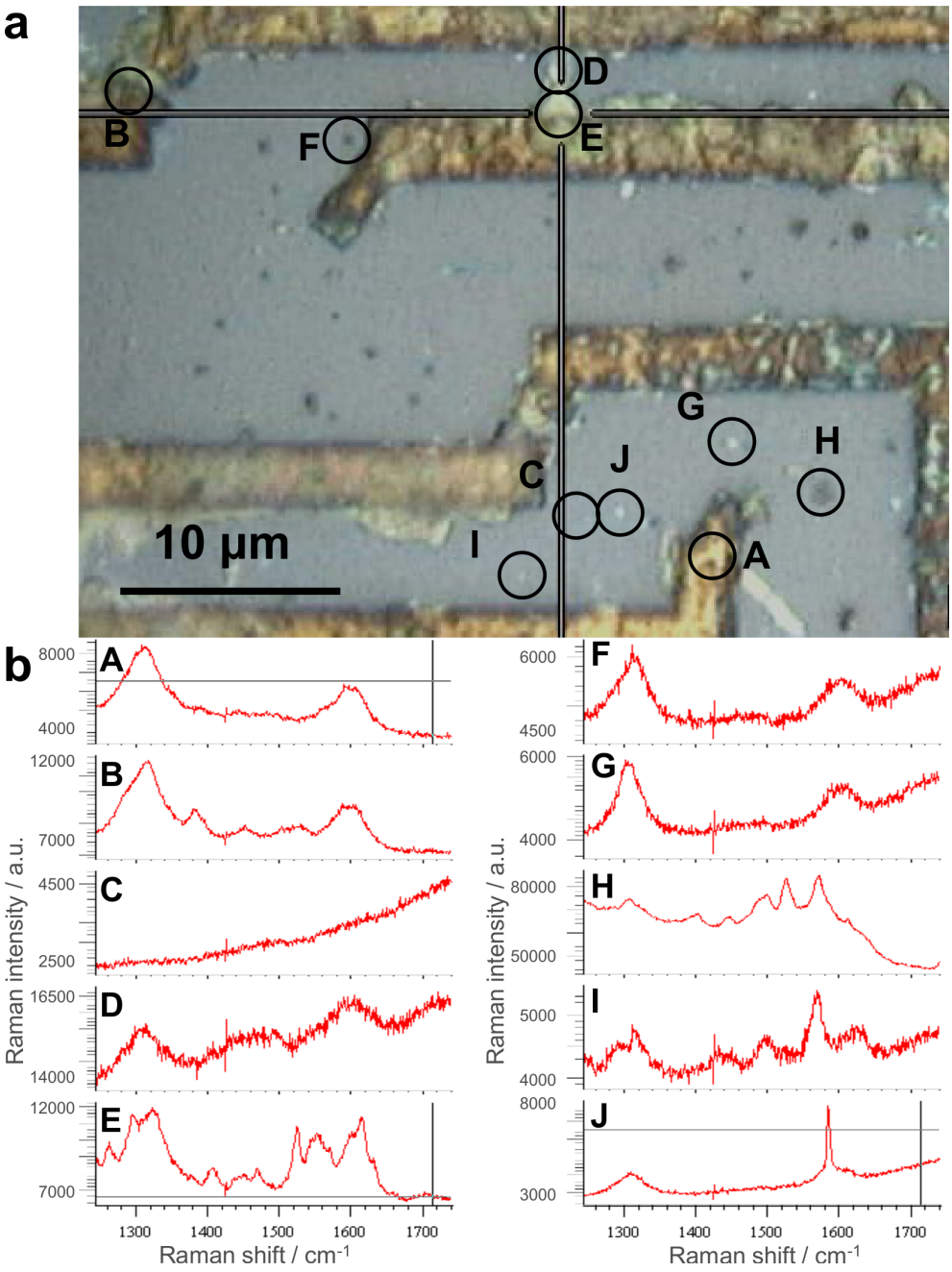

Figure I.2: (a) A sample containing SWNTs, electrodes and gold nanoparticles and (b) Raman spectra taken at different places. A: on an electrode showing only amorphous carbon; B: on an electrode with small extra peaks; C: on clear SiO_2 surface showing no peaks; D: on a gold "puddle" with poorly defined peaks; E: on a gold "puddle" with clearly defined peaks; F–I: on gold nanoparticles with a range of Raman responses.

and sometimes did not appear but it was not possible to distinguish nanoparticles from the surface roughness of the electrode, optically or by AFM. Where extra peaks were observed they fluctuated with time.

Literature reports of spectral fluctuations

Large fluctuating features in Raman spectra using SERS substrates have been observed since the 1990s, including in the paper presenting the first individual SWNT Raman spectra [116]. The first systematic studies on them were performed in 2000 [150, 151] and since then further research has been performed with goals of understanding the causes of the fluctuating peaks and developing approaches to eliminate them when unwanted [133, 152–156].

Large fluctuations are now recognised as occurring at hotspots on SERS substrates suitable for single-molecule SERS (SM-SERS) [156]. Hotspots have very high enhancement factors but small spatial volume so molecular species moving in and out of the enhanced region give radically different spectra in subsequent measurements. The movement of species in solution-phase measurements is assumed but the appearance of fluctuating peaks in solid samples implies that there is also mobility of molecules adsorbed on dry metal surfaces [155, 156].

The identity of the species being observed in fluctuating peaks is so far less well defined. In some studies specific molecular material was deposited on a SERS substrate and in others no specific analyte was added and fluctuations still appeared. In general, the fluctuations are attributed to amorphous carbon, where the term amorphous refers to the bulk structure while its local structure can be highly ordered, containing small crystalline clusters, carbon nanotubes, graphite domains and a range of structures of carbon chains [150, 151, 157]. In some studies such forms of carbon were created by decomposition of CO [150], biological molecules [152] or other molecular species [153] but in others the carbon film has no specific traceable origin and it has therefore been described by one author as "omnipresent" [155].

Several approaches have been reported to eliminate or minimise the fluctuations. Low temperatures (*e.g.* 77 K) were reported to suppress the fluctuations [155, 156] but this was not observed in all studies [157]. The number and height of fluctuations was reported to be reduced by switching the gas environment during Raman measurements to an inert gas such as nitrogen, suggesting that the presence of oxygen contributes to the fluctuations [150]. Similarly, switching

to a water environment also reduced the fluctuations [157]. Chemically removing the contaminating species from the hotspots by functionalising the surface with thiols or dye molecules prevented the fluctuations from occurring [154]. The thiol layer could be removed by oxidation then rinsing with a methanol to leave a clean surface with a larger enhancement than before cleaning [158]. Different instrument optics influence the occurrence of fluctuations, for example, using an objective lens with a lower magnification and lower numerical aperture reduced fluctuations [150], as could off-resonance excitation and lower laser powers, but these approaches led to longer acquisition times [133]. Highly specialised instrumentation to eliminate the fluctuations by rapidly scanning over a sample has been developed but is not widely available [133].

Explanation of fluctuations

After the initial observation of fluctuating peaks in the Raman spectra of samples containing SWNTs and gold nanoparticles, further studies were performed on simpler samples with only gold particles. 150 nm AuNPs were deposited on cleaned silicon wafers by either dropping and air drying or dropping and spin-coating, as described in Section 5.2. When they were examined by Raman spectroscopy, some of the particles deposited in this way exhibited large fluctuating peaks, very similar to those of the samples containing SWNTs. Figure I.3 shows how the Raman spectra change with time, over 300 s with 30 s measurements and over 180 s with 1 s measurements. Fluctuations are clearly observed on both timescales, indicating that the fastest changes occur faster than the limits of the spectrometer but also that 30 s is not long enough to get an average incorporating all the different contributions. Figure I.3 also shows that the fluctuations occur throughout the Raman shift range of 200 cm^{-1} up to nearly 1700 cm^{-1}. Above 1700 cm^{-1} almost no fluctuations were seen except one peak in the region of 2150 cm^{-1} that did vary in intensity and precise position but was only observed on some nanoparticles but not on others. This peak may be caused by water.

50 nm AuNPs were also deposited and, when studied with 785 nm laser light, they too showed signs of additional anomalous fluctuating peaks where their

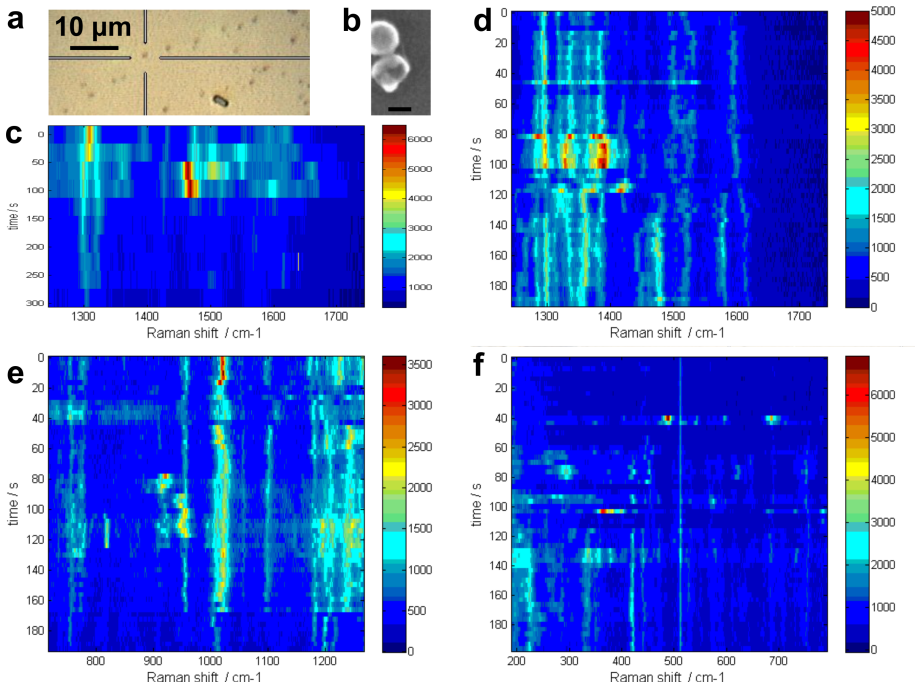

Figure I.3: Raman spectra measured on a particle that was (a) visible in an optical microscope image and (b) seen in SEM to be a dimer. (c) Ten repeated measurements of 30 s were made with no change in position and they are plotted as a colour map where colour represents Raman intensity and the y axis denotes time. (d) The measurement time was reduced to 1 s, with approx. 2 s between each of the 60 measurements and this was plotted in the same way. (e and f) Other spectral ranges were also probed and fluctuating peaks were seen on the 1 s timescale from 200 cm^{-1} up to nearly 1700 cm^{-1}. The scale bar for the SEM image is 100 nm.

density was very high at the edge of a droplet or in clusters large enough to appear as a particle in the optical microscope. Irradiation of either size of particle with 514 nm light did not reveal any fluctuations, despite the plasmonic resonance of the 50 nm AuNPs being close to this wavelength.

The optical microscope picture that was used to position the sample for Raman spectra showed isolated particles but it was not able to resolve separate nanoparticles from within a cluster (Figure I.4b). SEM on the same area (Figure I.4a), performed after Raman measurements were completed, did allow the number of particles to be counted. The number of particles was compared to the total intensity (in the range 1248–1740 cm^{-1}) measured for 60 s, which was long enough to give an average of some of the fluctuations (Figure I.4c). This showed that the largest intensities were only achieved with four or more nanopar-

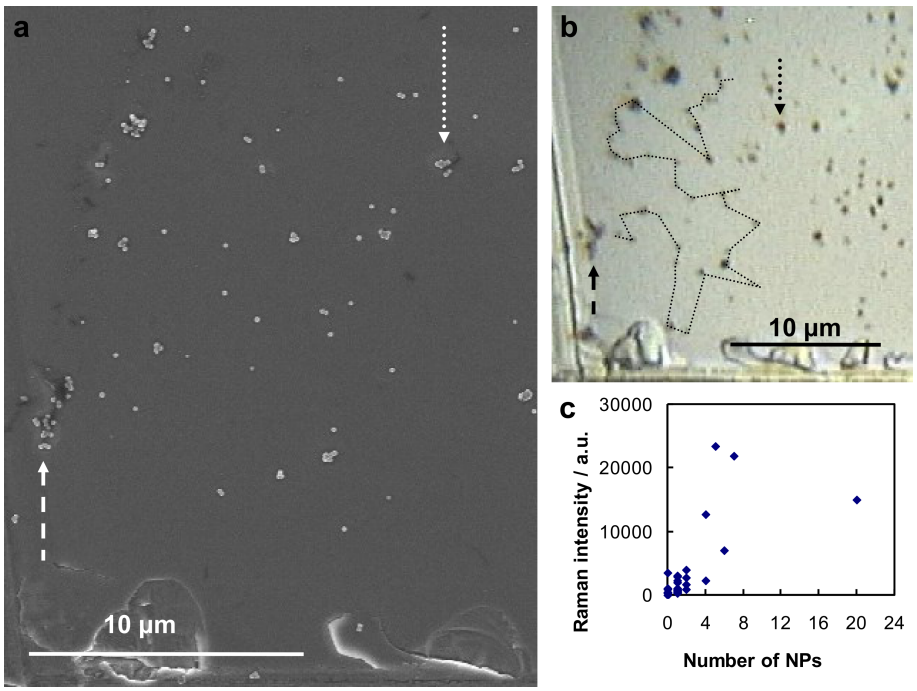

Figure I.4: (a) SEM and (b) optical microscope images of 150 nm AuNPs deposited on a clean silicon substrate. Raman spectra were measured at every corner of the light grey line on the optical image. (c) The total measured Raman intensity over 60 s was integrated and plotted against number of particles. Note that some particles that were seen in the optical microscope during Raman measurements were lost before the SEM. The arrows point to the same places on each image, to aid alignment and comparison.

ticles clustered together.

The large scatter of points observed in Figure I.4c and the variations observed in the Raman spectra are not fully explained by simply the number of nanoparticles in the agglomerate. Higher resolution SEM revealed that the particles are not perfectly spherical, as might have been assumed from their commercial presentation. Figure I.5 shows that some particles had craters in their surface and some particles, in a different production batch, had large chunks missing from their shell. These irregularities go a long way towards explaining the variations in behaviour and the occurrence of spectral fluctuations. Compared to the modest SERS enhancement offered by a spherical particle, particles with sharp corners or points have greatly increased and more localised field enhancement at the sharp point. In addition, Figure I.5 shows several dimers with a closer relationship between the particles than theoretical models would assume, which could increase

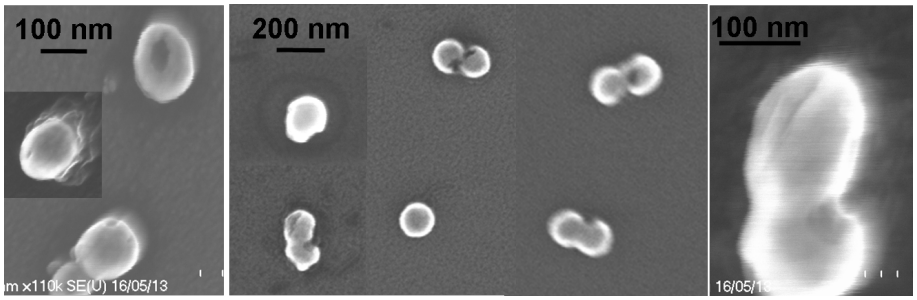

Figure I.5: High resolution SEM images of 150 nm AuNPs, showing craters in their surface, large chunks missing from their shell and intimate coupling to produce AuNP dimers. Note that the elliptical shape in the final image is an artefact caused by thermal drift during image acquisition.

the strength of the plasmon coupling and give a stronger overall resonance. Together these observations explain how single-molecule SERS conditions have been achieved with AuNPs and why fluctuations are observed.

In addition, the lack of fluctuating peaks observed with the 514 nm laser can be explained with the knowledge obtained from the SEM images. It can be seen that single AuNPs do not show large fluctuating peaks, presumably because they do not have a structure that has a hotspot with a particularly high enhancement. When two or more nanoparticles cluster together to form a larger total structure, the resonance is red-shifted. So it would seem that individual 50 nm AuNPs have a plasmonic resonance at 514 nm that is too weak to cause fluctuations while agglomerates of 50 nm AuNPs can have a strong plasmonic resonance with a fluctuation-causing hotspot that is red-shifted enough to be excited by 785 nm light.

Approaches taken towards eliminating fluctuations

If the fluctuations observed during Raman measurements were caused by laser heating leading to increased molecular mobility on the surface then they might be eliminated or reduced by making short measurements with a longer period without laser exposure between them. This is a simple version of the sophisticated

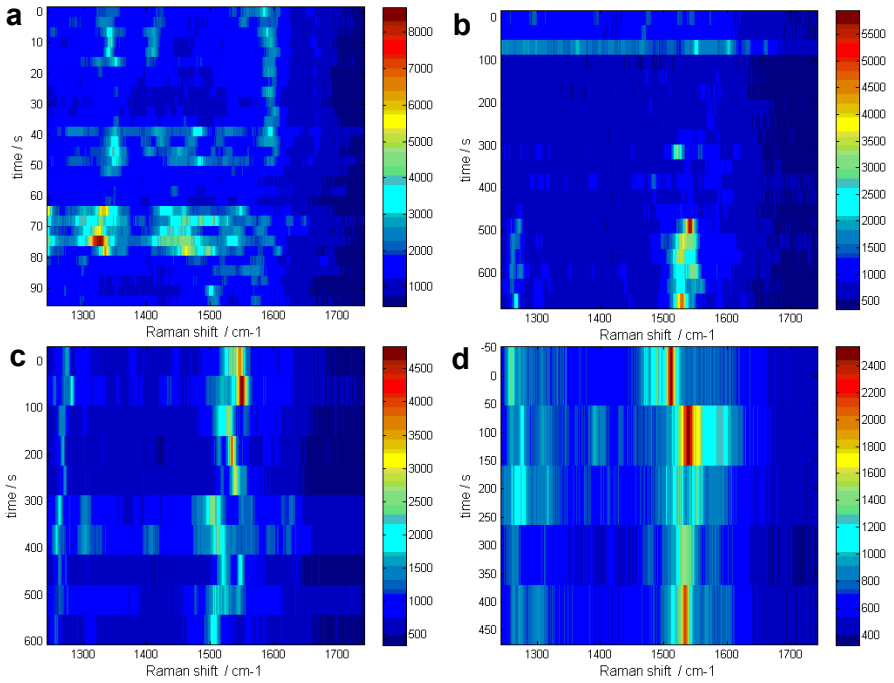

Figure I.6: Raman spectra, with intensity represented by colour, from repeated measurements, each with 1 s acquisition time and with varying time between subsequent measurements: (a) 0 s, (b) 30 s, (c) 60 s and (d) 120 s.

instrumentation developed by Yeo *et al.* [133]. Figure I.6 shows the results of repeated measurements of 1 s with intervals of 0 s, 30 s, 60 s and 120 s during which time the laser shutter was closed. Clearly fluctuations still occur in all cases. The average intensity of the spectra decreases by a factor of two between 0 s and 30 s but there is no significant additional change with 60 s or 120 s delays. This indicates that laser heating may have some effect, which may be minimised by having a gap in laser irradiation between measurements. However, the fluctuations are not eliminated entirely so if laser heating is the cause then shorter pulses than 1 s must be used, which were not possible with the available Raman instrument.

Removing the oxygen from the atmosphere has also been reported as a way of reducing SERS fluctuations [150]. This was tested by placing a sample with 150 nm AuNPs deposited on a silicon wafer into a chamber with optical window and gas inlet and outlet (Linkam LTS350 chamber with TMS94 controller, from Linkam Scientific Instruments, UK). Repeated measurements were made (Figure I.7), starting with the chamber filled with air and continuing as a flow of nitrogen

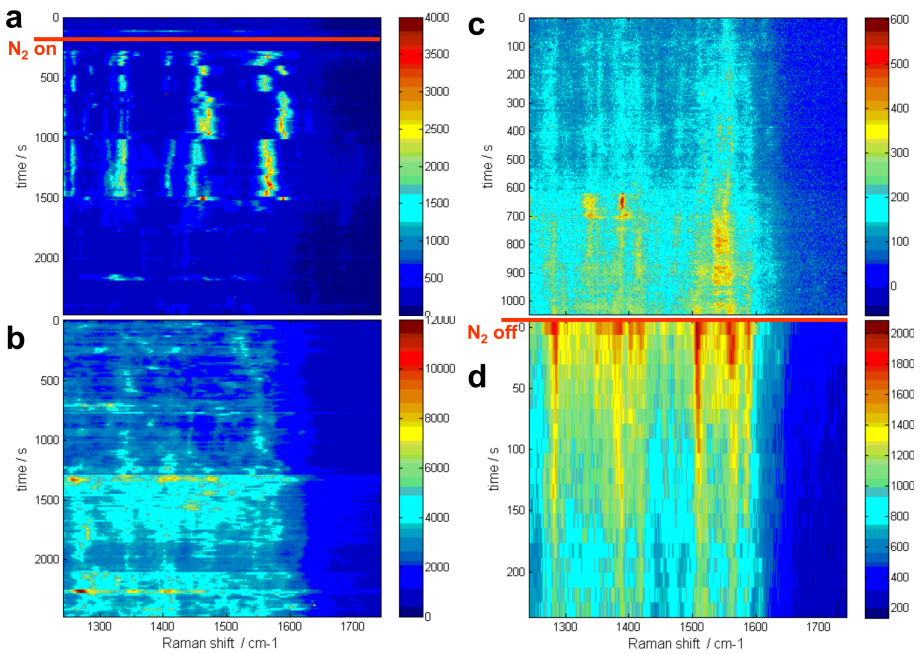

Figure I.7: Raman spectra, with intensity represented by colour, from repeated measurements, initially in air and then with a flow of N_2 gradually replacing the air in a sealed chamber until it was turned off, at which point air could diffuse slowly back into the chamber. Consecutive measurements were made of (a) 200 spectra of 10 s acquisition, (b) another 200 spectra of 10 s acquisition, (c) 300 spectra 1 s acquisition and finally (d) 20 spectra of 10 s acquisitions after the N_2 gas was turned off.

was added to the chamber. The chamber remained at ambient pressure as the gas outlet was open to the laboratory through a 3 cm length of tubing. Over two hours measurements were continued and the fluctuations decreased in neither size nor rate. Contrary to the literature, the overall intensity of the spectra, caused by the SERS fluctuations, increased in a nitrogen atmosphere. Indeed, there was a 40% increase in total spectrum intensity for the average of the final 30 spectra measured in N_2 in comparison with the first 30 spectra taken before any N_2 was applied.

Similar experiments were performed on another sample that exhibited intense fluctuating SERS peaks. Again, switching to nitrogen gas did not prevent the fluctuations from occurring. The increase in intensity was not as striking but there was a gradual increase in the total spectral intensities from the first to the last spectrum of each measurement, as the nitrogen proportion was increased. Some large peaks were still sometimes seen after the nitrogen was added to the

chamber.

It was hoped that the carbon contaminant that causes the fluctuating peaks could be burned off by heating the sample in air. This was tested with the same sample as above, also in the Linkam chamber, which allows heating. The chamber is most effective at controlling the temperature with the lid shut but the image quality through the window is worse and, since an air environment was desired, the experiments were performed with the lid open. Figure I.8 shows some of the results obtained from this experiment. A particle that displayed strong fluctuations at room temperature (Figure I.8a) was heated up to 200 °C with Raman spectra being measured at various temperatures. Thermal drift increased significantly meaning that at higher temperatures the sample would drift out of focus or away from the laser spot before many the series of repeated measurements was complete but extra fluctuating peaks were still seen at the highest of temperatures. When the sample was cooled to room temperature the fluctuations were clearly seen again (Figure I.8b). Another cycle of heating was immediately begun, going up to 250 °C. Again, at the high temperatures drift occurred but extra peaks and fluctuations were still seen (Figure I.8c). The same experiment was performed on another occasion, going to a maximum temperature of 130 °C with the same results being obtained (not shown).

A plot of average Raman intensity against temperature for each of the measurements in the heating cycle (Figure I.8d) shows that the average intensities of the spectra increase with temperature. It was therefore concluded that heating to temperatures of between 200 °C and 250 °C in air was not effective at eliminating SERS fluctuations by burning.

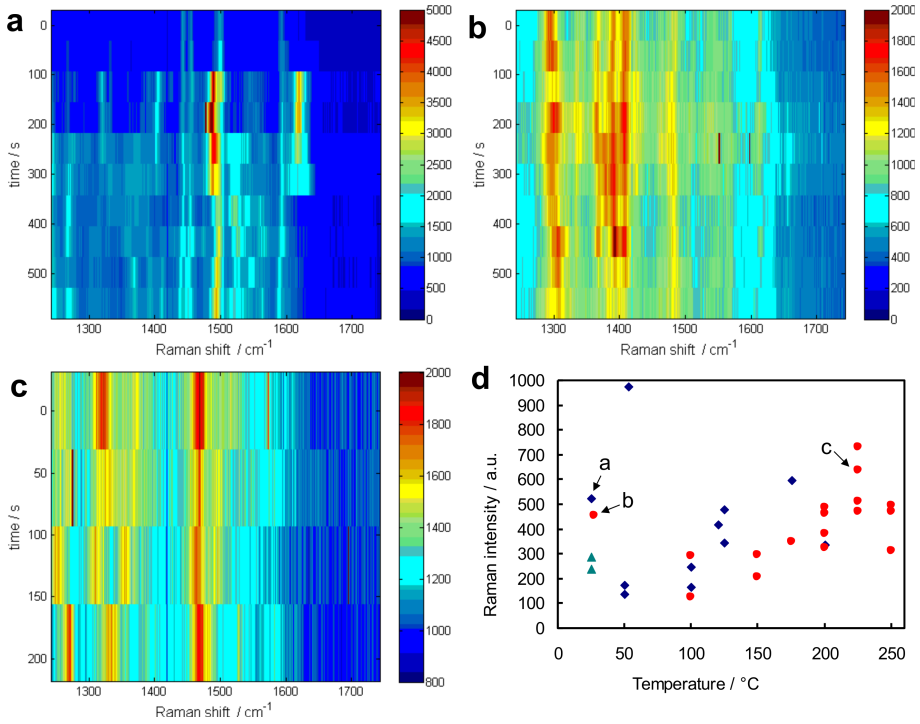

Figure I.8: Raman spectra, with intensity represented by colour, from repeated measurements all with 60 s acquisition time, (a) initially at room temperature, (b) after being heated to 200 °C then returning to room temperature and then (c) again being heated to 225 °C. The total integrated area of each spectrum within these series was measured and an average taken for all spectra within each series. (d) These average values, from the series shown in parts a, b and c as well as the others measured during the heating cycle are plotted against temperature. Blue diamonds represent the first heating from room temperature to 200 °C, red circles represent the second heating cycle from room temperature to 250 °C and green triangles represent the final room temperature measurements after the heating.